

## **Manuel Rocha Lecture**



**Manuel Rocha** (1913-1981) was honoured by the Portuguese Geotechnical Society with the establishment of the Lecture Series bearing his name in 1984.

Having completed the Civil Engineering Degree at the Technical University of Lisbon (1938) he did post-graduate training at MIT. He was the driving force behind the creation of the research team in Civil Engineering that would lead to the foundation of the National Laboratory for Civil Engineering (LNEC), in Lisbon. He was Head of LNEC from 1954 to 1974 and led it to the cutting edge of research in Civil Engineering.

His research work had great impact in the area of concrete dams and rock mechanics. He was the 1<sup>st</sup> President of the International Society for Rock Mechanics and organized its 1<sup>st</sup> Congress in Lisbon (1966). He did consultancy work in numerous countries. He was Honorary President of the Portuguese Geotechnical Society, having promoted with great commitment the cooperation between Portugal and Brazil in the area of Civil Engineering, and member of the National Academy of Sciences of the USA. Recognized as a brilliant researcher, scientist and professor, with a sharp, discerning intellect allied to a prodigious capacity for work and management, he was truly a man of many talents.



**Prof. EDUARDO E. ALONSO**, Civil Engineer (Madrid, 1969) and Ph.D. (Northwestern University, 1973), Full Professor at UPC, Barcelona in 1986 and member of the Royal Academy of Engineering of Spain in 1995. His areas of expertise include probability and statistics, unsaturated soil mechanics, rock mechanics, thermo-hydro-mechanical behaviour of soils, embankment dams and slope stability. He was awarded twice the Thomas Telford Medal, ICE, UK (1994 & 2006), the 2009 & 2010 Geotechnical Research Medals and the 2005 Crampton Prize; the José Torán Award (1995), Spanish Committee on Large Dams; the 2000 Narcis Monturiol Award, Generalitat de Catalunya and the Monterri Award (2014), Switzerland. He was the 2<sup>nd</sup> Coulomb Lecturer (2003), 11<sup>th</sup> Buchanan Lecturer (2003), 10<sup>th</sup> Sowers Lecturer (2007), 10<sup>th</sup> Arrigo Croce Lecturer (2011), 1<sup>st</sup> Heim Lecturer (2012) and 3<sup>rd</sup> Kezdi Lecturer (2013).

**Soils and Rocks**  
**v. 37, n. 1**



# Fracture Mechanics and Rockfill Dams

Eduardo E. Alonso

**Abstract.** Rockfill behavior is dominated by particle breakage, a phenomenon which is analyzed from the perspective offered by the subcritical propagation of cracks within individual particles. Propagation velocity depends on stress concentration in particles as well as on the ambient Relative Humidity (RH). RH controlled oedometer and triaxial tests are reviewed and constitutive models reproducing the main features of observed behavior are outlined. The relevant issue of size effects is then introduced and some rules and possibilities to account for these effects in practice have been given. The Distinct Element Method is also a powerful tool to investigate rockfill behavior. Recent developments are described. The model developed incorporates particle breakage, delayed effects and the action of water. In the final part two real cases are presented: the response of a high rockfill embankment against a four year long rainfall regime and the analysis of Beliche dam. The lecture closes by a general discussion of partial saturation in granular materials ranging from coarse granular aggregates, such as rockfill, to clayey soils in an attempt to provide an integrated overview of water effects in soils.

**Keywords:** rockfill, fracture mechanics, crack propagation, relative humidity, suction controlled testing, constitutive models, embankments, dams, case histories.

## 1. Motivation

The use of rockfill as a construction material goes back to early civilizations. An outstanding example is Sadd-el-Kafara dam (Fig. 1) built in Egypt in 2,600 B.C. (Schnitter, 1994). The dam, 14 m in height, had an impervious core protected by two rockfill shoulders, bounded by a

masonry fabric. However, it was at the beginning of the 20<sup>th</sup> Century that the design of dams including rockfill was generalized. Two types were designed: either a zoned structure which integrates rockfill shoulders and some internal impervious core, or an entire rockfill resisting structure, made impervious by an upstream blanket.

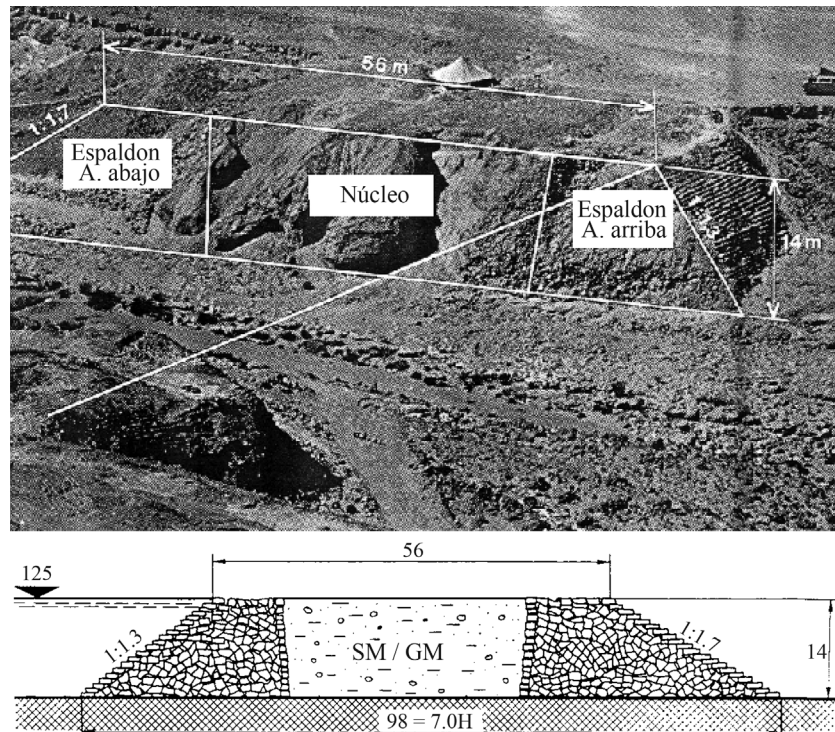


**Figure 1** - Sadd-el-Kafara. Rockfill dam built in Egypt in 2600 b.C. (Schnitter, 1994). Following Casagrande classification, SM/GM describes the core material. SM: silty sand, GM: silty gravel. Dimensions in meters.

A modern example of a large dam (136 m in height) of triangular section made of compacted gravels and an upstream concrete face is Caracoles dam in the Argentinian Andes, close to the city of San Juan (Fig. 2). The construction material was, in this case, alluvial gravel compacted in layers (Fig. 3). This type of design is a popular one in the Andes mountain range, where there is often the possibility of building with river gravels, as clay is rather scarce.

A common design in Spain is the zoned rockfill dam: Imperviousness is guaranteed by the central compacted clay core and the stability of the entire structure is ensured by the large rockfill shoulders on both sides of the core. Most typically the rockfill comes from a quarry. Lechago dam, on the Pancrudo River, in the province of Teruel, is a recent example of this type of dams (Figs. 4-8). The quartzitic shale gravel (Figs. 7 and 8), used in the construction of this dam, has been analyzed in some detail in the last decade in the UPC Geotechnical Laboratory. Its behavior, which is described below, allowed also formulating elastoplastic constitutive models for these materials.



**Figure 2** - Caracoles dam under construction (2007). San Juan, Argentina.



**Figure 3** - Caracoles dam under construction (2007). San Juan, Argentina. Detail of the gravel fill.

In these large structures, settlements are observed, which may be rapid settlements (associated with the wetting of the upstream rockfill shoulder, for instance by the reservoir impoundment) or long-time settlements. Wetting



**Figure 4** - Lechago dam, Teruel, Spain. Aerial view. February 2008.



**Figure 5** - Lechago dam, Teruel, Spain. February 2008.



**Figure 6** - Lechago dam. Core, filters and rockfill shoulders.



**Figure 7** - Lechago dam. Detail of rockfill.



**Figure 8** - Lechago dam. Outcrop of Cambrian quartzitic shales quarried for rockfill material.

induced settlement (collapse) is a consequence of the volumetric contraction experienced by the rockfill when the pores are filled with water. Figures 9 to 11 illustrate this phenomenon in two dams: Calanda dam, in Teruel, and Martín Gonzalo dam, in Córdoba. Figure 10 shows the effect of these deformations on the crest of the dam, and Fig. 11 shows the large settlement (in the upstream direction) observed in Martín Gonzalo dam, due to the wetting of the lower part of the resisting rockfill section. The upstream impervious membrane eventually fissured and reservoir water could freely saturate the rockfill.

Figure 12 illustrates a very significant phenomenon: settlement of the dam at different heights is well-correlated with rainfall. The figure shows that settlements concentrate in the periods of the year having the strongest rainfalls. In drier periods the settlement rate slows. In fact, the plot in Fig. 12 allows defining two types of settlements: a maintained, slow motion (which could be designated as creep) in dry periods, and a rapid settlement associated with intense

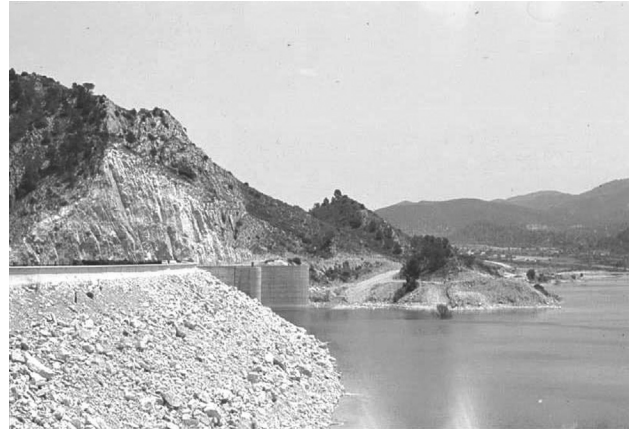


**Figure 9** - Calanda dam, Teruel, Spain.



**Figure 10** - Collapse settlements of rockfill in Calanda dam.



**Figure 11** - Collapse settlements of rockfill in Martín Gonzalo dam, Córdoba, Spain.

rainfall (which wets the rockfill and results in collapse deformations). These collapse settlements disappear after the first three years of life of the dam. The reason for this behavior will be given later. Before, some basic discussion of

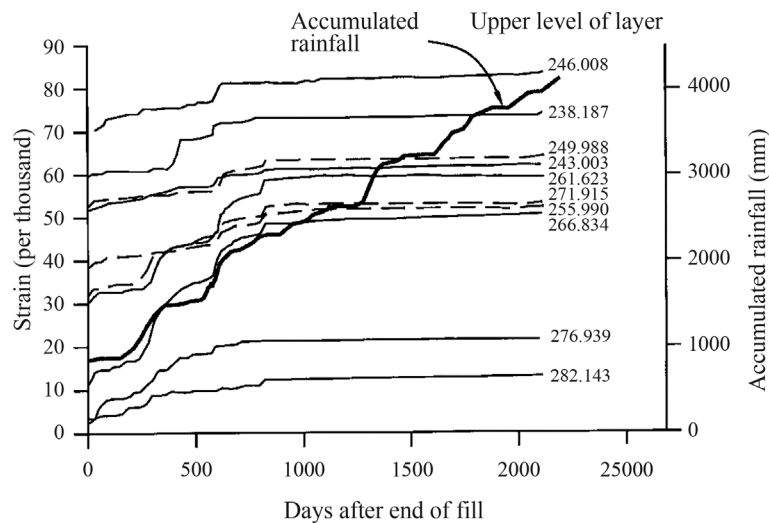


**Figure 12** - Martín Gonzalo dam. Settlement of plates located at different heights in the axis of the dam maximum cross section and accumulated rainfall. Justo and Durand (2000).

the fundamentals of rockfill mechanics should be introduced.

The systematic measurement, for decades, of dam settlements after construction provides also interesting data on these structures (Sowers *et al.*, 1965; Sherard & Cooke, 1987; Marsal *et al.*, 1976). Figure 13 shows a summary of results published by different authors. Dams are classified in four groups. In ancient concrete face rockfill dams (CFRD) rock fragments were dumped without compaction. They suffer large settlements which may amount to more than 1% of dam height. However, modern CFRD dams, built with compacted rockfill exhibit much lower after compaction settlements. It was found that compacting these dams in layers, which is the common practice in earthfills, substantially reduced settlements. Data published by Sherard and Cooke (1987) show that, in compacted rockfill, postconstruction settlements remain in the order of 0.13% of dam height. Figure 13 shows similar results.

Settlements of dams made of alluvial gravels are also small. The reason goes back to the rounded nature of the particles and, also, to the often well graded materials found in alluvial deposits. Both characteristics limit the particle breakage.

Note also that recently built dams, made of compacted rockfill (Beliche in Portugal; Rivera de Gata in Spain) experienced large post-construction settlements. This behavior is explained by the type of rockfill. Fissile and brittle clayey rocks such as schists, shales, slates and grauwackes are prone to particle breakage which leads to comparatively larger settlements.

A common characteristic to all settlement curves in Fig. 13 is the long term record of settlements. Settlements are being measured after 20-30 years after the dam construction. Most of the curves in Fig. 13 may be described by a linear relationship between settlement and logarithm of

time. Deformation does not stop although the settlement rate decreases continuously.

Post-construction settlements of rockfill dams may impair the dam safety or its operability. But, in general, no serious problems have been reported. Extreme cases such as Ataturk dam in Turkey (Cetin *et al.*, 2000), which exhausted the crest guard, five years after the dam commissioning, are rare events.

Rockfill embankments are frequently used in transport infrastructure. In high speed railway lines strict limits are applied to the expected total and differential settlements in order to guarantee the safe operation of trains.

Models for delayed deformations have been published by a few authors (Sowers *et al.*, 1965; Mesri & Castro, 1987; Charles, 1991; Soriano & Sánchez, 1999; Athanasu *et al.*, 2005). Stress-strain models such as the hyperbolic Charles (1989) model and the visco-elastic formulation of Justo & Durand (2000) are phenomenological approximations to observed behavior. But a more detailed knowledge of basic physical phenomena at particle level may provide better models. This is the case for delayed deformations but also for the evaluation of strength, compressibility, water action and, in general, for a comprehensive constitutive behavior of these materials.

This paper starts by examining the breakage of particles as a fundamental mechanism to explain the behavior at a larger scale. Particle breakage, in turn, is explained by the propagation of cracks or fissures. Key aspects such as the velocity of crack propagation and the controlling factors (stress state, ambient Relative Humidity) will provide a satisfactory explanation to observations. They are also useful to conceive experimental programs aiming at developing constitutive models. A different approach, namely the capability of the Distinct Element Method, will be also described. At the end, it is the comparison between model

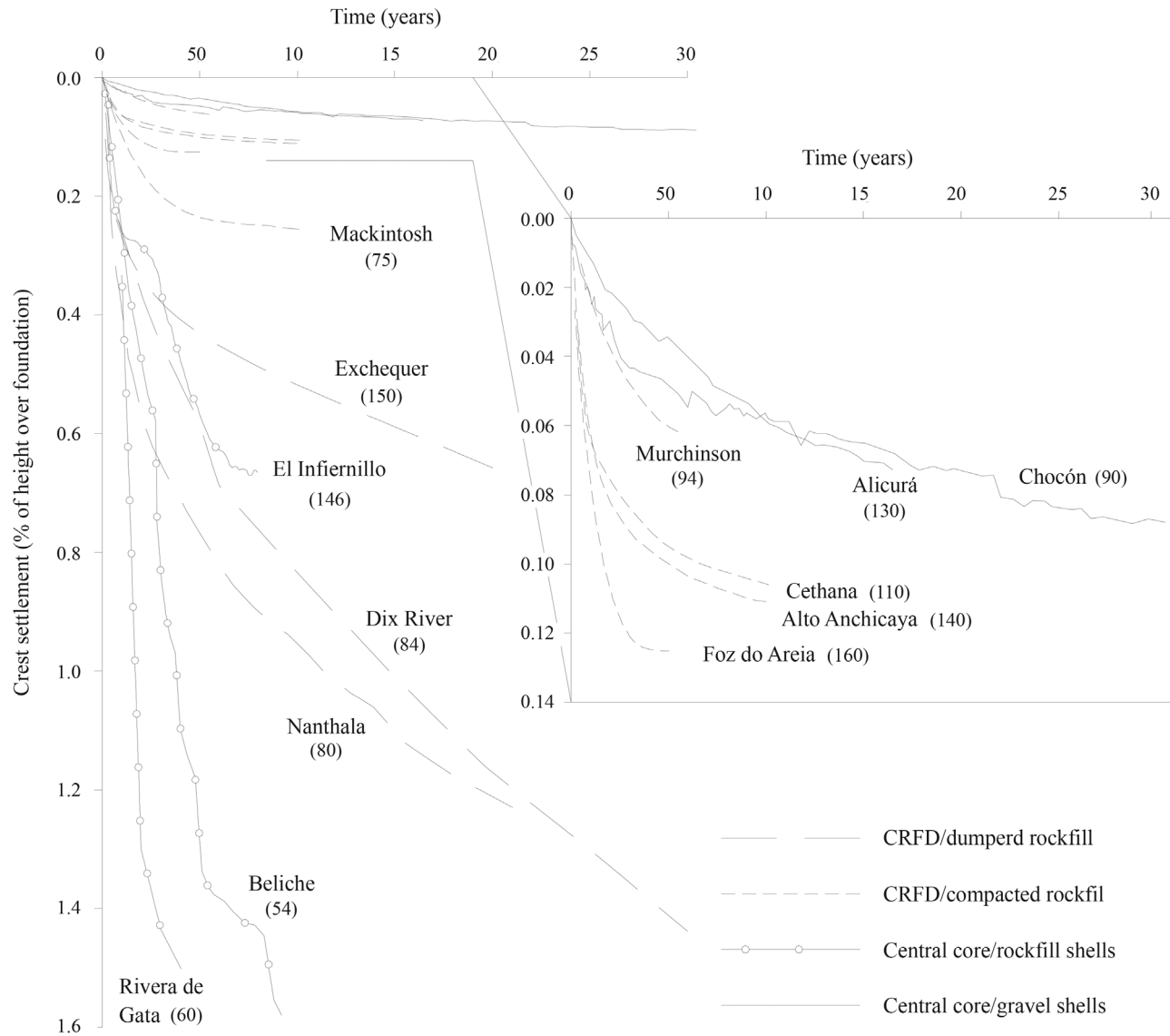


**Figure 13** - Records of crest settlement of different types of rockfill dams built during the 20th century. Name (height in m) of the dam next to each curve. (data sources: Sherard & Cooke, 1987; Naylor *et al.*, 1997; Soriano *et al.*, 1992; Marsal *et al.*, 1976).

predictions and “in situ” behavior the necessary check to establish the practical applications of the ideas and models presented.

## 2. Background

### 2.1. Water induced collapse of rockfill

The action of water is fundamental to explain the development of settlements. Collapse of upstream rockfill shoulders, a phenomenon taking place during the first reservoir impoundment, is well known. The term “collapse” refers here to the increase of volumetric compression, at constant confining stress, induced by the action of water.

In parallel to field observations, laboratory tests in which samples of gravel were loaded and wetted at constant stress also experienced collapse deformations. Terzaghi

(1960) attributed this behavior to particle breakage due to the weakening effect of water on the wetted rock.

Collapse settlements in dams and laboratory tests were reported by Sowers *et al.* (1965); Marsal (1973); Nobari & Duncan (1972). Figure 14a,b reproduces the results of oedometer tests performed on a crushed shale from Pyramid dam (Nobari & Duncan, 1972). Flooding samples initially dry, either at constant stress or at constant porosity, took the sample state to the compression curve for saturated conditions. This is a result formally identical to the behavior observed in partially saturated soils (Alonso *et al.*, 1987).

However, the deformation mechanisms of coarse granular aggregates and fine soils (fine sands and smaller particle size) should be fundamentally different. To illustrate this statement, Fig. 15 shows the variation of attractive cap-

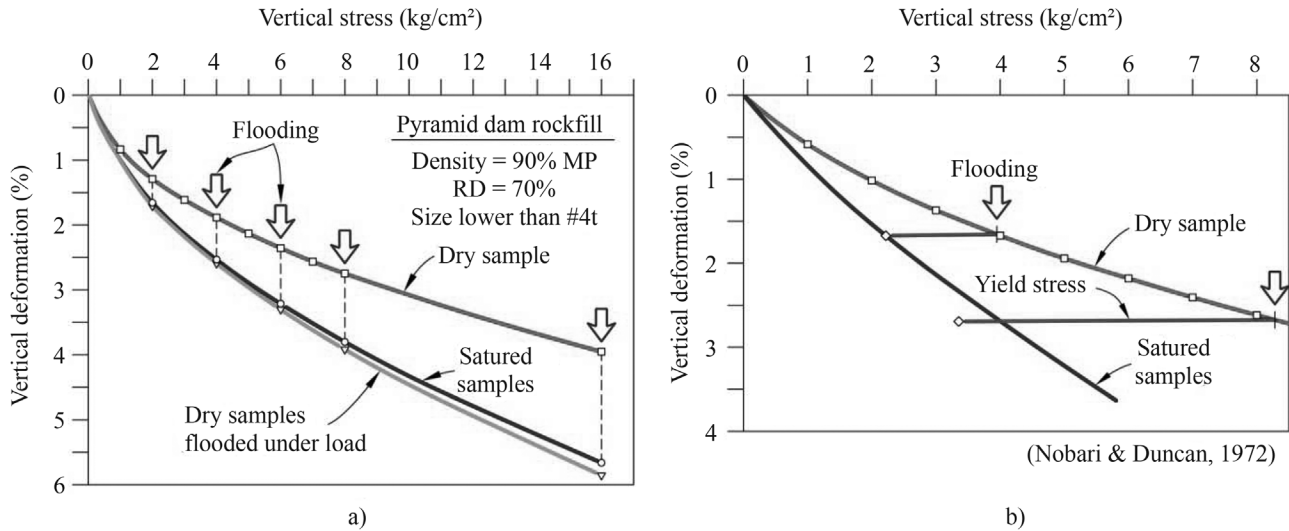


Figure 14 - Oedometer tests reported by Nobari & Duncan (1972) a) flooding at constant stress; b) flooding at constant volume.

illary force between two spherical particles when there is a water meniscus at the contact. The attractive force,  $F_w$ , was calculated following the theory of toroidal meniscus described in Gili (1988). In the four cases presented (“rockfill”, diameter  $D = 50$  cm; “gravel”,  $D = 10$  mm; medium sand,  $D = 0.5$  mm and medium silt,  $D = 0.01$  mm) the particle weight is used as an appropriate scale for the capillary force. For sizes larger than the size of small gravel, the particle weight is higher than the maximum capillary force

in isolated menisci. Therefore, the internal capillary forces will tend to be negligible in coarse granular soils.

Figure 16 shows, in absolute terms, the capillary forces  $F_w$ . They are also represented as a normal stress across a reference plane which connects the contact points among spheres in a regular cubic array. The rapid reduction of the number of contacts when the particle size increases explain the low stress intensities calculated for the coarse aggregates. This is the case shown in Fig. 16 for the four materials considered in this example. It is concluded that capillary forces are not relevant to explain the effect of water on rockfill materials.

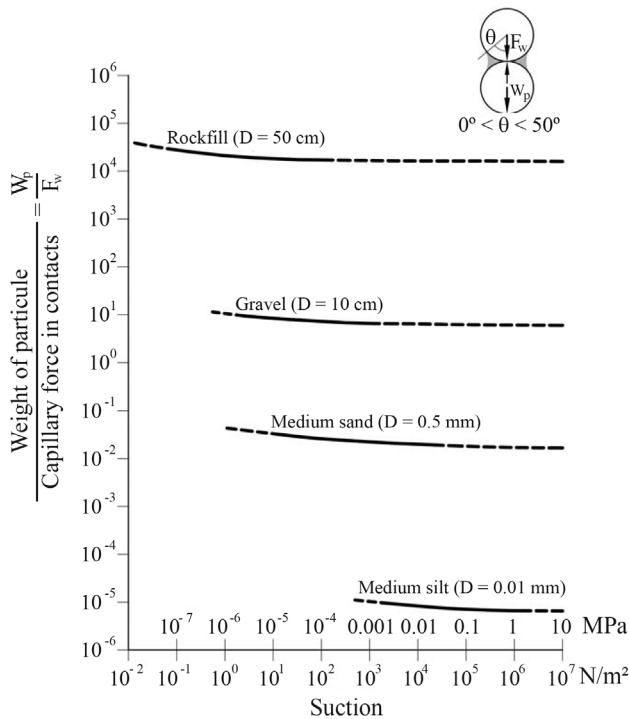


Figure 15 - Attraction capillary force in simple spherical cubic array.

On the other hand compression tests on rock wedges in contact with surfaces of the same rock or against other material, performed by some authors (Sowers *et al.*, 1965; Marsal, 1973; Clements, 1981) suggest that contact failure is the fundamental mechanism explaining rockfill deformation and also explain water effects. Figure 17a shows a compression test of a rock wedge (vertex angle  $169.1^\circ$ ) reported by Clements (1981). The effect of saturating the contact point, two hours after the application of the compression load, is to suddenly accelerate the deformation in a manner similar to observations in oedometer tests on samples of crushed greywacke and sandstone described by Sowers *et al.* (1965) (Fig. 17b).

These tests suggest that the deformation of the granular aggregate under the water action has to be explained, to a certain extent, as a result of the fracture of the rock matrix. These phenomena are revisited later.

## 2.2. Shear strength

The research carried out in the 60’s and 70’s of the 20<sup>th</sup> century clearly established the particle breakage as the dominant deformation mechanism of rockfill and gravels. Marsal (1973) and Hardin (1985) proposed breakage indi-

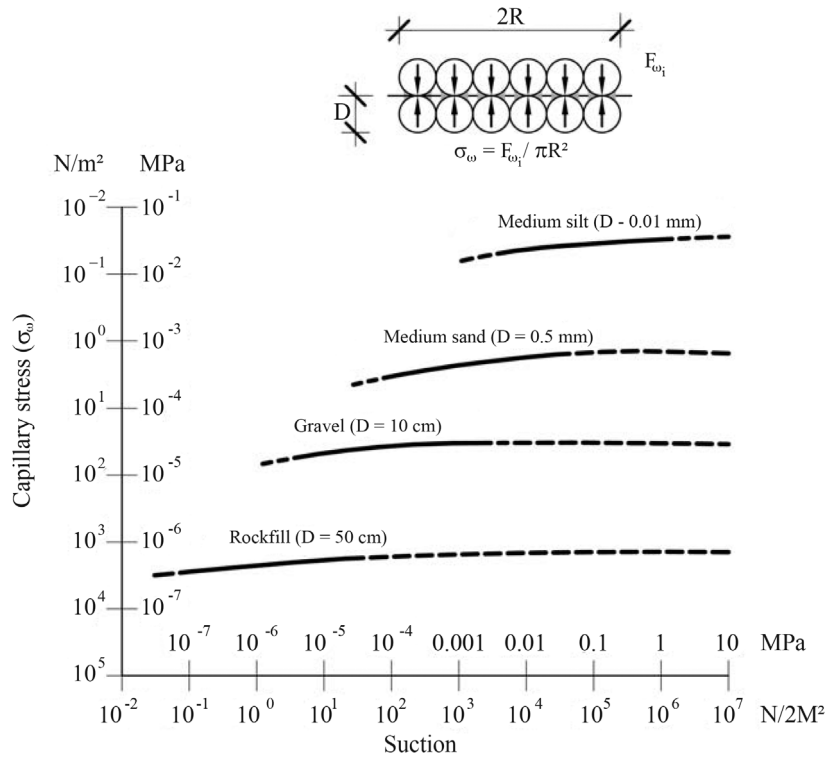


Figure 16 - Capillary attraction stress in a simple spherical cubic array.

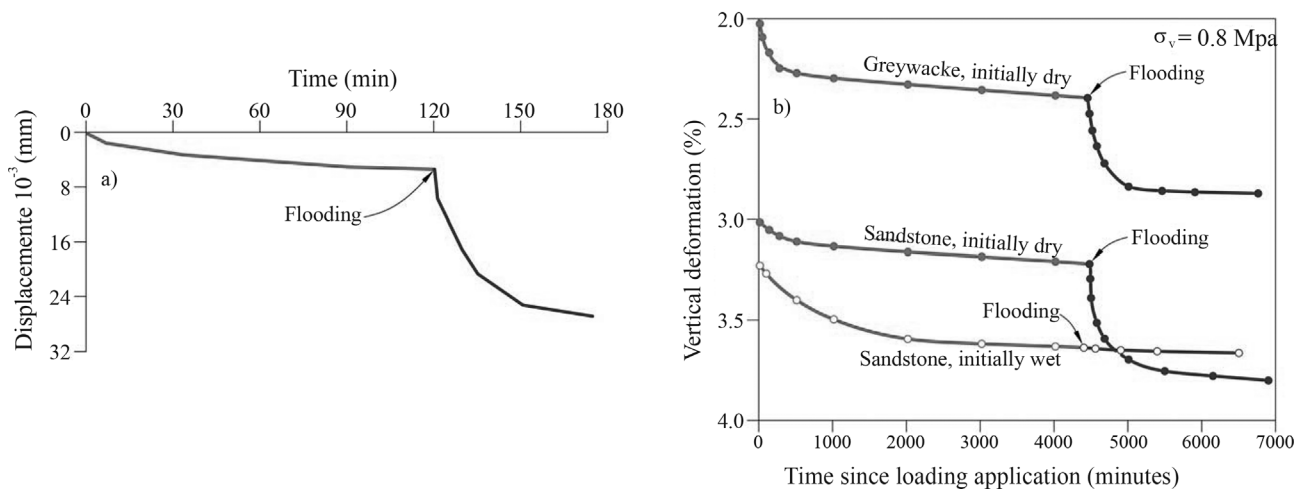


Figure 17 - a) Flooding test on a rock wedge (Clements, 1981); b) Effect of flooding the sample in oedometer tests of crushed rock under a constant vertical stress of 0.8 MPa (Sowers *et al.*, 1965). Oedometer diameter: 190 mm, sample height: 100 mm; maximum size of particles: 38 mm.

ces to quantify particle breakage. Large scale triaxial tests were also performed (Fumagalli, 1969; Marachi *et al.*, 1969; Marsal, 1973) in connection with the construction of large dams, especially in Mexico and the United States. The objective was to find the failure envelope, fundamental information to calculate the stability of dams. Charles & Watts (1980) stressed that the failure envelope was curved, especially for low confining stresses. This was one of the

most relevant differences found when comparing soils and rockfill. For instance, the curved envelope:

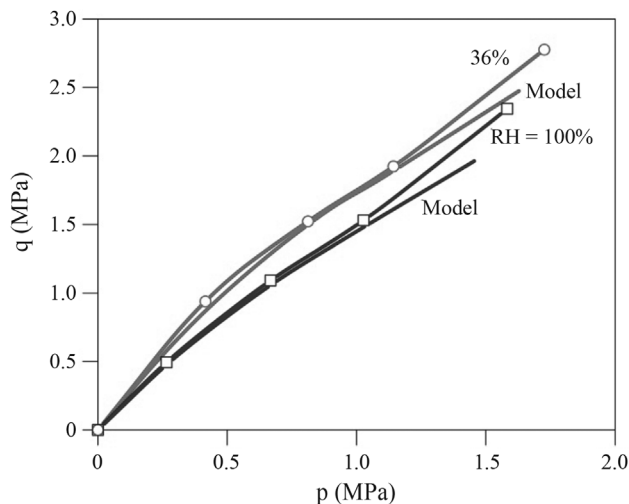
$$\tau_f = A(\sigma)^b \tag{1}$$

where  $A$  and  $b$  are empirical constants, was proposed by De Mello (1977). The nonlinearity was attributed to the particle breakage during the entire stress path (confining and deviatoric stages).

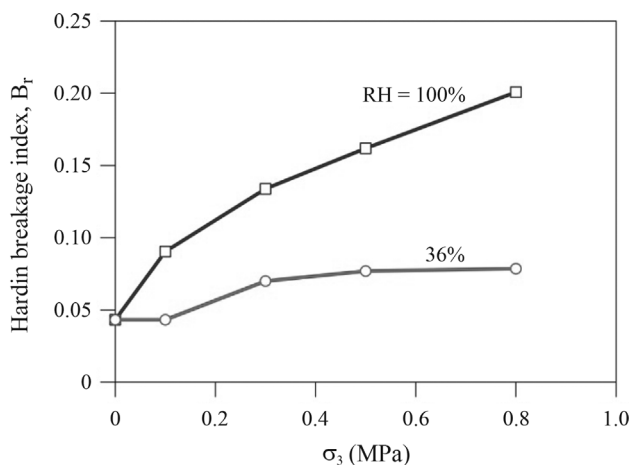
Wetting tests at some instant during the performance of triaxial tests in large diameter samples (Veiga Pinto, 1983; Naylor *et al.*, 1986) also identified the partial collapse under the combined effect of average and deviatoric stress. This collapse resulted in a decrease of the strength of saturated samples, if compared with “dry” samples.

Figure 18 shows the strength envelope of the shale gravel used in the construction of Lechago dam. The gravel was tested in a suction controlled large diameter cell in the geotechnical laboratory of UPC. The attention given to suction (or, alternatively, Relative Humidity) is discussed below in more detail. The increase in RH of the sample resulted in a decrease of the sample shear strength.

The grain size distributions determined at the end of the triaxial tests, at different RH (Fig. 19), indicated that particle breakage (quantified by Hardin index) increases with RH. In the figure the breakage index is plotted in terms



**Figure 18** - Shear strength envelope of Pancrudo shale for RH = 36% and RH = 100% (Chávez, 2004).



**Figure 19** - Hardin breakage index determined in RH controlled triaxial tests on compacted Pancrudo shale (Chávez, 2004).

of the confining stress in the triaxial cell. The breakage index for  $\sigma_3 = 0$  indicates the effect of compaction. Samples were in this case compacted under an energy equivalent to Standard Proctor.

The experimental and theoretical research on rockfill behavior came to standstill during the last two decades of the 20<sup>th</sup> century, perhaps as a consequence of the reduction of large hydraulic works in developed countries. The interest on these materials has resumed in recent years because of the need to develop prediction models which could compare with methods available for soils in general.

Probably, the best starting point to understand the accumulated experimental knowledge on rockfill behavior and, also, with the purpose of developing models of behavior at a macroscopic scale, is to examine in more detail the particle breakage phenomena.

### 2.3. Particle breakage

Figure 20a is a photograph of a sample of hard gravels of sandstone crushed and prepared to be tested in an oedometer cell having 30 cm in diameter and control over relative humidity. The gravel particles had a uniform size, which ranged 20 to 30 mm. The sample was not compacted initially. However, it was subjected to a cycle of loading reaching 2.3 MPa and later unloaded.

Figure 20b is a detail of the sample after the test. The breakage of particles is concentrated at the grain to grain contacts or else it divides the gravel into fragments of similar size. Very often the breakage plane crosses in a diametrical way the grain, whereas in other cases (Fig. 20c) the breakage is more complex.

Granular media have been analyzed extensively in the case of soils by the Distinct Element Method (DEM), following the pioneering work of Cundall & Strack (1979). It was found that the external stress applied to the assembly of grains is distributed into dominant forces that go through a series of well-defined chains of particles. Particles in these chains receive loadings concentrated at some contacts. The remaining particles, which constitute the granular media, are only slightly loaded and they contribute to stabilize the main loading chains. This interpretation explains the results of a DEM model, which includes capillary forces at the contacts, developed by Gili & Alonso (2002). Figure 21 shows how, in an aggregate of spheres, the contact forces follow well-defined chains. Entire areas of the granular media remain unloaded.

Therefore, it is reasonable to start the discussion on the breakage of particles by considering a single particle loaded in a diametrical way, as shown in Fig. 22. The breakage of particles observed in tests suggests that particles are broken due to crack propagation. In fact, the classic theory of Griffith, which explains the strength observed in rock samples, is based on a fracture mechanics concept, which attributed a fundamental role to the size of an initial defect

or discontinuity inside the rock matrix. This defect may be identified with an imperfect contact among crystals or else with pores or fissures of any nature.

Let us assume that particles are idealized as discs of diameter  $D$  and width  $B$ , having a defect or flaw in the cen-



a)



b)



c)

**Figure 20** - a) Sample of hard crushed sandstone in an oedometer cell; b) Grain breakage after testing; c) Detail of a broken particle.

tral position, of size  $2a_i$  in the direction of the two concentrated forces which act on opposite extremes of the diameter. The assumed loading on these particles is similar to the classic Brazilian Test. The diametral loading induces a uniform tensile stress perpendicular to the flaw.

These idealized assumptions lead to a Mode I (or pure traction mode) mode of failure in the theory of fracture

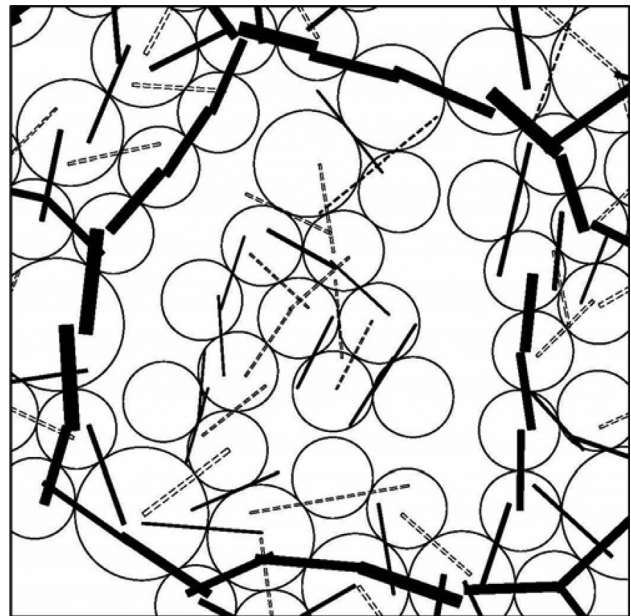


**Figure 21** - Force chains in a loaded array of spheres. Thoroidal menisci exist at the grain to grain contacts. The thickness of plotted segments is proportional to the concentrated load. Discontinuous segments identify dominant capillary forces. (Gili & Alonso, 2002).

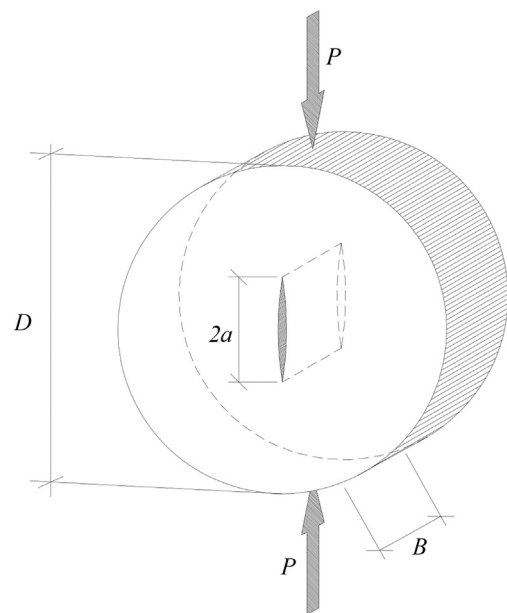


**Figure 22** - Particle model for crack propagation (Oldecop & Alonso, 2007).

propagation of fracture mechanics. The implications of this model are explored below.

### 3. Crack Propagation in Particles

The propagation of the flaw in Tensile Mode 1 is associated in fracture mechanics to the concepts of toughness and stress intensity factor. The latter is defined as:

$$K_i = \beta_i \sigma_i^* \sqrt{\pi a_i} \quad (2)$$

where  $a_i$  is the initial length of the defect,  $\beta_i$  is a dimensionless factor that depends on  $(a_i/D)$  and  $\sigma_i^*$  is the tensile stress normal to the fracture plane if the particle is assumed to be intact. The  $\sigma_i^*$  stress should be related to the external "macro" stress on the granular aggregate. Therefore,  $\sigma_i^*$  increases with the external stress.

When  $K_i$  ( $i$  being an arbitrary crack) is lower than the material toughness,  $K_c$ , (units:  $\text{MPa}\cdot\text{m}^{1/2}$ ) the crack will propagate at a certain speed. This is known as the subcritical propagation of the crack. Crack propagation velocities, determined in experiments, have been collected in terms of  $(K/K_c)$  in Fig. 23. Experimental data may be approximated by a simple exponential relationship:

$$V = V_0 (K / K_c)^n \quad (3)$$

which is the dimensionless version of the equation originally proposed by Charles (1958).  $V_0$  and  $n$  are model parameters. It should be stressed that Fig. 23 suggests that there is a velocity  $V_0 = 0.1 \text{ m/s}$  for  $K = K_c$ . The exponent  $n$  changes with the prevailing suction. The information about

the basalt, granite and marble, which is given in Fig. 23, is used to illustrate in Fig. 24 the approximate relationship between exponent  $n$  and RH. Data on synthetic quartz and glass suggests that  $n$  increases fast if the RH reaches low values. In other words, under conditions of extreme dryness, the propagation velocity of cracks tends to reach extremely low values.

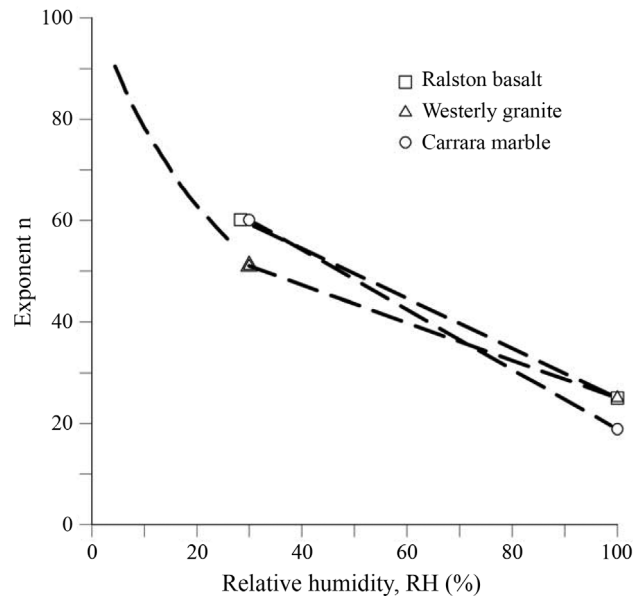


Figure 24 - Relationship between exponent n of Charles law and RH.

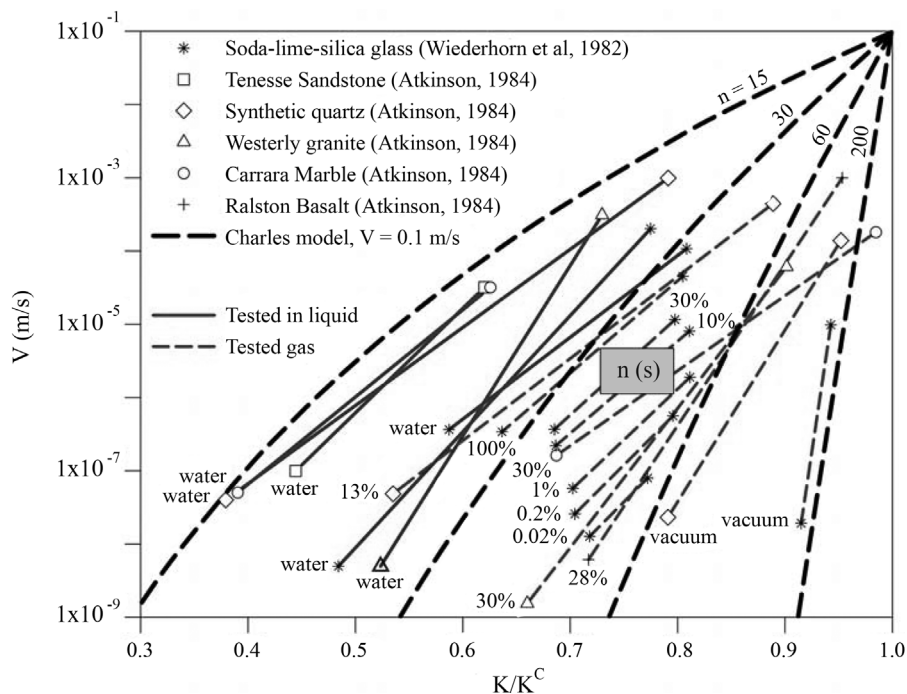


Figure 23 - Crack propagation velocities for different rocks, synthetic quartz and glass. Numbers (in %) indicate the RH of each experiment. Also shown are curves of Charles model (Oldecop & Alonso, 2007).

The velocity of propagation of cracks,  $V_i$ , may be expressed, taking into account Eqs. 2 and 3 as:

$$V_i = \frac{da_i}{dt} = A_i a_i^{n/2} \tag{4}$$

where

$$A_i = V_0 \left( \frac{\beta_i \sigma_i^* \sqrt{\pi}}{K_c} \right) \tag{5}$$

Equation 4 may be integrated if  $A_i$  is assumed to be constant, an approximation that is justified in Oldecop & Alonso (2007). Bearing in mind that the values of  $n$  are high (20-200), the failure time of the particle is given by:

$$t_i^b = \frac{2}{n-2} \frac{a_{0i}}{v_{0i}} \tag{6}$$

where

$$V_{0i} = V_0 \left( \frac{\beta_i \sigma_i^* \sqrt{\pi a_{0i}}}{K_c} \right)^n \tag{7}$$

is the velocity of propagation of the crack of length  $a_{0i}$ .

Equation 6 is plotted in Fig. 25 for the following set of parameters:  $D = 500$  mm,  $V_0 = 0.1$  m/s (taken from Fig. 23),  $s = 7$  MPa and  $K_c = 1$  MPa $\zeta$ m<sup>0.5</sup>. The plot shows the failure time for different average lengths of initial defects and for the variable RH. The average relationship between  $n$  and the RH was taken from Fig. 24.

The plot shows what can be expected in the wetting phase (increasing RH): a significant reduction (of several orders of magnitude) of the breakage time. Breakage times of many years change into a few seconds. In practice this phenomenon is equivalent to a sudden failure if the entire granular assembly is considered. The macroscopic observation will be a sudden deformation (typically volumetric compressions or collapse).

For a given rock type (characterized by  $K_c$  and to a certain extent by  $a_{0i}$ ) and a given particle size the failure

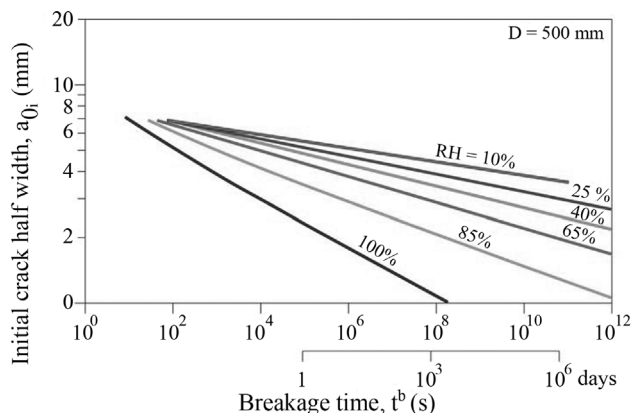


**Figure 25** - Failure times for different initial crack lengths and different RH.

time is also very sensitive to the stress applied, due to the high value of exponent  $n$  in Eq. 7. Therefore, an increment of  $\sigma$  will lead to the breakage of some grains and, as a consequence, it will induce an immediate deformation, even if the initial granular structure is kinematically “blocked”.

An additional important aspect is that stressed fissures always increase in size, even if the crack propagation rate is very low. Therefore, at the scale of the rockfill in the field, creep deformations will always be present.

The information provided by experimental data (Fig. 23) can be synthesized in a conceptual model, which is plotted in Fig. 26.

The plot shows, again, the relationship between the velocity of propagation of a fissure and the stress intensity factor  $K$ . The velocity becomes infinite when  $K$  reaches the value of rock toughness  $K_c$ . The velocity depends also on the RH of the environment where the experiment is performed. If RH increases (which implies an increase in vapor concentration) so does the velocity of propagation. This effect is explained if the chemical reactions occurring at the tip of the crack are examined. The water acts as a corrosive agent of these reactions. The higher the energy of the water (increasing RH, lower suction), the higher the corrosive effect, and thus the velocity of fracture propagation. For every RH there is a threshold  $K$  below which there is no propagation (this threshold value is indicated as  $K_0$  in Fig. 26). Therefore for a given RH, the values for  $K$  that lead to a given velocity of fissure progression are limited between  $K_0$  and  $K_c$ .

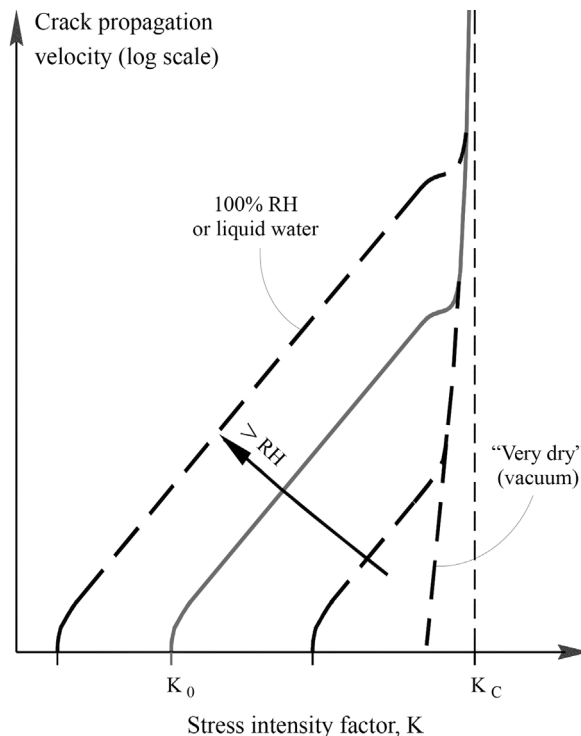


**Figure 26** - Conceptual relationship between crack propagation velocity, stress intensity factor and Relative Humidity.

In a granular medium subjected to stress (rockfill dam) there will be a large number of loaded particles. Each of them will correspond to a value of  $K$  in the abscissas axis of Fig. 26. Given a RH, three different scenarios can be distinguished: fissures that do not propagate (region I:  $K < K_0$ ), fissures which propagate at an increasing velocity with  $K$  (region II:  $K_0 < K < K_c$ ), fissures that have already reached their maximum propagation velocity and the particle is broken (region III:  $K = K_c$ ).

An increase in stress at constant RH will imply that several values of  $K$  will reach  $K_c$ . There will be a breakage of particles and the reorganization of the granular structure of the sample will be externally perceived as an increase of deformation. Moreover, the systematic increase of all the values of  $K$  implies an increase of the velocity of propagation and thus a further increase of particle breakage. In other words, there will be an increase of the deformation velocity of the granular medium.

The effect of an increase in RH is similar. The increase in the breakage velocity in all propagating fissures will lead to some breakage of grains, which will again result in volumetric contractions. Non active particle will become active and break in the future.

The perception of rapid settlement or collapse, when rockfill is wetted, is therefore the result of a series of internal breakages and the subsequent reorganization of the granular structure. Since RH plays a significant role in the breakage of particles, the next logical step is to perform suction-controlled experiments (total suction is involved, because total suction and RH are related through the psychrometric relationship).

## 4. Suction Controlled Oedometer and Triaxial Tests

### 4.1. Oedometer tests and constitutive modelling

Oldecop & Alonso (2001, 2007) described the results of large diameter (30 cm) suction controlled oedometer tests. The cell was described by Oldecop & Alonso (2004). Figure 27 shows the scheme of the test and the oedometer cell developed. Figure 28 shows the 30 cm diameter cell built. The experimental work performed confirmed the fundamental role of water. Figure 29 reproduces some results. The tested material was the Pancrudo shale used in Lechagadam, compacted to Standard Proctor energy.

The evolution of settlements with time for two RH (50% and 100%) and several confining stresses is consistent with the conceptual model of crack propagation in particles. In fact every load increment results in an acceleration of deformations. In a few minutes the deformation vs. time (log scale) curves exhibit a stationary creep. The slope of these stationary curves,

$$\lambda' = \frac{d\varepsilon}{d(\ln t)} \quad (8)$$

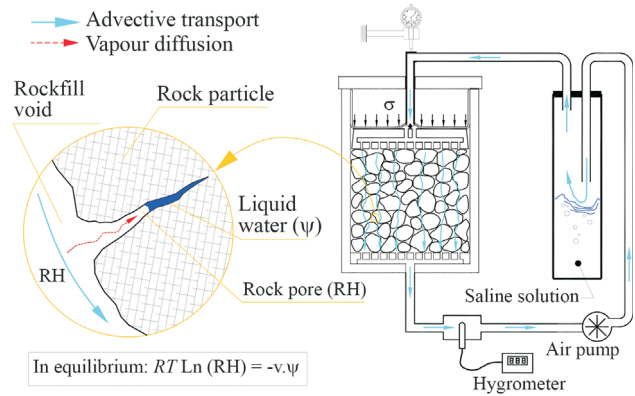


**Figure 27** - Scheme of a suction controlled oedometer apparatus (Oldecop & Alonso, 2004).

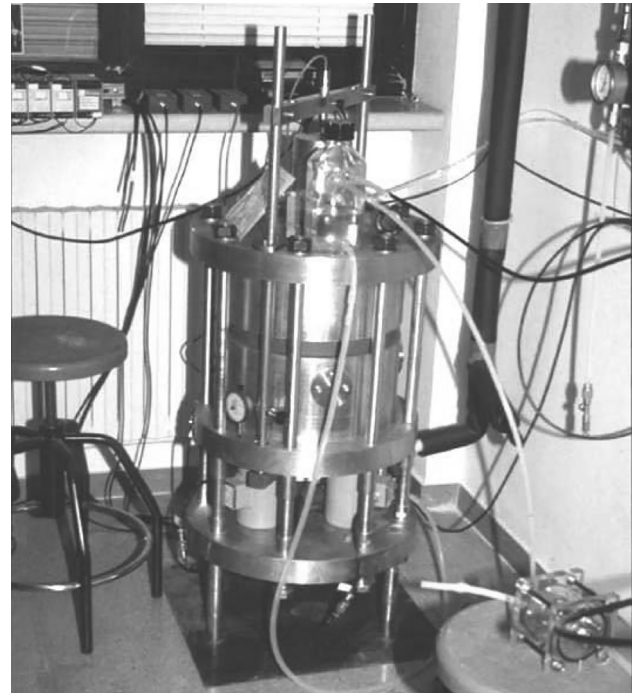


**Figure 28** - Oedometer equipment with suction control developed by the geotechnical Laboratory of UPC.

becomes constant in time and increases with the applied stress. Suction reduction (wetting) leads also to an increase of the delayed compressibility index (Fig. 29).

Figure 30 shows that, for a limited range of stresses (say from 0 to 1.5 MPa) the delayed compressibility index may be described by the following expression:

$$\lambda' = \mu p \left( 1 - \beta \ln \frac{s + p_{atm}}{p_{atm}} \right) \quad (9)$$

which shows the effect of confining stress,  $p$ , and suction,  $s$ .  $p_{atm}$  is the atmospheric pressure and  $(\mu, \beta)$  are model parameters.

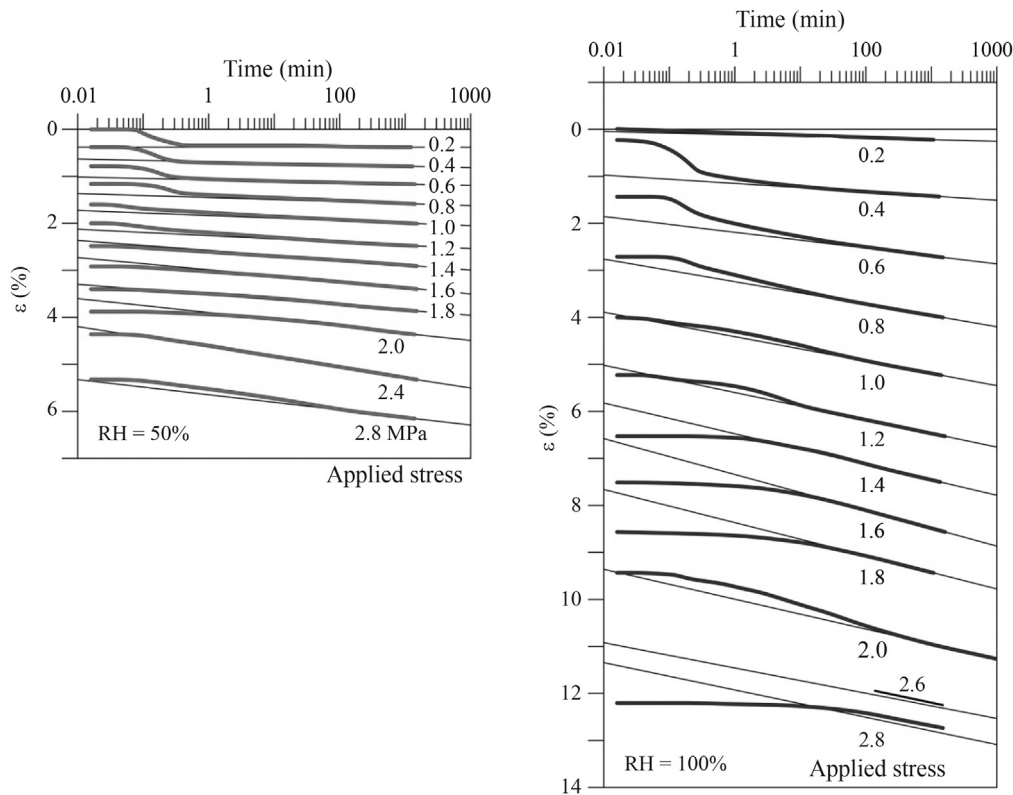


**Figure 29** - Time -deformation records for oedometer tests on compacted Pancrudo shales at two different RH (50% and 100%) (Oldecop & Alonso 2007).

If deformations are selected at some particular time, stress-deformation relationships may be plotted for a stress and suction path applied to the sample. This

is the case of Fig. 31 which shows the compressibility of compacted Pancrudo shale for a wide range of applied suctions and vertical stresses. The plot indicates that the compressibility reduces when suction increases, the collapse phenomena and the linear relationship between stress and deformation (natural scale) in a deformation range reasonably high (0-8%). Moreover, for stresses lower than a given threshold (around 0.2 MPa), compression behavior seems to be independent of applied suction (*i.e.*, independent from water content). This observation is consistent with the idea of a threshold of the stress intensity factor ( $K_0$ ) described previously. Oldecop & Alonso (2003) identified and interpreted these features and they proposed an elasto plastic model to describe this behavior. The model could be justified physically by the crack propagation phenomena already described.

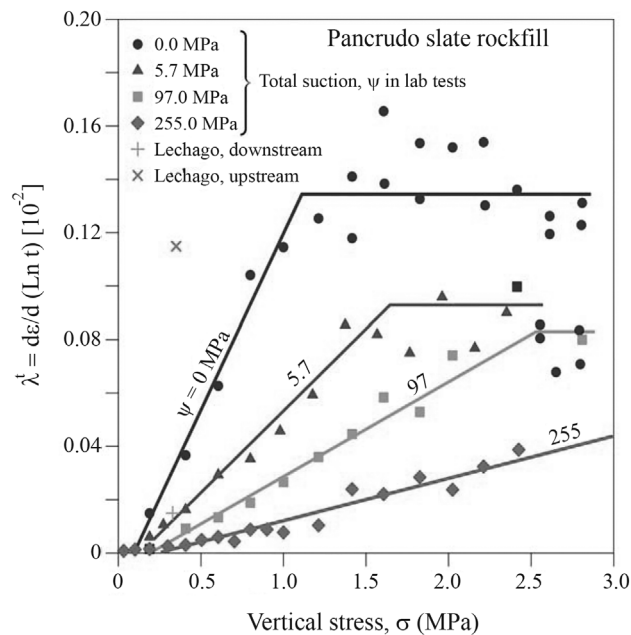


**Figure 30** - Delayed compressibility index for Pancrudo shale. Effect of confining stress and applied suction (Oldecop & Alonso, 2007).

Compression curves in Fig. 31 are similar to the behavior of a “standard” unsaturated soil. Alonso (2006) discussed the similarities and differences in behavior between a compacted rockfill and a partially saturated soil.

It can be shown that the experimental volumetric behavior illustrated in Fig. 32 may be described by a strain hardening constitutive model (Oldecop & Alonso, 2001, 2003). The yield locus in a vertical stress-suction plane is defined by the equation:

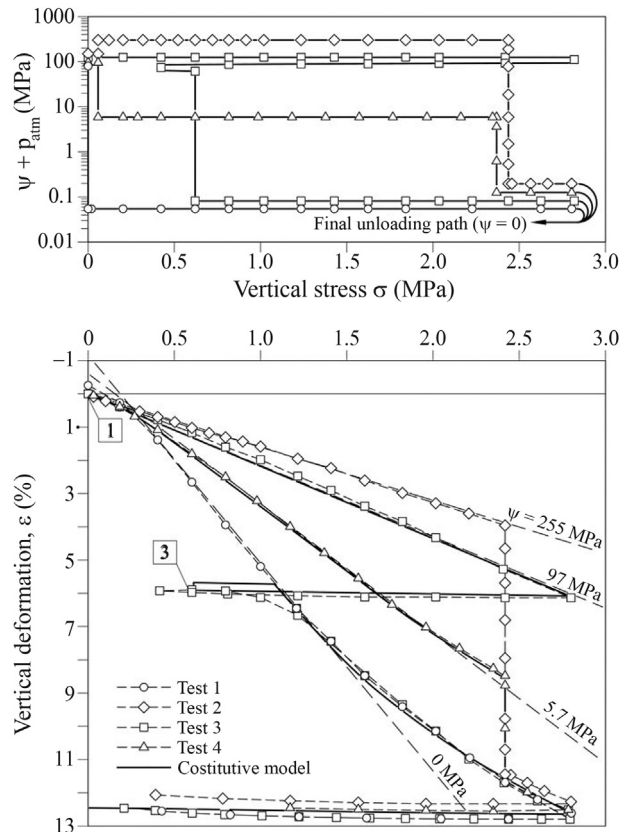


**Figure 31** - Results of a series of oedometer tests on compacted Pancrudo shale. a) Stress paths; b) Stress-strain curves. Also indicated are model predictions (Oldecop & Alonso, 2003).

$$F(\sigma, \psi) = \sigma[\lambda(\psi) - \kappa] - \sigma_y [\lambda(\psi) - \lambda^i] - \sigma_0^* (\lambda^i - \kappa) = 0 \quad (10)$$

where the suction-dependent compressibility index is given by

$$\lambda(\psi) = \lambda_0 - \alpha_\psi \ln \frac{\psi + p_{atm}}{p_{atm}} \quad (11)$$

where  $\sigma_0^*$  is the hardening parameter,  $\lambda_0$  is the saturated compressibility,  $\lambda^i$  compressibility for a very dry state,  $\sigma_y$  is the stress limit for particle re-arrangement and  $\alpha_\psi$  is a parameter describing the increase of stiffness with suction.

Equation 10 is similar to the “Loading Collapse”, LC, yield function defined for unsaturated soils (Alonso *et al.*, 1990). A main conceptual difference is that suction, in the case of rockfill has no any capillary stress interpretation. Equation 10 has been plotted in Fig. 32 for an increasing deformation. Also indicated in the figure are some frontiers which define the transition of deformation mechanisms in the manner described by McDowell & Bolton (1998): the transition from particle rearrangement (PR) and Clastic Yielding (CY) and the transition between Clastic Yielding and Clastic Hardening (CR).

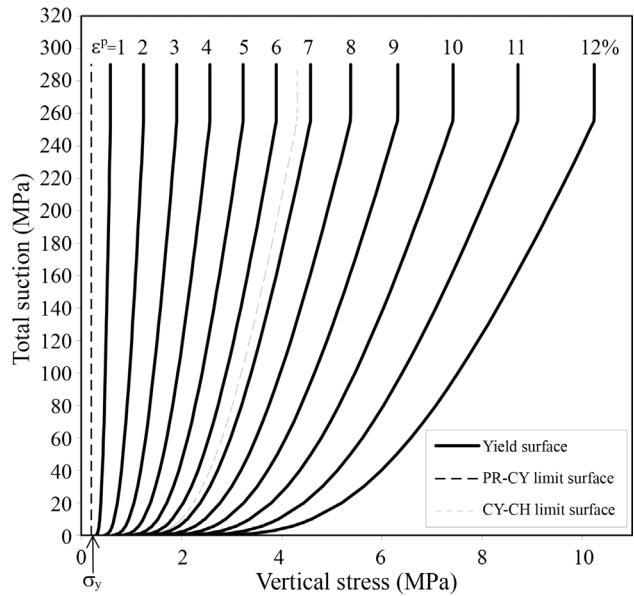


**Figure 32** - Yielding (LC) curves for increasing values of plastic volumetric strain.

Figure 33 illustrates the capability of the model to simulate a stress path involving loading, unloading, wetting and reloading of an oedometer test on compacted gravel.

The model described was generalized to isotropic stress states, triaxial states (by adopting elliptical yield curves in the deviatoric plane) and, finally to general stress states. It was also introduced in the finite element code CODE\_BRIGHT as the “Rockfill Model”. Examples of application of this model to the analysis of a rockfill embankment and a zoned earth and rockfill dam are given later. In

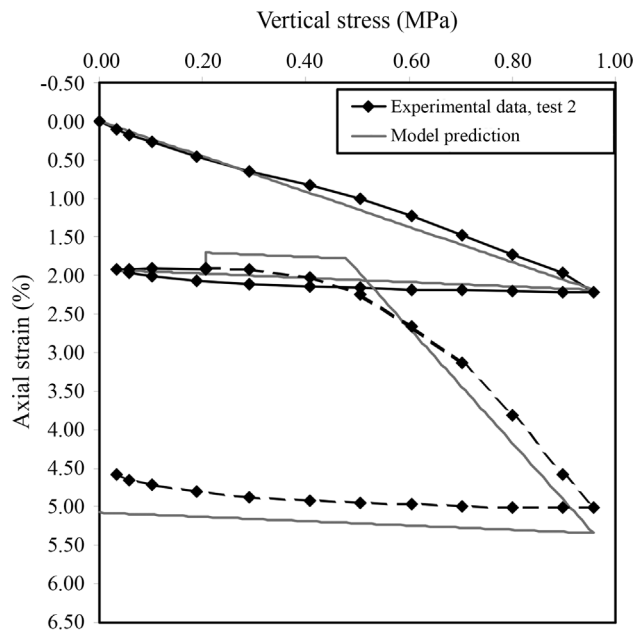


**Figure 33** - Comparison of measured response of Pancrudo shale in an oedometer test and model predictions.

the remaining of this section the response of the rockfill under triaxial stress states will be briefly presented.

### 4.2. Triaxial stress states

Suction controlled triaxial tests were performed in the equipment described in Fig. 34 (Chávez *et al.*, 2009) with the purpose of investigating yielding and plastic flow behavior. One procedure to investigate the shape of yield loci was described by Poorooshasb *et al.* (1966) (Fig. 35). The shape of the yield locus and vectors of plastic strain increment are given in the figure. They suggest that hardening of rockfill is due to a combination of volumetric and deviatoric plastic strains. Plasticity is non-associated. Chávez & Alonso (2003) developed a full elasto-plastic model which was in part based on previous developments concerning the compressible behavior of rockfill identified in oedometer tests. The model incorporated a set of experimental observations:

- Critical state is found at the end of shearing paths. Suction contributes to maintaining higher void ratios if com-



Figure 34 - Suction controlled large diameter triaxial cell of UPC geotechnical Laboratory.

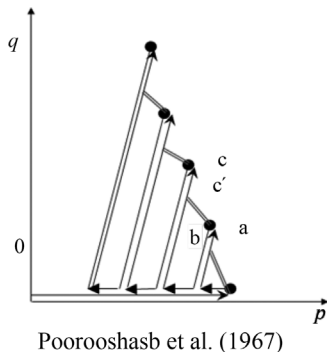


Figure 35 - Protocol for the investigation of yielding function shape in the deviatoric plane and yield locus for Pancrudo shale as reported by Chávez (2004).

pared with saturated tests. Ultimate stress ratio increases with suction.

- The critical deviatoric stress is a nonlinear function of isotropic confining stress
- Two yield surfaces are proposed: a deviatoric one ( $q/p = \text{constant}$ ) and an isotropic or “cap” surface (Fig. 36).
- Deviatoric behavior is described by means of a hyperbolic hardening rule which may also reproduce softening. Hardening is described by means of an effective plastic work and a deviatoric plastic strain. The effective plastic work is a procedure to account for the degradation of the material due to particle breakage.
- The plastic potential is based on a modified version of a Rowe dilatancy rule.

Figure 37 compares the model behavior with experimental results.

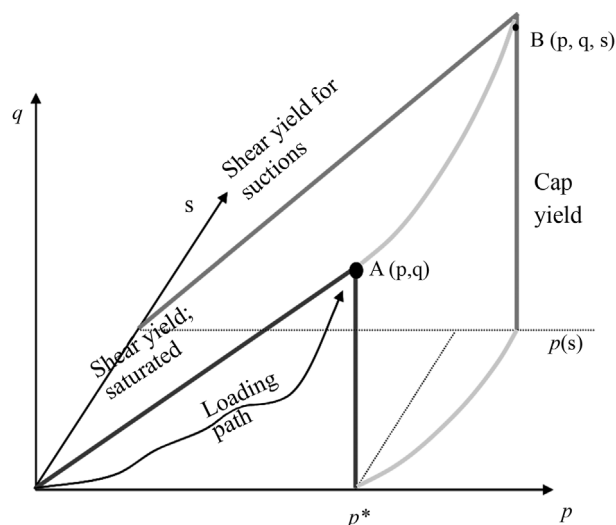
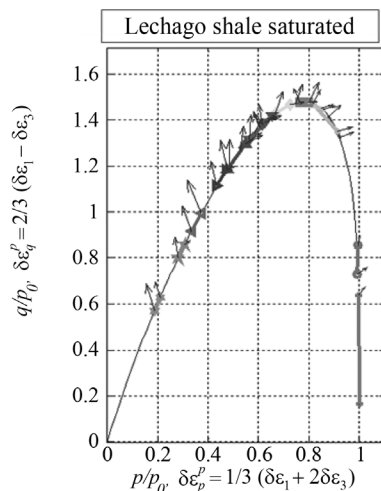
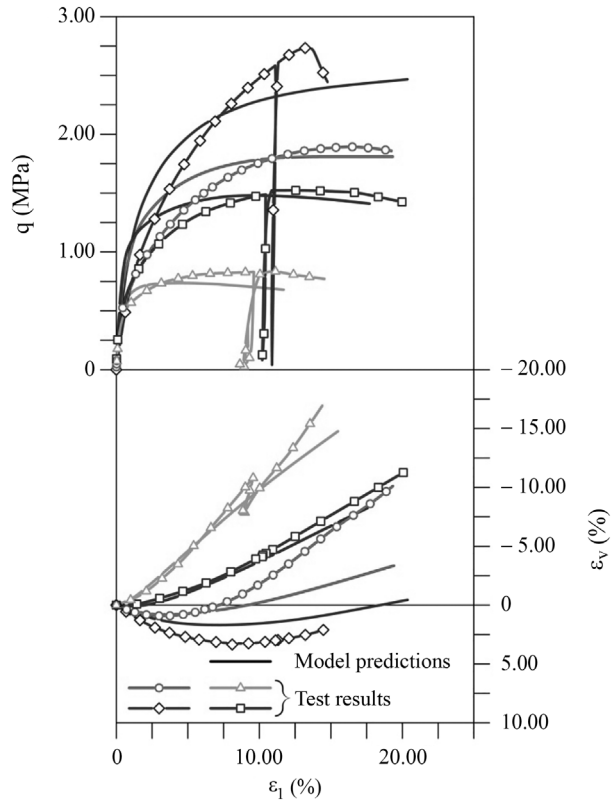


Figure 36 - Yield surfaces in Chávez & Alonso (2003) model.





**Figure 37** - Triaxial tests on Pancrudo shale at a RH = 36% and model predictions (Chávez & Alonso, 2003).

## 5. Scale effects

Experimental evidence indicates that rock strength decreases as sample size increases. A common explanation is that the probability of finding a largest crack or defect in a critical direction increases with sample size.

In experiments which reproduce Type I (tensile) stress conditions, strength is shown to decrease with sample size. Figure 38 shows some results published by Lee (1992). The figure shows the type of test (an irregular particle is loaded along a diameter by means of two parallel polished rigid plates) and the relationships load-displacement. Local failures are initially detected at the grain-plate contacts, before a global diametric failure takes place. Tensile stresses on the diametric plane may be approximated from the well-known expression for the Brazilian test. This stress may be then compared with the average particle size of the sample. The results for three different lithologies are given in Fig. 38c.

The expression:

$$\sigma_f \approx d^\alpha \quad (12)$$

where  $\sigma_f$  is the tensile strength and  $\alpha$  is a coefficient varying between -0.34 y -0.42, reproduces experimental results.

Fracture mechanics provides also an explanation for the experimental results. Cracks propagate when the stress

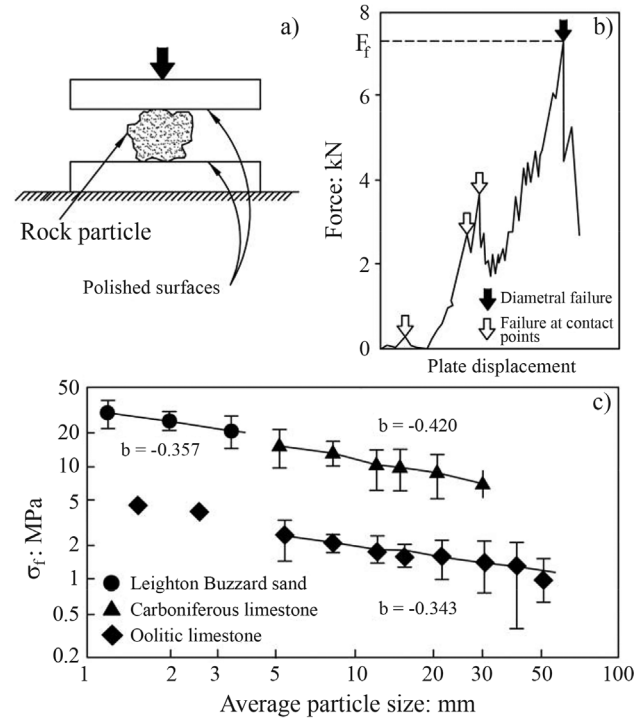


**Figure 38** - Test on rock particles (McDowell & Bolton, 1998 quoting Lee, 1992): a) Test layout for determining the tensile strength of rock fragments. b) Typical load-displacement record. c) Variation of average tensile strength with particle size

intensity factor  $K$  reaches the material toughness  $K_c$ . Therefore, following Eq. 2 the tensile strength which leads to the propagation of the fissure is:

$$\sigma_f = \frac{K_c}{\beta\sqrt{\pi a_i}} \sim a_i^{-0.5} \quad (13)$$

It may be argued that the largest the particle diameter, the largest the initial defect in statistical terms. Therefore, the particle size defines the maximum size of a defect, critically oriented, capable of initiating a crack propagation leading to failure. Then,

$$\sigma_f \sim d^{-0.5} \quad (14)$$

Coefficients  $\alpha$  in Eq. 1, experimentally determined by Lee (1992), are close to the theoretical coefficient given by Eq. 14 (-0.5). Consider now the relationship between the external stress,  $\sigma_{ext}$ , and the tensile stress,  $\sigma_t$ . In a particle loaded in the direction of a diameter, the concentrated load,  $P$ , is proportional to the tensile stress and the square of the diameter,

$$P \sim \sigma_t d^2 \quad (15)$$

and, in view of Eq. 14:

$$P \sim d^{-0.5} d^2 \sim d^{3/2} \quad (16)$$

will be the failure load.

In a regular arrangement of particles (assumed to be spheres) (Fig. 39), equilibrium will require:

$$\sigma_{ext} l^2 = \sum P = P \frac{1}{d} \frac{1}{d} = \frac{P}{d^2} \quad (17)$$

Therefore,

$$P = d^2 \sigma_{ext} \quad (18)$$

and, Eq. 16 will lead to:

$$d^2 \sigma_{ext} \sim d^{3/2} \quad (19)$$

and

$$\sigma_{ext} \sim d^{-0.5} \quad (20)$$

In other words, the external stress able to break particles of diameter  $d$  is inversely proportional to  $d^{0.5}$ . The largest the particles, the easier its breakage for a given external stress. If, instead of Eq. 13, the starting point is Eq. 12, experimentally derived, Eq. 20 will transform into:

$$\sigma_{ext} \sim d^{-\alpha} \quad (21)$$

where  $\alpha$  varies between 0.3 and 0.5.

Therefore, the mechanical properties of rockfill, which are controlled by particle breakage, will experience a scale effect, associated with to particle size. Eqs. 20 or 21 are useful to estimate the scale effect.

Consider rockfill compressibility. Due to the linear stress-strain relationship for an extended deformation range (Fig. 31), the compressibility coefficient, for a given suction, may be simply defined as:

$$\lambda \sim \frac{\Delta \epsilon}{\Delta \sigma} \quad (22)$$

and, taking Eq. 21 into account:

$$\lambda \sim d^\alpha \quad (23)$$

If the compressibility of two granular aggregates, defined by diameters  $d$  and  $d_0$ , is compared:

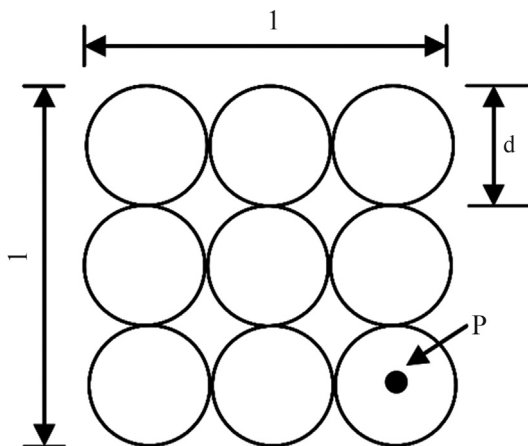


Figure 39 -.Simple arrangement of spheres. Plan view.

$$\lambda^d = \lambda^{d_0} \left( \frac{d}{d_0} \right)^\alpha \quad (24)$$

Figure 40 shows experimental results of gravel compressibility. Samples of hard crushed limestone of uniform size (40-30 mm, 30-20 mm, 25-20 mm and 20-10 mm) were tested in a 30 cm diameter odometer test (Ortega, 2008). The linear coefficient of compressibility for saturated conditions is plotted in terms of the maximum grain diameter. Two packing states were tested: a loose sample ( $e_0 = 0.947$ ) and a dense state ( $e_0 = 0.502$ ). Figure 40b shows the scaled compressibility, following Eq. 24 and taking  $d_0$  as the maximum size of the simple grains. The plot shows that the exponent  $\alpha = 0.5$  fits almost perfectly well the results for  $e_0 = 0.947$ . The dense aggregate ( $e_0 = 0.502$ ) requires a value  $\alpha = 0.3$  for a good fit of experiments. The scaling law is therefore affected by the degree of compaction.

Frossard (2009) discusses scale effects in a similar manner. When shear strength is considered (Eq. 1), the scaling law should be applied to the shear strength,  $\tau_f$ , and the confining stress,  $\sigma$ . Then:

$$\frac{\tau_f}{\left( \frac{d}{d_0} \right)^{-\alpha}} = A_0 \sqrt[2]{\frac{\sigma}{\left( \frac{d}{d_0} \right)^{-\alpha}}} \quad (25)$$

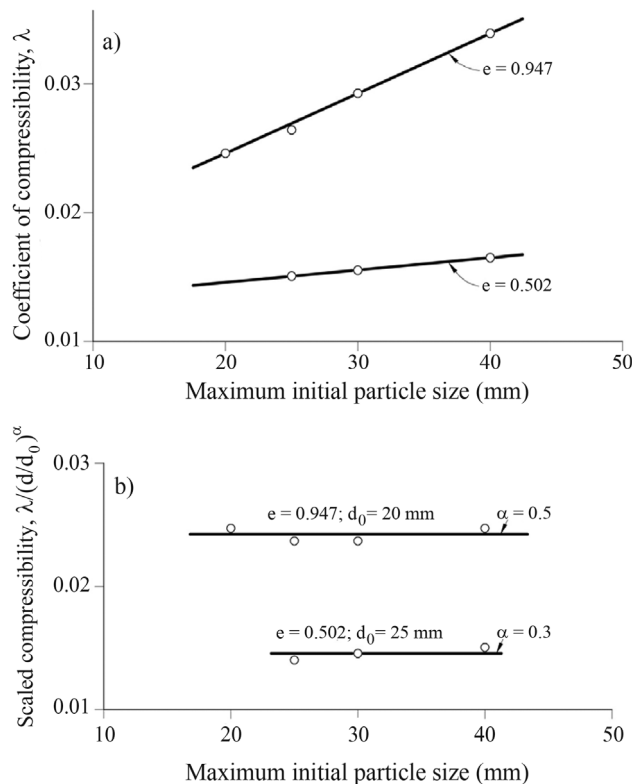


Figure 40 - a) Compressibility coefficient of uniform limestone gravels in terms of the maximum particle size (Ortega, 2008). b) Compressibility corrected for scale effects.

and:

$$\tau_f = A_0 \sigma^b \left( \frac{d}{d_0} \right)^{\alpha(1-b)} \quad (26)$$

This relationship provides the shear strength of a rockfill having a particle size  $d$  if the strength envelope of a rockfill having a particle size  $d_0$  ( $\tau_{f0} = A_0 \sigma^b$ ) is known.

The discussion on scale effects becomes more complex if non uniform grain size distributions are considered. In this case some of the assumptions leading to the preceding relationships are not satisfied, even in an approximate manner. In addition, a full characterization of the stress-strain behavior of a rockfill requires a number of parameters, defined in the adopted constitutive model. Scale effects do not affect only compressibility and shear strength.

However, if a given constitutive model is adopted, there is a possibility of testing different grain size distributions and constitutive parameters could be related to some indices describing grain size distribution. This approach was followed by Ramon *et al.* (2008), when they tested Pancrudo shale gravels, defined in Fig. 41. Three of the grain size distributions are characterized by a common  $D_{50}$  and a variable content of fines. The elastoplastic constitutive model adopted has been outlined above.

It was found that the best parameter identifying the grain size distribution was in this case the index  $D_{max}/D_{min}$ . Compressibility parameter  $\lambda_0^d$  decreases continuously when  $D_{max}/D_{min}$  increases (Fig. 42a). Parameter  $\chi$  (Fig. 42b) which describes collapse intensity seems to decrease with  $D_{max}/D_{min}$  (Fig. 42b). The elastic compressibility parameter,  $\kappa$ , does not change with grain size distribution in this particular case. The delayed compressibility index,  $\lambda'$ , maintains

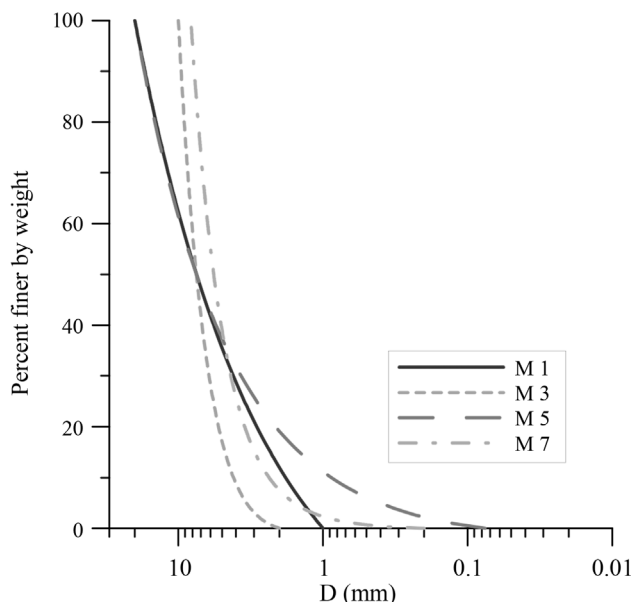


**Figure 41** - Tested grain size distributions (Ramon *et al.*, 2008).

a constant relationship with the compressibility index,  $\lambda$ , and this result defines the scale effect for  $\lambda'$ .

Scale effect is an interesting research topic, very relevant in practice, due to the limitations of laboratory testing. This topic will be examined again when introducing the capabilities of the Distinct Element Method to analyze rockfill behavior.

## 6. Rockfill Behavior Through DEM

Why does the Distinct Element Method (DEM) offer an interesting alternative to investigate the behaviour of coarse granular aggregates?

At least, for three reasons:

- Improving understanding of basic deformation mechanisms.
- It is a good complement to laboratory testing. Unlike fine soils, the number of particles in a laboratory test on gravels is within the practical limits of today's DEM capabilities.
- Even large structures, such as rockfill embankments, may be approximated through DEM in a not so distant future.

The performance of DEM to reproduce rockfill behavior has been investigated in recent years. Some highlights are given here.

The guiding idea was to develop a realistic model which could simulate three distinct aspects already discussed: scale effects, delayed (creep) deformations and environmental effects. The first aspect is particularly interest-

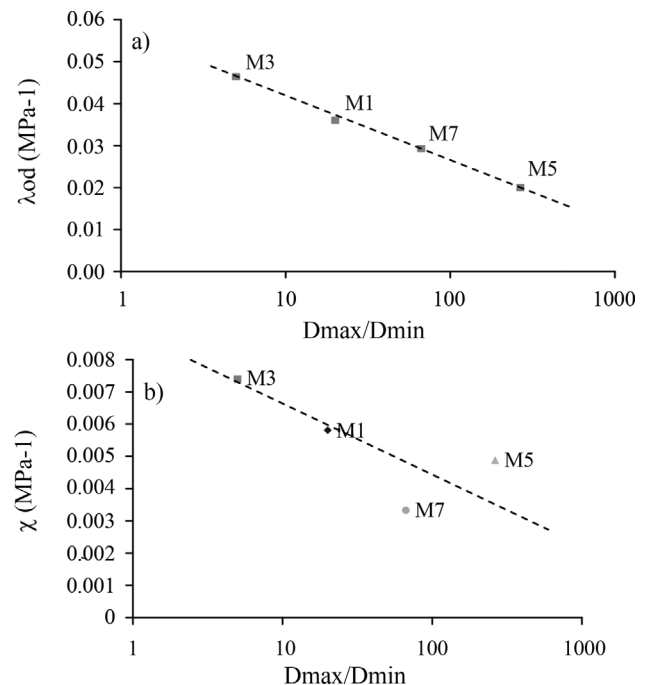


**Figure 42** - Scale effects on: a) Compressibility parameter  $\lambda_0^d$  for unsaturated oedometer tests. b) Parameter  $\chi$ . Grain size distributions are defined by the index  $D_{max}/D_{min}$  (Ramon *et al.*, 2008).

ing in practice because of the difficulty and cost of testing large samples in the laboratory. The model developed includes the following characteristics:

- Actual particle shape is reproduced in an acceptable manner.
- Particle breakage is introduced following some results from fracture mechanics. In particular, the subcritical crack propagation inside particles is the basic mechanism leading to the division of grains. In this way, time, scale (size) and humidity effects are automatically accounted for.
- A breakage protocol which tries to reproduce some experimental observations.
- Validation against actual testing results.

Figure 43 shows the DEM model of triaxial and oedometer samples of uniform gravel. The dimensions correspond to the equipment of the Geotechnical Laboratory of UPC.

Particle shapes are reproduced by aggregation of spheres. The starting geometry in all cases is a pyramid of 14 “microparticles” as shown in Fig. 44. The figure shows a gravel of a crushed limestone actually tested.

The selection of shapes implies a trade-off between geometrical accuracy and computational time. The basic code used in the simulations presented here is the PFC3D code developed by Itasca. An extensive programming of the basic kernel was required to include the simulation features outlined here.

The calculation relies on three basic steps:

1. Stress calculations on macroparticle.
2. Failure criteria for macroparticles.
3. Division of macroparticles and re-arrangement of the granular structure.

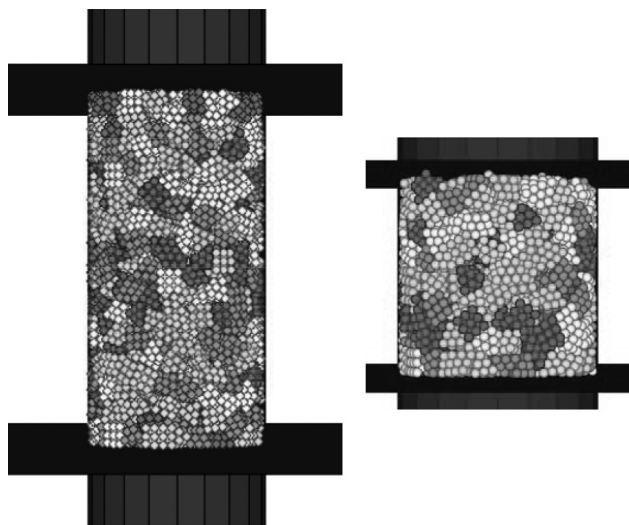


**Figure 43** - DEM approximations of triaxial (height 0.50 m; diameter 0.25 m) and oedometer (height 0.25 m; diameter 0.25 m) samples.

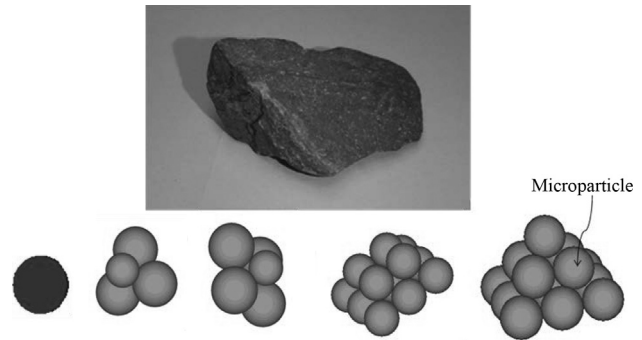


**Figure 44** - “Clump” models of 1, 4, 5 and 14 microparticles.

The first step starts by identifying the maximum forces acting on each macroparticle of the sample. These forces are typically part of the force chains developed in the aggregate of particles. The calculation of tensile stresses inside each particle follows the closed form solution presented by Russell & Wood (2009) for loaded spheres. By introducing a set of flaws of randomly distributed flaw lengths in particles, a stress intensity factor,  $K$ , may be computed for each macroparticle.

The second step is summarized in Fig. 45  $K$  is first compared with the rock toughness,  $K_c$ . If  $K \geq K_c$  a particle division is applied in the manner explained below. If not, crack propagation starts following the velocity derived in Eqs. 4 to 7. When the size of the flaw,  $a$ , reaches half the equivalent diameter of the particle, a division is applied.

The third step is illustrated in Fig. 46. Two main possibilities are envisaged: either a “big” failure (crushing in equal volumes) or a contact crushing (comminution). The protocol is self explanatory in the figure. Note that once an isolated sphere is produced as a result of successive breakage, an additional fine division in small spheres is applied with the purpose of capturing better the generation of fines in the sample. The results given here correspond to a simple protocol of breaking (crushing in equal volumes) and fine subdivision is not applied.

The behavior of a uniform ( $D = 25\text{-}30$  mm) hard limestone gravel subjected to oedometer and triaxial loading has been simulated. The main parameters are the friction coefficient at contacts,  $\mu$ , the toughness,  $K_c$ , and the normal contact stiffness,  $K_n$  (shear stiffness was taken equal to normal stiffness in the simulations presented here). Consider first an oedometer test in which load was applied in steps, following the protocol, shown in Fig. 47. It corresponds to an actual test performed in the laboratory. Test results were used to determine parameters of the numerical model. Delayed deformations were measured at each loading stage and the sample was flooded at maximum vertical stress.

Model parameters were identified by fitting the compression curve and the evolution of the grain size distribution. This is shown in Figs. 48 and 49.

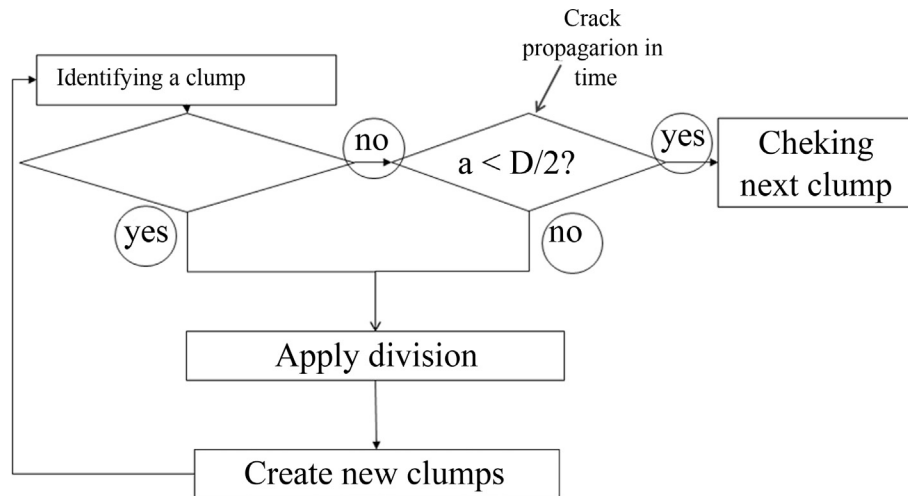


Figure 45 - Failure criteria for macroparticles.

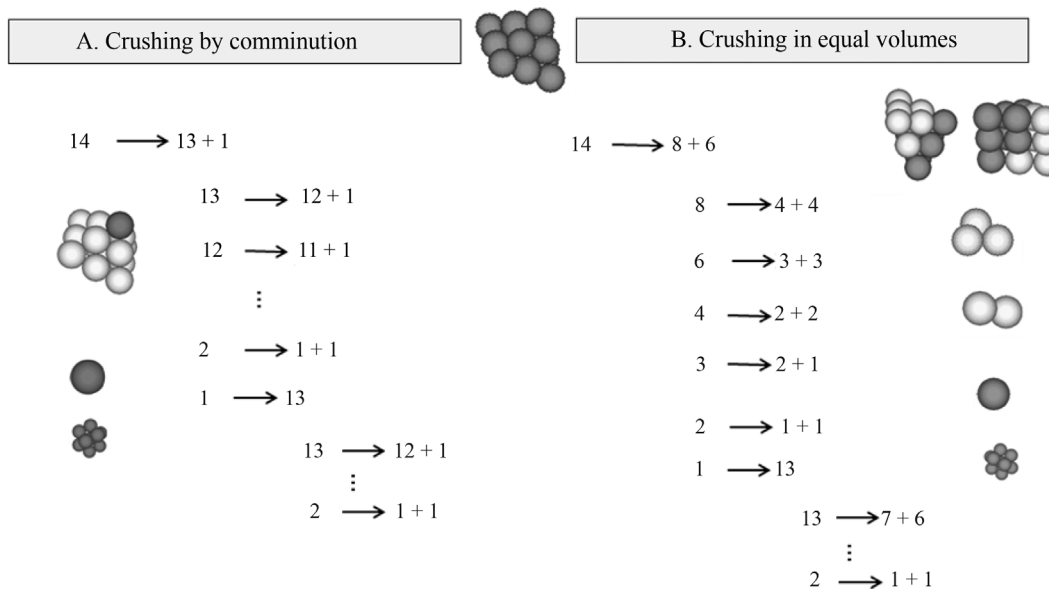


Figure 46 - Breakage criteria for a particle made of 14 spheres.

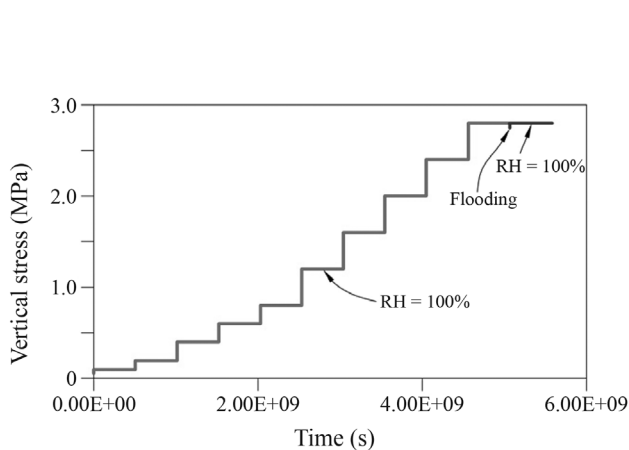


Figure 47 - Loading protocol of oedometer test.

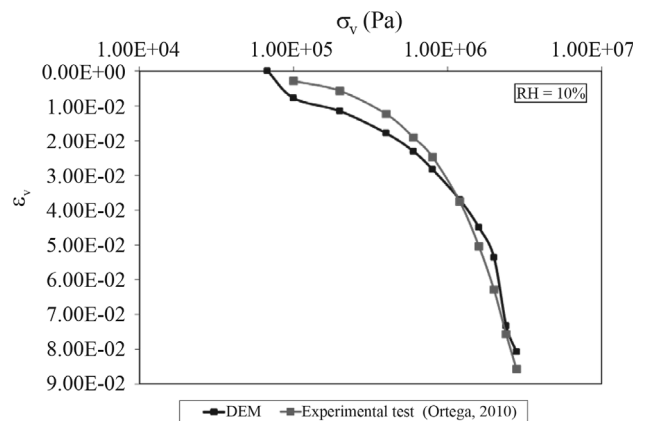


Figure 48 - Oedometer test on hard limestone gravel. Compression curve. Comparison of test results and DEM modeling.

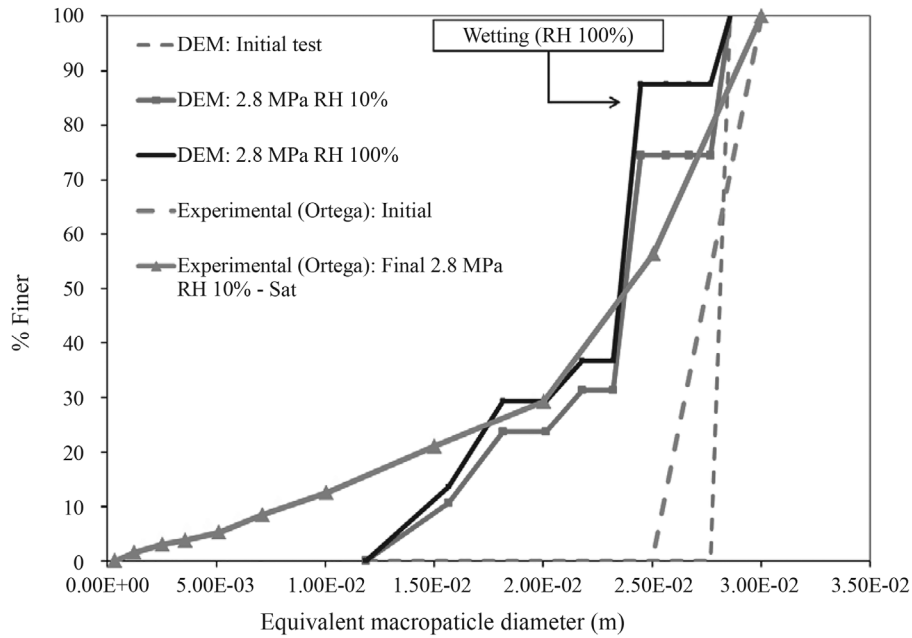


Figure 49 - Oedometer test on hard limestone gravel. Grain size distributions. Comparison of test results and DEM modeling.

The compression curve is well captured by the model. The evolution of grain size is not so well reproduced. The development of fines is limited by the minimum size of the microparticle selected. However, results are reasonable and the fitting allowed identifying the following model parameters:  $\mu = 0.3$ ;  $K_c = 5e6 \text{ Pa}\cdot\text{m}^{0.5}$  and the normal contact stiffness,  $K_n = 4e6 \text{ N/m}$ .

Calculated delayed deformations for each loading stage are remarkably similar to actual test results. This is shown in Fig. 50. This result adds confidence to the set of assumptions made to build the numerical model. In particular, the subcritical crack propagation theory seems to offer a

realistic framework to reproduce creep deformations of rockfill.

From a macroscopic perspective the oedometer test is just a particular stress path. It introduces some overall shearing, but it does not approach limiting shearing conditions. However, it may be argued that from a microscopic point of view it probably includes all the complexities of grain interactions, including grain breakage. It may be then accepted that the DEM model identified through an oedometer test is, in fact, a general model and, therefore, it should be capable of predicting the sample response under any other stress path. For instance, a triaxial test. This idea was checked by comparing the results of an actual triaxial

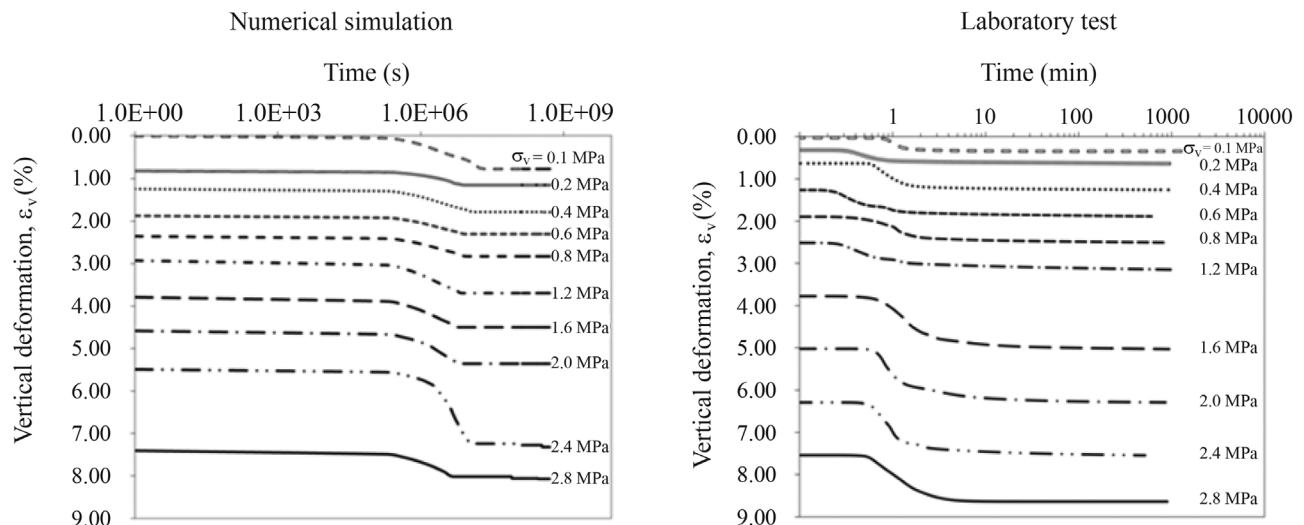
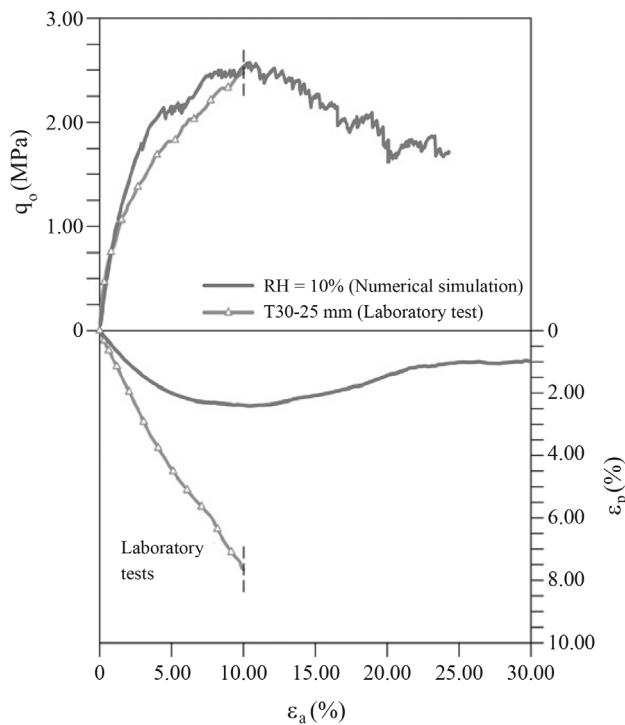


Figure 50 - Oedometer test on hard limestone gravel. Comparison of calculated and simulated delayed deformations.

test on the same crushed limestone gravel with the DEM prediction. The comparison is given in Fig. 51. The laboratory test was run under “dry” conditions and it was flooded when strength conditions were reached. This is why experimental results are limited to a maximum deformation of 10%. The stress-strain curve is very well reproduced by the model. This is an encouraging result.

However, measured volumetric deformations are higher than DEM predictions. This is probably a consequence of the particle division protocol used in this simulation, unable to enter into the fine particle divisions.

The capability of the model developed to explore size effects will now be illustrated. The objective is to know the



**Figure 51** - Triaxial test on hard limestone gravel. Comparison of calculated and simulated DEM results.

effect of grain size on the oedometric compressibility. The formulation of the analysis is summarized in Fig. 52.

Particle sizes of initially uniform samples were selected in a wide range (2.8 mm to 0.56 m). Four samples were built, having all of them the same initial porosity ( $n = 0.53$ ). The sample size, also given in Fig. 52 illustrates the difficulties of laboratory testing. A sample of boulders having a mean diameter of 56 cm would require a diameter of no less than 5 m to maintain a reasonable diameter to particle size ratio. Even for gravels of no more than 14 cm in size the oedometer diameter reaches 1.25 m in order to preserve the same diameter/particle size ratio. The numerical tests were performed under “dry” conditions at a  $RH = 10\%$ .

The calculated compressibility curves are given in Fig. 53. The compressibility coefficient was calculated in the final part of the curves, for stresses in excess of 1 MPa. They are represented in Fig. 54.

Also indicated in the figure are three experimental values determined by Ortega (2008) in experimental tests. They occupy a relatively narrow range but they help to add confidence to the simulation.

Obviously DEM could be applied to investigate the effect of particle size on any constitutive parameter. In a more general case, particle “size” could be changed into

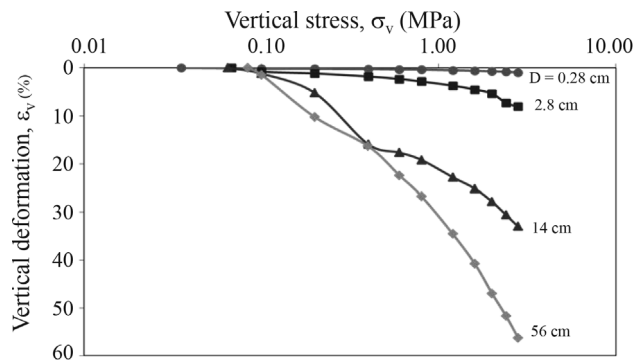
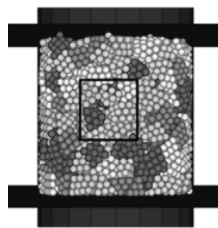


**Figure 53** - Simulated oedometer tests on samples of different initial uniform grain sizes.



Contact stiffness, kN: N/m	$4 \times 10^6$
Shear stiffness, ks: N/m	$4 \times 10^6$
Friction coefficient, $\mu$	0.3
Toughness, $K_c$ : Pa.m <sup>1/2</sup>	$5 \times 10^6$

Sample	Relative scale	Sample size		Equivalent macroparticle diameter (mm)	Initial porosity
		Height (mm)	Diameter (mm)		
S25	0.1	25	25	2.8	0.5314
S250	1	250	250	28	0.5314
S1250	5	1250	1250	140	0.5337
S5000	20	5000	5000	560	0.5314

**Figure 52** - Size effects on confined compressibility. Data for DEM analysis.

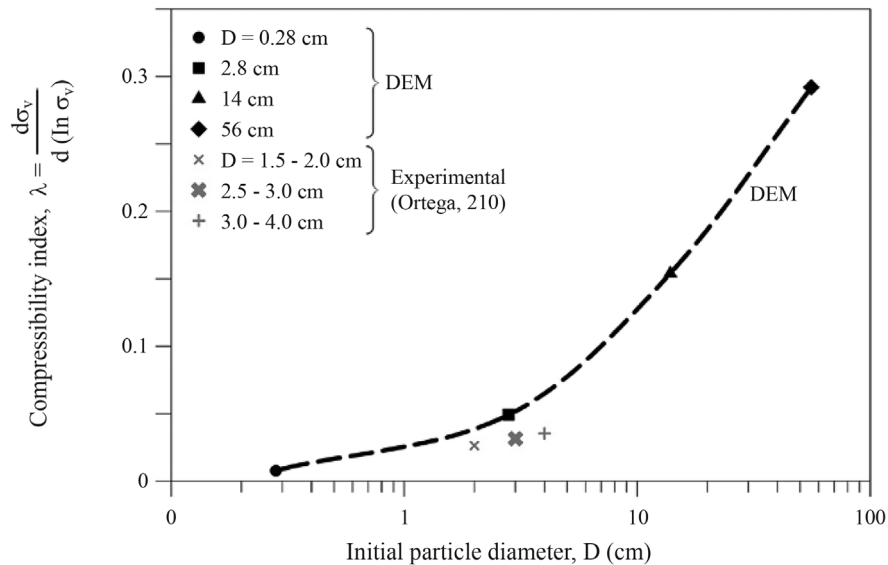


**Figure 54** - Variation of oedometric compressibility index with initial grain size.

grain size distribution, a possibility which is beyond the possibilities of some theoretical approximations (Frossard *et al.*, 2012) based on a given initial size distribution.

## 7. Behavior of Rockfill Embankment Under Rainfall Action

An interesting case that shows the capability of the elasto-plastic rockfill models is the response of a rockfill embankment 40 m high (Fig. 55) located in the Madrid-Seville high-speed railway. The rockfill was made of compacted schists. Figure 55 shows a good correlation between the rainfall intensity and the velocity of the crest settlements. The correlation is excellent for three periods of intense rainfall in 1994, 1996 and 1997. However, the final period of intense rainfall represented in Fig. 55 did not result in any significant acceleration of the motions.

This case will be analyzed with the purpose of investigating the effect of some key parameters. Fig. 55 also indicates that there is a constant base velocity not affected by rain, which can be identified as a pure creep phenomenon. It is clear that the rockfill deformation models should include creep if they are to be used to simulate long-term behavior. The experimental tests mentioned before indicate that this basic creep is also controlled by RH.

In order to study this case, the finite element program Code\_Bright (Olivella *et al.*, 1994, 1996) was used. A rockfill embankment, 40 m in height with symmetric slopes (1V:3H) and a crest width of 8 m, was modelled. The elastoplastic formulation of the model used has been described in Oldecop & Alonso (2001) and Alonso *et al.* (2005).

Table 1 collects the set of constitutive parameter describing the rockfill. The properties of the rockfill embankment of the Seville-Madrid line are not known in detail

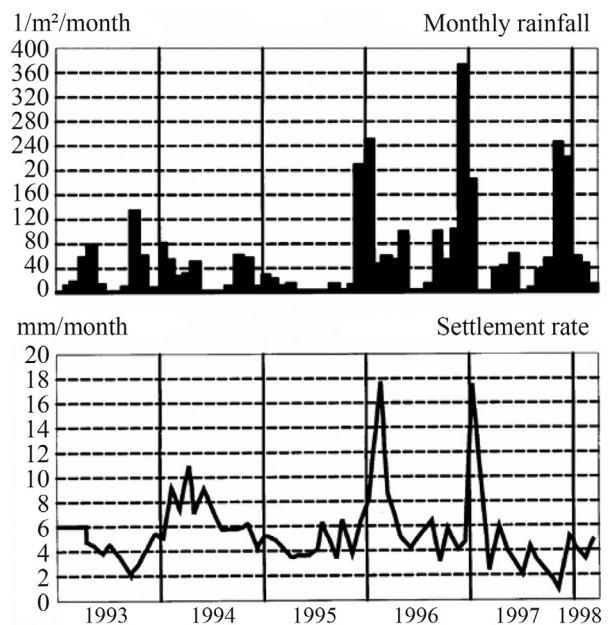


**Figure 55** - Rockfill embankment in Madrid-Sevilla high speed railway line. Correlation between settlement rates and rainfall (Soriano & Sánchez, 1999).

(Soriano & Sánchez, 1999 only offer a brief description). However, the set of available data for Beliche dam for a material which is similar to the material used for the railway embankment are a good starting point to develop the calculations in this case.

The analysis performed focused only in three parameters: the air entry value of the retention curve of the compacted schist,  $p_o$ , the creep parameters,  $\mu$ , and the intrinsic permeability. The solved cases are grouped in Table 2. The initial state of the embankment is characterized by an initial

**Table 1** - Mechanical and hydraulic constitutive parameters for the simulation of the rockfill embankment.

I. Elastic behaviour			
Elastic modulus	E	MPa	150
Poisson coefficient	$\nu$	-	0.3
II. Plastic behaviour			
Plastic instantaneous compressibility, virgin	$\lambda^i - \kappa$	-	0.025
Elastic virgin compressibility for saturated conditions	$\lambda_{v_0}^d$	-	0.028
Parameter describing the variation of elastic compressibility with total suction	$\alpha_s$	-	0.010
Slope of the strength envelope at critical state. Dry conditions	$M^{dry}$	-	1.75
Slope of the strength envelope at critical state. Saturated conditions	$M^{sat}$	-	1.30
Parameter controlling the increase of cohesion with suction	$k_s$	-	0
Mean threshold stress for the development of elastic deformations	$p_y$	MPa	0.01
Parameter to define the associativity of plastic potential	$\alpha$	-	0.3
III. Hydraulic properties			
Intrinsic permeability	k	m/s	Back analyzed
Van Genuchten parameter describing the air entry value	$p_0$	MPa	Back analyzed
Van Genuchten parameter describing the slope of the water retention curve in its intermediate range	$\lambda$	-	0.33

average yielding stress,  $p_o^* = 0.04$  MPa. An initial constant suction  $s_0 = 1.5$  MPa was imposed to the whole structure.

An equilibrium stage was first calculated (in this phase the boundaries are assumed to be impervious). The initial void ratio is  $e_0 = 0.5$ . The calculated response of the embankment as a result of the rainfall record is given in Fig. 56. Settlement rate and the evolution of suction in a particular representative point at the base of the embankment are given. The correspondence between calculations and “in situ” measurements is very poor. In fact, the model indicates that most of the collapse occurs during the first year and a half, when, the rockfill was exposed to a moderate rainfall. Beyond this initial settlement phase, the calculated suction remained essentially constant and the model did not predict any further settlements.

Consider now, Case B. The only change introduced is an increase in air entry value ( $p_0 = 0.1$  MPa). In this way the material may store more water at any applied suction. Figure 57 shows the result of calculations. They now show a much better agreement between model and measurements. Rainfall records of 1993 and 1994 produced a moderate collapse. The strong rainfall, at the beginning of 1996 and

1997 triggered a fast acceleration of settlements, which is also predicted by the model. At the beginning of 1997, before the rainfalls of 1996, the suction in the embankment reaches its lowest value and the collapse potential disappears. This explains the lack of reaction when facing the upcoming strong rainfalls at the end of 1997. At that time, the embankment maintains the water in an efficient way and suction is kept below the values calculated for Case A.

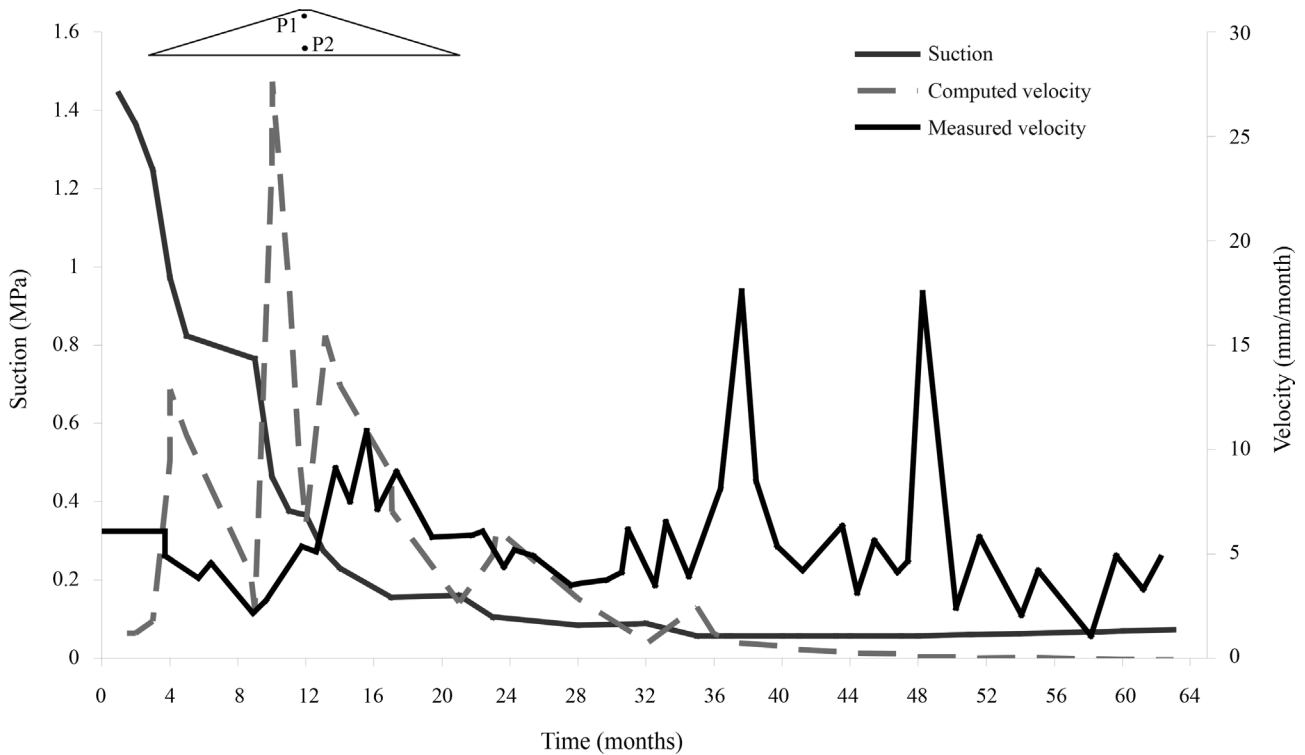
The settlement velocities calculated and presented in Fig. 57 underestimated the field measurements in moderate or non-existent rainfall periods. Suction is clearly maintained constant during these periods of time and the reason for a constant rate of settlement is a creep phenomenon. Increasing this component improves the reproduction of the field records.

Figure 58 offers an additional analysis of the collapse mechanisms associated with rainfall and the specific water retention properties of the rockfill. The figure illustrates the stress paths ( $p, s$ ) in a reference point, of the rockfill embankment for Cases A and B. The points highlighted in the plot refer to specific times, which are also shown in the figure. Also indicated is the position of the LC yield curve at some specific times. The intensity of the collapse is directly related to the displacements of the yielding point along of axis  $p$ . The stress path for Case B displaces towards the right because the vertical net stress increases with the increasing water content of the rockfill, which is controlled by the retention curve. The large displacements of the yield curve in Case A during the first wetting episode (rainfalls in 1993-1994) induced large collapse deformations. The low suction that is reached later on indicates the slight possibil-

**Table 2** - Rockfill embankment. Madrid-Sevilla railway. Analyzed cases.

Case	Air entry value, $p_0$ (MPa)	Flow parameter, $\mu$ (MPa <sup>-1</sup> )	Intrinsic permeability (m <sup>2</sup> )
A	0.01	0.0012	10 <sup>9</sup>
B	0.10	0.0012	10 <sup>9</sup>

ity that some additional collapse may occur. On the other hand, the rockfill described by Curve B loses suction more gradually and the displacements of the yield curve are smaller. At the end of the first rainfall period, the existing



**Figure 56** - Case A. Comparison of measured and calculated settlement rates in point P1. Also shown are suction changes in point P2 (Pinyol *et al.*, 2008).

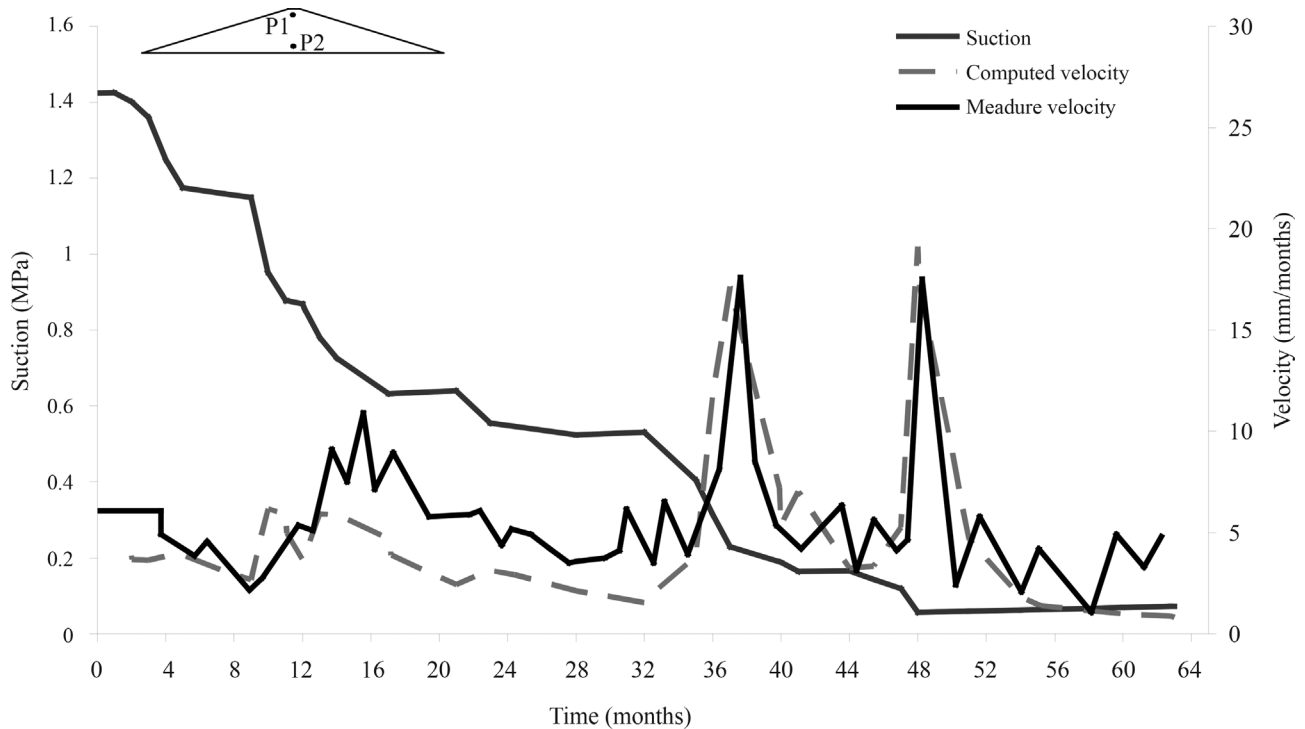


**Figure 57** - Case E. Comparison of measured and calculated settlement rates in point P1. Also shown are suction changes in point P2 (Pinyol *et al.*, 2008).

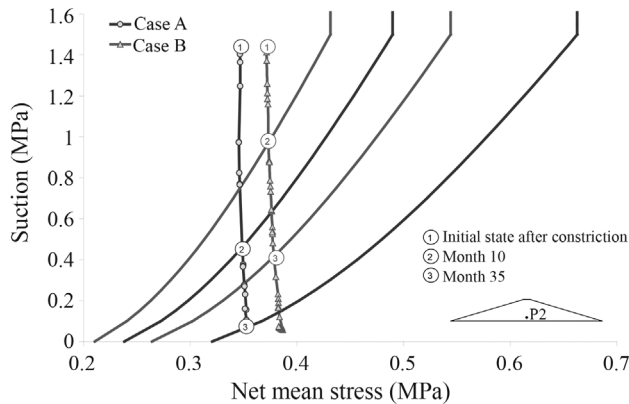


**Figure 58** - Stress-suction paths for point P2 in cases A and B. Also show is the evolution of isotropic yield locus (Pinyol *et al.*, 2008).

suction still has significant collapse potential. Note that due to the shape of the yield curve, the changes in suction in the low range of values are especially effective to induce significant collapse.

This case demonstrates that the water retention curve of the materials has a large effect in the development of collapse settlements in time for a given rainfall regime. However, the intrinsic permeability has an insignificant effect. The time necessary to produce settlements, due to humidity changes, is controlled not only by some key properties of the rockfill (those which characterize the retention properties of water), but also by the specific rainfall regime. Extreme rainfalls induce more collapse settlements only if they imply an additional increase in RH beyond the maximum value reached previously. Creep deformations also depend on the weather, because RH controls delayed deformation, as explained above. Creep deformations also affect hydraulic collapse, because they are irreversible volumetric deformations that harden the material. A hardened fill reacts with lower collapse potentials against any new wetting episode. In practice, distinguishing between long-term deformations induced by wetting or by pure creep is not easy. However, deformations induced by changes in water content tend to concentrate in singular rainfall events that take place in a relatively short time.

## 8. Beliche Dam

Beliche dam is a remarkable case in the literature of rockfill dams because of the wide interest given to this case by many research and technical groups. In addition to several papers published in *Géotechnique* (Naylor *et al.*, 1986, 1997; Alonso *et al.*, 2005) the dam has received a considerable attention in Doctoral dissertations and other Conference and journal papers. There are some reasons for this interest: the dam behavior was well documented, the LNEC performed a singular set of large diameter tests on the material of dam shoulders and the behavior of the downstream shell was rather unexpected. In fact, measured settlements

were as high as those measured upstream when the reservoir was filled. The case has been analyzed from the perspective offered by the conceptual and mathematical models described in this paper (Alonso *et al.*, 2005)

The mechanical parameters of the elastoplastic model developed (Rockfill model; Alonso *et al.*, 2005) were determined by back-analyzing tests reported in Naylor *et al.* (1986, 1997). Figure 59 provides a comparison of measured results and model performance for an oedometer and a triaxial test. Flooding the triaxial test at an advanced state of shearing provided interesting information, which could be well reproduced by the model. The agreement shown in Fig. 59 is reasonably good with the exception of the dilatant behavior of the triaxial sample. This is a shortcoming of the model, which was described, in the  $(q, p)$  plane by regular ellipses.

The rockfill model is one in the library of models available in Code-Bright and has been used in the analysis of several earth and rockfill dams after the pioneering work conducted in Beliche.

Figure 60 shows the pore pressure evolution of four points (1, 2, 3, 4) located in the lower part of the dam. Two of them are located in the upstream inner shell (1) and in the core, close to the upstream boundary. Points 3 and 4 are their downstream symmetric counterparts. The upstream locations essentially follow the reservoir elevation and they exhibit positive pore pressure values at an early stage in the simulation. Situation “E” (at a time  $t = 1440$  days) is not yet at steady state conditions. The map of pore pressures inside the dam is also given in Fig. 60 for the same time. The saturation line displaces slowly inside the core as an approximately vertical front.

Pore pressures of the downstream location are negative (suction) and they essentially reflect the rainfall history. In the simulation performed, due to the high permeability of the exposed shoulders, the total precipitation was imposed as an external flow rate. Evapo-transpiration from the rockfill shoulders is probably minor in this case. Most of the oscillations in suction plotted in Fig. 60 take place in an elastic regime (at essentially constant mean stress). However, whenever suction reaches a lower value than any other suction value in the past record, irreversible strains will develop, leading to dam settlements.

This is illustrated in Fig. 61, which shows a map of plastic volumetric strains at time “E” and the history of these irreversible strains during the early life of the dam. Note that calculated deformations of points 1 and 4, located in the inner rockfill shell, upstream and downstream of the impervious core essentially develop similar strains despite the fact that the upstream point was fully saturated at an early time and Point 4 never experienced saturated conditions if suction calculations are correct. In fact, a low suction is capable of maintaining these materials essentially “dry” because of their very low air entry value. The deformation map shows a fairly symmetric distribution of strains

with respect to dam axis. The flowing water through the core, however, enhances the volumetric deformations of the upstream part of the clay core.

Calculated and measured vertical strains at three different positions and at five different times are compared in Fig. 62. The comparison is good for the dam axis (core).

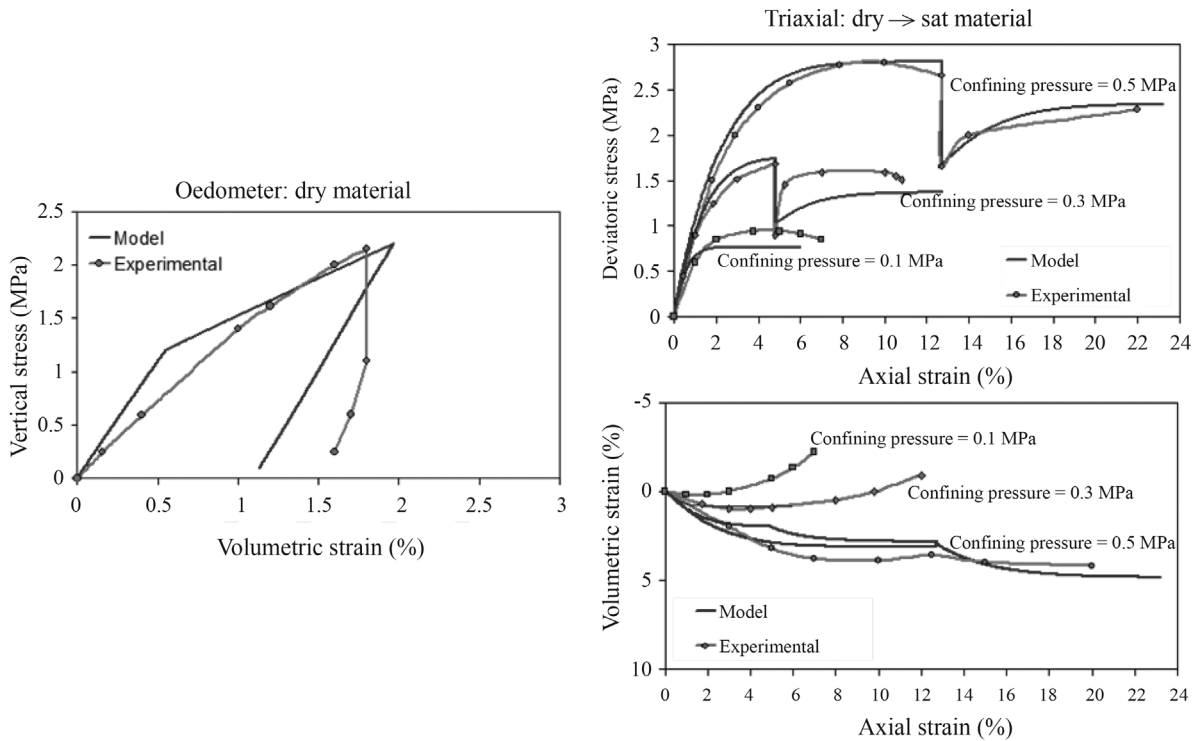


Figure 59 - Modelling oedometer and triaxial experiments of Beliche dam greywacke outer shell.

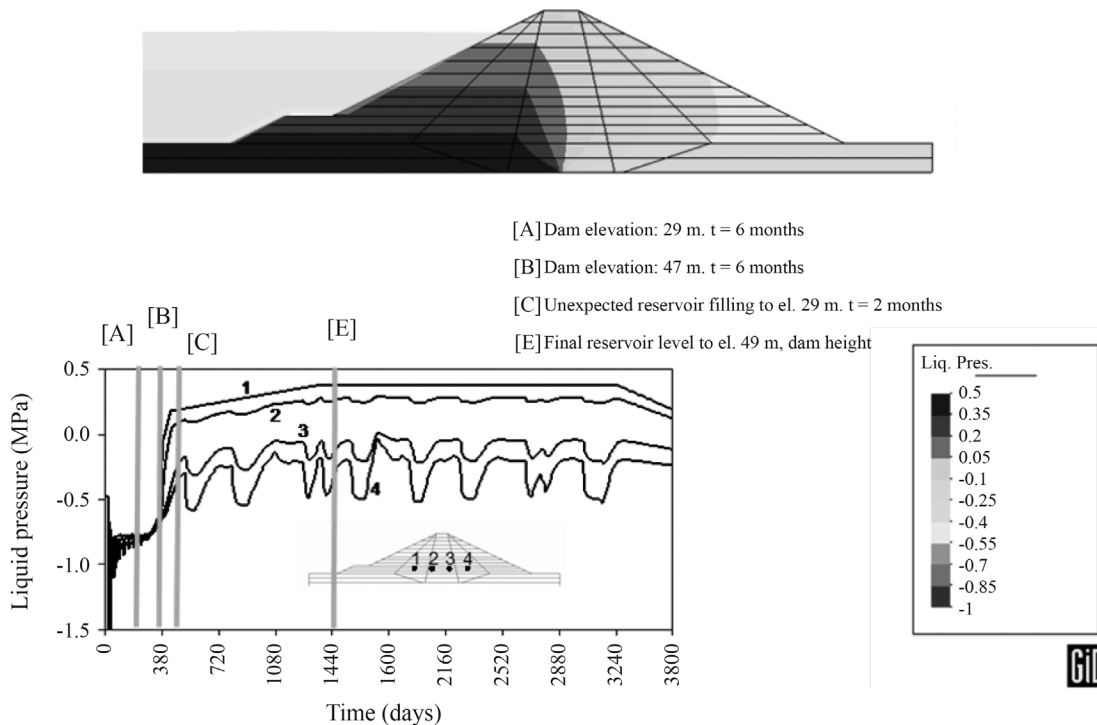
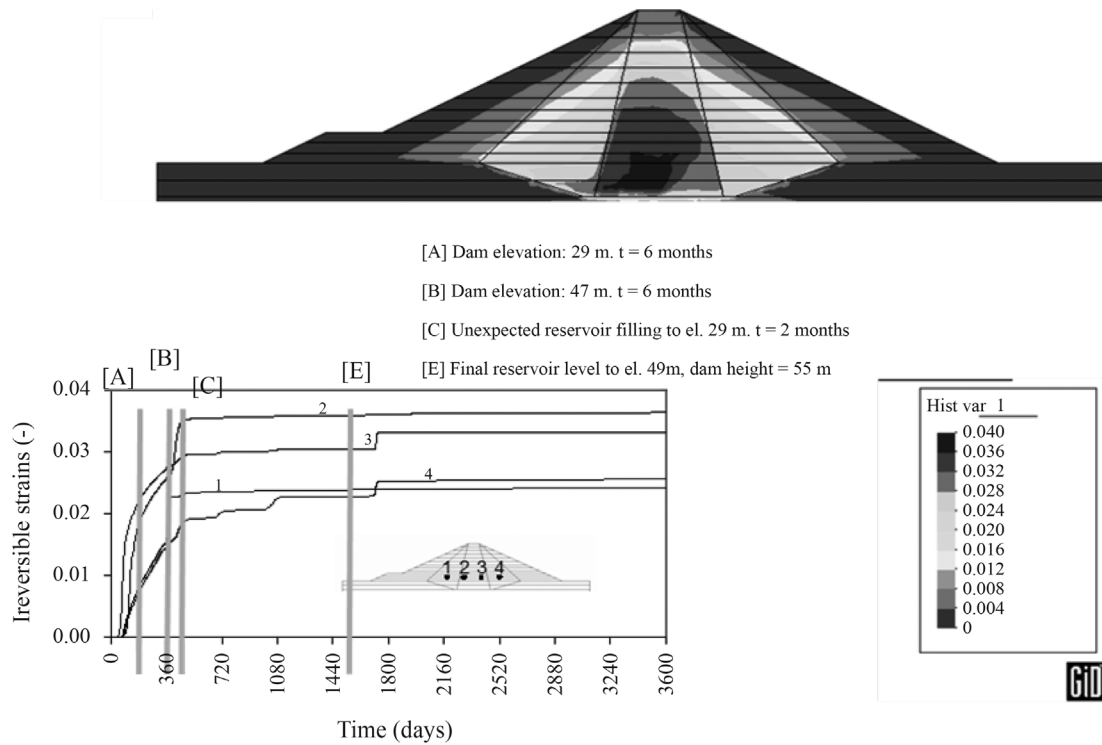


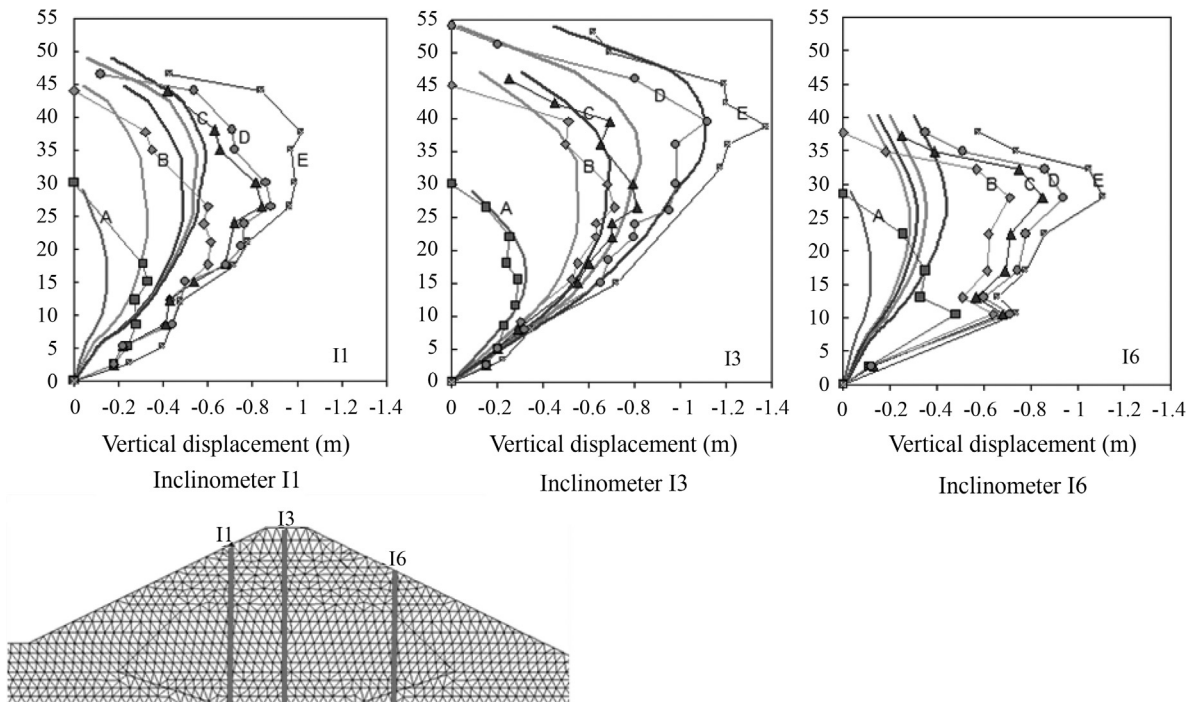
Figure 60 - Beliche dam. Pore water pressure distribution at time (E) and evolution of pore pressures at four points (1, 2, 3 and 4) located in the lower part of the dam.

Field deformations are higher than calculated ones in the rockfill shells. It should be noted that predictions were based on laboratory test results. Two modifications led to

a better fit: the introduction of size effects in the manner discussed in this paper and the consideration of creep strains.



**Figure 61** - Beliche dam. Map of plastic volumetric deformations at time (E) and evolution of plastic volumetric strains at four points (1, 2, 3 and 4) located in the lower part of the dam.



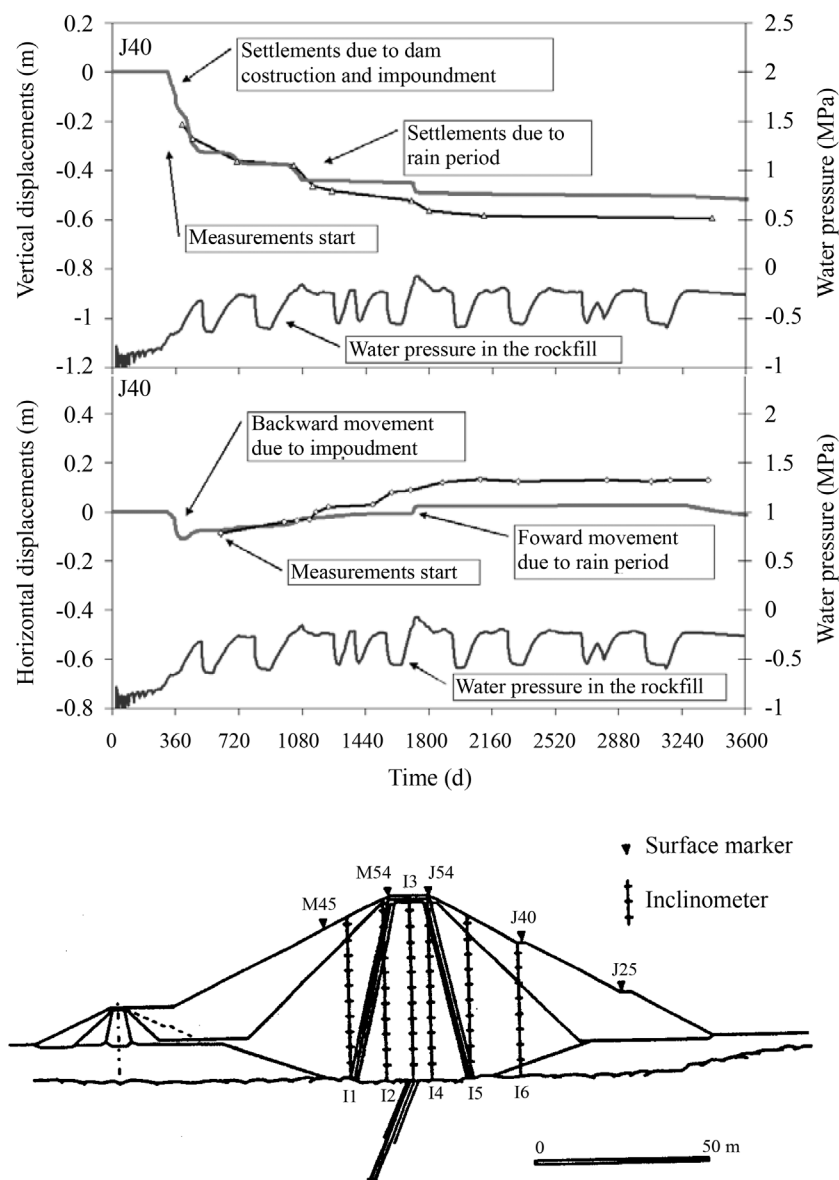
**Figure 62** - Comparison of recorded and calculated vertical strains at five different times at the position of extensometers I1, I3 and I5.

Figure 63 shows the measured and calculated surface displacements of a marker located on the downstream shell. Vertical settlements are particularly well captured. Settlements increase suddenly at the time of intense rainfalls. The calculated records of (negative) pore pressures at the base of the inner downstream shell provide a nice explanation: Settlements are the result of collapse strains which are induced when suction reaches a value lower than any value in the previous history of the shell. For most of the time the rockfill remains under elastic conditions, except for the unavoidable sustained creep explained by a progressive breakage of particles subjected to a subcritical propagation of cracks.

## 9. Epilogue

The behavior of coarse granular materials, described in this paper, requires for its correct interpretation, a wider framework, the one offered by the mechanics of unsaturated soils. This epilogue recalls this wider framework with the purpose of providing a reference to the developments described here. It is interesting to start describing the recent evolution of knowledge of unsaturated soils.

After a large stage dominated by empiricism, during the 80's of the 20<sup>th</sup> Century, the systematic research on the mechanical behavior of unsaturated soils started. It could be thought at that time that a unique theory would perhaps be able to solve in a satisfactory and complete manner the effect of lack of saturation in soils. When some papers on



**Figure 63** - Measured and calculated surface displacements of downstream marker J40. The evolution of calculated water pressure in the inner downstream shell (Point 4 in previous figures) is also indicated.

fundamental research are examined, the impression is that the authors look for this general paradigm.

However, the situation progressively unfolded was more complex and exhibited more difficulties than initially expected. In the 90's attention started to be paid to the microstructure of soils and more specifically to the size and distribution of pores. In fact, the intensity of the capillary forces is directly related to a radius of curvature of the air-water interfaces which could develop in pores. This focus on microstructure is still very active in the fundamental research of unsaturated soils.

Laboratory research concerns frequently a limited class of soils: silts and clays of low plasticity. The reasons for this situation are easy to understand: these are materials where the capillary concepts are of direct application and moreover their permeability is sufficiently high so as to allow relatively reduced testing times. These soils are often fabricated by static compaction, which reduces heterogeneity. Their void ratios are high, which ensures a response easily measurable with the equipment available in the laboratory.

This trend, which is justifiable in university research, neglected a great amount of natural soils and construction materials (compacted soils from any conceivable geological formation), and in particular, rockfills and gravels. In fact, most of the interesting soils in practice were left out-side fundamental research.

Fortunately, the need to solve some new problems, of great significance due to their relationship to safety issues (a singular example would be radioactive waste storage in

deep geological repositories) forced the attention towards materials that do not share some of the favorable circumstances mentioned before. There was a need to investigate very expansive and very dense materials (compacted bentonite, either pure or mixed with sand or well-compacted in high-density pellets). Those are very impervious materials, in which the physical and chemical aspects (as opposed to capillary aspects) are significant in order to examine their relationship with interstitial water.

At the other extreme of grain size distribution, many orders of magnitude above, another class of materials, gravels and rockfill, was known for a long time to be sensitive to the presence of water. It was also known that they deform as a consequence of the breakage of particles, but the relationship between particle breakage and the presence of humidity was not well understood. The behavior of these materials brought again the concept of suction.

The fundamental deformation mechanisms of the wide range of natural, as well as compacted soils, lead to the abandonment of the idea that the unique constitutive framework could be applied to all granular materials just because they were unsaturated. Specific attention should be paid to the physics of deformation at an elementary level, at particle or pore scale.

Let us review the effect of suction in different soils, characterized, as a simple criterion, by grain size. This discussion has been synthesized in Fig. 64.

- The size of particles in rockfills and gravels varies approximately between diameters separated by two orders of magnitude: centimeters and meters. Deformation, as

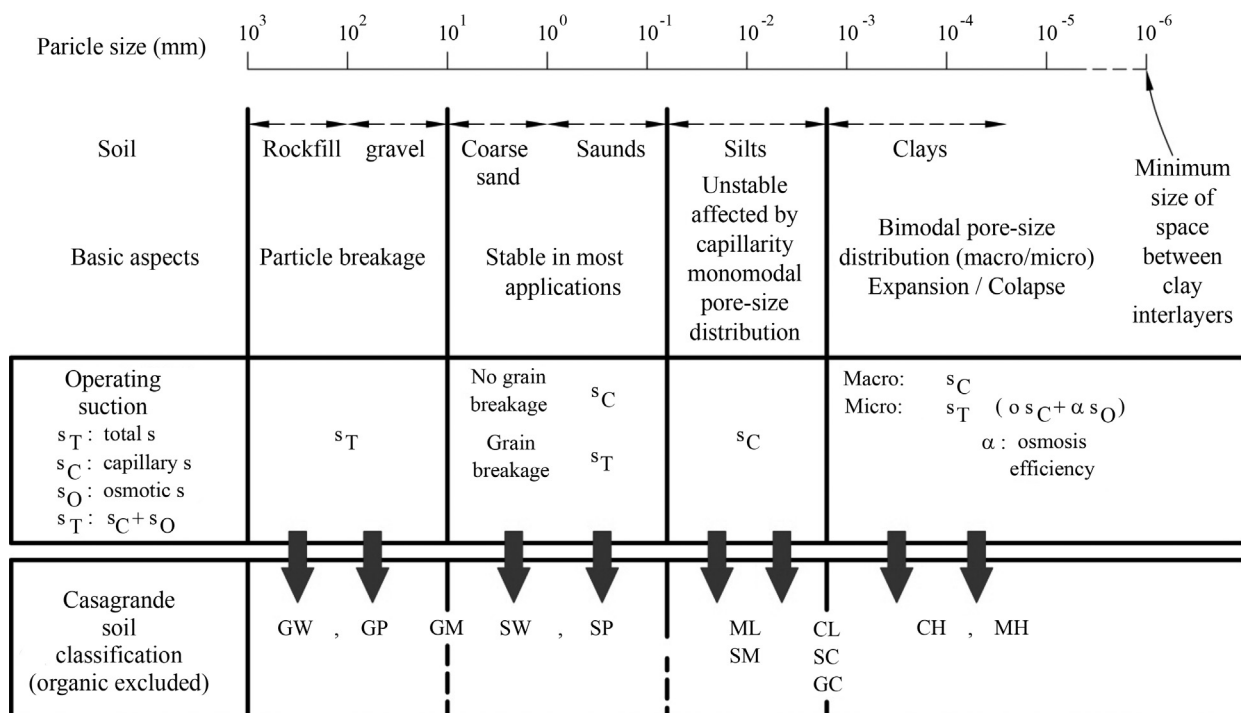


Figure 64 - Type of soils and operative suction.

explained in this paper, is dominated by the breakage of particles (fragments of rock) and the subsequent rearrangement of the granular structure. The breakage of particles is associated with the propagation of fissures in rock fragments.

- Fracture is possible because the size of the grains results in a low number of contacts per unit area or unit volume of the aggregate. On the other hand, the weight of the aggregate only depends on the density and global porosity, and those are magnitudes that essentially do not change with grain size. As a result, concentrated loadings inside the rockfill increase with the size of the grain. Their intensity is high enough to reach stress intensity factors which are close or above the toughness of rocks. This facilitates the propagation of fissures. RH controls also the velocity of the propagation of fractures. The velocity increases when the water energy is high (high RH). One alternative measure of this energy is total suction, directly related to the RH.
- When the grain size decreases to  $10^1$ - $10^{-1}$  mm, we are in the presence of sands. The number of contacts per unit area (for a given reference stress which remains unchanged) increases substantially if compared to gravel and rockfill. Conceptually, this is an “scaled” material of rockfill and gravel, but in this case the concentrated loading at the contacts decrease substantially. The stress intensity factor, which can be calculated in loaded particles, is small, and it is far from the toughness of the rock or mineral that constitutes the grain. Therefore, unless external stresses are very high, those derived from explosions, for instance, the breakage of particles is irrelevant. Therefore the effect of RH in the deformation of these materials disappears. However, if the particles (and therefore the pores) decrease in size (which is the case in fine sands), capillary forces begin to increase. These forces become closer in intensity to the forces between particles originated by the soil weight or the loads of foundations and structures. Therefore the variation of these capillary forces has a particular effect on the mechanical behavior of fine sand. This effect remains small. In any case, it is controlled by the capillary suction.
- In silts, which are materials without plasticity and whose particle sizes range between  $8 \times 10^{-2}$  and  $2 \times 10^{-3}$  mm, the capillary forces become much more intense. They are now similar or higher than those originated by soil weight or by the external loads. Again capillary suction is the “effective” component of the total suction. Capillary suction increases the resistance and stiffness of these materials. Microstructure continues to be simple. The pores are typically distributed around a single dominant pore size.
- The transition towards clay soils implies a fundamental change. On the one side, there is often a bi-modal structure of pores, characterized by two main sizes, separated by several orders of magnitude. They are the “macro”

and “micro” components of the soil structure. On the other side, the capillary concept, which is still interesting to understand the macro behavior, loses its utility in the micro behavior, in which physical and chemical phenomena that link water to mineral surfaces predominate. The small size of the spaces between clay crystals or laminae suggests that the clay aggregates may act as semi-permeable membranes, at least to some extent. This idea and some experimental results suggest that the suction that controls the deformation of aggregates is total suction, although the osmotic component would be probably affected by a reduction factor. In this way, a more complete framework to understand the effect of suction on the behavior of clays may be developed. Capillary suction controls (as in granular media) the arrangement of aggregates. The total suction will explain the deformation of the aggregates themselves.

- Other materials. The idea of resorting to the size of particles to describe the type of soil is useful to explain the fundamental concepts, but it is far from giving a precise description of actual soils. The soil classifications, in particular Casagrande classification, are a resourceful alternative. In Fig. 64 there is a proposal to relate the type of soil (GW, GP, CH, MH) to the “operative” suction to explain the mechanical behavior. Some soils are easy to assign because they directly reflect grain size distribution. Others occupy transition spaces. Among them a very wide class of natural and compacted soils may be found. They are the medium to low plasticity clays, and mixtures of silt-clay, or even gravel-clay.
- Those materials often exhibit a double structure, but physical and chemical phenomena of clay-water interaction are less remarkable than in high plasticity clays. Their expansivity is also lower and this implies that “simpler” constitutive models, such as BBM (Barcelona Basic Model; Alonso *et al.*, 1990), can be applied. Figure 64 does not include all the soils of interest in geotechnical engineering. In fact, cemented soils are a wide class of materials, which are often unsaturated in practice. This is the case of loess, alluvial soils in arid and semi-arid climates, residual soils and tropical soils.
- Finally, soft argillaceous rocks are frequent in geotechnical projects. They are typically materials somewhat cemented and having low porosity. Their degradation against atmospheric cyclic action can be analyzed with some advantage from the perspective of the mechanics of unsaturated soils. They are soils that exhibit properties shared with gravels and rockfills (when the suction is high, that is, when they are dry) and clay and silts (when the suction is low).

The groups of soils identified previously required constitutive models which are differentiated, simply because the mechanism of deformations and the nature of suction controlling the behavior are different. Despite this, the models developed show some dependency among them,

which contributes to provide some additional order to the described scenario.

In the core of this order we may locate the models that are developed around the concept of yield function LC (Loading-Collapse), which has been described in this paper although its origin started with the BBM. The fundamental contribution of these models is to link the behavior under load to the collapse phenomenon, which is a key characteristic of the lack of saturation in a granular medium. The BBM reproduces in a reasonable manner the behavior of low to medium plasticity soils. It was formulated in terms of two independent stress fields: net stress and capillary suction. When examining, in one of the extremes of the grain-size distribution, the behavior of gravel and rockfill, there are interesting similarities with this basic model developed for conventional soils. In fact, the model described in Section 4, could be also called an “LC” type of model even if the collapse mechanisms are very different from those found in soils. Suction has no a stress or capillary interpretation. Rather, it is the energy interpretation of suction, associated with its role in fracture propagation, which explains the laboratory and field observations.

## Acknowledgments

The author wishes to thank the excellent work performed by his past Doctorate students, Prof. L. Oldecop, Prof. C. Chávez and Dr. E. Ortega. Their findings and test results are at the core of this lecture. Thanks are extended to Dr. N. Pinyol and Prof. S. Olivella who helped the author in all computational aspects. The chapter on DEM modeling is part of the ongoing work of the Doctorate student Ing. M. Tapias. The laboratory developments mentioned in the lecture could not have been achieved without the intense involvement of the Geotechnical Laboratory staff: Prof. E. Romero, T. Pérez, J. Sánchez and V. Lozano. The help received from Lic. M. Obrador and R. Giménez during the preparation of the manuscript and figures is acknowledged with thanks. Part of the research reported has been financed by Research Projects awarded by the Spanish Ministry of Education.

## References

- Alonso, E.E. (2006) Field applications of unsaturated soil mechanics. *Geotechnical Special Publication*, v. 148, p. 1-33.
- Alonso, E.E.; Gens, A. & Hight, D.W. (1987) Special Problem Soils. General Report. Proc. 9<sup>th</sup> European Conference on Soil Mechanics and Foundation Engineering. Dublin, v. 3, p. 1087-1146.
- Alonso, E.E.; Gens, A. & Josa, A. (1990) A constitutive model for partially saturated soils, *Géotechnique*, v. 40:3, p. 405-430.
- Alonso, E.E.; Olivella, S. & Pinyol, N.M. (2005) A review of Beliche Dam. *Géotechnique*, v. 55:4, p. 267-285.
- Athanasiau, C.; Simonsen, A.S.; Soereide, O.K. & Tistel, J. (2005). Elastic and creep settlements of rock fills. Proc. 16th Int. Conf. Soil Mech. Geotech. Engng., Osaka, p. 1837-1843.
- Cetin, H.; Laman, M. & Ertunç, A. (2000) Settlement and slaking problems in the world’s fourth largest rock-fill dam, the Ataturk Dam in Turkey. *Engineering Geology*, v. 56:3-4, p. 225-242.
- Charles, R.J. (1958) Static fatigue of glass. *Journal of Applied Physics*, v. 29, p. 1549-1560.
- Charles, J.A. (1989). Geotechnical properties of coarse grained soils. Proc. of the 12th Int Conf on Soil Mechanics and Foundation Engineering, Rio de Janeiro, p. 2495-2519.
- Charles, J.A. (1991). Laboratory compression tests and the deformation of rockfill structures. *Advances in Rockfill Structures*. NATO ASI Series E, v. 200, p. 73-95.
- Charles, J.A. & Watts, K.S. (1980) The influence of confining pressure on the shear strength of compacted rockfill. *Géotechnique*, v. 4:3, p. 353-398.
- Chávez, C. (2004) Estudio del Comportamiento Triaxial de Materiales Granulares de Tamaño Medio con Énfasis en la Influencia de la Succión. PhD Thesis, Universitat Politècnica de Catalunya. Barcelona, Spain.
- Chávez, C.; Romero, E. & Alonso, E.E. (2009) A rockfill triaxial cell with suction control. *Geotechnical Testing Journal*, v. 32:3, p. 1-13.
- Chávez, C. & Alonso, E.E. (2003) A constitutive model for crushed granular aggregates which include suction effects. *Soils and Foundations*, v. 43:4, p. 215-227.
- Clements, R.P. (1981). The Deformation of Rockfill: Inter-Particle Behavior, Bulk Properties and Behavior in Dams. PhD. Thesis, Faculty of Engineering, King’s College, London University.
- Cundall, P.A. & Strack, O.D.L. (1979) A discrete numerical model for granular assemblies. *Géotechnique* 29:1, p. 47-65.
- De Mello, V.F.B. (1977) Seventh Rankine Lecture: Reflections on design decisions of practical significance to embankment dams. *Géotechnique*, v. 27:3, p. 279-356.
- Frossard, E. (2009) On the structural safety of large rockfill dams. Proc. 23<sup>rd</sup> Conf. on Large Dams. Q. 91-R. 39 Brasilia.
- Frossard, E.; Hu, W.; Dano, C. & Hicher, P.-Y. (2012) Rockfill shear strength evaluation: a rational method based on size effects. *Géotechnique*, v. 62:5, p. 415-427.
- Fumagalli, E. (1969) Tests on cohesionless materials for rockfill dams. *J. Soil Mech. Found. Engng Div.*, v. 95(SM1), p. 313-330.
- Gili, J.A. (1988) Modelo Microestructural para Medios Granulares No Saturados. PhD Thesis. Universitat Politècnica de Catalunya. Barcelona, Spain.

- Gili, J.A. & Alonso, E.E. (2002) Microstructural deformation mechanisms of unsaturated granular soils. *Int. J. Numer. Anal. Meth. Geomech.*, v. 26, p. 433-468.
- Hardin, B.O. (1985) Crushing of soil particles. *Jnl. of Geotech. Engng.*, v. 111:10, p. 1177-1192.
- Justo, J.L. & Durand, P. (2000) Settlement-time behavior of granular embankments. *Int. J. Numer. Anal. Methods Geomech.*, v. 24, p. 281-303.
- Lee, D.M. (1992). *The Angles of Friction of Granular Fills*. Ph.D. dissertation, University of Cambridge.
- Marachi, N.D.; Chan, C.K.; Seed, H.B. & Duncan, J.M. (1969) *Strength and Deformation Characteristics of Rockfill Materials*. Department of Civil Engineering. Report No. TE-69-5. University of California.
- Marsal, R.J. (1973) Mechanical properties of rockfill. In: *Embankment Dam Engineering*. Casagrande. R.C. Hirschfeld & S.J. Poulos (eds) John Wiley & Sons, New York, p. 109-200.
- Marsal, R.J.; Arellano, L.R.; Guzmán, M.A. & Adame, H. (1976) *El Infiernillo: Behavior of Dams Built in Mexico*. Instituto de Ingeniería, UNAM, Mexico.
- McDowell, G.R. & Bolton, M.D. (1998) On the micro-mechanics of crushable aggregates. *Géotechnique*, v. 48:5, p. 667-679.
- Mesri, G. & Castro, A. (1987).  $C_u/C_c$  concept and  $K_0$  during secondary compression. *J. Geotech. Engng, ASCE* v. 113:3, p. 230-247.
- Naylor, D.J.; Maranha das Neves, E.; Mattar, D. Jr. & Veiga Pinto, A.A. (1986) Prediction of construction performance of Beliche Dam. *Géotechnique*, v. 36:3, p. 359-376.
- Naylor, D.J.; Maranha das Neves, E. & Veiga Pinto, A.A. (1997) A back-analysis of Beliche Dam. *Géotechnique*, v. 47:2, p. 221-233.
- Nobari, E.S. & Duncan, J.M. (1972) *Effect of Reservoir Filling on Stresses and Movements in Earth and Rockfill Dams*. Department of Civil Engineering, Report No. TE-72-1. University of California.
- Oldecop, L.A. & Alonso, E.E. (2001) A model for rockfill compressibility. *Géotechnique*, v. 51:2, p. 127-139.
- Oldecop, L.A. & Alonso, E.E. (2003) Suction effects on rockfill compressibility. *Géotechnique*, v. 53:2, p. 289-292.
- Oldecop, L.A. & Alonso, E.E. (2004) Testing rockfill under relative humidity control. *Geotechnical Testing Journal*, v. 27:3, p. 1-10.
- Oldecop, L.A. & Alonso, E.E. (2007) Theoretical investigation of the time-dependent behavior of rockfill. *Géotechnique*, v. 57:3, p. 289-301.
- Olivella, S.; Carrera, J.; Gens, A. & Alonso, E.E. (1994) Nonisothermal multiphase flow of brine and gas through saline media. *Transport in Porous Media*, v. 15, p. 271-293.
- Olivella, S.; Gens, A.; Carrera, J. & Alonso, E.E. (1996) Numerical formulation for simulator (Code\_Bright) for coupled analysis of saline media. *Engineering Computations*, v. 13:7, p. 87-112.
- Ortega, E. (2008) *Comportamiento de Materiales Granulares Gruesos. Efecto de la Succión*. Ph.D. Thesis. Universitat Politècnica de Catalunya, Barcelona, Spain.
- Poorooshasb, H.; Holubec, I. & Sherbourne, A. (1966) Yielding and flow of sand in triaxial compression. Part I. *Canadian Geotech. Jnl.*, v. 3:4, p. 179-190.
- Ramon, A.; Alonso, E.E. & Romero, E.E. (2008) Grain size effects on rockfill constitutive behavior. *Proc. of the 1<sup>st</sup> European Conf. on Unsaturated Soils*. Taylor & Francis, p. 341-347.
- Russell, A.R. & Wood, D.M. (2009) Point load tests and strength measurements for brittle spheres. *International Journal of Rock Mechanics & Mining Sciences* v. 46, p. 272- 280
- Schnitter, N.J. (1994) *A History of Dams. The Useful Pyramids*. Balkema, Rotterdam.
- Sherard, J.L. & Cooke, J.B. (1987). Concrete-face rockfill dam: I. Assessment. *J. Geotech. Engng ASCE*, v. 113:10, p. 1096-1112.
- Soriano, A. & Sánchez, F.J. (1999) Settlements of railroad high embankments. *Proc. 12<sup>th</sup> European Conf. on Soil Mech. and Geotech. Eng.*, Amsterdam, The Netherlands, p. 1885-1890.
- Sowers, G.F.; Williams, R.C. & Wallace, T.S. (1965) Compressibility of broken rock and settlement of rockfills. *Proc. 6th Int. Conf. on Soil Mech. & Found. Engng*. Montreal, Canada, p. 561-565.
- Terzaghi, K. (1960) Discussion on salt springs and lower bear riverdams. *Transportations*, v. 125:2, p. 139-148.
- Veiga Pinto, A.A. (1983) *Previsao do Comportamento Estrutural de Barragens de Enrocamento*. Ph.D. Thesis, Laboratorio Nacional de Engenharia Civil, Lisbon.



## ***Articles***

***Soils and Rocks***  
**v. 37, n. 1**



# Tunnel Face Reinforcement by Bolting - Numerical Modelling of Centrifuge Tests

J.P. Janin, D. Dias

**Abstract.** This paper presents the results of numerical investigations on the deformation behaviour of a tunnel face reinforced by longitudinal pipes. The three dimensional finite difference calculations are based on series of reduced-scale centrifuge model tests (Al Hallak, 1999). Numerical analyses are developed and carried out with particular emphasis on the validation of the excavation method. Geomechanical parameters of two constitutive models are calibrated on triaxial and oedometric tests. The numerical models are then compared with the centrifuge model results. This comparison concerns especially the tunnel face extrusion, the ground surface settlements and the minimum pressure that guarantees the face equilibrium before failure. Bolting influence on these parameters is studied.

**Keywords:** numerical modelling, reinforcement, bolting, tunnel, constitutive model.

## 1. Introduction

The excavation of a tunnel produces a modification of the initial ground mass stress field. Deformations of soil (extrusion and pre-convergence) are triggered in the core ahead the tunnel face, afterwards spread in the cavity and towards the surface. This happens especially in shallow depth tunnels. In urban zones, it is essential to control these ground surface settlements in order to avoid damages on neighbouring buildings. Several studies and real cases have shown that it is possible to control and limit the ground mass deformation response by acting on the core-face system rigidity (Lunardi, 2008).

In this aim, the application of fibre glass or steel bolts in tunnel has known, during these last twenty years, several applications. The pre-confinement of the core with horizontal bolts has been generally combined with other methods, such as the realization of “pre-arches” using mechanical pre-cutting, sub-horizontal jet-grouting, steel or fibre glass elements (injected with grout) according to the type of ground and stress-strain conditions. This mixed technique assures, on one hand, stability of the excavation and safety of workers and, on other hand, it permits to control movements and to limit settlements on ground surface.

In order to optimize reinforcement technique, it is important to predict deformation response of the bolted ground mass to excavate. In addition to theoretical methods, experimental tests can be realized to study the three-dimensional problem of tunnel digging. It is possible to study these phenomena by full-scale models or scale-down models. Because of cost and difficulties to realize tests on full-scale models, scale-down models are often preferred. This last type of physical models permit to better control the initial state of stress, they are faster and they can be used until failure. Nevertheless, different researches have dem-

onstrated that scale-down models have to respect some similitude laws to guarantee mechanical behaviour similitude with the full-scale model. These similitude laws are based on dynamic equations, the law of mass conservation and the stress-strain laws of materials (Mandel, 1962; Weber, 1971; Garnier, 2001). In this context, different researchers have shown that experimental test results on scale-down models, submitted to gravity acceleration, reflect measures in situ with a better approximation. Centrifuge facility allows models to have a stress-strain behaviour in good agreement with reality.

The aim of this study is to develop and validate a numerical excavation simulation method of a tunnel reinforced using longitudinal pipes ahead the face. The following research is based on experimental tests realized on a centrifuge scale-down model (Al Hallak, 1999). A three-dimensional numerical model is carried out using FLAC<sup>3D</sup> in order to simulate the physical centrifuge model. Numerical results are then compared with scale-down outcomes. This comparison concerns especially the tunnel face extrusion, the ground surface settlements and the minimum pressure that guarantees the face equilibrium before failure. Bolting influence on these parameters is then studied.

## 2. Experimental and Numerical Model Descriptions

### 2.1. Centrifuge tests on a scale-down model

The bolting face influence during tunnel excavation has been studied by Al Hallak (1999) on the stability and on movements of the surrounding soil mass. Centrifuge tests were realized using a scale-down model.

The physical model (Fig. 1) simulated a full scale tunnel having a 10 m diameter and an overburden equal to two times the diameter. The chosen scale factor was 1/50. Con-

---

Jean Pierre Janin, PhD, Terrasol, 42-52 quai de la Rapée, CS 71230, 75583 Paris, France. e-mail: jp.janin@terrasol.com.  
Daniel Dias, PhD, Professor, LTHE, Grenoble Alpes University, 38000 Grenoble, France. e-mail: daniel.dias@ujf-grenoble.fr.  
Submitted on February 19, 2013; Final Acceptance on September 24, 2013; Discussion open until July 31, 2014.

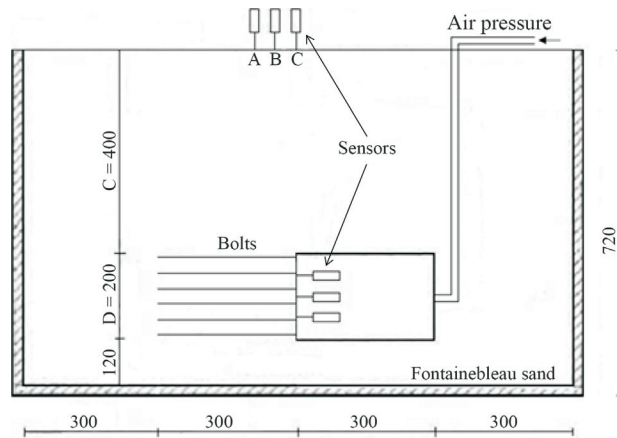


**Figure 1** - Scale-down model characteristics (dimensions in mm).

sequently, the scale-down model geometrical characteristics were the followings:

- Diameter (D) = 200 mm;
- Overburden (C) = 400 mm.

The rule, that guarantees the behaviour similitude between the scale-down model and the full-scale one, is the following:

$$g.l = 1 \quad (1)$$

where  $g$  is the gravity and  $l$  represents a model dimension. Therefore, in order to respect this law, the studied model was submitted to an acceleration of 50 times the gravity.

The container and the tunnel lining were steel made and supposed to be not deformable. The tunnel face was made in a deformable latex membrane where air pressure can be applied. The ground mass, that enclosed the tunnel lining, was “Fontainebleau” sand, a fine homogeneous material often used in France for rheological investigations ( $D_{50} = 0.2$  mm et  $\gamma = 15.7$  kN/m<sup>3</sup>). Several sensors placed in the model permitted to measure the:

- Tunnel face displacements;
- Surface Settlements;
- Pressure on the latex membrane.

Two types of reinforcement were chosen: threaded steel bars or PVC sand-coated pipes. The latter permitted to simulate fibre glass reinforcement in a scale-down model. The bolting geometry adopted (diameter, length, density)

was based on medium values normally used in tunnels construction and especially on the first Toulon tube tunnel (Dias *et al.*, 2002).

The test was characterized by two phases:

1. The model was submitted to an acceleration increasing from 1 to 50  $g$ . During this phase an air pressure was applied to the latex membrane in order to assure the face stability. Air pressure value in this phase was kept equal to the geostatic stress at the tunnel centreline (in this case,  $p_{50g} = 200$  kPa).
2. Once acceleration of 50  $g$  was reached, the tunnel excitation was simulated by decreasing the air pressure on the latex membrane until failure occurred. During this process, sensors measured soil displacements corresponding to decreasing pressure values.

Different tests were realized varying reinforcement parameters such as the material composition, the number of bolts and their length (Table 1).

The tests showed that:

- Reinforcement of the core ahead the tunnel face using longitudinal bolts reduces by an half the limit confinement face pressure and reduces significantly the extrusion and the ground surface settlements.
- Increasing the bolting density permits to further reduce the face limit confinement pressure.
- 130 mm length bars (0.7D) give the same resistance as longer bolts.

This experimental study is the reference for our research.

## 2.2. Three-dimensional numerical model

Numerical simulations are carried out and compared to the above experimental results. A 3D finite difference numerical model was performed using FLAC<sup>3D</sup> (Itasca, 2005). Geometrical characteristics and dimensions of the model are the same as the physical model. Nevertheless, only one half of the model (Fig. 2) is modeled due to its symmetry. The model is made of about 56000 zones (soil elements).

For the displacement boundary conditions, the bottom boundary is assumed to be fixed and the vertical boundaries are constrained in motion in the normal direction.

**Table 1** - Different test configurations.

Test n°	Reinforcement type	Number of bars	Length (mm)	Diameter (mm)	Bolting density at prototype scale (bolts/m <sup>3</sup> )
I / II	-	-	-	-	-
III	PVC sand-coated bar	28	300	3.5	0.4
IV	PVC sand-coated bar	48	300	3.5	0.6
V	PVC sand-coated bar	28	130	3.5	0.4
VI	threaded steel bar	37	300	2	0.5

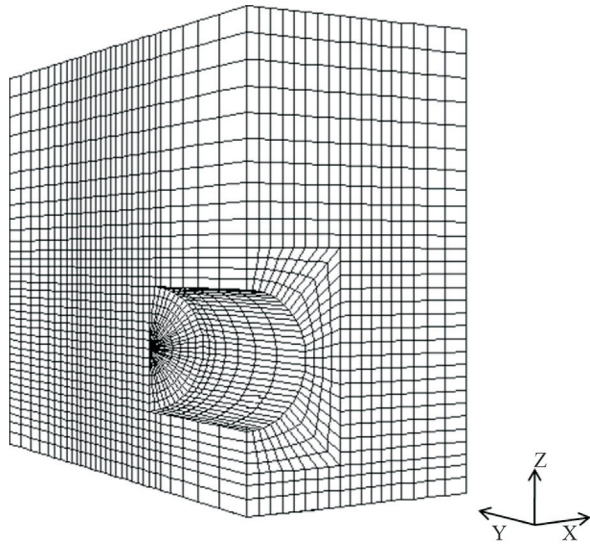


**Figure 2** - FLAC<sup>3D</sup> Model.

An interface element is introduced around the cavity to allow the soil to slide on the lining. A friction angle between the tunnel lining and the sand is chosen to be equal to 2/3<sup>rd</sup> of the sand friction angle. This value reproduces better the reality than a perfect adherence around the cavity wall. In Table 2, the principal interface characteristics are presented.

In the numerical simulation, the process is reproduced as in the experimental tests. The model is submitted to an acceleration equal to 50 g. A 200 kPa pressure is applied to the tunnel face. Then, tunnel digging is simulated decreasing pressure until failure occurs.

Surface settlements and face extrusion are analysed and compared with the experimental results.

**2.3. Constitutive models and geotechnical parameters**

Two constitutive models with an increasing complexity were chosen to take into account the behaviour of the Fontainebleau sand:

- A linear elastic perfectly plastic model with a failure criterion of Mohr-Coulomb type;
- An elastoplastic model with two mechanisms named CJS2 (Jenck & Dias, 2004; Maleki, 1998; Cambou & Jafari, 1988, Hejazi *et al.*, 2008).

The CJS2 model is a simplified version of the original CJS model developed by Cambou & Jafari (1988) for cohesionless soils. It is based on an elastic nonlinear part with two plasticity mechanisms: a deviatoric and an isotro-

**Table 2** - Interface characteristics.

Normal stiffness (kN/m)	3.10 <sup>11</sup>
Tangential stiffness (kN/m)	3.10 <sup>11</sup>
Cohesion	0
Friction angle	(2/3) φ <sub>soil</sub>

pic mechanism. It allows taking into account the nonlinearity of the behaviour at low stress level and the existence of dilatancy before the failure for dense or overconsolidated materials. The use of this model requires the determination of two elastic parameters, five deviatoric mechanism parameters and one isotropic mechanism parameter. The description of the model is given in Jenck *et al.* (2009).

The sand used in the scale-down test is considered as a pure frictional material.

The geotechnical model parameters were back-analysed from triaxial and oedometric tests on the Fontainebleau sand.

Triaxial tests were performed with three different confinement pressures: 30 kPa, 60 kPa and 90 kPa. Figure 3 illustrates the relationship between the deviatoric stress and the axial strain. Two triaxial tests results for a confinement pressure of 60 kPa are shown; the back analysis has been done on all the confinement pressures. A limit of these triaxial tests is the fact that the experimental applied confinement pressures are lower than the pressures values applied at the tunnel face during the centrifuge tests. The curves obtained with Mohr-Coulomb (M-C) and CJS2 simulations are compared with the experimental results.

In the M-C model, the initial Young modulus and plastic threshold values reflect experimental outcomes. However, it appears that this model simulates approximately the real soil behaviour due to its linearity. On the other hand the CJS2 model better represents the non linear soil behaviour since the model is based on a non linear elastic part and two plastic mechanisms.

The volumetric strain and the axial deformation are shown on Fig. 4. As observed regarding the deviatoric stress, the CJS2 model allows better representation of the real soil behaviour.

Oedometric tests were simulated using FLAC<sup>3D</sup>. Loading and unloading cycles were applied.

Figure 5 illustrates the relationship between the mean pressure and strain. Curves obtained with M-C and CJS2 constitutive models are again compared with the experimental one.

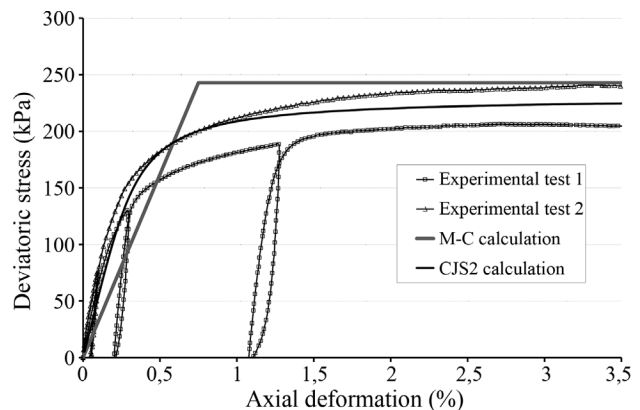


**Figure 3** - Deviatoric stress vs. axial deformation (triaxial tests 1 and 2 with a 60 kPa confinement pressure).

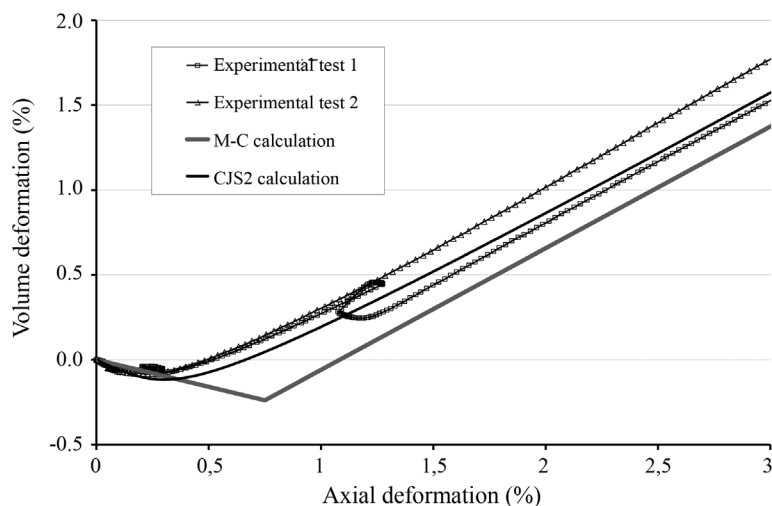


**Figure 4** - Volume deformation vs. axial strain (triaxial tests with a 60 kPa confinement pressure).

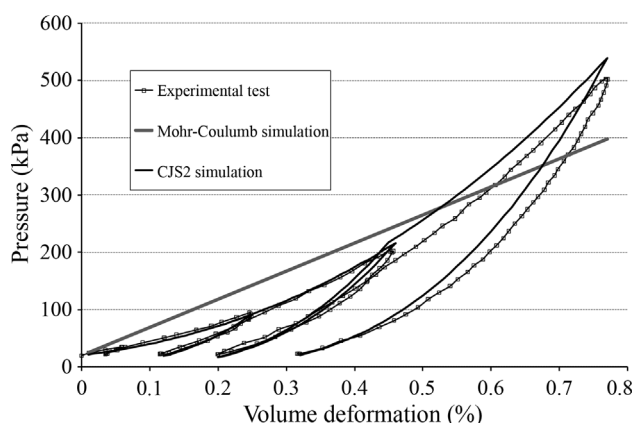


**Figure 5** - Mean pressure vs. axial strain (oedometric test).

The M-C constitutive model linearity appears clearly in this graph. The Young modulus value for the M-C constitutive model was chosen equal to 33 MPa which corresponds to approximately the vertical stress at the upper part of the tunnel face. It is not possible using this constitutive model to distinguish loading and unloading phases, whereas the CJS2 model permits to better simulate ground response with accuracy.

Table 3 and Table 4 summarize, respectively for Mohr-Coulomb and CJS2 models, parameters that fit the experimental curves.

### 3. Comparison between Numerical and Experimental Results

Physical tests were simulated using the constitutive model parameters adjusted to laboratory tests results. For tests n° I and n° II, no reinforcement was applied ahead the tunnel face. Afterwards, the bolting influence on ground movements was analysed.

**Table 3** - MC model parameters.

Parameter	Value
Young modulus: E (MPa)	33
Poisson ratio: $\nu$	0.33
Cohesion: $c'$ (kPa)	0
Friction angle: $\phi'$ ( $^\circ$ )	42
Dilatancy angle: $\psi$ ( $^\circ$ )	15.3

**Table 4** - CJS2 model parameters.

Parameter	Value
Shear modulus: $G_0$ (MPa)	37.7
Volumetric modulus: $K_0^e$ (MPa)	87.7
Material parameters: n	0.6
Dilatancy slope: $\beta$	-0.75
Size of the characteristic surface: $R_c$ (m)	0.20
Deviatoric slope: A	0.002
Size of the failure surface: $R_m$ (m)	0.33
Shape of the failure surface: $\gamma$	0.86
Plastic bulk modulus for the reference pressure $P_a$ : $K_0^p$ (MPa)	100

Numerical results, such as face extrusion, surface settlements and limit equilibrium pressure until failure occurs, were compared to experimental results.

#### 3.1. No reinforcement simulation - Reference case (Test II)

Figure 6 presents the confinement pressure vs. the tunnel centerline face extrusion. In an initial phase, when the pressure starts decreasing, the displacements are lim-

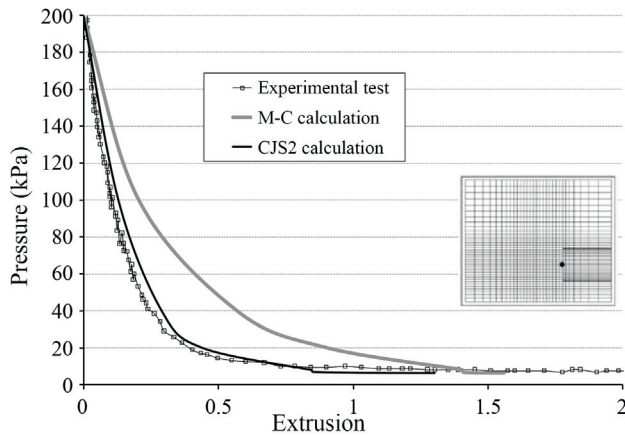


**Figure 6** - Confinement pressure vs. axial face displacement, comparison between experimental and numerical results.

ited. Then extrusion increases until the limit pressure is reached and the face failure occurs. Numerical results show good agreement with the experimental ones. However, there is a significant difference between the two used constitutive model results. CJS2 model fit better the experimental results.

The relationship between surface settlements and the confinement pressure is shown in Fig. 7. The settlement refers to the surface point above the tunnel face (point C).

A considerable difference between numerical and physical results is noted for the M-C calculation. This difference increases with the internal pressure decrease. The numerical simulation underestimates the surface settlements. The calculation considering the CJS2 constitutive model is in better agreement with the experimental results.

The experimental limit confinement face pressure before failure occurs, is compared to the numerical one, as shown on Table 5.

In the numerical calculation, the limit confinement pressure is the last pressure for which the model reaches an

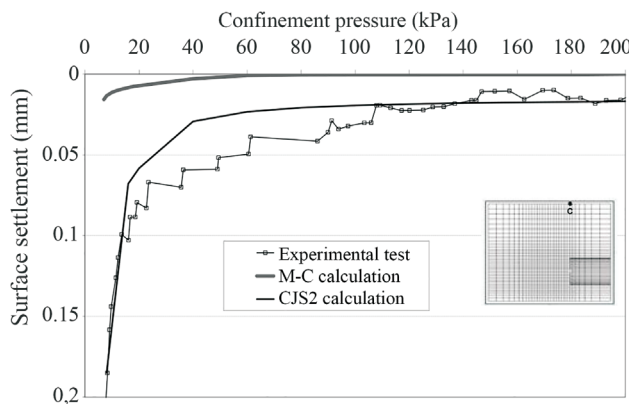


**Figure 7** - Surface settlement (point C) vs. confinement pressure, comparison between experimental and numerical simulation results.

**Table 5** - Limit pressure, calculation criterion.

	Limit equilibrium pressure (kPa)
Physical test	8
M-C calculation	7.8
CJS2 calculation	7.9

equilibrium status. The equilibrium state in FLAC<sup>3D</sup> is identified when the largest ratio of maximum unbalanced force to the average applied force is below a specified limit called “equilibrium ratio” (the default value is equal to 0.001). The unbalanced force indicates when a mechanical equilibrium state (or the onset of plastic flow) is reached for a static analysis. A model is in exact equilibrium if the net nodal force vector at each grid point is zero. The maximum nodal force vector is monitored in FLAC (called the unbalanced force) and will never reach exactly zero on a numerical analysis. The model is considered to be in equilibrium whenever the value of the maximum unbalanced force is small compared to the total applied forces in the problem (Itasca, 2005). In our calculations, equilibrium is reached when the unbalanced force ratio reaches  $10^{-8}$  (the default is set to  $10^{-5}$ ). Effective convergence must then be checked by verifying the grid-point velocities, which must be very small when static equilibrium is reached in our problem, less than  $10^{-11}$  m/ step.

Under the limit confinement pressure a failure occurs and a horizontal threshold appears (Fig. 6).

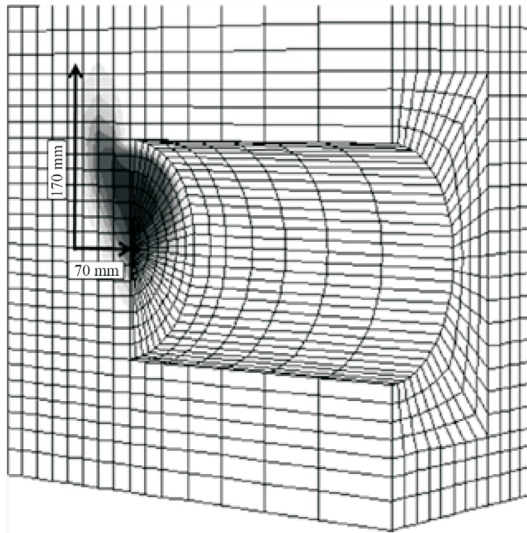
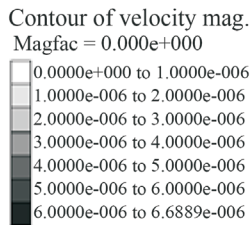
The limit pressure values, obtained with numerical simulations, are in good agreement with the physical values. The difference with the experimental value is respectively equal to 2.5% and 1.3% for the M-C case and the CJS2 one.

Figure 8 shows the failure mechanisms obtained with the two constitutive models. The failure mechanism is represented with the contour of velocity magnitude.

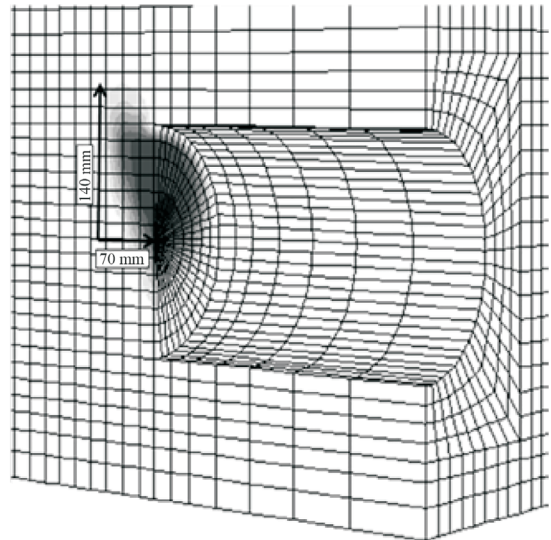
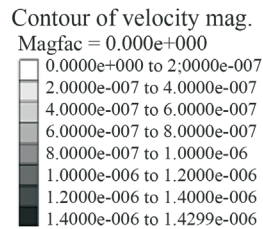
With the M-C constitutive model the failure mechanism has the same width but is higher than the CJS2 one. As it can be seen in Fig. 8, the failure only occurs in the upper half part of the tunnel face. The same phenomenon has been obtained by Mollon *et al.* (2013). This observation is important, some theoretical models (Mollon *et al.*, 2009; Mollon *et al.*, 2010; Dias *et al.*, 2008) consider that the failure always concerns all the face.

The plastic zones at the failure moment are visible in Fig. 9 and are almost the same for M-C and CJS2. The classical chimney rupture appears and the horizontal extension width is about 100 mm in the numerical case against 67 mm measured in experimental test (Fig. 10). Such a rupture extension is reported by Chambon & Corté (1994).

The previous comparison between numerical calculation and experimental test shows CJS2 model allows reproducing better the physical outcomes. Therefore, all the



(a) M-C



(b) CJS2

Figure 8 - Failure mechanisms.

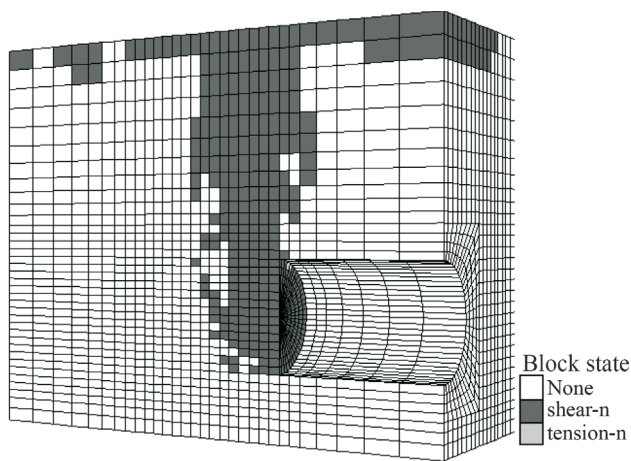


Figure 9 - Numerical plastic zones.

following studies are realized using only the CJS2 constitutive model.

### 3.2. Bolting reinforcement simulation

In this part, the bolting influence on ground movements is analysed. Physical test n° III, IV, V and VI were simulated. The interface between bolts and soil is modelled using zero cohesion and a frictional angle equal to 2/3 of the

sand frictional angle. These interface behaviour properties are the key parameters allowing representation of the real bolting influence on face stability and soil displacements. Numerical studies of Sudret & De Buhan (1999), Bourgeois *et al.* (2001), Wong *et al.* (2000), Wong *et al.* (2004) and Wong *et al.* (2006) highlight this problem.

Other cases were also considered in order to study the relationship between the soil mass movements and the bolting characteristics such as the density, the bolt length and material.

In the physical model, 28 PVC sand-coated pipes were placed ahead the tunnel face in order to simulate the fibre glass reinforcement in a scale-down model.

The bolting characteristics used in the simulation of test III are shown in Table 6.

The bolts Young modulus is determined thanks to traction tests on the PVC pipes.

At prototype scale, the corresponding bolting density is about 0.4 bolt/m<sup>2</sup>. In numerical simulation only an half of tunnel is simulated as shown in Fig. 11.

Figure 12 presents the confinement pressure vs. the tunnel centerline face extrusion. Test n° II (without reinforcements) is compared with the test n° III. Both experimental outcomes and numerical results are shown.

Numerical calculation confirms the physical major result: the application of reinforcements in the core ahead

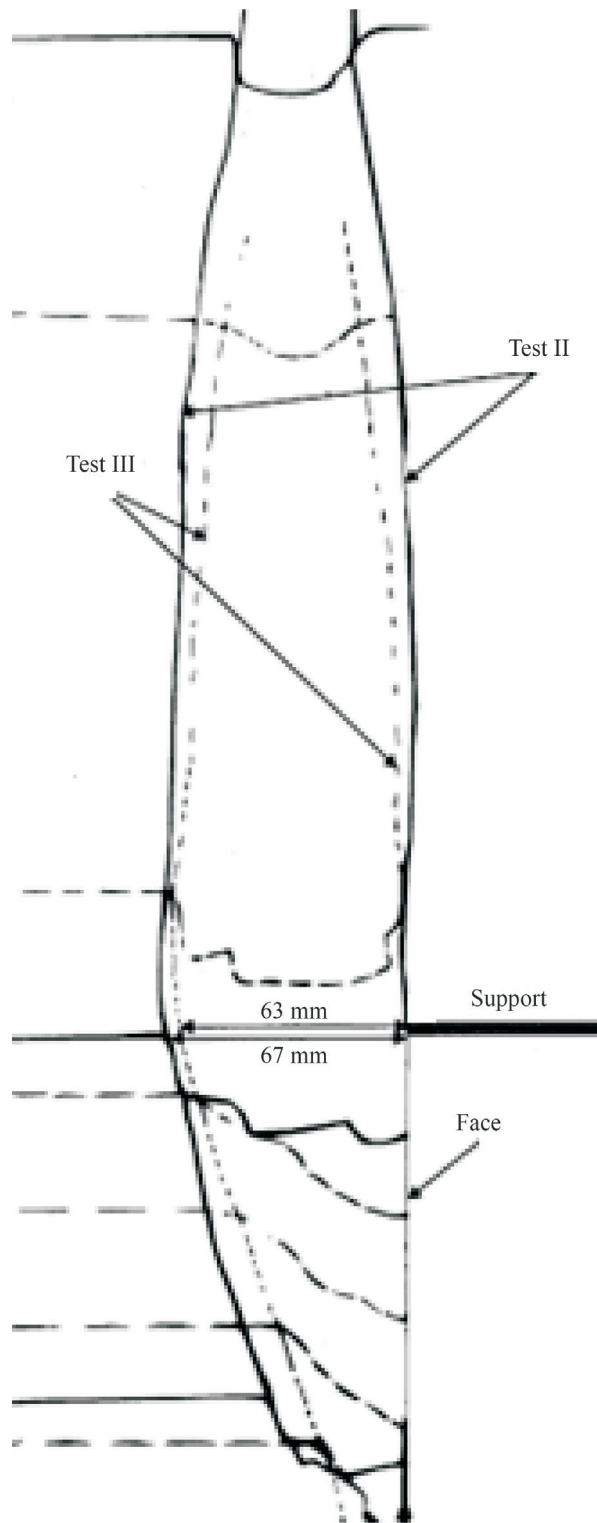


Figure 10 - Centrifugal experimental test (Al Hallak, 1999).

the face tunnel permits to reduce considerably the ground extrusion. Besides, the limit confinement pressure is reduced from 8 kPa to 5.5 kPa in the experimental test. A similar reduction interval is obtained with calculation. Numerical simulation corresponds with a good accuracy to

Table 6 - Bolting characteristics (test III).

Bolt diameter (mm)	3.5
Bolt length (n D)	1.5
Bolt Young Modulus (GPa)	3

physical outcomes. At limit pressure vicinity ( $p = 6$  kPa), the difference between numerical and experimental extrusion is only of 5%. Therefore, the interface parameters chosen, between pipes and sol, correctly reflect the real ones.

The relationship between surface settlements at point C and the confinement pressure is shown in Fig. 13. As is in the no reinforcement case, the numerical simulation correctly predicts the measured surface settlements.

Nevertheless, calculation confirms that reinforcing the core ahead the tunnel face permits to reduce also the surface settlements, in addition to the extrusion and the limit confinement pressure. In Table 7 the decrease of these measures is shown. The numerical values are in good concordance with the physical ones.

Test n° IV differed from previous test only by the inclusions number. In this case 48 bolts were placed ahead the face tunnel with a corresponding bolting density of  $0.6 \text{ bolt/m}^2$  at the prototype scale.

The comparison between the two different tests is shown in Fig. 14. Experimental results proved that increasing the bolts number permits to reduce the extrusion face movement and to decrease the limit confinement pressure from 5.5 kPa to 4 kPa. Even in this case, numerical simulation confirms these outcomes with a accuracy. At limit pressure, the difference between numerical and experimental extrusion is equal to 4%.

Nevertheless, the outcomes proximity between the test III and IV seems to indicate that there is a limit beyond which it is not effective to increase the bolts density.

Therefore, in order to study the relationship existing between the ground movement (extrusion and settlements) and the reinforcement density, a parametric study is realized varying only the inclusions number.

Figure 15 shows the maximum tunnel face extrusion vs. the bolts density. Due to gravity, this value is always located below the tunnel axis. The extrusion outcomes are compared at the same confinement pressure value of 8 kPa. This enables to present on the graph the case without reinforcement as well. Bolting experimental tests outcomes are also visible on the graph and the agreement with numerical results is confirmed.

First of all, the results show that a small reinforcement density ( $d = 0.2 \text{ bolt/m}^2$ ) is already able to reduce the centreline face extrusion of 34% in comparison to the no reinforcement case.

Besides, a significant curve trend change appears on the graph, highlighted by the intersection of two straight lines. The trend modification corresponds to a bolting den-

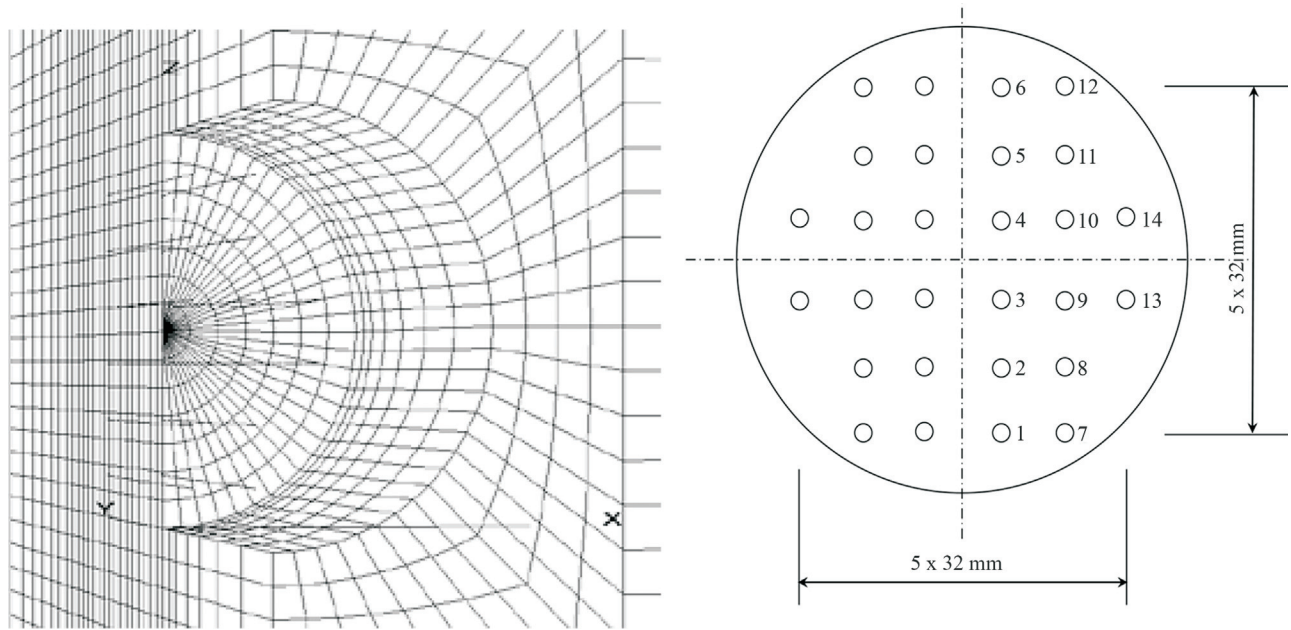


Figure 11 - PVC pipes repartition in test simulation n° III.

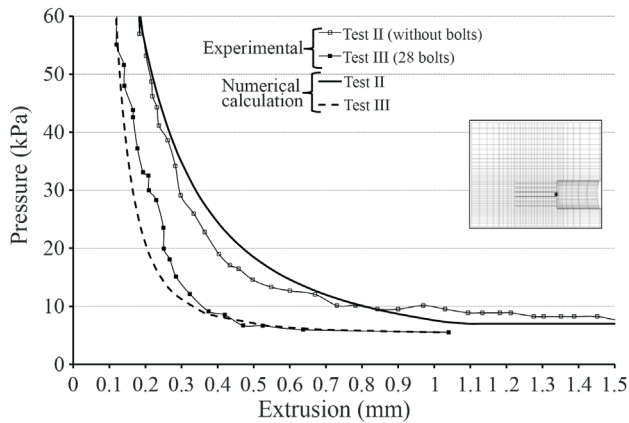


Figure 12 - Confinement pressure vs. axial face displacement, comparison between experimental and numerical results (Test II and Test III).

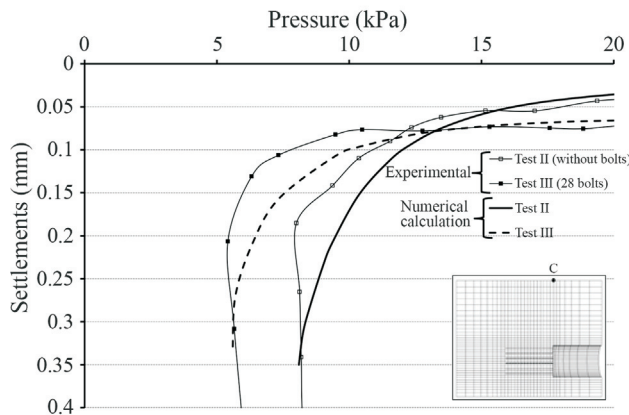


Figure 13- Surface settlement (point C) vs. confinement pressure, comparison between experimental and numerical simulation results (Test II and Test III).

Table 7 - Bolting influence.

	Bolting experimental decrease (%)	Bolting calculation decrease (%)
Limit confinement pressure	30	34
Extrusion (p = 8 kPa)	62	60
Surface settlement (p = 8 kPa)	42	41

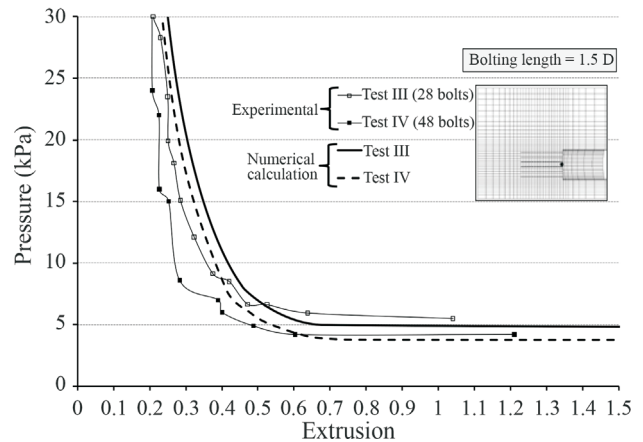


Figure 14 - Confinement pressure vs. axial face displacement, comparison between experimental and numerical results (Test III and Test IV).

sity just lower than 0.4 bolt/m<sup>2</sup>. Beyond this value, the reinforcement efficacy decreases. Similar results are obtained by other researchers as Dias & Kastner (2005) and Janin (2012) who found the same trend, simulating with FLAC<sup>3D</sup>

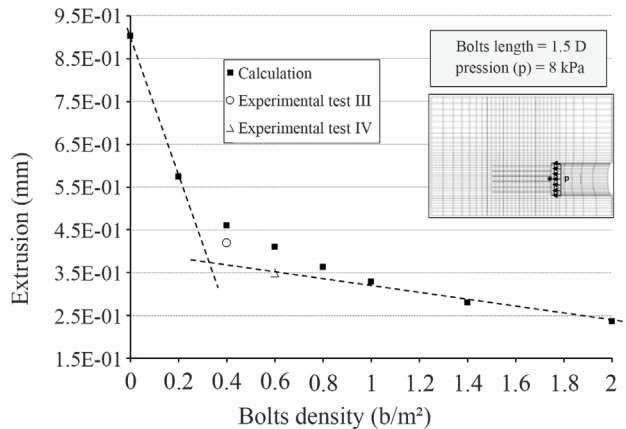


Figure 15 - Axial face extrusion vs. bolts density.

and Plaxis3D the first and second Toulon tube excavation. This outcome is also supported by the results of field measurements reported by Poma *et al.* (1995). The field measurements were carried out for a 18-m-diameter tunnel with a cover depth of 100 m constructed in a clay formation. Finally, Lunardi (2008) obtained a threshold value equal to 0.4 bolt/m<sup>2</sup> using a procedure based on the interpretation of the extrusion curves carried out from triaxial extrusion tests.

The reinforcement density influence on surface settlement (point C) is analysed as well (Fig. 16). Even in this case, a curve trend change of the surface settlement appears beyond a bolting density value equal to about 0.4 bolt/m<sup>2</sup>. Nevertheless, the trend modification seems to be less obvious than in extrusion movement.

Experimental test V maintained the same bolting characteristics (material, density) of test III, except the pipes length reduced from 300 mm to 130 mm. Unfortunately, during this test, sensors malfunctioned and the results could not be analyzed. Only the failure extension ahead the face tunnel showed that it was similar to test III.

As for the density parameter, the pipe length influence on ground movements was studied using numerical

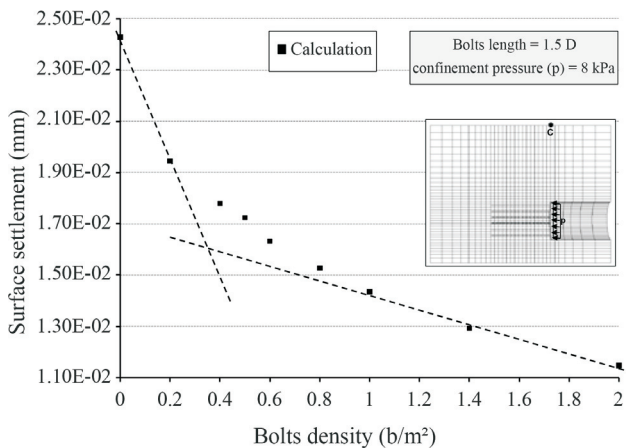


Figure 16 - Surface settlement (point C) vs. bolts density.

calculation. In addition to the test V simulation, other calculations are done, varying only the PVC pipes length (density = 0.4 bolt/m<sup>2</sup>).

The relationship between the tunnel centerline face extrusion and the bolts length is shown in Fig. 17. The extrusion results are compared at the same confinement pressure value of 8 kPa in order to present on the graph also the no reinforcement case. The experimental extrusion measured in test III is also visible on the graph and is in good agreement with the numerical curve trend.

The two straight lines highlight a significant curve trend change corresponding to a bolts length equal to about 0.4 D. This result suggests that the length of reinforcements has to be longer than 0.4 D in order to have a favourable effect on face stability.

This conclusion is in accordance with the current design practice, which adopts a minimum overlap length of approximately 0.3-0.4 D (Peila *et al.*, 1996). Yoo & Shin (2003) obtained a comparable critical value of pipes length in their 3D numerical investigations on the deformation behaviour of tunnel face reinforced with longitudinal pipes. A threshold value lightly higher ( $L_c = 0.5 D$ ) was found in the numerical study of Wong *et al.* (1997), Dias (1999) and Dias *et al.* (2002). This value has confirmed thanks to centrifuge experimental tests and 2D calculations (distinct element method) carried out by Kamata & Mashimo (2003).

The bolting length influence on surface settlement (point C) is analysed as well (Fig. 18). Even in this case, a significant settlement reduction appears with bolts longer than 0.4 D.

Test VI was the experimental test using threaded steel bolts instead of PVC pipes to reinforce the core ahead the tunnel face.

The bolting characteristics used in this simulation are shown in Table 8.

In addition to bolt diameter, another major difference in respect to PVC pipes is the Young modulus. The steel tension characteristic was adopted in the numerical calculations.

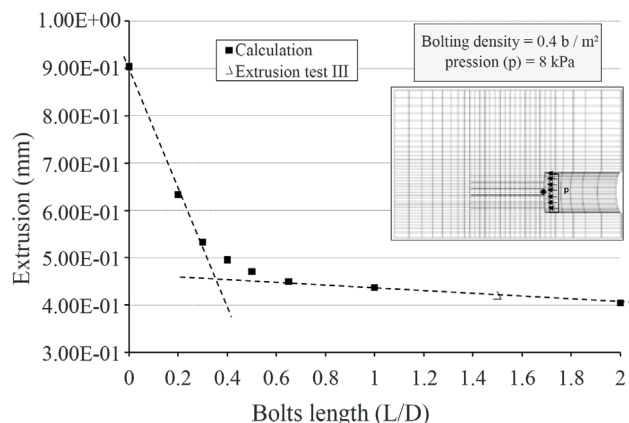


Figure 17 - Axial face extrusion vs. bolts length.

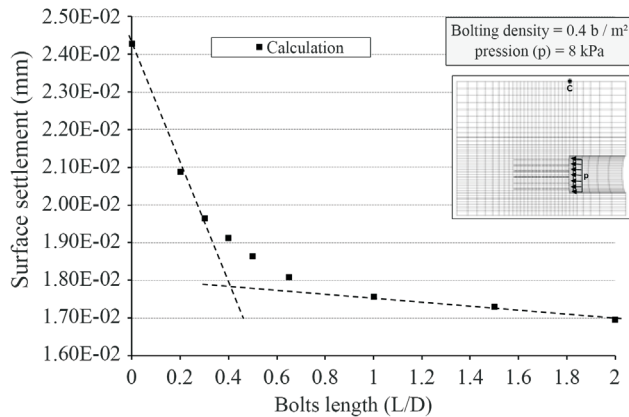


Figure 18 - Surface settlement (point C) vs. bolts length.

Table 8 - Bolting characteristics (test VI).

Bolt diameter (mm)	2
Bolting density (bolt/m <sup>2</sup> )	0.5
Bolt length (n D <sub>tunnel</sub> )	1.5
Bolt Young Modulus (GPa)	210

In order to study the stiffness reinforcement influence on ground movements and limit pressure, results of numerical test VI are compared to another case simulation. This calculation using PVC reinforcements has the same characteristics as steel pipes (number, diameter, length...) but a different Young modulus (3 GPa).

Figure 19 presents the confinement pressure vs. the tunnel centerline face extrusion. The comparison between physical model results and numerical simulations shows that, until the limit pressure vicinity, numerical calculation seems to slightly overestimate the experimental extrusion values. Nevertheless, the gradient curves are similar. Be-

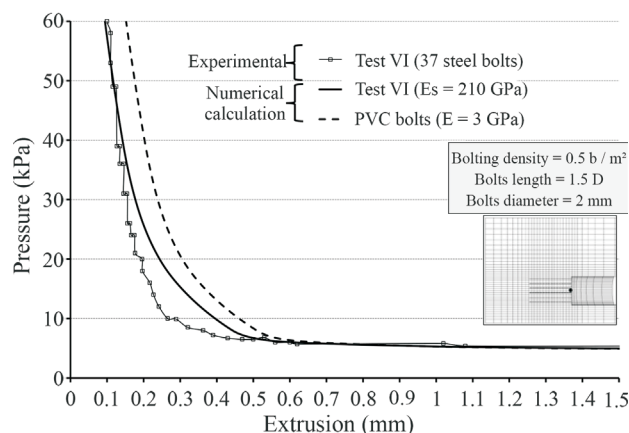


Figure 19 - Confinement pressure vs. axial face displacement, comparison between experimental and numerical results (Test VI) and stiffness reinforcement influence.

sides, the limit numerical confinement pressure is exactly the same as physical one ( $p = 4.8 \text{ kPa}$ ).

Comparing the steel bolting case with the PVC one, it appears evident that the differences are not important. Although the extrusion with the steel bolts is smaller, the maximum difference is equal to 20%. Besides, the numerical calculation reaches the equilibrium at the same limit pressure value.

For the excavation geometry and soil characteristics analysed in this study, the increase of the bolt stiffness is irrelevant in respect to the face stability and ground movements. The surface settlements analysis confirms this conclusion.

The PVC pipes, with a Young modulus of 3 GPa, are effective against the stress in the soil caused by the tunnel excavation. The main parameters controlling the soil deformations and the face stability are the length bolts and the density reinforcement.

#### 4. Conclusions and Perspectives

Numerical calculations were developed and carried out with the particular emphasis on the validation of the excavation simulation method, simulating various reduced-scale centrifugal model tests (Al Hallak, 1999). Comparing numerical results to physical model results, the study focuses on the bolting influence on the face extrusion, the ground surface settlements and the limit confinement pressure. The influence of reinforcement characteristics such as density, length and stiffness are studied as well. Based upon the comparison with the centrifuge tests, some conclusions emerge.

An elastoplastic constitutive model with two mechanisms permits to simulate with accuracy the soil response in the case of a tunnel excavation. It is able to correctly represent the non linearities of the soil. The common linear elastic perfectly plastic M-C constitutive model is also tested.

Numerical simulation of the no reinforcement case, with CJS2 model, shows that the face extrusion displacements, the surface settlements and the limit pressure are in agreement with the experimental values. The M-C constitutive model appears to be too simple and is insufficient when dealing with soil deformations.

Numerical simulations of bolting face tests are in agreement with physical results. The tunnel behaviour is especially well simulated at the limit pressure vicinity and in the failure zone. The interface properties, between pipes and soil, are the key parameters allowing representation of the real bolting influence. Numerical outcomes confirm that the reinforcement of the core ahead the face tunnel permits to reduce the limit confinement pressure, the face extrusion and the surface settlements.

Numerical analysis of bolting parameters shows that:

- A small reinforcement density ( $d = 0.2 \text{ bolt/m}^2$ ) is already able to reduce substantially the centreline face extrusion in comparison with the no reinforcement case. A

significant further reduction of ground movements is evident until a bolts density equal to  $0.4 \text{ bolt/m}^2$ . Beyond this value, the reinforcement efficacy decreases sensibly.

- The bolt length has to be longer than  $0.4 D$  in order to have a favourable effect on face stability and ground movements (extrusion and surface settlements).
- In relation to the soil characteristics and the excavation geometry analysed in this study, increasing bolt stiffness is irrelevant in respect to the face stability and ground movements. The PVC pipes are sufficiently effective to limit and control the strains caused by the tunnel excavation.
- Same results on the influence of bolting density, bolt length have been obtained by others authors using on-site field measurements, laboratory experiments and numerical studies.

## References

- Al Hallak, R. (1999) Etude Expérimentale et Numérique du Renforcement du Front de Taille par Boulonnage dans les Tunnels en Terrains Meubles. Thèse de Doctorat, Ecole Nationale des Ponts et Chaussées, Paris, 283 p.
- Bourgeois, E.; Garnier, D.; Semblat, J-F.; Sudret, B. & Al Hallak, R. (2001) Un modèle homogénéisé pour le boulonnage du front de taille des tunnels: Simulation d'essais en centrifugeuse. *Revue Française de Genie Civil*, v. 5:1, p. 9-38.
- Cambou, B. & Jafari, K. (1988) Modèle de comportement des sols non cohérents. *Revue Française de Géotechnique*, v. 44:2, p. 43-55.
- Chambon, P. & Corte, J-F. (1994) Shallow tunnels in cohesionless soil: stability of tunnel face. *Journal of Geotechnical Engineering*, v. 120:7, p. 18-37.
- Dias, D. (1999) Renforcement du Front de Taille des Tunnels par Boulonnage: Etude Numérique et Application à un Cas Réel en Site Urbain. PhD Thesis, INSA de Lyon, France, 320 p.
- Dias, D.; Janin, J.P.; Soubra, A.H. & Kastner, R. (2008) Three-dimensional face stability analysis of circular tunnels by numerical simulations. The Challenge of Sustainability in the Geoenvironment 'GeoCongress 2008', New Orleans, USA, 8 p.
- Dias, D. & Kastner, R. (2005) Modélisation numérique de l'apport du renforcement par boulonnage du front de taille des tunnels. *Canadian Geotechnical Journal*, v. 42:6, p. 1656-1674.
- Dias, D.; Kastner, R. & Jassionnesse, C. (2002) Sols renforcés par boulonnage. Etude numérique et application au front de taille d'un tunnel profond. *Geotechnique*, v. 52:1, p. 15-27.
- Garnier, J. (2001) Modèles physiques en géotechnique: état des connaissances et évolutions récentes. In: CFMS Ed. Proc. of the Int. Conf. Albert Caquot, 1ère Conférence Coulomb, Paris, 12 p.
- Hejazi, Y.; Dias, D. & Kastner, R. (2008) Impact of constitutive models on the numerical analysis of underground constructions. *Acta Geotechnica*, v. 3:4, p. 251-258.
- Itasca (2005) FLAC 3D: Fast Lagrangian Analysis of Continua, User's Guide. Itasca Consulting Group, Inc. Minneapolis, 107 p.
- Janin, J.P. (2012) Tunnels en Milieu Urbain: Prévisions des Tassements Avec Prise en Compte des Effets de Pré-Soutènements. PhD Thesis, INSA de Lyon, France, 267 p.
- Jenck, O. & Dias, D. (2004) Analyse tridimensionnelle en différences finies de l'interaction entre une structure en béton et le creusement d'un tunnel à faible profondeur. *Geotechnique*, v. 8:54, p. 519-528.
- Jenck, O.; Dias, D. & Kastner, R. (2009) Discrete element modeling of a granular platform supported by piles in soft soil - Validation on a small scale model test and comparison to a numerical analysis in a continuum. *Computers & Geotechnics*, v. 36:2, p. 917-927.
- Kamata, H. & Mashimo, H. (2003) Centrifuge model test of tunnel face reinforcement by bolting. *Tunnelling and Underground Space Technology*, v. 18:3, p. 205-212.
- Lunardi, P. (2008) Design and Construction of Tunnels - Analysis of Controlled Deformation in Rocks and Soils (ADECO-RS). Springer-Verlag, Berlin, 577 p.
- Maleki, M (1998) Modélisation Hiérarchisée du Comportement des Sols. PhD Thesis, Ecole Centrale de Lyon, Ecully, France, 243 p.
- Mandel, J. (1962) Essais sur modèle réduits en mécanique des terrains. Etude des conditions de similitude. *Revue de l'Industrie Minérale*, v. 44:3, p. 611-620.
- Mollon, G.; Dias, D. & Soubra, A.H. (2010) Face stability analysis of circular tunnels driven by a pressurized shield. *Journal of Geotechnical and Geoenvironmental Engineering*, ASCE, v. 3:1, p. 215-229.
- Mollon, G.; Dias, D. & Soubra, A.H. (2009) Probabilistic analysis and design of circular tunnels against face stability. *International Journal of Geomechanics*, ASCE, v. 9:6, p. 237-249.
- Mollon, G.; Dias, D. & Soubra, A. (2013) Range of the safe retaining pressures of a pressurized tunnel face by a probabilistic approach. *J. Geotech. Geoenviron. Eng.*, v. 139:11, p. 1954-1967.
- Peila, D.; Oreste, P.P.; Pelizza, S. & Poma, A. (1996) Study of the influence of sub-horizontal fiber-glass pipes on the stability of a tunnel face. *Proc. Int. Conf. on North American Tunneling*, Washington DC, v. 1, p. 425-431.
- Poma, A.; Grassi, F. & Devin, P. (1995) Finite difference analysis of displacement measurements for optimizing tunnel construction in swelling soils. *Proc. Field Measurements in Geomechanics 4th International Symposium*, Bergamo, p. 225-236.
- Sudret, B. & Buhan, P. (1999) Modélisation multiphasique de matériaux renforcés par inclusions linéaires. *CR Acad. Sci. Paris*, v. 327:IIb, p. 7-12.

- Yoo, C. & Shin, H.-K. (2003) Deformation behaviour of tunnel face reinforced with longitudinal pipes - Laboratory and numerical investigation. *Tunnelling and Underground Space Technology*, v. 18:5, p. 303-319.
- Weber, J.D. (1971) *Les Applications de la Similitude Physique aux Problèmes de la Mécanique des Sols*. Eyrolles, Paris, 87 p.
- Wong, H.; Subrin, D. & Jassionnesse, C. (1997) Comportement du front de taille d'un tunnel renforcé par des inclusions en fibre de verre - Modèle analytique, 4<sup>ème</sup> réunion annuelle, GE097, Aussois, p. 133-147.
- Wong, H.; Subrin, D. & Dias, D. (2000) Extrusion movements of a tunnel head reinforced by finite length bolts - A closed form solution using homogenisation approach. *Int. J. Num. Anal. Geomech.*, v. 24:4, p. 533-565.
- Wong, H.; Subrin, D. & Dias, D. (2006) Convergence-confinement analysis of a bolt-supported tunnel using homogenization method. *Canadian Geotechnical Journal*, v. 43:5, p. 462-483.
- Wong, H.; Trompille, V. & Dias, D. (2004) Extrusion analysis of a bolt-reinforced tunnel face with finite ground-bolt bond strength. *Canadian Geotechnical Journal*, v. 41:2, p. 326-341.

# Analysis of Chemical Mobility of Leachate Contaminants in Gneiss Saprolite of Belo Horizonte Solid Waste Landfill (CTRS BR 040), South-Eastern Brazil

Q.C.G. Ferreira, L.A.P. Bacellar

**Abstract.** Municipal solid waste landfill is a potential source of contamination due to the harmful elements of the leachate, such as trace elements. In the Belo Horizonte landfill, the waste is partially disposed of directly on gneiss saprolites, with lower capacity to mitigate contaminants than upper soil horizons. Column tests were made to analyse the attenuation capacity of this saprolite. The analysis of the chemical elements concentration in soil and leached effluent after the tests and the calculation of the saturation index with PHREEQC software showed the ability of saprolite to mitigate the contamination, mainly by chemical precipitation and immobilization in the colloidal fraction.

**Keywords:** saprolite, landfill leachate, column tests, PHREEQC modeling.

## 1. Introduction

A major concern in municipal solid waste (MSW) landfills is the contamination of soil and groundwater by leachates. Major ions such as Na, K, Ca, Mg,  $\text{NH}_3$ ,  $\text{Cl}^-$ , sulphide / sulphate are among the various types of components usually present in high concentrations in MSW leachates (Christensen *et al.*, 2001), while the concentrations of trace elements are small (Kjeldsen *et al.*, 2002), although they are the most critical elements due to their high pollution potential.

Soils are traditionally considered barriers for groundwater contamination, with high attenuation capacity, which is intensified when pH values are neutral to high (Patrick and Verloo 1998; Kjeldsen *et al.*, 2002). In saprolites (C pedological horizon), adsorption may be small, because their levels of adsorbent constituents are usually much lower than those of surface horizons (Alloway, 1995), especially in areas of crystalline basement rocks. The elements can also be retained in complexes or in the form of insoluble precipitates in the presence of sulphides, carbonates, hydroxides and phosphates, and the two first anions are common in landfills (Pohland, 1991; Kjeldsen *et al.*, 2002). Often, precipitation is the most important phenomenon for the retention of trace elements in soils (Young *et al.*, 1996), although adsorption tends to increase with more alkaline pH, which is predominant in MSW landfills in methanogenic phase (Apello & Postma, 2005).

The study area is the landfill of the Center for Solid Waste Treatment at BR-040 (CTRS BR 040), which is located in Belo Horizonte city (Fig. 1), in Minas Gerais state, southeastern Brazil. The landfill area is located in the gneiss-migmatite basement (Belo Horizonte Complex),

predominantly composed of fine to coarse grained gneisses, with trondjhemitic composition (Beato *et al.*, 2003). The soil surface horizons (Oxisols and Ultisols) are of clayish texture composed of quartz and kaolinite, and secondarily of magnetite, ilmenite, hematite and goethite (Sousa, 1998). The saprolite usually has silt-sandy composition and is 10 to 20 m thick.

The local unconfined aquifer system is composed of an intergranular porosity layer in the regolith, with hydraulic communication with a fissural aquifer in the rock (Beato *et al.*, 2003). The top of the aquifer is usually found at the base of the saprolite (C horizon), which shows estimated hydraulic conductivity of  $10^{-8}$  and  $10^{-9}$  cm/s. According to mathematical flow models, the hydraulic gradient reaches maximum value of 4% near the landfill (SLU, 2010).

The aquifer in the northwestern sector of the landfill is clearly contaminated, but apparently the contaminant

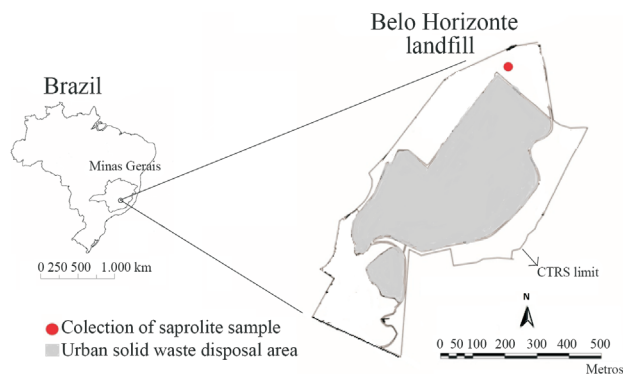


**Figure 1** - Location of the CTRS-BR040 Landfill and the soil sampling site.

Quênia de Cássia Goulart Ferreira, PhD. Student, Universidade Federal de Ouro Preto, Campus Morro do Cruzeiro, 35400-000 Ouro Preto, MG, Brazil. e-mail: kenya.goulart@gmail.com.

Luis de Almeida Prado Bacellar, Associate Professor, Universidade Federal de Ouro Preto, Campus Morro do Cruzeiro, 35400-000 Ouro Preto, MG, Brazil. e-mail: bacellar@degeo.ufop.br.

Submitted on April 4, 2013; Final Acceptance on December 9, 2013; Discussion open until July 31, 2014.

plume has not reached neighbouring districts (Tecisan, 2005; SLU, 2010). The concentration of some chemical elements in this plume exceeded the water potability limits established by legislation in the world and in Brazil (Brasil, 2011), especially for ammonia, chloride, total dissolved solids, iron and manganese. Some trace elements have also been detected at abnormally high levels, and the most problematic are: aluminium, barium, lead, chromium and mercury (Tecisan, 2005; Bacellar & Filho, 2008).

In this landfill, one of the largest in Brazil and located within the urban area, part of the waste was disposed of directly on the gneiss saprolite (C horizon), with no impermeable base (Sousa, 1998), which facilitated the contamination. This situation is relatively common in basement rock areas of Brazil, where the construction of impermeable bases are difficult due to the steep relief.

The objective of this study was to establish the actual chemical attenuation capacity of the saprolite found in the CTRS-BR040 landfill. This issue is relevant because hilly-rolling relief associated with gneisses is one of the most abundant landscapes in southeastern and northeastern Brazil. Since it is difficult to establish an attenuation degree in the field (Barella, 2011), column tests were carried out. Geochemical modelling softwares have evolved over the years, and today there are several tools for modelling natural and contaminated systems, such as the PHREQCEE 2.18 (Appelo & Postma, 2005). This hidrogeochemistry modelling program was used to calculate the speciation and saturation index of the leachate before and after its passage through the soil column in order to confirm the possible chemical reactions during the test.

## 2. Material and Methods

The compilation of previous data allowed defining representative areas for soil (gneiss saprolite) and leachate sampling to be used in the column tests. Undisturbed and disturbed saprolite samples were collected (Fig. 1), as well as 25 l of leachate samples from a 10 years old residue cell, in which temperature, Eh, pH and electrical conductivity were measured *in situ* with a multiparameter equipment (Myron, model 6PII). Soil was characterized with respect to: mineralogical determination by X-Ray diffractometry (Rigaku X-Ray Diffractometer / Rotaflex Ru-200Z), particle size; physical and chemical parameters (unit weight, particle specific gravity, dry unit weight, porosity, void ratio, moisture content, pH, cation exchange capacity (CEC) and organic matter content).

The concentration of major and trace elements in soil and in the leachate was characterized by ICP-OES (SPECTRO, model CYRUS CCD), the first one with sample digestion according to EPA standard method 3051A (USEPA, 2007). Sulphate, chloride and alkalinity of the leachate were determined by titration and turbidimetry, according to procedures 4500-SO<sub>4</sub><sup>2-</sup>B, 4500-Cl<sup>-</sup>B and 2320B, respectively (Greenberg *et al.*, 1999). Since pH and Eh con-

ditions varied during the column tests, the chemical and physicochemical properties of the same leachate were determined twice, the first one during the sampling (1<sup>st</sup> measure) and the second one during the column tests (2<sup>nd</sup> measure - 90<sup>th</sup> day of test). It was also made the partial digestion of particles retained in filter membranes, according to Standard Methods 3030F (Greenberg *et al.*, 1992) to quantify elements associated with colloids, via ICP-OES.

The tests were carried out simultaneously on two glass columns of 78.54 cm<sup>2</sup> and 70 cm long, fixed on wooden support within thermal boxes to ensure thermal insulation. The soil was placed in layers in the columns and it was compacted with the same field unit weight ( $\gamma = 16.0 \text{ kN/m}^3$ ). Geotextile membranes were positioned under and over the soil (Fig. 2) to equalize the flow and prevent piping erosion.

The average seepage velocity in the columns was approximately 150 times higher than that determined in the field with slug tests in order to obtain enough effluent volume for the chemical analyses (SLU, 2010). This was done by increasing the hydraulic gradient magnitude by setting a hydraulic head of 0.50 m of leachate, corresponding to a hydraulic gradient of 5 that was maintained throughout the test. The reproducibility of the two tests was considered good, since the flow, and consequently the hydraulic conductivity, of the leached effluent in both columns varied in a range consistent with that determined with slug tests in

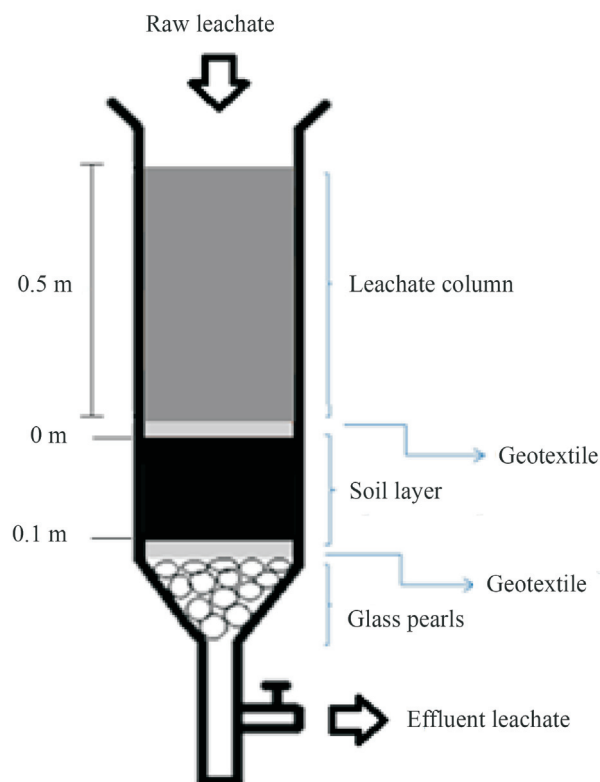


Figure 2 - Scheme of the experimental column.

the field ( $10^{-6}$  a  $10^{-7}$  m/s). The concentration of major and trace elements in the effluent of columns was also similar throughout the experiments (Ferreira, 2012). The duration of the column tests was 100 days, corresponding to a pore volume of 50 and 25 for columns 1 and 2, respectively, since the soil in first column was twice more permeable. Based on previous hydrogeological data of the landfill region (SLU, 2010) and dimensional analyses, it was estimated that the 100-day test would correspond to 40 years of groundwater flow near the landfill (Ferreira, 2012). The leached percolated in columns was collected in pre-set intervals for chemical and physicochemical characterization. The results were plotted against the number of pores that represents the soil volume vs. the porosity of the soil in percentage. At the end of the tests, the saprolite of each column was carefully removed and cut into 10 sub-layers. In each sub-layer, the concentrations of major and trace elements have been determined by ICP and also by the EPA 3051A method (USEPA, 2007).

The PHREEQC software 2.18 (Appelo & Postma, 2005) was used for the calculation of speciation and saturation index (SI) of the infiltrating leachate (hereinafter called raw leachate) and of the effluent (percolated through the saprolite) in column tests. The SI is used to calculate the saturation state of mineral species in the groundwater, and is the ratio (expressed in log) of the ionic activity product (IAP), which consists of the activities of free ions in solution to the solubility product (K) (Appelo & Postma, 2005). When the SI values are positive, there are supersaturation conditions and there is a possibility of formation of solid mineral phase. SI negative represents an unsaturated solution without conditions of formation of solid mineral phase. This hydrogeochemical modelling was performed in four stages: raw leachate, leached effluent in the initial phase (4<sup>th</sup> day), intermediate phase (40<sup>th</sup> day) and final phase (100<sup>th</sup> day) of tests.

### 3. Results and Discussion

#### 3.1. Soil and leachate characterization

The C horizon of the gneiss shows clay-sandy texture and is predominantly composed of quartz, kaolinite, mus-

covite, rutile and microcline. It has high porosity (48%) and it is slightly acidic ( $\text{pH}(\text{H}_2\text{O}) = 5.68$  and  $\text{pH}(\text{KCl}) = 4.31$ ), with low CEC (1.49 cmolc/dm<sup>3</sup>) and organic matter content (0.13 dag/kg), confirming its limited adsorption capacity. The soil has high amounts of aluminium, iron, magnesium, barium and lead (Table 1). Since lead is found in the area outside of MSW disposal sites (Souza, 1998), it is possible that part of it has anthropogenic origin, coming from the burning of fuel of vehicles (Filippelli *et al.*, 2005) that travel over the urban network and roads in the landfill vicinities.

The leachate has high electrical conductivity, total dissolved solids (STD), chloride, and alkalinity values (Table 2). The sulphate values are small due to its instability, since in reducing environment, it tends to be converted to sulphide. The pH is slightly basic and Eh is negative, showing a reducing and alkaline environment, typical of MSW landfills in methanogenic phase (Kjeldsen *et al.*, 2002). Trace elements occur at low concentration as usual in landfill environments (Christensen *et al.*, 2001), especially those in developing countries, where the proportion of organic matter is higher (Bosco, 2008). The two measurements made in the raw leachate were obtained from the same sample, but in different times, in order to evaluate possible modifications of leachate during the experiments. Iron, aluminium and zinc ions tend to concentrate in the colloidal fraction (Table 3), as evidenced by the analysis of particles retained on the leachate filtering process (0.45  $\mu\text{m}$ ) (Ferreira, 2012).

#### 3.2. Column tests

The flow of leached effluent in columns decreased progressively during the test, reducing around 75% compared to the initial baseline (initial and final flow were respectively  $1.4 \times 10^{-9}$  and  $5.8 \times 10^{-10}$  m<sup>3</sup>/s) (Ferreira, 2012). This behaviour was probably the result of the progressive reduction in porosity by precipitation and growth of microorganisms (Kjeldsen *et al.*, 1998).

The column test results show that while the pH values of the raw leachate were slightly alkaline (about 7.5), the first measurements of the leached effluent showed acid values ( $\text{pH} = 4$ ), but from the 6<sup>th</sup> day, the pH started to rise until

**Table 1** - Chemical characterization of the soil.

Element	Al	Ba	Ca	Cr	Cu	Fe	K	Li	Mg	Mn	Na	P
Unity	mg/kg											
Measure	26038	75.6	91.0	5.04	11.01	19501	1063	6.06	692	2.49	138	62.4
Element	Pb	S	Sc	Si	Sr	Th	Ti	V	Y	Zn	Zr	
Unity	mg/kg											
Measure	18.5	31.0	0.944	124.4	1.04	13.7	119	18.4	12.9	25.6	2.5	

LQ = limit of quantification.

Note: As, Be, Cd, Co, Li, Mo and Ni occur below the limit of quantification (LQ).

**Table 2** - Table 2: Physicochemical characterization of the raw leachate.

Elements	Conductivity	pH	Eh	STD	Temperature	Alkalinity	Chloride	Sulphate	Al	Ba	Ca	Co	Cr
Unity	$\mu\text{S/cm}$	-	mV	PPT	$^{\circ}\text{C}$	mg/L	mg/L	mg/L	mg/L	mg/L	mg/L	mg/L	mg/L
1 <sup>st</sup> Measure	14200	7.38	-225	12.48	34.2	5632.5	2327	8.7	0.0048	0.229	68.4	0.0458	0.0688
2 <sup>nd</sup> Measure	12500	7.55	112	11.50	21.2	-	-	-	0.0541	0.158	66.8	0.0618	0.0607
Elements	Cu	Fe	K	Mg	Mn	Na	Ni	P	S	Sr	Ti	V	Zn
Unity	mg/L	mg/L	mg/L	mg/L	mg/L	mg/L	mg/L	mg/L	mg/L	mg/L	mg/L	mg/L	mg/L
1 <sup>st</sup> Measure	0.0107	1.833	754	73.8	0.0986	584	0.126	2.70	14.7	1.99	0.0709	0.0402	0.0162
2 <sup>nd</sup> Measure	0.0693	2.358	764	91.4	0.1137	791	0.144	1.05	32.7	2.39	0.0435	0.0373	0.0771

Note: As, Be, Cd, Li, Mo, Pb and Y occur below the limit of quantification (LQ).

it reached values of around 8.0 and 8.5 (Fig. 3a), as in areas under the influence of MSW landfills in methanogenic phase (Christensen *et al.*, 2001; Kjeldsen *et al.*, 2002). With low pH (hereinafter called acid phase), the concentration of various trace elements in the leached effluent increased, as expected.

At the collection moment, the leachate redox potential value (Eh) was very low (Eh = -225 mV), but upon contact with oxygen during the sampling operations and column assembling, it became more oxidant (Eh = 225 mV). Due to the presence of oxygen in the saprolite pores, the Eh values in the effluents collected in the first days (acid phase) are higher (around 250 mV), decreasing progressively with soil saturation and with oxygen depletion (Fig. 3b). A progressive reduction of the Eh in the columns was observed, prob-

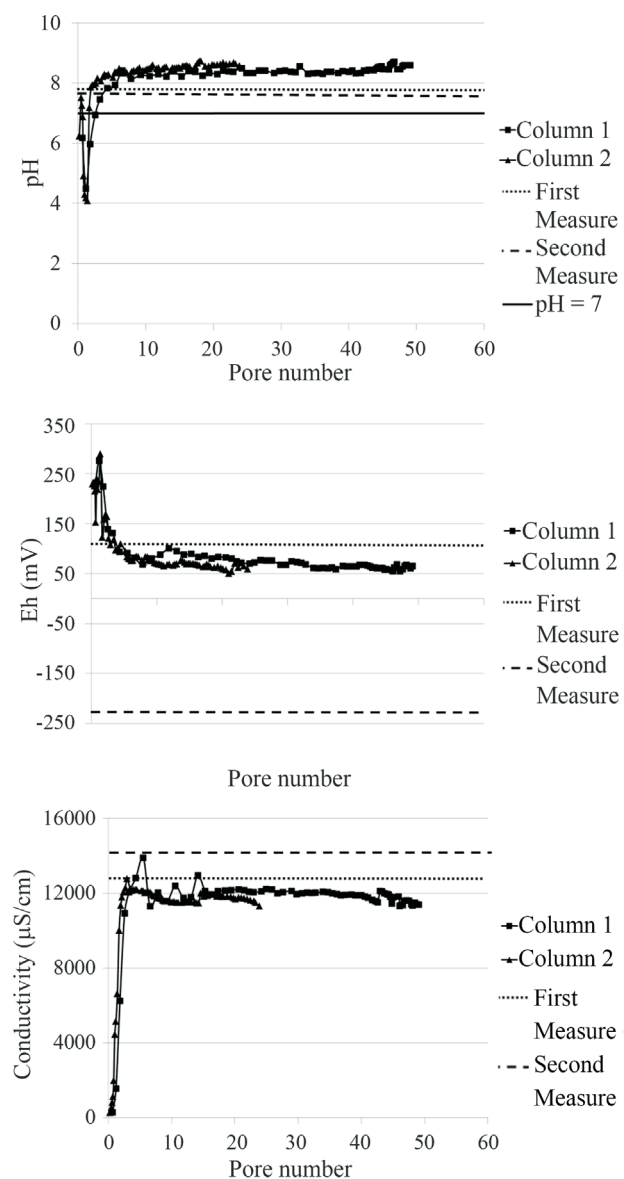


**Figure 3** - Values of pH (a), Eh (b) and EC (c) in the leached effluent.

**Table 3** - Concentration of the chemical elements in the particles retained in the filter paper.

Elements	Al	As	Ba	Be	Ca	Cd	Co	Cr	Cu	Fe	K	Li	Mg
Unity	mg/L	mg/L	mg/L	mg/L	mg/L	mg/L	mg/L	mg/L	mg/L	mg/L	mg/L	mg/L	mg/L
Measure	1.822	< LQ	0.0821	< LQ	7.58	< LQ	< LQ	0.0313	0.0867	6.89	20.38	< LQ	2.627
Elements	Mn	Mo	Na	Ni	P	Pb	S	Sr	Ti	V	Y	Zn	
Unity	mg/L	mg/L	mg/L	mg/L	mg/L	mg/L	mg/L	mg/L	mg/L	mg/L	mg/L	mg/L	
Measure	0.0274	< LQ	22.37	< LQ	2.415	< LQ	2.941	0.1736	0.057	0.0116	< LQ	0.1692	

LQ = limit of quantification.

ably as a consequence of the reduced porosity, which hinders the oxygen diffusion through the soil column. The Eh values in groundwater wells near the landfill are higher (around 250 mV) Bacellar & Filho (2008), probably due to the dissolved oxygen brought by water of recharge events.

The electrical conductivity values (and also the STD, with which it showed strong positive correlation) were small in the first measures, gradually increasing, while maintaining lower values than those in the raw leachate (Fig. 3c), suggesting that even after 100 days of test (40 years in the actual scale), there is still some type of chemical retention in the soil. The EC values in column 1 are larger than in column 2, probably due to the higher percolation rate in the first column, providing less contact time of soil with the leachate, with lower ion retention by the soil (Ferreira, 2012).

The PHREEQC software 2:18 was used to calculate the speciation of the raw leachate and also the leached effluent from column 2 in the initial (4<sup>th</sup> day, when the pH is acidic), intermediate (40<sup>th</sup> day) and final stages (100<sup>th</sup> day). This column was selected because it showed more regular results over time. The mineral phases that tend to precipitate were mainly carbonates, oxides, hydroxides, sulphides, sulphates and phosphates. Barite was an exception because it only tends to precipitate in the initial acid stage, when the other mineral phases tend to solubilize. In the raw leachate, a large amount of sulphides tend to precipitate due to the very negative Eh value. The other mineral phases tend to precipitate in the raw leachate and in the last two stages.

With regard to the column effluent, the As, Be, Cd, Li, P, Pb and V concentrations were below the limit of quantification (LQ) of ICP OES. Al, As, Ba, Ca, Cu, Mn, Ni, S, Sr, Y and Zn were sensitive to low pH values, considerably increasing their concentration in the acid phase, and elements As and Pb only showed measures greater than those of LQ in this stage (Ferreira, 2012). The values of elements Al, As, Ba, Co, Cr, Mn, Ni and Pb were higher than the intervention values for contaminated groundwater adopted in Brazil (FEAM, 2010), proving the pollution potential of the leachate to soil and groundwater.

The chemical analyses of the leached effluent and the soil profile after column tests showed different behaviours for the different chemical elements. Some were leached from the soil, such as Ba, Cu, Cr, Y, V and others were re-

tained in the soil, such as Al, Ca, S, Sr, P, Mg, Mn, K, Na, Ti, Zn, Co and Li. Ions with higher concentration in the raw leachate are Na, K, Ca (Table 2) and probably bicarbonate (high alkalinity), and of these, only calcium was retained, which explains the small reduction in electrical conductivity (Fig. 3a) during the test. However, these ions do not offer very high risks to health when compared to others commonly found in MSW landfills. In relation to Pb, one cannot tell whether there was leaching or retention, since the concentration difference in the soil before the test is very small (Ferreira, 2012).

Sulphur was retained in the soil (Fig. 4a) and its concentration in the leached effluent is lower than in the raw leachate (Fig. 4b). The modelling with PHREEQC software showed that in the raw leachate recently collected in the field, with negative Eh and slightly basic pH, there is predominance of sulphur in the form of sulphides, which can precipitate several elements, including trace elements such as Cu, Fe, Co, Ni and Zn (Ferreira, 2012). When the Eh values increases, sulphide concentration decreases and the precipitation of metals ceases. However, at low pH and high Eh values, sulphur turns into sulphate, precipitating Ba.

The geochemical modelling also indicates a tendency to precipitate barite (barium sulphate) in the initial phase, when pH is low and Eh is high, conditions which favour the occurrence of sulphur as sulphate (Ferreira, 2012) and barium in solution (Fig. 5a). There is also the possibility of barium precipitation as carbonate ( $\text{BaCO}_3$  and  $\text{BaCa}(\text{CO}_3)_2$ ). Since the modelling shows that barite is unstable in the subsequent phases of the column test, it is assumed that it has been progressively leached from the soil (Fig. 5b).

Aluminium was also retained (Figs. 6a and 6b), justifying its low concentration in the groundwater in monitoring wells in the landfill area (SLU, 2010). The modelling with the PHREEQC software indicates that this element tends to precipitate as gibbsite, and perhaps in the form of carbonates.

The copper concentration in the leached effluent is smaller than in the raw leachate (Fig. 7a). However, as this element has been leached from the soil (Fig. 7b), it is assumed that it is retained in the colloidal form (Ferreira, 2012). The modelling shows the tendency of copper to pre-

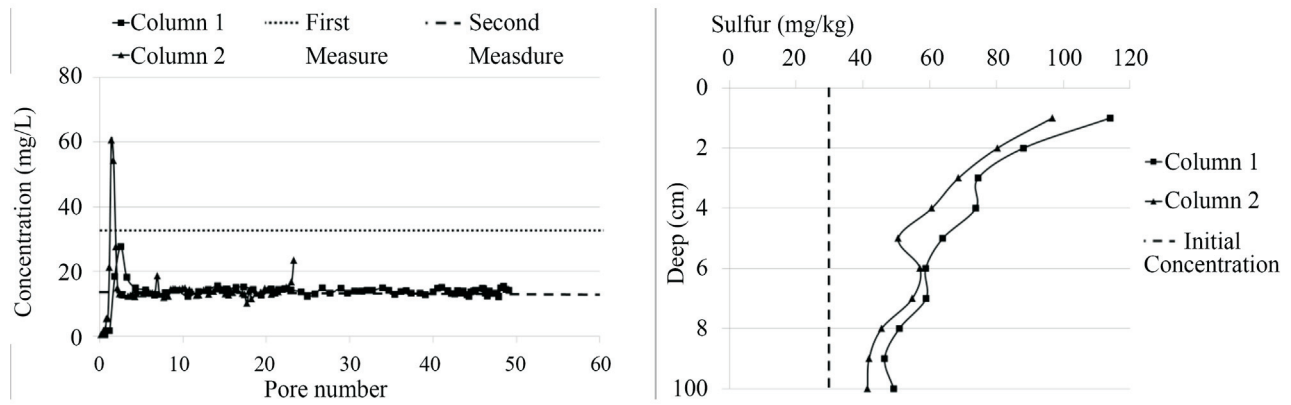


Figure 4 - Sulphur concentration: a) in the column effluents; b) in the soil after the test.

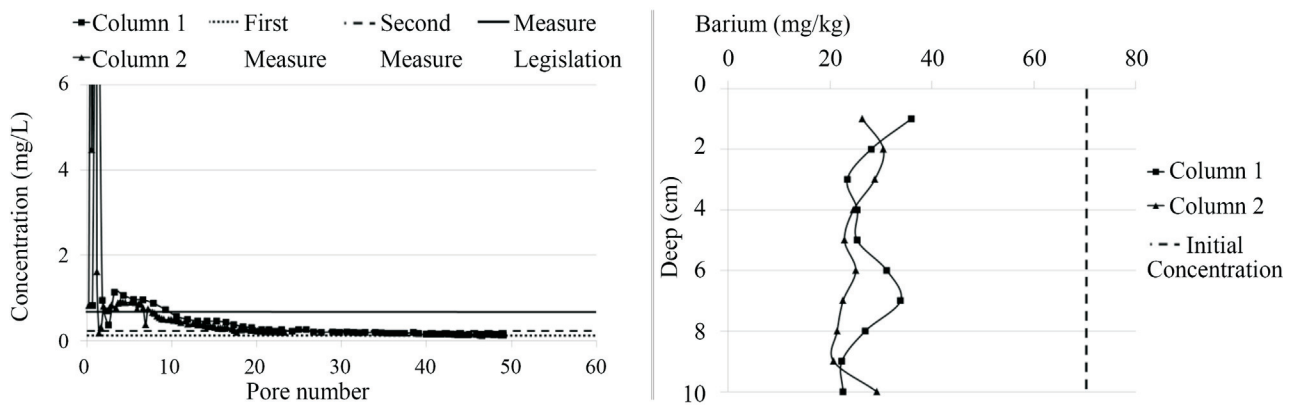


Figure 5 - Barium concentration: a) in the column effluents b) in the soil after the test.

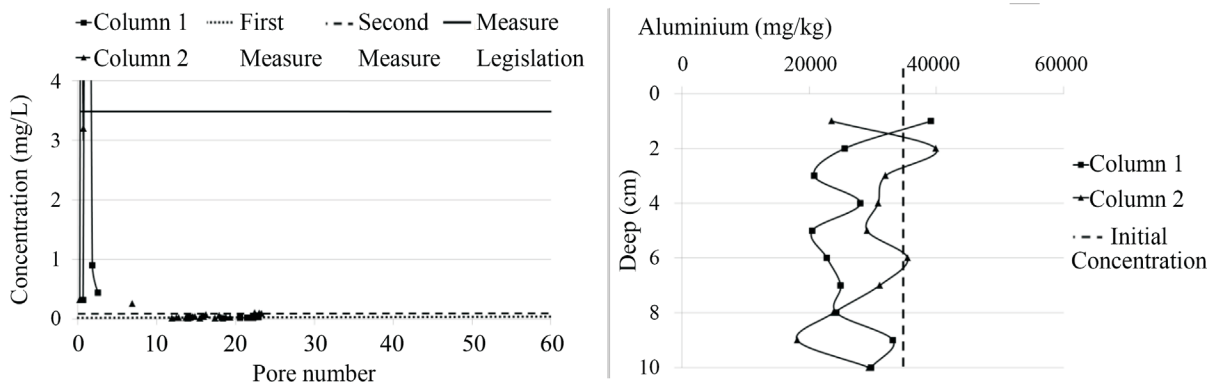


Figure 6 - Aluminium concentration: a) in the column effluents b) in the soil after the test.

precipitate with sulphides, especially with highly reducing Eh (Eh < 0).

Iron was retained throughout the test, since its concentration in the effluent increased gradually, but always keeping lower than in the raw leachate (Fig. 8a). Since this element has been strongly leached from the soil (Fig. 8b), a considerable part of it should be associated with the colloidal phase, as evidenced by the digestion analysis of parti-

cles retained on a 0.45- $\mu$ m filter (Ferreira, 2012). According to the geochemical modelling, iron tends to precipitate, as the leached effluent is supersaturated of carbonates, oxides and hydroxides. Similar behaviour was observed for titanium.

Considerable amount of phosphorus and calcium was retained at the top of the soil column (Fig. 9a and Fig. 9b), the same was observed for other elements that exhibited

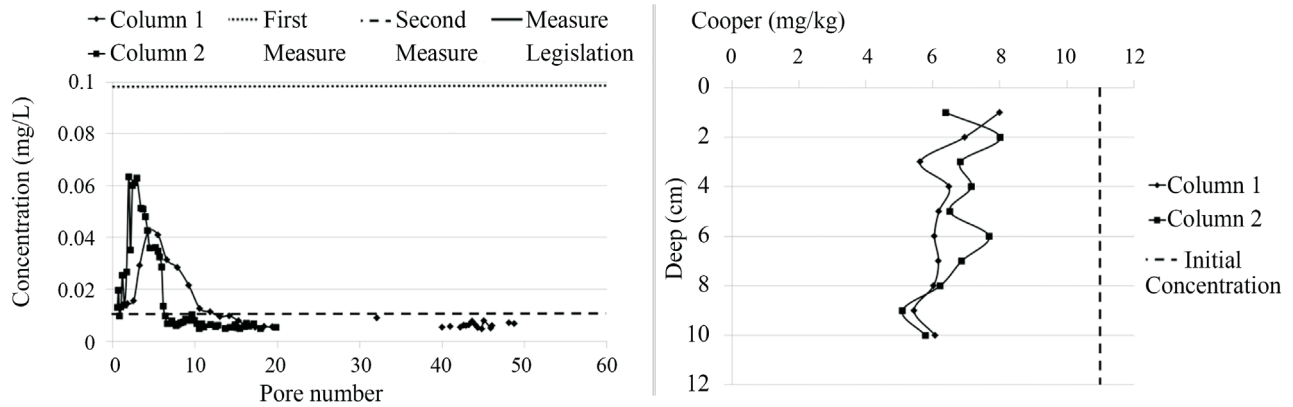


Figure 7 - Copper concentration: a) in the column effluents b) in the soil after the test.

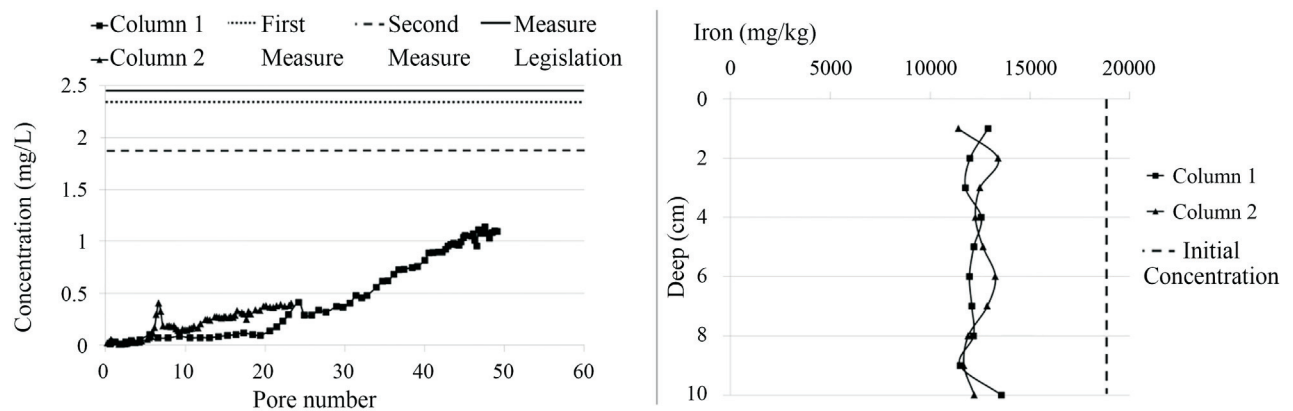


Figure 8 - Iron concentration: a) in the column effluents b) in the soil after the test.

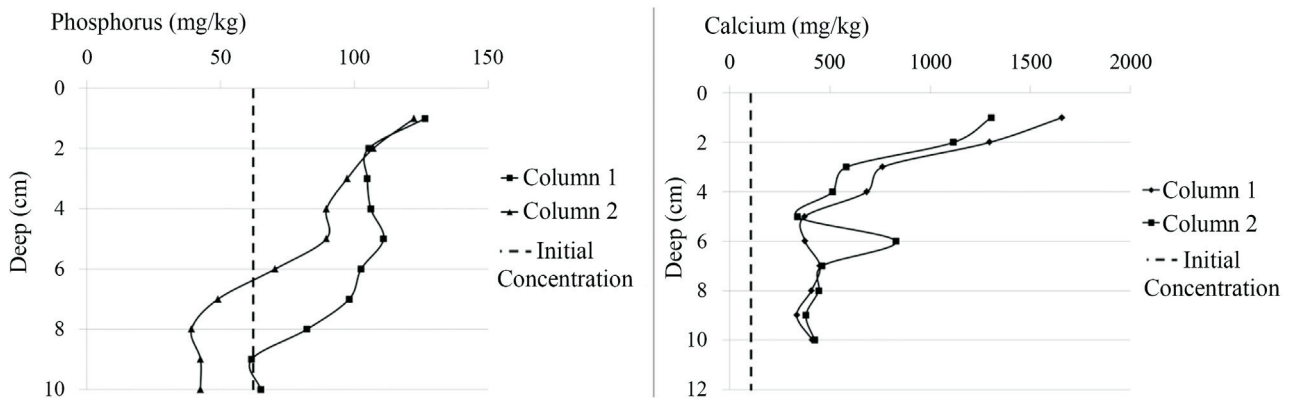


Figure 9 - Chemical concentration in the soil after column test: a) Phosphorus, and b) Calcium.

good positive correlations with them, such as strontium, manganese and yttrium. According to the saturation index calculated for the leached effluent, phosphate may have precipitated with calcium in the form of apatite.

The manganese concentration in the raw leachate is slightly higher than the maximum allowed by legislation for drinking water (Brasil, 2001); however, concentrations found in the column effluents are much smaller, indicating strong soil retention (Ferreira, 2012). Saturation index val-

ues calculated by the PHREEQC software show a tendency to precipitate it as carbonates and phosphates.

The chromium concentration in the leached effluent is above the maximum allowed by law, constituting a potential source of groundwater contamination in the landfill area. Chromium was initially retained, but its concentration gradually increased, exceeding that in the raw leachate (Fig. 10a). The small soil leaching (Fig. 10b) may have contributed to the progressive increase of its concentration in

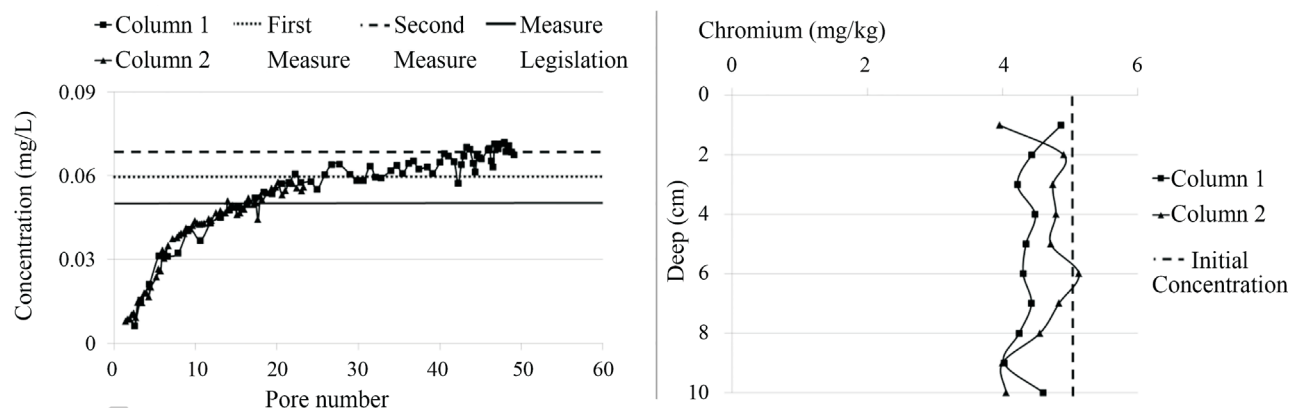


**Figure 10** - Chromium concentration: a) in the column effluents b) in the soil after the test.

the column effluents and this may be a consequence of the progressive alteration of the Eh/pH conditions.

Other important trace elements such as lead, arsenic and cadmium were not detected in the leachate due to the low limit of detection of ICP-MS.

#### 4. Conclusions

The study showed a significant reduction in the hydraulic conductivity of the saprolite during the tests, which can be explained by the progressive reduction of the porosity due to the precipitation of salts and maybe because of the growth of microorganisms. The analysis of data regarding the concentration of major and trace elements in soil and in the leached effluent after the tests, combined with the calculation of the saturation index with PHREEQC software, shows that the saprolite has some ability to mitigate the contamination from the MSW leachate, since several elements were retained in it, such as Al, Ca, Co, Li, S, Sr, P, Mg, Mn, K, Na, Ti and Zn. Chemical precipitation was certainly an important process in this mitigation process. Other elements were leached from the saprolite, such as Ba, Cu, Cr, Fe, Y and V, but some of these, such as Cu and Fe, are apparently immobilized on the colloidal fraction.

Na, K, and possibly bicarbonate constitute a significant part of the leachate solid load, and the first two tend to have conservative behaviour in the contamination plume identified in the landfill (SLU, 2010). Therefore, the slight reduction found in the electrical conductivity of the leached effluent compared to the raw leachate confirms that other ions have been retained even after 40 years of groundwater flow. As the saprolite thickness is greater and the hydraulic head exerted by the leached liquids is about 150 times smaller in the field, the actual retention power should be much more effective.

However, the retention capacity of saprolite is not complete, since the leaching of some elements such as Cr, S, Cu, Co, K, Na, Ni, V, occurred at different times during the column test. So, they can contaminate groundwater, as already shown in previous studies. Therefore, further stud-

ies should be carried out in order to elucidate the dynamics of contaminants transport in this medium.

#### Acknowledgments

The authors would like to thank the Belo Horizonte Urban Cleaning Department (SLMU) for the provision of data and permission to collect data in the landfill and FAPEMIG (PPM Project) and CNPq for the financial support.

#### References

- Alloway, B.J. (1995) *Heavy Metals in Soils*, 2<sup>nd</sup> ed. Blackie Academic & Professional, London, p. 339.
- Appelo, C.A. J & Postma, D. (2005) *Geochemistry, Groundwater and Pollution*. Balkema Publishers, Amsterdam, p. 649.
- Bacellar, L.A.P & Filho, W.L.O. (2008) Parecer Técnico do Monitoramento das Águas Subterrâneas da CTRS BR 040. Superintendência de Limpeza Urbana de Belo Horizonte, CTQ Análises Químicas e Ambientais, Relatório Interno, Belo Horizonte, p. 118.
- Barella, C.F. (2011) Avaliação de Indicadores Geoquímicos no Processo Natural de Atenuação da Fração Orgânica do Percolado na Região do Aterro Sanitário de Belo Horizonte - MG. Dissertação de Mestrado, Escola de Minas, Universidade Federal de Ouro Preto, Ouro Preto, 181 p.
- Beato, D.A.C.; Medeiros, M.J.; Drews, M.G.P & Dutra, G.M. (2003) Impactos urbanos em águas subterrâneas - Bacia da Lagoa da Pampulha, Belo Horizonte - MG. *Revista Águas Subterrâneas*, v. 17:1, p. 49-68.
- Bosco, M.E.G. (2008) *Geotecnia Ambiental*. Oficina de textos, São Paulo, p. 248.
- Brasil (2011) *Dispõe Sobre os Procedimentos de Controle e de Vigilância da Qualidade da Água para Consumo Humano e seu Padrão de Potabilidade - Portaria nº 2914*.
- Christensen, T.H.; Kjeldsen, P.; Bjerg, P.L.; Jensen, D.L.; Chris, J.B.; Baun, A.; Albrechtsen, H. & Heron, G.

- (2001) Biogeochemistry of landfill leachate plume. *Applied Geochemistry*, v. 16:7-8, p. 659-718.
- Ferreira, Q.C.G. (2012) Estudo da Mobilidade Química de Elementos Maiores e Traços em Saprolito de Gnaiss no Aterro sanitário (CTRS - BR040) de Belo Horizonte (MG). Dissertação de Mestrado, Departamento de Geologia, Universidade Federal de Ouro Preto, Ouro Preto, 165 p.
- Filippelli, G.M.; Laidlaw, M.A.S.; Latimer, J.C. & Raftis, R. (2005) Urban Lead Poisoning and Medical Geology: An Unfinished Story. *GSA Today*, v. 15:1, p. 1-11.
- FEAM (2010) Institui o Programa Estadual de Gestão de Áreas Contaminadas, que Estabelece as Diretrizes e Procedimentos para a Proteção da Qualidade do Solo e Gerenciamento Ambiental de Áreas Contaminadas por Substâncias Químicas - Deliberação Normativa Conjunta COPAM/CERH nº 2.
- Greenberg, A.E.; Clesceri, L.S & Eaton, A.D. (1992) *Standard Methods for the Examination of Water and Wastewater*, 18<sup>th</sup> ed. American Public Health Association, Washington DC, p. 1100.
- Kjeldsen, P.; Andersen, J.S.; Grundtvig, A. & Winther, P. (1998) Characterization of an old municipal landfill (Grindsted, Denmark) as a groundwater pollution source: landfill history and leachate composition. *Waste Management Research*, v. 16:3, p. 14-22.
- Kjeldsen, P.; Barlaz, M.A.; Rooker, A.P.; Baun, A.; Ledin, A. & Christensen, T.H. (2002) Present and long term composition of MSW landfill leachate: A review. *Science and Technology*, v. 32:4, p. 297-336.
- Patrick Jr W.H. & Verloo M (1998) Distribution of soluble heavy metals between ionic and complexed forms in saturated sediment as affected by pH and redox conditions. *Water Science and Technology*, v. 37:6-7, p. 165-172.
- Pohland, F.G. (1991) Fundamental principles, management strategies for landfill codisposal practices. In: *Proceeding of the Third International Landfill Symposium, Sardinia 91*, Environmental Sanitary Engineering Centre, Cagliari, Italy, p. 1445-1460.
- SLU (2010) Relatório de Monitoramento da Central de Tratamento de Resíduos da BR 040 de Belo Horizonte (CTRS BR-040). Superintendência de Limpeza Urbana, Relatório Técnico, Prefeitura Municipal de Belo Horizonte, Belo Horizonte, p. 96.
- Sousa, H.A. (1998) Estudo da Contaminação Ambiental na Área do Aterro Sanitário da BR - 040, da Prefeitura Municipal de Belo Horizonte - MG. Dissertação de Mestrado, Departamento de Geologia, Universidade Federal de Ouro Preto, Ouro Preto, 147 p.
- Tecisan (2005) Diagnóstico Hidrogeológico Preliminar para Avaliação do Potencial de Contaminação. Relatório Técnico, Central de tratamento de resíduos sólidos CTRS BR 040, Brasil, v. 2, p. 176.
- USEPA (2007) Technical Document: Microwave Assisted Acid Digestion of Sediments, Sludges, Soils, and Oils - EPA 3051A.
- Young R.N.; Mohamed A.M.O & Warkentin B.P. (1996) *Principles of Contaminant Transport in Soils*, 2<sup>nd</sup> ed. Elsevier, Amsterdam, p. 328.



# Proposal of an Energy Comparison System in the SPT

G.W. Barreto, J.C.A. Cintra, N. Aoki

**Abstract.** This paper describes a mechanical device to compare the energy transference from the blow of a hammer to the stem referring to standardized and non-standardized equipment in Brazil. The device allows to measure the vertical displacement of a sleeve due to one or more blows of a hammer falling freely. Tests were carried out using three pieces of equipment for the SPT measurements, but only one was mounted on a tripod standardized by the NB 6484:2001 norm. Based on the displacement values, a comparative analysis of the available energies of the equipment was conducted. The efficiency of the standard tripod for the test performed without a strict control of the fall of the hammer relative to the transfer efficiency of the test performed with a strict control of the fall height was 82.5%, showing a significant influence of human factor on the results. The lowest coefficient of variation of the displacements (5.05%) was obtained for the test using mechanized equipment with an automatic hammer. From the standpoint of the available energy of the system, it is possible to use non-standard equipment by applying the correction factor ( $C_f$ ) to SPT results. Finally, static tests were performed on the sleeve and the energy transferred to the system was calculated.

**Keywords:** *in situ* testing, SPT, instrumentation, energy measurement.

## 1. Introduction

Many researchers have discussed the N value obtained from SPT and/or the energy delivered to the rod stem (e.g.; De Mello, 1971; Kovacs *et al.*, 1977, 1978; Palacios, 1977; Schmertmann & Palacios, 1979; Kovacs & Salomone, 1982; Robertson *et al.*, 1983; Belincanta, 1985, 1998; Belincanta & Cintra, 1998; Decourt *et al.*, 1988; Decourt, 1989; Teixeira, 1993; Aoki & Cintra, 2000; Cavalcante, 2002; Schnaid *et al.*, 2002; Schnaid *et al.*, 2004; Neves, 2004; Odebrechet, 2003; Odebrecht *et al.*, 2005; Odebrecht *et al.*, 2007; Schnaid, *et al.*, 2009; Lukiantchuki, 2012).

In Brazil, the Standard Penetration Test (SPT) is, in most cases, the only geotechnical investigation available (Cavalcante & Danziger, 2011), therefore it is indispensable for the elaboration of projects of foundations. The Brazilian norm foresees the lifting of the hammer by hand, but it allows the usage of automatic devices as long as the transferred energy has been proven.

Although, according to the norm these energies must be obtained from the usage of an instrument with load cells and accelerometers, this instrumentation is not used routinely.

On the other hand Brazilian laws and international recommendations from more developed countries suggest a conflict with the NBR 6484:2001 (ABNT, 2001) regarding the weight lifting and handling.

According to Pellenz (2005), Brazilian experts in ergonomics, when appointed as experts in labor contests, have been using the NR 17 standard published by the Brazilian Labor and Employment Ministry (Ministério do Tra-

balho e Emprego, 1978) and the NIOSH Method (1994) for the submission of opinions on jobs that involve the lifting and/or handling of weights. NR 17 is a norm of the Brazilian Labor and Employment Ministry, which deals with workplace ergonomics. In June 1978 the first issue of NR 17 was published, and so was the last revision in June 2007. The National Institute for Occupational Safety and Health (NIOSH) is the U.S. Federal Agency responsible for conducting research and making recommendations for the prevention of work-related injury and illness.

Merino (1996) reports the recommendations of some countries regarding the maximum weights that can be raised, which, depending on the working conditions, age and gender, are significantly lower than the weight of 637 N standardized by NBR 6484:2001. It is good to remember that the Brazilian practice of using two people to lift the weight is not appropriate once its liberation does not usually occur simultaneously, thus jeopardizing the result of the test.

As dynamic measurements of force and acceleration during the event of SPT test have not been used routinely and the hand lifting of the hammer is not compatible with the current technological stage in most countries, this paper deals with the development of a device that allows comparing the energy available in the system following the procedures adopted by the NBR 6484:2001 with other non-standard procedures in Brazil. The usage of this device would allow a more frequent application of mechanized equipment to perform SPT test, as it is entirely mechanical, easy to use, consisting of a simple assembly, with low cost and easy interpretation results.

---

G.W. Barreto, MSc, PhD Student, Escola de Engenharia de São Carlos, Universidade de São Paulo, 13.560-970 São Carlos, SP, Brazil. e-mail: gilmarbarreto2@gmail.com.  
J.C.A. Cintra, PhD, Full Professor, Escola de Engenharia de São Carlos, Universidade de São Paulo, 13.560-970 São Carlos, SP, Brazil. e-mail: cintrajc@sc.usp.br.  
N. Aoki, PhD, Assistant Professor, Escola de Engenharia de São Carlos, Universidade de São Paulo, 13.560-970 São Carlos, SP, Brazil. e-mail: nelson.aoki@uol.com.br.  
Submitted on March 28, 2013; Final Acceptance on October 24, 2014; Discussion open until July 31, 2014.

## 2. Material and Methods

### 2.1. Conception

The idea is to measure the average vertical displacement of a blow, from 15 blows of a hammer of 65 kg mass in a free fall height of 0.75 m over a two-part brass bushing pressed against a cylindrical steel rod. The bushing is connected to the rod by eight bolts with a tightening torque of 30 Nm. One reason for the choice of torque 30 Nm is that the authors wish the displacements of the bush, in a blow, to be such that match  $N_{spt}$  values in the range of 30 to 50 blows. On the other hand, the 30 Nm torque is located in the central range of variation of the torquemeter (5 to 50 Nm), which is interesting from the standpoint of accuracy. The relationship between the average displacement obtained by using standard equipment NBR 6484:2001 and that obtained using the alternative equipment corresponds to the average efficiency of the alternative equipment to the standard one. This procedure will allow the alternative equipment to be used in SPT by applying the correction coefficient obtained in the test.

### 2.2. Device

The device is composed of a steel base which supports a damping system comprised of four pads of neoprene with hardness shore A in the 88 to 92 range (Fig. 1). This neoprene hardness, besides having good properties related to: flexibility, mechanical strength, impermeability, durability, resistance to sunlight exposure and high temperature, has a higher impact resistance compared to a lower hardness neoprene.

A rod is mounted on the plate (Fig. 2) and a bronze bi-partite bushing (Fig. 3) is fixed to a support (Fig. 4). The tightening of the bush against the cylindrical surface of the stem is provided by eight screws (Fig. 5) whose torque is controlled by an analogical torque wrench (Fig. 6). Figure 7 shows the device assembled and with the anvil used in the drilling equipment mounted on the truck.

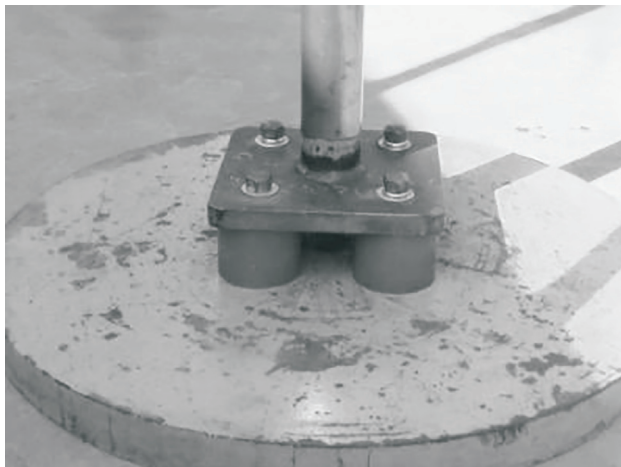


**Figure 1** - Base and damping plate.

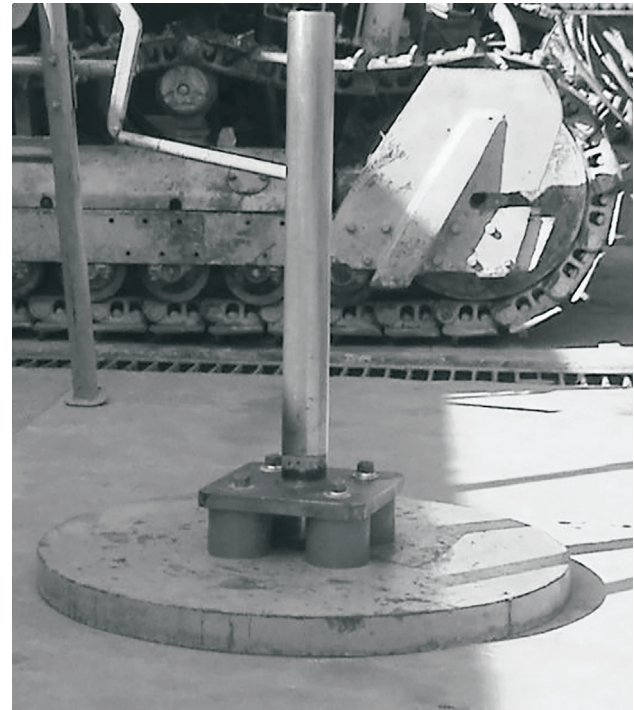


**Figure 2** - Stem threaded in the damping plate.

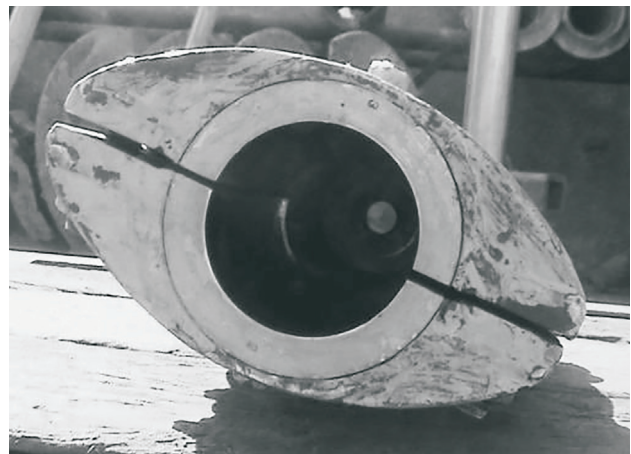


**Figure 3** - Bushing mounted on the support.



**Figure 4** - Support.

Figures 8 to 15 show the designs of the main parts of the device.



Figure 5 - Detail of the tightening bolts.

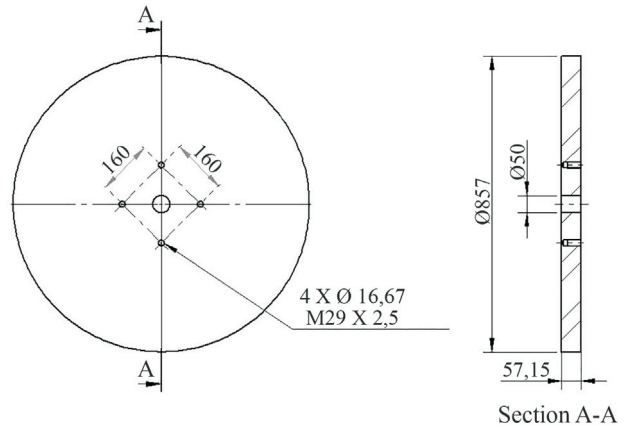


Figure 8 - Base.



Figure 6 - Torquemeter.

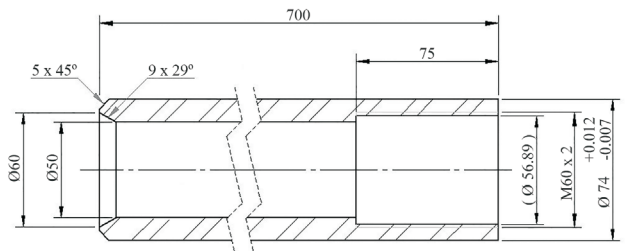


Figure 9 - Stem.



Figure 7 - Device mounted.

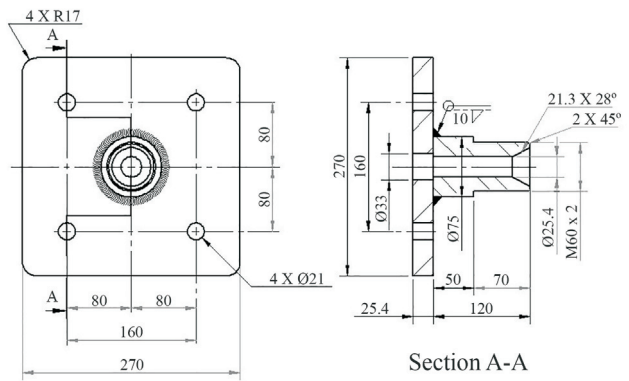


Figure 10 - Damping plate.

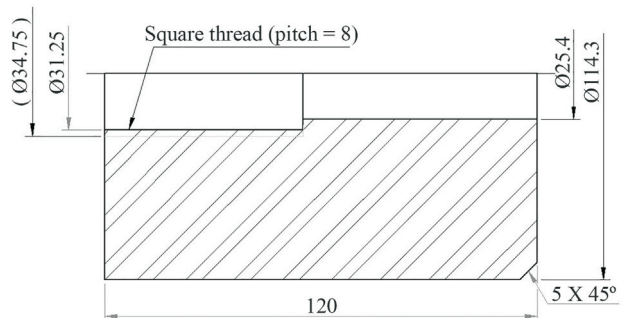


Figure 11 - Threaded bushing.

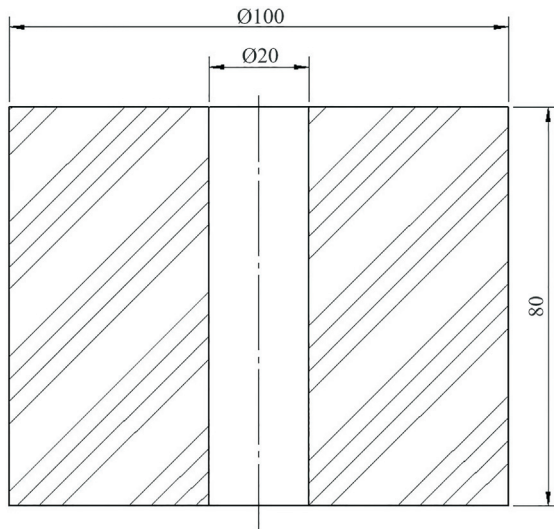


Figure 12 - Neoprene damper.

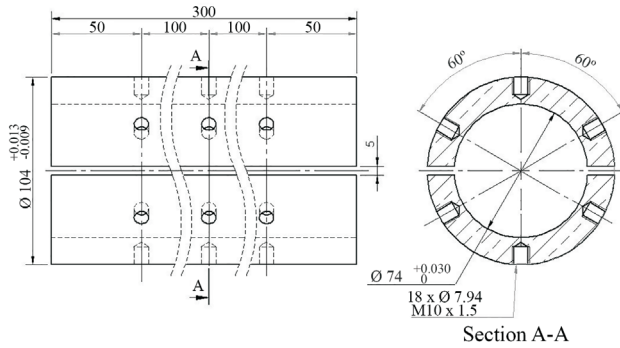


Figure 13 - Bushing.

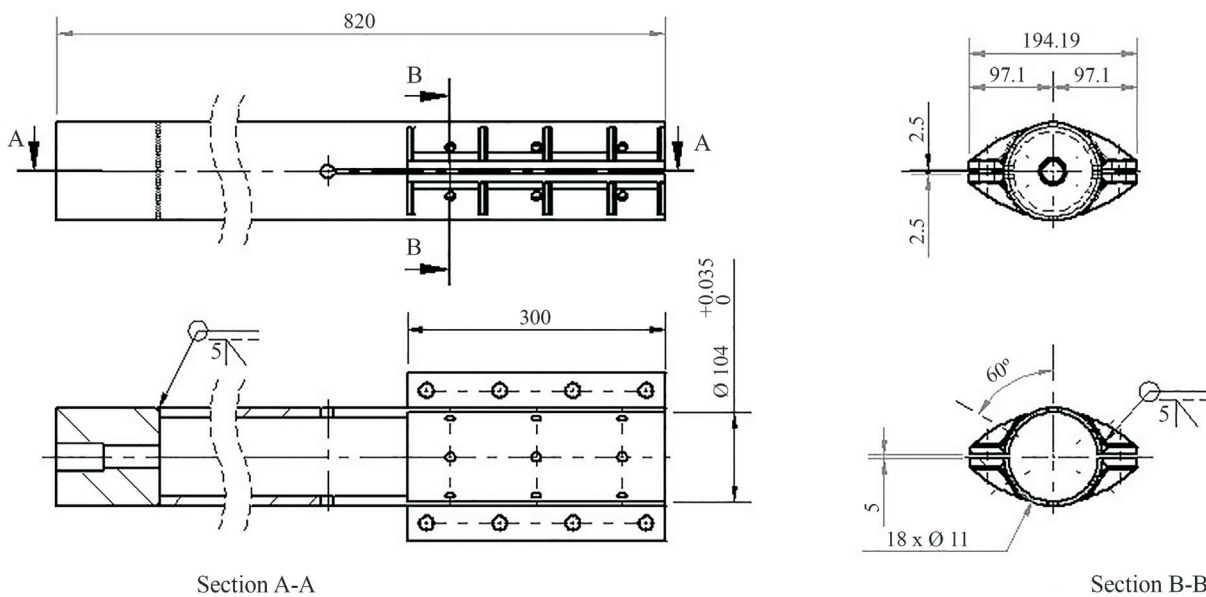


Figure 14 - Support of the bushing.

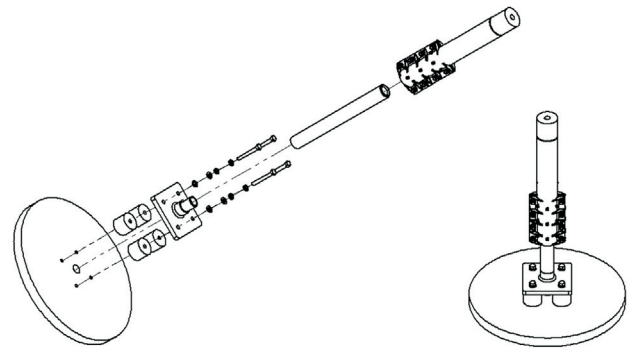


Figure 15 - Assembling of the device.

### 2.3. Instruments and procedures

An analog torquemeter with readings from 5-50 Nm to 0.50 Nm precision (Fig. 16) and a 1 mm precision steel scale (Fig. 17) were used in the dynamic tests. A hydraulic unit, a hydraulic cylinder, an analog manometer for measurements from 0 to 7000 kPa with 100 kPa precision and six extensometers with readings of 0-50 mm and 0.01 mm precision were used in the static tests. Although the steel scale used in the tests (ED-1 to ED-4) has a precision of 1 mm, it could be used without restriction as the mean displacement of the hammer that was obtained by dividing the accumulated displacement of the bushing by the number of hammer blows, resulting in a small error. On the other hand, the uncertainty associated with the reading of the scale and with the need to interpolate between scale markings is relatively easy to estimate. So, considering the millimeter markings on a ruler scale, it is reasonable to say that

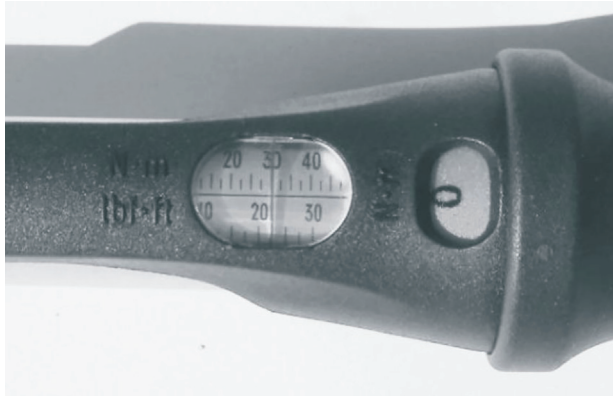


Figure 16 - Analog Torquemeter with 0.50 Nm.

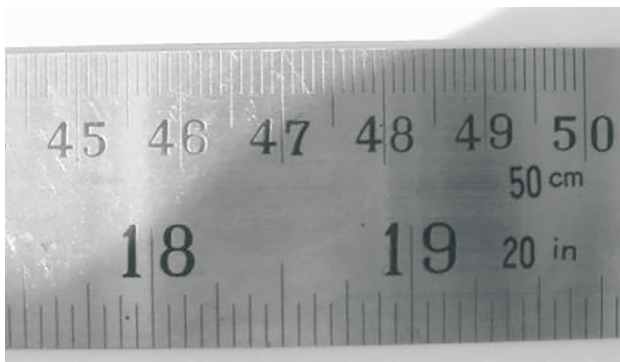


Figure 17 - Steel scale with 1 mm precision. precision.

the length could be read to the nearest millimeter at best. Therefore, a reasonable estimate of the uncertainty in this case would be  $\delta_l = \pm 0.5$  mm which is half of the smallest division.

A more precise instrument for the measurement of displacement was not used since one of the goals of this experiment was to opt for simple thinks that work quite well.

The procedures to be followed for the testing are shown below.

- a. The base was backed and kept in an undeformable, flat and horizontal place during all the tests to maintain the rigidity of the system and the vertical position of the rod, since the process is based on the comparison of displacements of the bushing relative to the shaft.
- b. The rod was mounted on the base so that there was no gap between the threads (base and rod).
- c. The bushing was mounted so that the space between its lower face and the upper face of the damping was 400 mm. A 25 mm diameter shaft was used as a template (Fig. 18).
- d. The screws were numbered from left to right and from top to bottom and tightened as follows:
  - d1) Screws seven and eight were tightened with the template in the correct position.

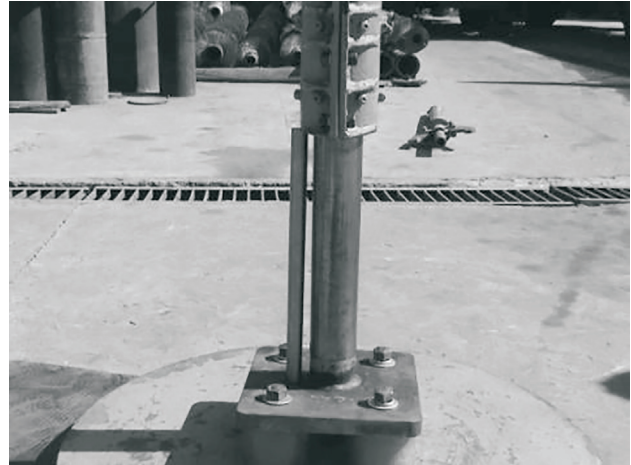


Figure 18 - Template positioned in the device.

- d2) The template was removed from the device and screws 1 to 6 were tightened.
- d3) The tightening torque of all screws was checked in the 1 to 8 order.
- e. The anvil, corresponding to the tested equipment, was positioned in such a way that there was no gap between the male and female threads.
- f. The test apparatus was placed so that the shaft was concentric with the hammer.
- g. The hammer was lifted to a 75 cm height and then the first blow was given.
- h. The distance from the lower face of the bushing to the upper face of the damping plate was measured.
- i. Screws 1 and 2 were released and tightened with the adopted torque.
- j. Screws 7 and 8 were released and tightened with the adopted torque.
- k. Screws 1 to 6 were released and tightened with the adopted torque.
- l. The tightening torque of screws 1 to 8 was checked.
- m. The hammer was lifted to a height of 75 cm and then the second blow was given.
- n. The procedures in items “i” to “m” were repeated until the fifteenth blow.

### 3. Results

Four experiments were performed and for each test 15 blows with a mass of 65 kg in free fall of 75 cm height were given. For each blow the displacement of the bushing relative to the rod fixed to the base was measured. The ED-1 test was performed using the manual lifting of the hammer by two men, with the tripod, pulleys, rope, hammer and other accessories in accordance with NBR 6484:2001. The test was conducted with a strict control of the standardized drop height of the hammer. Before each blow, the hammer was sustained for several seconds at a height 75 cm and then allowed to fall freely. The second

test (ED-2) was conducted using a tripod equipped with a Borros Standard Penetration Test automatic trip hammer (Fig. 19).

The third test (ED-3) was carried out with the equipment mounted on a truck and equipped with an automatic hammer similar to CME - Central Mine Equipment Company (Fig. 20). The ED-4 test was performed with a tripod standardized by NBR 6484:2001; the hammer was lifted by two men, but with no strict control of the fall height. This procedure deliberately simulated a common practice.

Table 1 shows the results of the tests and Table 2 shows the various values calculated from the results.

The correction factor ( $C_f$ ) based on the energy transferred from the hammer to the rod can be expressed by

$$C_f = \frac{\delta_{mTEST}}{\delta_{mSTANDARD}} \quad (1)$$

where  $\delta_{mTEST}$  is the average displacement in the test and  $\delta_{mSTANDARD}$  is the average displacement test standardized by ABNT.

Therefore N-value must be corrected by the correction factor for the efficiency of the standard equipment as shown below:

$$N_{STANDARD} = C_f \cdot N_{TEST} \quad (2)$$

where  $N_{STANDARD}$  is the N-value corrected for the standard efficiency and  $N_{TEST}$  is the N-value obtained in the test.

A static test (EE-1) with screw tightening torques of 10 Nm, 15, 20, 25 and 30 Nm was performed to determine the loads of slip, simulating a static load test in the standard

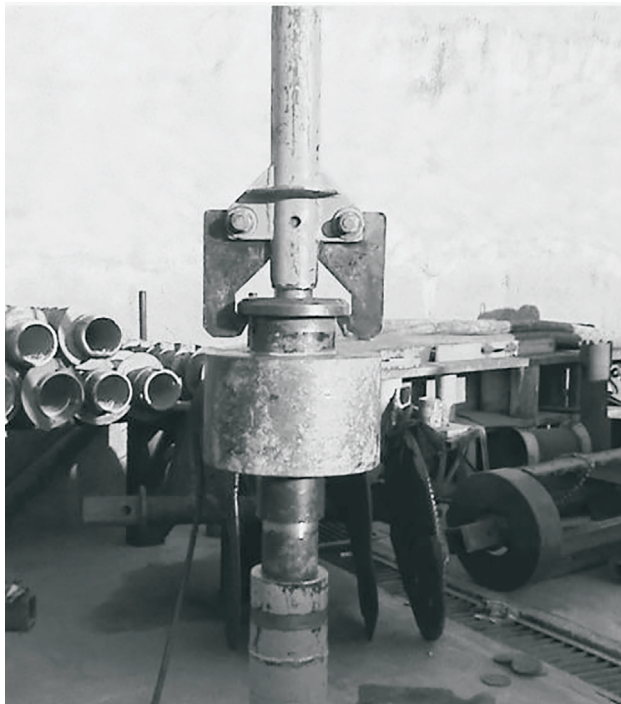


**Figure 19** - Borros SPT automatic hammer.



**Figure 20** - Equipment mounted on a truck.

sampler (Aoki *et al.*, 2007) and two static tests (EE-2 and EE-3) with tightening torque of 30 Nm were conducted to obtain the load-displacement curve of the bushing. Figure 21 shows the assembling of the test and Fig. 22 shows the results.

Whereas the displacement of the bushing relative to the rod just before reaching the friction load between two parts is too small, a simplified load-settlement curve was adopted (Fig. 23) for the torque tightening of 30 Nm on the screws. This simplification facilitates the determination of the efficiency of the SPT test system.

The efficiency of the SPT test system can be expressed by

$$\eta = \frac{W}{U} \quad (3)$$

where  $\eta$  is the average efficiency of the SPT test system,  $W$  is the work done by force “ $F$ ” necessary to slip the bushing and  $U$  is the standard potential energy - approximately 478.1 J - of the SPT.

The work done by force ( $F$ ) is approximately equal to the area under the load-settlement curve, as Aoki, *et al.* (2007).

Table 3 shows the transfer efficiencies on the basis of the work done by force “ $F$ ” and the relationship between efficiency and relative efficiency for each SPT test system for a tightening torque of 30 Nm using equation  $F = 1.3714 T$ .

Two load tests (EE-2 and EE-3) were performed using a comparing device of SPT to validate the simplified load-settlement curve. The loading and unloading phases were separated, respectively, into 13 and 7 stages. For both tests the tightening torque of the screws that creates the radial tensions in the rod was 30 Nm and the displacements of the bushing and the damping plate were measured at times  $t = 0$  min and  $t = 5$  min. using four dial gages with 0.01 mm accuracy and 50 mm displacement.

**Table 1** - Displacement of the bushing (mm).

Number of the blow	$Li_{ED1}$	$\delta_{ED1}$	$Li_{ED2}$	$\delta_{ED2}$	$Li_{ED3}$	$\delta_{ED3}$	$Li_{ED4}$	$\delta_{ED4}$
1	392	8	393	7	391	9	392	8
2	384	8	386	7	381	10	386	6
3	375	9	378	8	372	9	381	5
4	368	7	371	7	363	9	373	8
5	360	8	364	7	353	10	366	7
6	353	7	357	7	344	9	360	6
7	346	7	350	7	335	9	353	7
8	339	7	344	6	326	9	347	6
9	331	8	337	7	317	9	341	6
10	324	7	331	6	308	9	335	6
11	317	7	324	7	299	9	329	6
12	310	7	317	7	290	9	323	6
13	303	7	310	7	282	8	319	4
14	295	8	303	7	273	9	313	6
15	287	8	296	7	264	9	307	6
$\delta t$	***	113	***	104	***	136	***	93
$\delta m$	***	7.5	***	6.9	***	9.1	***	6.2

$Li_{ED1}$  - reading on the scale for ED-1 test;  $Li_{ED2}$  - reading on the scale for ED-2 test;  $Li_{ED3}$  - reading on the scale for ED-3 test;  $Li_{ED4}$  - reading on the scale for ED-4 test.

$\delta_{ED1}$  - displacement for test ED-1;  $\delta_{ED2}$  - displacement for test ED-2;  $\delta_{ED3}$  - displacement for test ED-3;  $\delta_{ED4}$  - displacement for test ED-4.  
 $\delta t$  - total displacement;  $\delta m$  - mean displacement.

**Table 2** - Values calculated based on the test results.

Test	Total displacement ( $\delta_t$ ) (mm)	Average displacement ( $\delta_m$ ) (mm)	Average standard deviation (sd) (mm)	Coef. of variation (%)	Relative efficiency ( $\eta_r$ )(%)	Factor of efficiency
ED-1	113	7.5	0.6	8.0	100	1.00
ED-2	104	6.9	0.5	7.2	92	0.92
ED-3	136	9.1	0.5	5.5	120	1.20
ED-4	93	6.2	1.0	16.1	82	0.82

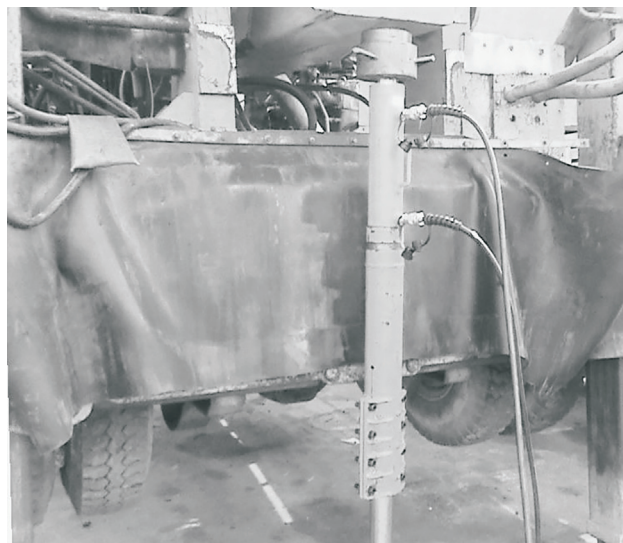


**Figure 21** - Assembling of the static test.

In the EE-2 test two dial gages, numbered 1 and 2, were used. The magnetic bases were fixed on the base of the device and the contact tips were lightly pressed against the lower face of the bushing. Four gages numbered 3 to 6 were also used; their magnetic bases were fixed on the base

**Table 3** - Efficiency of SPT test system.

Test	$\delta_m$ (mm)	F (N)	W (J)	$\eta$ (%)	$\eta/\eta_r$
ED-1	7.5	41142	310	65	0.65
ED-2	6.9	41142	285	60	0.65
ED-3	9.1	41142	373	78	0.65
ED-4	6.2	41142	255	53	0.65

$\delta_m$  is the average displacement;  $F$  is the load slip bronze bushing;  $W$  is the work done by force “ $F$ ”;  $\eta$  is the transfer efficiency of the SPT tested system;  $\eta_r$  is the relative transfer efficiency of the standard SPT test system = 100%.

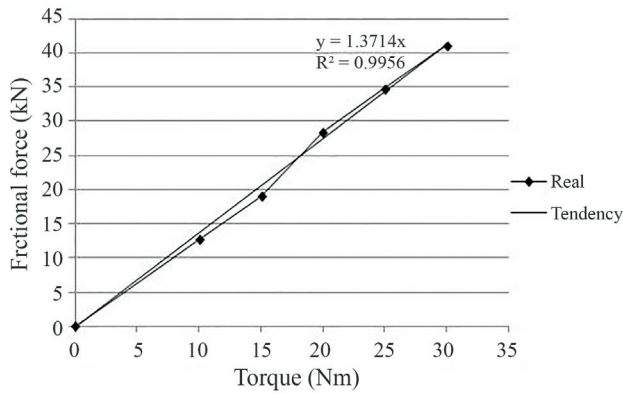


Figure 22 - Load slip bronze bushing (EE-1).

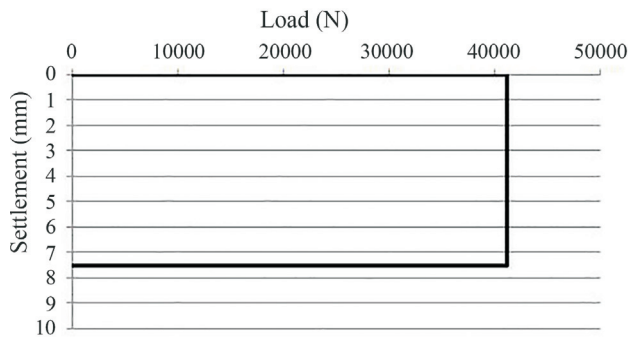


Figure 23 - Simplified load-settlement curve.

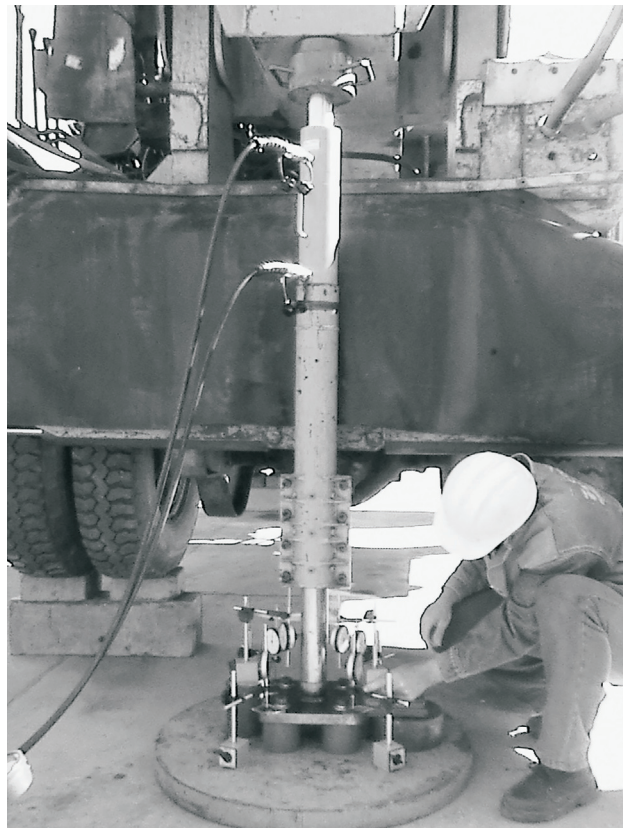


Figure 24 - Mounting of the load test.

of the device and the contact tips were lightly pressed against the upper face of the damping plate. Figure 24 shows the assembly of this test and Fig. 25 shows the assembling of the dial gages. A drill rig weighing approximately 170 kN was used as the reaction system.

To draw the load-settlement curve of the bushing, the loads were obtained multiplying the pressure by the cross-sectional area of the hydraulic jack and the displacements were obtained by the difference between the means of the displacements of extensometers 1 and 2, and 3 to 6.

This procedure was necessary because the area under the load-settlement curve of the bushing must represent the work done by the non-conservative forces, since the displacements of extensometers 1 and 2 are already embedded in the displacements relative to the base of the damper plate.

Figure 26 shows the load-settlement curve of the bushing. The area under this curve represents the work done by the non-conservative forces, *i.e.* 292.1 J considering the upper limit of 7.5 mm (ED-1). The work was obtained by the trapezoid method integration, for displacement values from 0 to 7.5 mm, *i.e.*:

$$W(x) = \int_0^x N(x)d(x) \tag{4}$$

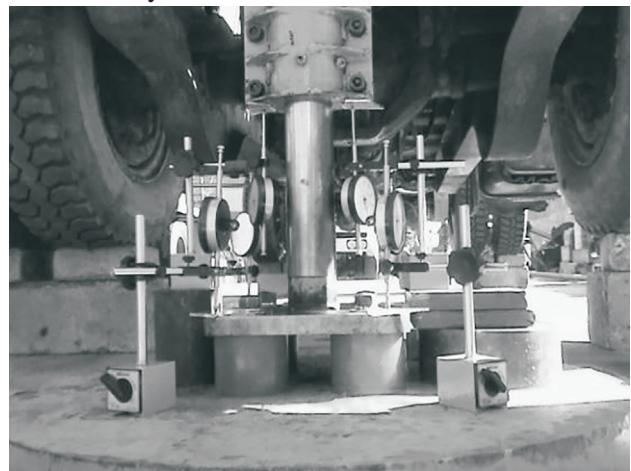


Figure 25 - Mounting of the dial gages.

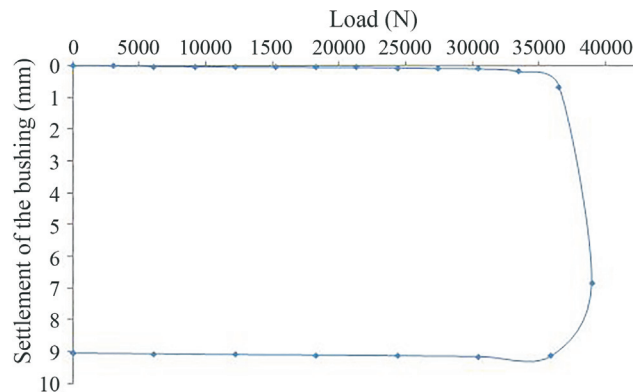


Figure 26 - Load-settlement curve (EE-2).

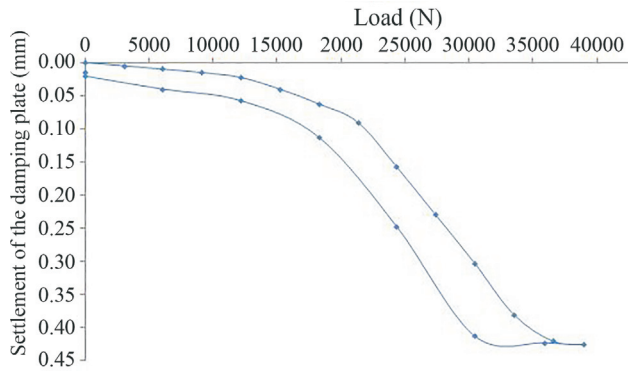


Figure 27 - Load-settlement curve of the damping plate (EE-2).

where  $W(x)$  is the work done by non-conservative forces and/or conservative forces and  $N(x)$  is the potential energy normalized (478.1 J) in the SPT.

Figure 27 shows the load-settlement curve of the damping plate. The area under the curve represents the work done by the conservative forces, whereas for the displacement of 7.5 mm of the bushing obtained in the dynamic test, the work done was 10.8 J.

The efficiency of the dynamic test (ED-1) can be calculated as the ratio between the total work done and the potential normalized energy of the SPT. Therefore,

$$\eta = \frac{Wt}{U} = \frac{292.1}{478.1} \times 100 = 61.1\% \quad (5)$$

where  $Wt$  is the work done by non-conservative forces and  $U$  is the standard potential energy - approximately 478.1 J - of the SPT.

The variation in the efficiency obtained by the model instrumented with dial gages compared to that obtained by the simplified model can be calculated by the expression

$$\Delta\eta = \frac{\eta_s - \eta_i}{\eta_i} = \frac{0.650 - 0.611}{0.611} \times 100 = 6.4\% \quad (6)$$

where  $\eta_s$  is the transfer efficiency of the SPT test system obtained by the simplified model and  $\eta_i$  is the transfer efficiency of the standard SPT test system obtained by the instrumented model.

In the EE-3 trial two dial gages, numbered 1 and 2 were used and their magnetic bases were fixed on the damping plate of the device and the contact tips were lightly pressed against the lower face of the bushing. The other procedures were identical to those for EE-2 test. Figure 28 shows the assembling of the test and Fig. 29 shows the assembling of the dial gages.

The area under the curve represents the work done by the conservative forces, whereas for the displacement of 7.5 mm of the bushing obtained in the dynamic test, the work done was 10.8 J.

The load-settlement curve of the bushing was obtained in the same manner as in the EE-2 test and settle-

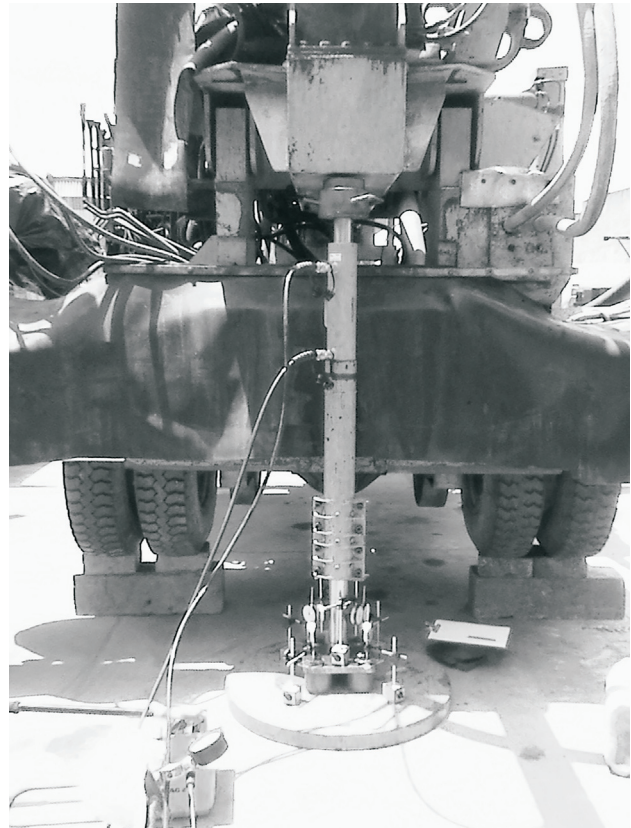


Figure 28 - Mounting of the load test.

ments were obtained directly from the readings in the first and second dial gages since these displacements correspond to those caused by non-conservative forces.

Figure 30 shows the load-settlement curve of the bushing. The area under this curve, which represents the work done by non-conservative forces, resulted in 312.7 J, considering the settlement of 7.5 mm obtained in the dynamic test.

Figure 31 shows the load-settlement curve of the damping plate. The area under this curve represents the work done by the conservative forces, whereas for the settlement of 7.5 mm of the bushing obtained in the dynamic test, the work done was 9.3 J.

The efficiency of the dynamic test (ED-1) can be calculated as the ratio between the total work done and the potential normalized energy of the SPT. Therefore

$$\eta = \frac{Wt}{U} = \frac{312.7}{478.1} \times 100 = 65.4\% \quad (7)$$

The variation in the efficiency obtained by the model instrumented by dial gages in comparison to that obtained by the simplified model can be calculated by the expression:

$$\Delta\eta = \frac{|\eta_s - \eta_i|}{\eta_i} = \frac{|0.650 - 0.654|}{0.654} \times 100 = 0.61\% \quad (8)$$

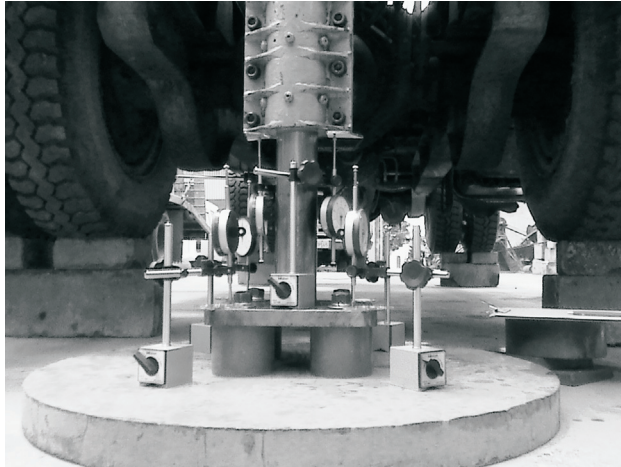


Figure 29 - Mounting of the dial gages (EE-3).

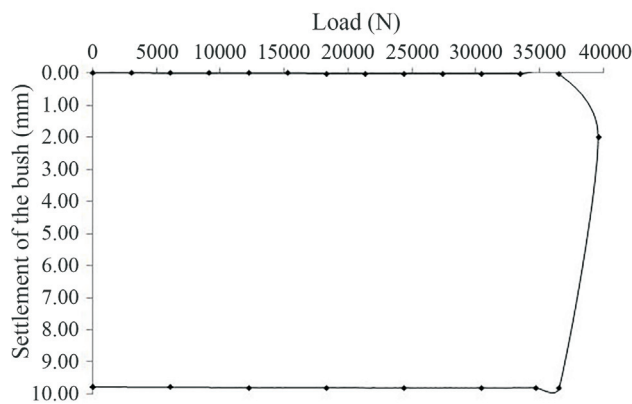


Figure 30 - Load-settlement curve of the bushing (EE-3).

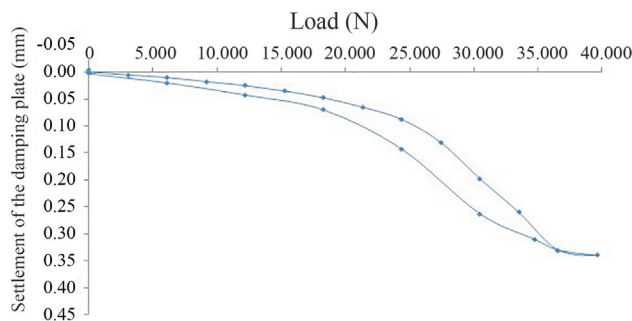


Figure 31 - Load-settlement curve of the damping plate. (EE-3).

The percentage change between the work done by the non-conservative forces, respectively, for tests EE-2 and EE-3 can be computed as

$$\Delta T = \frac{Wt_{EE-3} - Wt_{EE-2}}{Wt_{EE-2}} \times 100 = \frac{321.7 - 292.1}{292.1} \times 100 = 7.1\% \quad (9)$$

where  $Wt_{EE-2}$  is the work done by conservative forces for test EE-2 and  $Wt_{EE-3}$  is the work done by conservative forces for test EE-3.

The load and unload curves of the damping plate were not coincident, probably due to the hysteresis effect.

#### 4. Conclusions

The lowest coefficient of variation of the displacements was obtained for the dynamic test using mechanized equipment mounted on the truck with an automatic hammer, suggesting a tendency of repeatability of this test.

The highest coefficient of variation of displacements was obtained for the standard manual test, but without a strict control of the fall of the hammer, showing a significant influence of human factor on the results.

The low variability of displacements that occurred in the tests with mechanized equipment suggests a tendency of repeatability of these tests.

The energy obtained with the simplified load-settlement curve was consistent with the energy calculated based on the real load-displacement curve, indicating that it is possible to use the simplified model to obtain the transferred energy efficiency.

Considering the results of the tests and simplicity of construction and operation of the device, it can be used routinely by universities and companies to calibrate and compare the efficiencies of any SPT test system and the standard equipment by applying the necessary correction factor.

Other tests to measure the displacement can be performed with different tightening torques in the screws to verify if the values of the efficiencies will be repeated.

#### References

- ABNT (2001) Solo - Sondagens de Simples Reconhecimento com SPT - Método de Ensaio. NBR 6484, Rio de Janeiro, 17 p.
- Aoki, N. & Cintra, J.C.A. (2000) The application of energy conservation Hamilton's Principle to the determination of energy efficiency in SPT tests. Proc. 6<sup>th</sup> Int. Conf. on the Application of the Stress-Wave Theory to Piles, São Paulo, v. 1, p. 457-460.
- Aoki, N.; Esquivel, E.R.; Neves, L.F.S. & Cintra, J.C.A. (2007) The impact efficiency obtained from static load test performed on the SPT sampler. Soils and foundations. Japanese Geotechnical Society. v. 47:6, p. 1045-1052.
- Belincanta, A. (1985) Energia Dinâmica no SPT - Resultados de uma Investigação Teórico - Experimental. MSc Thesis, Escola Politécnica, Universidade de São Paulo, São Paulo, 217 p.
- Belincanta, A. (1998) Avaliação de Fatores Intervenientes no Índice de Resistência à Penetração do SPT. DSc Thesis, Escola de Engenharia de São Carlos, Universidade de São Paulo, São Carlos, 141 p.

- Belincanta, A. & Cintra, J.C.A. (1998) Avaliação de fatores intervenientes em Variantes do método ABNT para a Execução do SPT. *Soils and Rocks*, v. 21:3, p. 119-133.
- Cavalcante, E.H. (2002) Investigação Teórico-Experimental sobre o SPT. DSc Thesis, Universidade Federal do Rio de Janeiro, Rio de Janeiro, 430 p.
- Cavalcante, E.H.; Danziger, B.R. & Danziger F.A.B. (2011) Measurement of drop height and impact velocity in the Brazilian SPT system. *Soils and Rocks*, v34:3, p. 207-218.
- Décourt, L.; Muromachi, T.; Nixon, I.K.; Schmertmann, J.H.; Thorburn, S. & Zolkov, E. (1988) Standard Penetration Test (SPT): International reference test procedure. Proc. of the ISSMFE Technical Committee on Penetration Testing - SPT Working Party, ISOPT I, Orlando, v. 1, p. 3-26.
- Decourt, L. (1989) The standard penetration test - State of-the-art. Proc. 12<sup>th</sup> Int. Conference on Soil Mechanics and Foundation Engineering, Rio de Janeiro, v. 4, p. 2405-2416.
- De Mello, V.F.B. (1971) Standard penetration test. Proc. of the 4<sup>th</sup> Panamerican Conference on Soil Mechanics and Foundation Engineering, Port Rico, v. 1, p. 1-86.
- Kovacs, W.D.; Evans, J.C. & Griffith, A.H. (1977) Towards a more standardized SPT. Proc. 9<sup>th</sup> International Conference on Soil Mechanics and Foundation Engineering, Tokyo, v. 2, p. 269-276.
- Kovacs, W.D.; Griffith, A.W. & Evans, J.C. (1978) An alternative to the cathead and rope for the standard penetration test. *Geotechnical Testing Journal*, ASTM, v. 1:2, p. 72-81.
- Kovacs, W.D. & Salomone, L.A. (1982) SPT hammer energy measurement. *Journal of the Soil Mechanics and Foundations Division*, ASCE, v.108:GT4, p. 599-620.
- Lukiantchuki, J.A. (2012) Interpretação de Resultados do Ensaio SPT com Base em Instrumentação Dinâmica. DSc Thesis, Escola de Engenharia de São Carlos, Universidade de São Paulo, São Carlos, 364 p.
- Merino, E.A.D. (1996) Efeitos Agudos e Crônicos Causados pelo Manuseio e Movimentação de Cargas no Trabalhador. MSc. Thesis, Universidade Federal de Santa Catarina, Florianópolis, 118 p.
- Ministério do Trabalho e Emprego (1978) Norma Regulamentadora NR 17 - Ergonomia. Brasília.
- Neves, L.F.S. (2004) Metodologia para a Determinação da Eficiência do Ensaio SPT Através de Prova de Carga Estática Sobre o Amostrador Padrão. M.Sc Thesis, Escola de Engenharia de São Carlos, Universidade de São Paulo, São Carlos, 90 p.
- NIOSH (1994) Applications manual for the Revised NIOSH Lifting Equation. National Institute for Occupation Safety and Health. Ohio, Cincinnati, 164 p.
- Odebrecht, E. (2003) Medidas de Energia no Ensaio do SPT. DSc Thesis, Universidade Federal do Rio Grande do Sul, Porto Alegre, 230 p.
- Odebrecht, E.; Schnaid, F.; Rocha, M.M. & Bernardes, G.P. (2005) Energy efficiency for standard penetration tests. *Journal of Geotechnical and Geoenvironmental Engineering*. ASCE, p. 1252-1263, Oct. 2005.
- Odebrecht, E.; Schnaid, F.; Rocha, M.M. & Bernardes, G.P. (2007) Discussion of energy efficiency for standard penetration tests. *Journal of Geotechnical and Geoenvironmental Engineering*, v. 133, p. 486-490.
- Palacios, A. (1977) Theory and Measurements of Energy Transfer During Standard Penetration Test Sampling. Ph.D Thesis, University of Florida, Gainesville, 391 p.
- Pellenz, C.C.O. (2005) Indicadores de Levantamento de Carga e Parâmetros Mecânicos da Coluna Vertebral. MSc Thesis, Universidade Federal do Paraná, Curitiba, p. 36.
- Robertson, P.K.; Campanella, R.G. & Wightman, A. (1983) SPT-CPT correlations. *Journal of Geotechnical Engineering*, ASCE, v. 109: 11, p. 201-209.
- Schmertmann, J.H. & Palacios, A. (1979) Energy dynamics of SPT. *Journal of the Soil Mechanics and Foundations Division*, ASCE, v. 105:GT8, p. 909-926.
- Schnaid, F.; Odebrecht, E.; Bernardes, G.P. & Rocha, M.M. (2002) Medidas de energia no ensaio SPT. In: XII COBRAMSEG - Congresso Brasileiro de Mecânica dos Solos e Engenharia Geotécnica, 2002, São Paulo. XII COBRAMSEG, v. 1.p. 107-117.
- Schnaid, F.; Odebrecht, E.; Rocha M.M. & Bernardes, G.P. (2004) Transferência de energia no ensaio SPT: efeito do comprimento de hastes e da magnitude dos deslocamentos. *Solos e Rochas*, v. 27, n. 1, p. 69-82.
- Schnaid, F.; Odebrecht, E.; Lobo, B.O. & Rocha, M.M. (2009) Discussion of SPT Hammer Energy Ratio versus Drop Height by T. Leslie Yound, Hannah W. Bartholomew and Jamison H. Steidl. *Journal of Geotechnical and Geoenvironmental Engineering*. v. 135, p. 1777-1778.
- Teixeira, A.H. (1993) Um aperfeiçoamento das Sondagens de Simples Reconhecimento a Percussão. *Solos do Interior de São Paulo*, ABMS-NRSP, São Carlos, p. 75-93.



# Investigations on Gas Flow in Cracked Granite Samples

M.C. He, C.G. Wang, J.L. Feng, L.R. Sousa

**Abstract.** In the case of rock-fluids interaction, numerous studies have mainly focused on field and numerical simulations regarding the existence of toxic gases and investigations about the possibility of gasburst. This paper is related to the development of experimental investigations for granite formations on samples obtained from Creighton mine, Sudbury, Canada. An experimental methodology was developed for intact samples submitted to uniaxial compression for a certain level of temperature, with the monitoring of gas releasing from the rock. A detailed description of the rock-gas interaction apparatus is made. The rock cores were obtained at 2,400 m deep from the mine and results from a sample are presented, as well as theoretical assumptions are discussed. Finally, some conclusions about the investigations on pre-existing fluids in fractured rocks are presented.

**Keywords:** gas transport, granite, laboratory tests, rock-fluid interactions.

## 1. Introduction

High *in situ* stress in a hard rock tunnel enables to trigger various types of failure such as spalling and rockburst during underground excavation at great depth (Diederichs *et al.*, 2004; He *et al.*, 2009). These events may take such proportions with serious consequences in the excavation process and the people involved in the work (Kaiser, 2009; He *et al.*, 2012). Particularly under the disturbance of mining activity, deformation of surrounding rock enables to redistribute the pore pressure in the fluid-rock systems to some extent, which provides conduits or closes fluids pathway, and in turn abnormal pressure can occur in regions where stress concentration appears around the cavities.

In the case of rock-fluid interaction, numerous studies have mainly focused on field observations, physical and theoretical interpretations and numerical modeling (Kidybinski, 1980; Rutqvist *et al.*, 2002; Xu *et al.*, 2006; Li & Hua, 2006; Benson *et al.*, 2008; Molli *et al.*, 2010).

Many efforts have been made to investigate scientific issues concerning gas diffusion, swelling induced by gas sorption particularly in coal formations by laboratory tests (Karacan, 2007; Wang *et al.*, 2007; Karacan *et al.*, 2008; Yi *et al.*, 2009; He *et al.*, 2010; Vandamme *et al.*, 2010). However, it is also needed to investigate gas transport to other types of rocks because of the existence of gases, sometimes toxic, and to investigate the possibility of gasburst.

Therefore, laboratory methods were performed at State Key Laboratory for GeoMechanics and Deep Underground Engineering (SKLGDUE) of Beijing to investigate the permeability of different types of rock samples sub-

jected to a particular stress condition. Although the pore fluid pressure applied to the rock system can relieve the rock matrix from part of the higher *in situ* stress, failure of the rock is probably controlled by effective stress rather than total stress (Fjaer *et al.*, 2008). Nevertheless, the experimental data necessary for the investigation of fluid flow are insufficient, because the pressurized fluid is more likely to suffer the influence of the changing porous structure on the stressed fluids. Fluid flow is strongly controlled by changes of porous structure of rock (Molli *et al.*, 2010), which can act as localized conduits, barriers or combined conduit-barrier (Storti *et al.*, 2003; Micarelli *et al.*, 2006).

It is noted that deep rock core, such as granite and peridotite, commonly show low permeability. Fluid inclusions will be localized in micro-cracks of the rock or within the infilling of microstructures (Lespinasse *et al.*, 2005). By taking advantage of the presence of fluid inclusions, it is possible to treat fluids inclusion as a preexisting gas reservoir stored in the rock.

In this article, instead of injecting selective stressed fluids into the tested rock core, intact granite samples obtained from Creighton mine in Canada were subjected to uniaxial compression at a particular temperature, being monitored the gas released from the rock samples. It is shown from one of a series of laboratory experiments that movement of original gas is similar to those observed during gasburst, and the relevant principle for evolution of pore fluid pressure during rock deformation is also discussed.

Apart from this brief Introduction, Section 2 presents the description of the apparatus developed at SKLGDUE

---

He Manchao, PhD, Professor, State Key Laboratory for GeoMechanics and Deep Underground Engineering of China University of Mining and Technology, 16 Tsinghua East Road, Haidian District, Beijing, China, 100083, e-mail: hemanhao@263.net.

Wang Chunguang, PhD, Professor, State Key Laboratory of Mining Disaster Prevention and Control Co-founded by Shandong Province and the Ministry of Science and Technology, 579 Qianwangang Road, Huangdao District, Qingdao 266590, China, E-mail: cgwang@sdust.edu.cn.

Feng Jili, Professor, PhD, State Key Laboratory for GeoMechanics and Deep Underground Engineering of China University of Mining and Technology, 16 Tsinghua East Road, Haidian District, Beijing, China, 100083, e-mail: fjl@cumt.edu.cn.

L. Ribeiro e Sousa, Professor, PhD, State Key Laboratory for GeoMechanics and Deep Underground Engineering, 16 Tsinghua East Road, Haidian District, Beijing, China, 100083, & University of Porto, Rua Dr. Rodrigo Frias, s/n, 4200-465, Porto, Portugal, e-mail: ribeiro.e.sousa@gmail.com.

Submitted on September 11, 2012; Final Acceptance on January 30, 2014; Discussion open until July 31, 2014.

and the experimental method used. Samples obtained from Creighton mine near Sudbury in Canada, are analysed in detail in Section 3 with a short description of the mine. Section 4 presents the results obtained in one sample with a detailed analysis. Section 5 discusses the assumptions that were made and conclusions are presented in Section 6. Acknowledgments and used references are also indicated.

## 2. Apparatus Description and Test Procedure

A new rock-gas interaction apparatus was specially developed to test original gas existing in rocks subjected to the external loading (Fig. 1).

The test system mainly comprises the following:

- 1) A servo-controlled hydraulic device that consists of an axial load cell and a pressure vessel containing oil to apply axial and confining pressure to the samples.
- 2) A heating unit is used to measure and control the temperatures in the inner chamber of the steel pressure vessel and in the surface of sample.
- 3) A gas monitoring unit for detecting, recording and analyzing the gas composition.

The specific requirements for the experiment were implemented in terms of rock deformation, gas transport and acoustic emission (AE) activity monitoring. A cantilever system was used to measure the relative displacements of four arms with strain gauges in order to accurately obtain circumferential deformation of the specimen. The four arms through ports on sleeve touch the surface of sample.

The ports between the arms and the heat-shrink tube are sealed using silicone gel. The axial deformation of sample is measured by relative displacement of the two platens against specimen by an axial strain jig.

The volumetric strain of sample is obtained from the following expression:

$$\varepsilon_v = \varepsilon_a + 2\varepsilon_r \quad (1)$$

where  $\varepsilon_v$ ,  $\varepsilon_a$  and  $\varepsilon_r$  are, respectively, the volumetric, axial and circumferential strains.

The specimen is firstly assembled outside the vessel and then placed on the pedestal of the vessel. The size of specimen in the experiments is approximately 80 mm length, and 36 mm in diameter, which permits to have enough space for the installation of the AE sensor. The AE system is equipped with two-channel digital monitoring system of full waveform (sampling frequency 20 MHz, resolution 12 bit). Both thermal detector and AE sensor are attached to the surface of specimen connected by two rods with pore fluid outlet, which is followed by the wrap using a heat-shrink tube.

The gas flow pipe is connected to the gas vent at the top platen. In the test the gas outlet through the piston is open to the gas monitoring unit. Before testing, high pressure air is piped into the steel pressure vessel to check the gastight performance of the gas vent in the loading piston.

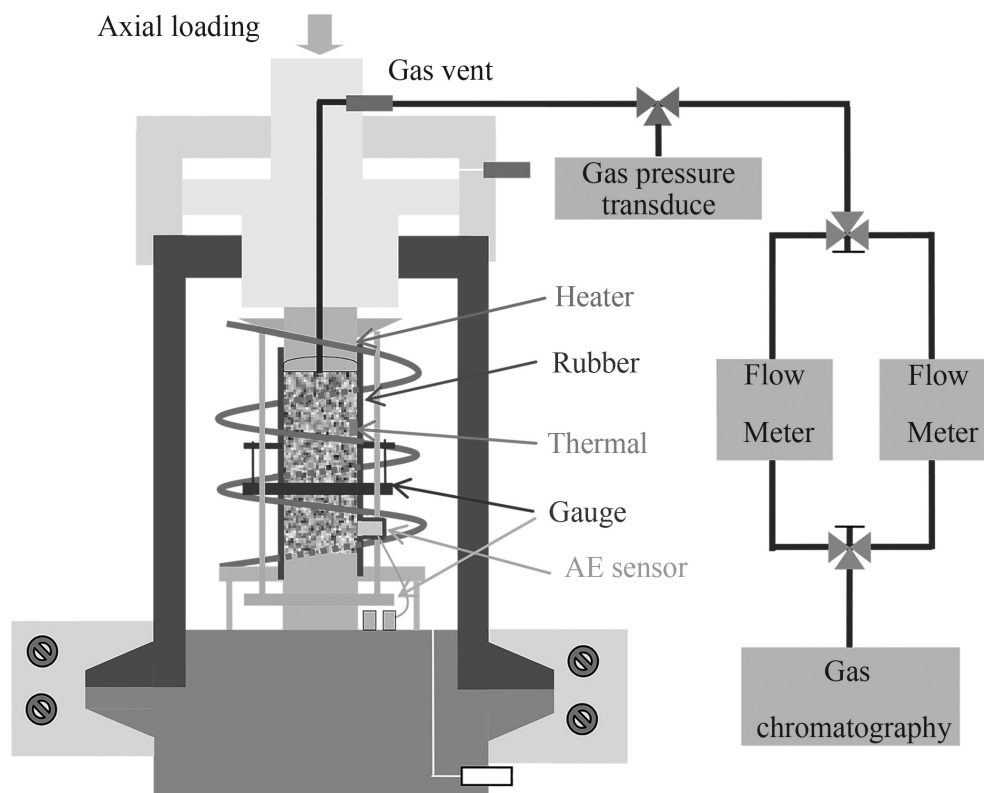


**Figure 1** - Schematic diagram of the internal component of the apparatus.

Hydraulic oil is used as the confined fluid and the heating medium.

The gas monitoring unit was equipped with a high-resolution gas pressure transducer (full scale  $\pm 1,000$  Pa, with a precision of 0.1%) manufactured by HELM Corporation, Germany, and with two different scale gas flowmeters by AALBORG Corporation, USA. The flowmeters can be alternatively selected according to the change of gas flux. Released gas from specimen is piped through the loading piston and enters in three-ways. One way is connected to a pressure transducer; the other ways are used as piping gases through a flowmeter and a Gas Chromatography (GC), successively. To monitor gas emission, pressure and flux data are recorded per second. The gas compositions are determined by a series of connected detectors that are equipped with a Thermal Conductivity Detector (TCD) and a Flame Ionization Detector (FID). The GC is calibrated repeatedly by the Universal Gas Calibration Standard before test. In order to obtain the relatively accurate concentration of gas component in mixed gases, FID is used as a dominant detector for hydrocarbon and carbon dioxide. The gas outlet condition is atmospheric.

The tests are performed by a computer-controlled system and monitored by data-acquisition software to record axial pressure, confining pressure, axial and circumferential strains, gas pressure, and gas flux.

In the experimental method used, the specimen set-up was assembled as described above. For the initial heating process, the temperature was programmed to heat the sample at a rate of  $0.04$  °C/min up to  $47$  °C, representative of the geothermal conditions of approximately  $2$  km beneath the ground surface. After reaching the set temperature, the system was left to thermal equilibrium for  $40$  min. The specimen was then loaded at a constant strain rate of  $12.5 \times 10^{-6}$  s<sup>-1</sup> until failure was seen in the stress-strain curve. Thereafter, the temperature of the fractured sample was linearly increased up to  $63$  °C again, which enabled the sample to release the existing gas. In the last stage, the confining pressure was applied to the deformed sample, which can drive out a large amount of gas.

The tests were all performed under uniaxial compression conditions, which are indeed different from the stress state of field granite masses at Creighton mine, where the *in situ* granite masses are structures under 3D stress and with high pore pressure actions. After excavating, 3D stress equilibrium of the granite masses can be changed into 2D stress one, like for example, for roadways and pillars. During failing process, shear failure of rock masses under 3D compressive conditions could be changed into flaking, spalling and possibly bursting of wall rock. Considering the limit of testing conditions, our investigation was focused on simulating the releasing process of gas from cracking of the granite samples under uniaxial compressive conditions.

The gas outlet is connected to atmosphere; the air in the laboratory was checked using GC to obtain the compo-

nent concentration in atmosphere, so that the concentration of gas from the granite could be modified by subtracting the air concentration from the checked value.

### 3. Granite Samples From Creighton Mine

Creighton mine is more than 100 years old and it is located on southern part of the Sudbury Basin, Canada (Camiro, 1996). Creighton's sulphide orebodies are present in the lower sublayer of the hanging wall norites. The footwall rocks are mainly granite. The ore has been mined from surface to the deepest present level. A cross section of the mine is shown in Fig. 2.

Mine geometry has a critical effect on the observed seismicity. Footwall areas below 6600 and 7000 levels at granite formations experienced high seismicity. At these levels the granite exhibits toxic gases.

The overall geotechnical parameters corresponding to the depth of about  $2,100$  m for the rock mass are indicated in Table 1. In the table, E means the Young's modulus;  $\nu$  the Poisson's ratio;  $\sigma_1$ ,  $\sigma_2$  and  $\sigma_3$  are, respectively, the *in situ* principal stresses,  $\sigma_t$  the tensile strength,  $c$  the cohesion and  $\phi$  the friction angle. The *in situ* state of stress was evaluated using overcoring tests.

The rock cores were obtained from the  $2,400$  m deep coring platform. With the greater production and increasingly deeper excavation, there exists an increasing variety of mining-induced accidents occurring in Creighton mine (Marisset, 2001; Mercer & Bawden, 2005).

The granite samples were cut to the measurement dimensions (diameter  $36$  mm, length  $80$  mm) in laboratory.

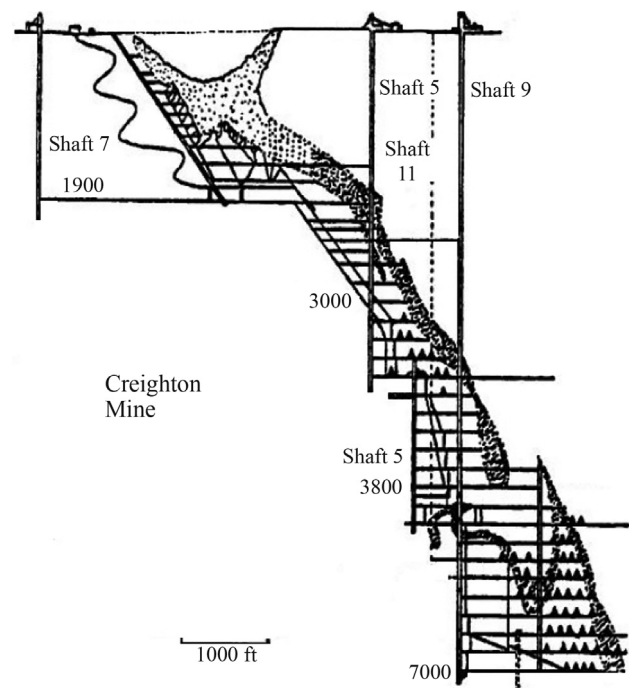


Figure 2 - Cross section of Creighton mine (Camiro, 1996).

**Table 1** - Geomechanical parameters for the rock mass (Camiro, 1996).

Elastic constants		
E (GPa)	$\nu$	-
30	0.25	-
Far field stresses		
$\sigma_1 = 94$ MPa; Dir. $90^\circ$ ; Dip = $0^\circ$		
$\sigma_2 = 60$ MPa; Dir. $0^\circ$ ; Dip = $0^\circ$		
$\sigma_3 = 60$ MPa; Dir. $0^\circ$ ; Dip = $90^\circ$		
Strength parameters		
$\sigma_i$ (MPa)	c (MPa)	$\phi$ ( $^\circ$ )
0	22	35

The mineralogical composition of the granite is reported in Table 2.

The samples were bored from about the depth of 2,347 m at Creighton mine. After taking out from the drill pipe, the cores were immediately put into a bag that was sealed by wax before sampling. It is assumed that the gases in the granite pores are not lost during coring, transporting, and sampling because granite is compact and its porosity is generally low.

Several modelling approaches were developed to examine occurred failure mechanisms observed at deep levels. A 3D view of the mine of the examined areas is shown in Fig. 3.

As said before, three tests were carried out. It was found from the results of all other tests that they had the same characteristics of releasing gases, basically connected with the cracking of the cores. Thus in the paper only the results of one test are presented.

#### 4. Results

The tests on the Creighton mine granite samples were performed under temperatures from 47 to 63 °C and strain rates at  $12.5 \times 10^{-6} \text{ s}^{-1}$ . In the paper, results from sample No. 123-127-660-2 are discussed in detail.

Figure 4 presents some results obtained. In a) the loading path and temperature are indicated; in b) the gas pressure at outlet; in c) the cumulative volume of releasing gas; in d) the releasing gas flux; and in e) the gas concentra-

**Table 2** - Mineral content of the granite sample.

Mineral	Percentage (%)
Plagioclase	78.70
Calcite	8.40
Dolomite	5.80
Clay	7.10
Moisture content	0.05

tion with time under loading at the temperature varying to 63 °C.

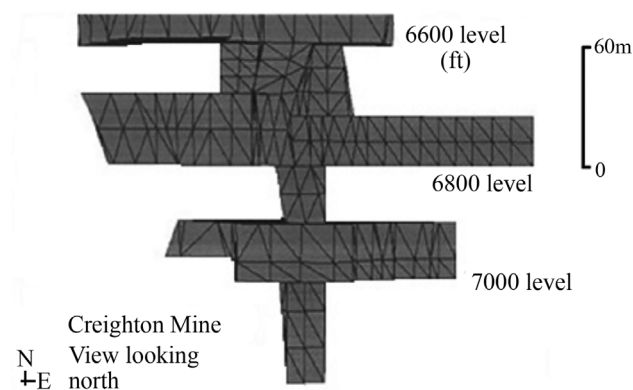
During the initial heating without the presence of other external loading, a slight increase in gas pressure was monitored due to the gas heat-expansion. But, as a result of the low porosity of intact granite, it can be assumed that some thermal expansion of the gas could increase pore pressure in the preexisting closed pore.

After the isothermal condition (47 °C) was achieved, the granite sample was subjected to uniaxial compression. Taking into account the presence of fissures generated in the igneous rock (the aperture is rather small), it is therefore accepted that stress concentration at the two ends during the deformation of rock matrix, leads to the change of deformation of the fissures.

More results of the test are presented in Figs. 5 to 8. Figure 5 illustrates the change of releasing gas pressure, flux and number hits of AE; Fig. 6 indicates frequency spectrum of AE activities for points A and B that are shown at Fig. 5; Figs. 7 and 8 are referred to the change in volumetric strain and of AE hits, respectively. In Fig. 7a, the zero strain point means that the evolution of volumetric strain is first shrinking and then dilatant, particularly the initial state of volumetric strain can be restored when dilatant strain is zero. In Fig. 7b, normalized pore pressure in unipore element is defined by  $P_n = (P - P_{\min}) / (P_{\max} - P_{\min})$ , where  $P_{\min}$  is the lower limit of pore pressure,  $P_{\max}$  indicates the upper limit of pore pressure, and  $P$  represents the current pore pressure.

According to the figures, the changes of volume of the specimen can evolve into the following two phases:

- 1) Closure of pre-existing pore and cracks and compression-induced volumetric shrinkage, characterized by the gradual increase in cumulative hit number of acoustic emission.
- 2) With the propagation and coalescence of crack, the volume of sample is changing from the compression to dilatancy, where the AE activity is dramatically increased in agreement with the previous conclusion on AE activity in rock salt (Alkana *et al.*, 2007).

**Figure 3** - View of the Creighton mine below 6600 level (Camiro, 1996).

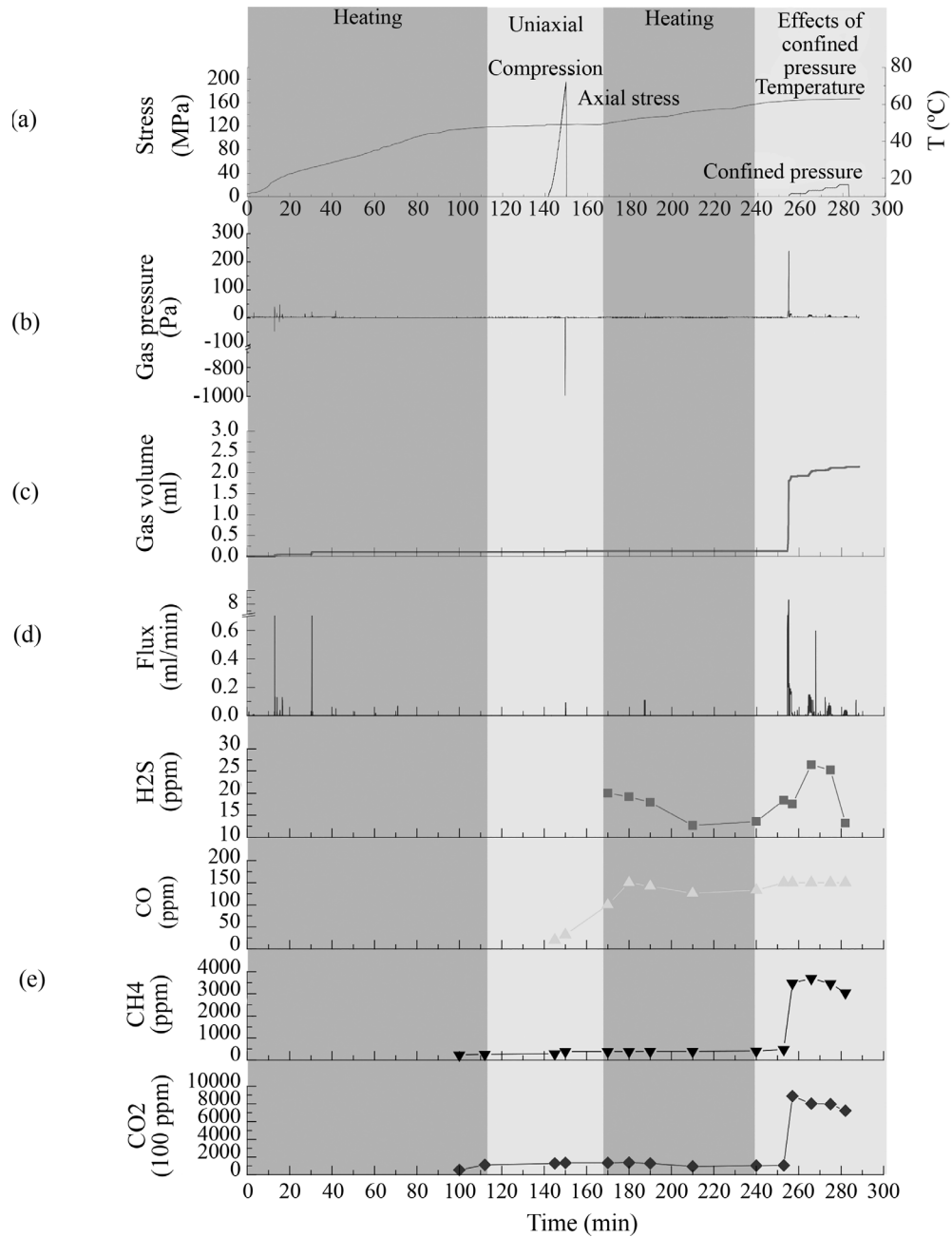


Figure 4 - Test results for a granite sample from Creighton mine.

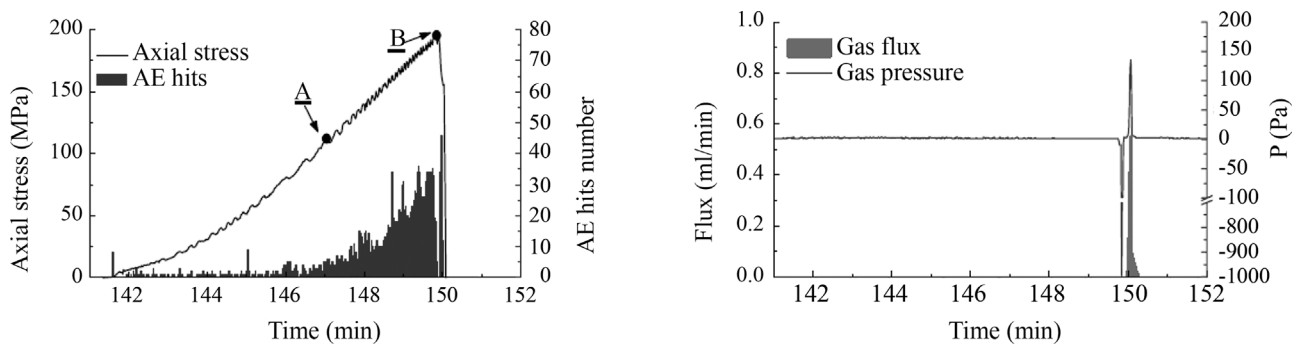
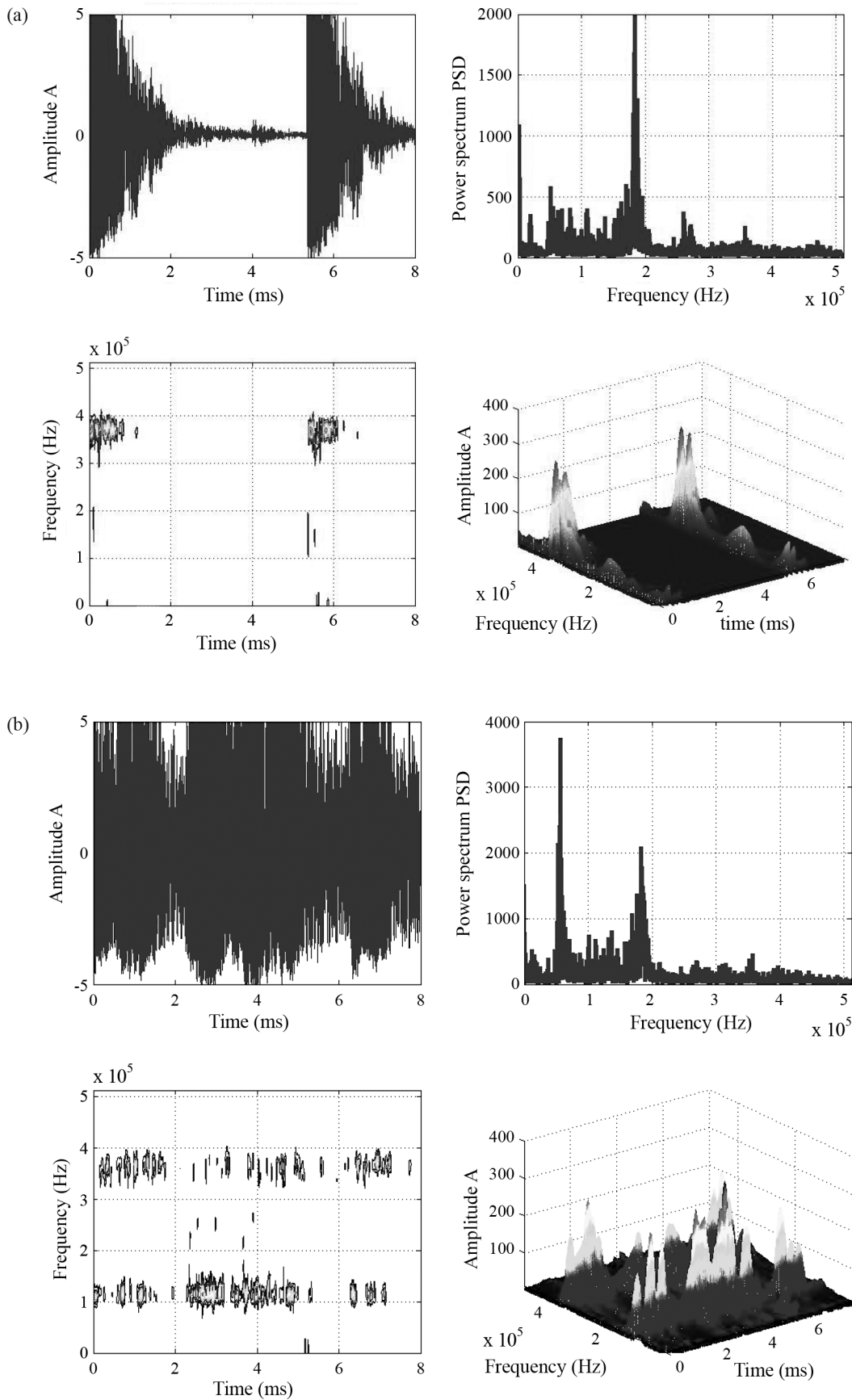


Figure 5 - Change of releasing gas pressure, flux and number hits of AE under uniaxial compression.



**Figure 6** - Frequency spectrum of AE activities at point A and point B during the uniaxial compression.

The crack generated in the stressed rock sample is featured by tensional failure because of the no confinement of the lateral surface of cylindrical specimen.

In order to interpret the development of crack during the loading, a short-time window Fourier transform was used from Matlab software to filter the AE data obtained, which is shown in form of frequency-time. In this paper, the two spectrograms were used to respectively exemplify the characteristics for AE activities generated in the elastic deformation and near-failure stage (Fig. 6).

During the elastic deformation of the sample, AE activity, corresponding to point A, appeared on the high-frequency region of 350-400 kHz. According to the time-frequency images, a series of AE activities intermittently occurred, which indicated the occurrence of brittle fracture. It is generally accepted that high-frequency AE is featured by the abrupt cracking while the propagation of cracks can also lead to the low-frequency AE activities. With increasing loading of axial stress, the gradual increase in amount of AE activity resulted in the coalescence between microcracks where the localized dilatancy was occurring and began to drive the pre-existing gas within rock matrix. As a result of the increasing axial stress, the frequency ranges of AE activities are characterized by 140 and 380 kHz, respectively. Its duration was becoming longer, which indicated that considerable cracks were developing at the less tension position of sample. At the moment of failure of specimen the releasing gas pressure firstly plummeted to 1,000 Pa, and then gas pressure returned to the atmosphere after three seconds, which was followed by shortly increase in gas flux

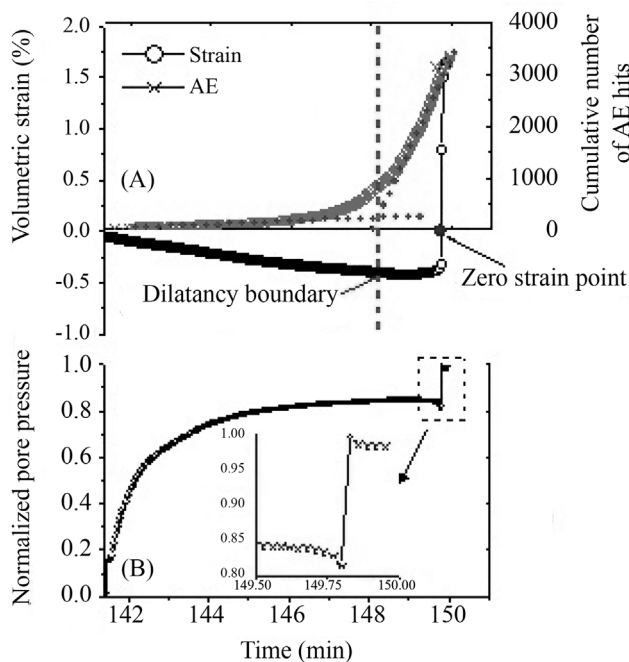


**Figure 7** - (a) Change in volumetric strain from the cumulative number of AE hit number; b) normalized pore pressure in unipore element.

up to 0.09 mL/min indicating a small amount of gas emission.

Thereafter, the heating process was performed again, which readily drove the original gas out due to the permeability improvement of post-test sample. Apart from the CO, CO<sub>2</sub> and CH<sub>4</sub>, it is also clear that sulfured hydrogen (H<sub>2</sub>S) started to release from the fractured granite rock, and its concentration tended to gradually fall down with increasing temperature. According to a series of SEM images (Fig. 9) of post-test sample, there are a number of intergranular and intragranular microcracks generated in rock matrix, which is more likely to split the fluids inclusion and in turn releases fluids included. The results for gas components are in agreement with the previous recorded data (Molnár *et al.*, 1999). Therefore it is postulated that gaseous mixture obtained, including CO, CO<sub>2</sub>, CH<sub>4</sub>, and H<sub>2</sub>S, probably come from fluid-inclusion trapped in fractured surfaces of sample.

Figure 8 shows that most of the gas in the rock was gradually exhausted by an increasing confining pressure, which is programmed to apply on the fractured sample at 63 °C. The concentration of gaseous components increased from 17.5 ppm to 26.4 ppm for H<sub>2</sub>S, from 410 to 480 ppm for CH<sub>4</sub>, and from 95110 to 103460 ppm for CO<sub>2</sub>, respectively. This period is referred to as the closure of crack, which is characterized by the occurrence of some AE activities, and in turn compressed the gas distributed on the tortuous regions. When both aperture and crack closed to some extent, gas exhaust was accordingly ended.

## 5. Discussion About the Results

The presence of the fluids inclusion can provide numerous gas reservoirs, particularly for CO<sub>2</sub> (Elsworth *et al.*, 2011; He *et al.*, 2011; Qu *et al.*, 2011). Reservoirs with igneous rock can also be considered (Sousa, 2011).

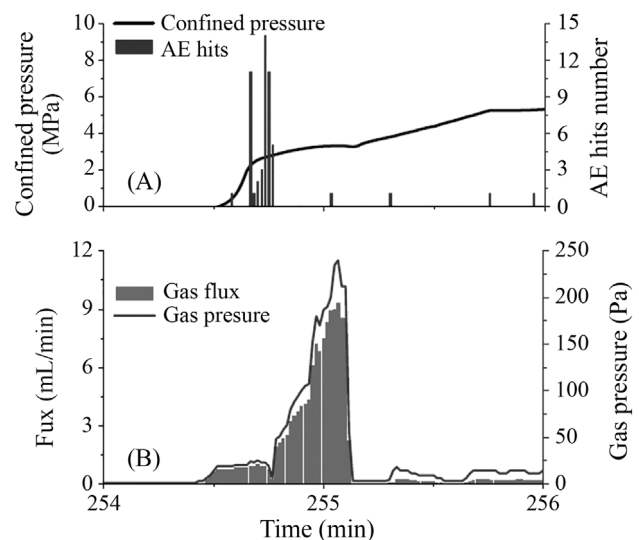


**Figure 8** - (a) Changing of the AE hits and the confining pressure; (b) gas pressure and flux.

Provided that the stress redistribution within the surrounding rock is as a function of the mining activities, fractures at rock matrix are generally initiated by stress concentrations at the tips or at the ends of fluids inclusion. The

fluids included may release and ultimately contribute to macroscopic failure of rock due to the coalescence of the cracks.

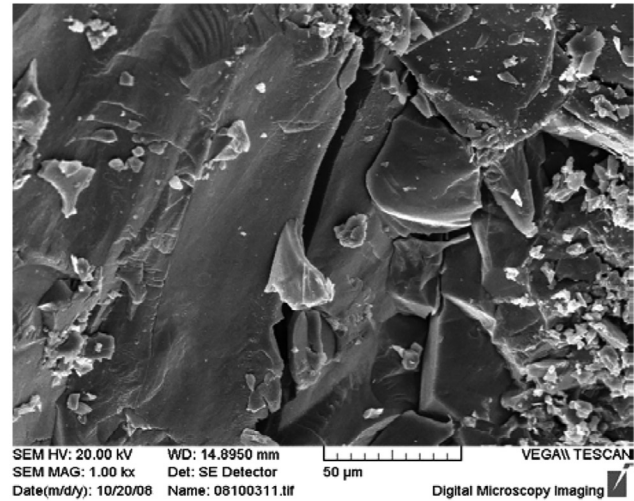
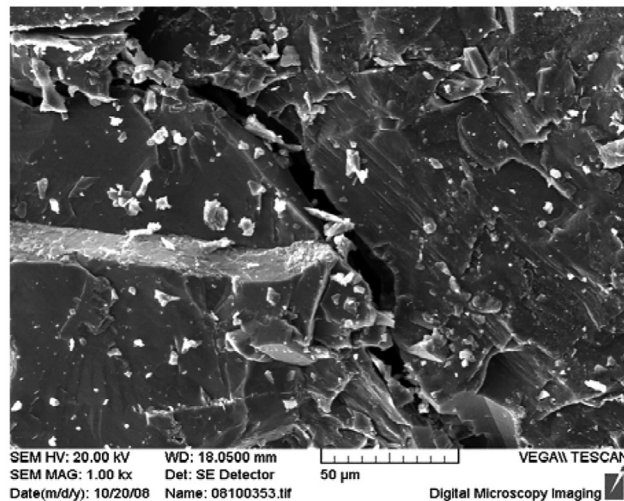
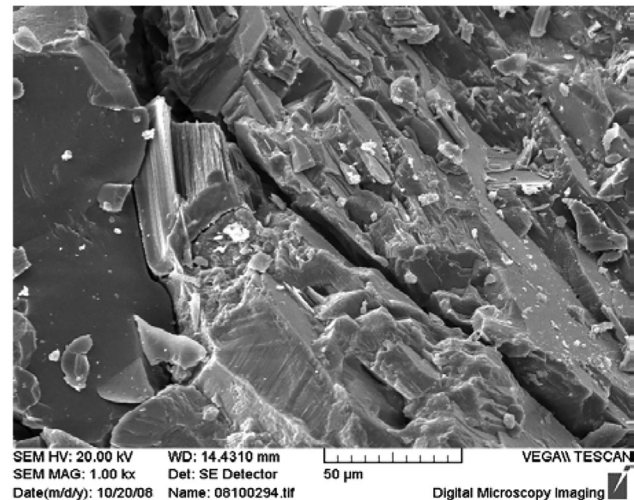
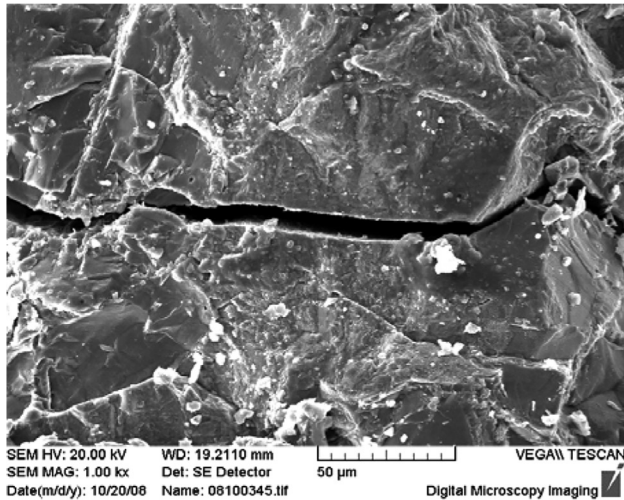
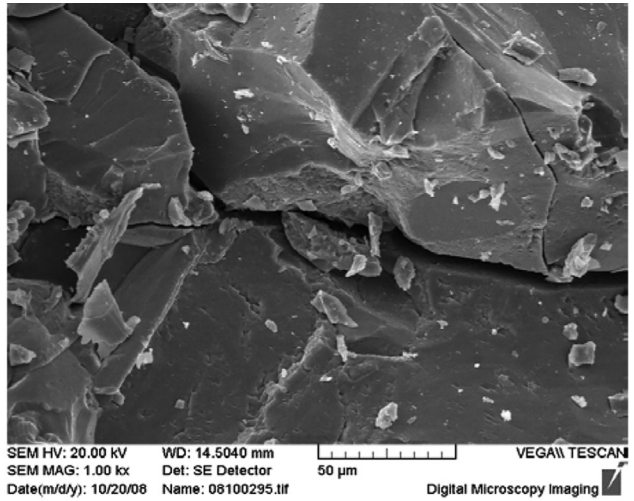
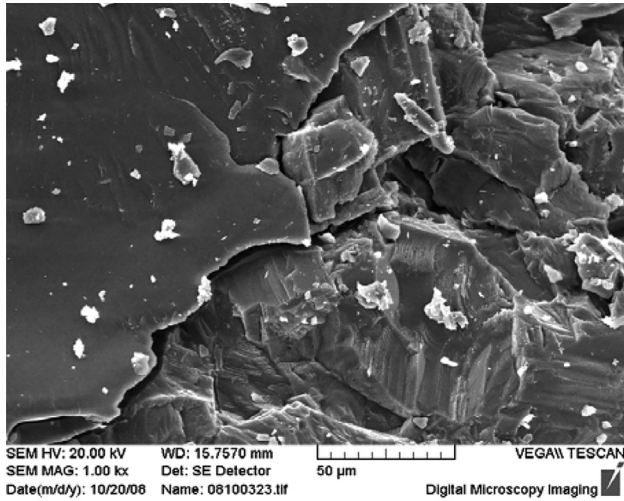


**Figure 9** - Photos of fractured sample and SEM images of rock fragments on different position of post-test sample.

Fluids transport in rock mass strongly depends on pressure gradient, which is often ascribed to the changes of the structure of the stressed rock (Vargas *et al.*, 2011).

During the rock deformation stage, brittle processes caused several main-fractures along the direction of loading from meso-scale CT images, and further generated a number of intergranular and intragranular micro-cracks from micro-scale SEM (Scanning Electronic Machine) images (Figs. 9 and 10). It can be therefore postulated that the microstructure of granite might be simply considered as a particular complex combination of crystal particle and pore, thereby applying *the approximate dilute density method* to interpret the pore pressure of the unipore subjected to the even stress field (Chen *et al.*, 2009). Two assumptions are employed:

- 1) Low porosity of granite is proposed by considering the specimen consisting of equal elements, namely each element contains the one pore.
- 2) The interaction of fissures could be neglected, and the boundary condition of each element is similar to that of specimen.

It is assumed that the volume of solid particle of granite,  $V_s$  remains constant, then that is  $V_s = (1 - n) V = \text{constant}$ , where  $n$  is porosity of granite.

Taking differentiation of  $V_s$  to time  $t$

$$\frac{\partial V_s}{\partial t} = -V \frac{\partial n}{\partial t} + (1-n) \frac{\partial V}{\partial t} = 0 \quad (2)$$

Eq. 2 can be rewritten in the form:

$$\frac{\partial n}{\partial t} = \frac{(1-n)}{V} \frac{\partial V}{\partial t} \quad (3)$$

If it is assumed that the gas pressure in closed pore is  $P$ , then gas statue equation yields

$$\rho = \frac{P}{RT} \quad (4)$$

$\rho$  is gas density,  $T$  temperature,  $R$  represents ideal gas constant. Eq. (4) can be given as

$$\frac{\partial \rho}{\partial t} = \frac{1}{RT} \frac{\partial P}{\partial t} \quad (5)$$

The conservation equation of gas mass is given by (Zhao, 1994):

$$\text{div}(\rho \cdot q) = -n \left( \frac{\partial \rho}{\partial t} + \rho \frac{\partial n}{\partial t} \right) \quad (6)$$

It is assumed that there is no mass transfer between elements due to low porosity of granite at shortly loading process. We can therefore consider divergence of the element is null at the deformation stage, then with the help of Eqs. 4 and 5, we can rewrite Eq. 6 in the form:

$$\frac{n}{RT} \frac{\partial P}{\partial t} + \frac{P}{RT} \frac{(1-n)}{V} \frac{\partial V}{\partial t} = 0 \quad (7)$$

Then

$$\frac{\partial P}{\partial t} + P \frac{V_s}{V(V-V_s)} \frac{\partial V}{\partial t} = 0 \quad (8)$$

It is postulated that the variation of void volume is approximately consistent with volumetric strain obtained from Eq. 1:

$$\frac{V_p}{V} \approx \varepsilon_v = \varepsilon_a + 2\varepsilon_r \quad (9)$$

The normalized pore pressure curve in Fig. 7 suggests that the compressed sample at elastic deformation may initially increase the pore pressure of closed pore without fluids mass transport, and then level out a certain value. After the volumetric strain overtook the dilatancy boundary (Alkana *et al.*, 2007), the volume of specimen underwent swelling. It is noted that the normalized pore pressure experienced a reverse process, just as breathing circulation. In other words, it firstly dropped, and then steep increased at the zero strain point, namely the volume of the sample tested returned to the initial volume without effects of stress.

It is clear from the CT images of post-test sample in Fig. 10 that the extensible cracks fully developed parallel to the loading direction. These observations imply that the dominant fluid flow is initially driven into the major dilatation zones by the fluid pore pressure gradient between new tortuous damaged zones and preexisting cracks. Subsequently, the rapid flow of the pore fluid fill the broken and damaged zones, so that the pore pressure distribution becomes in equilibrium within and around the gas reservoir, expelling the redundant gas. In contrast with the permeabil-

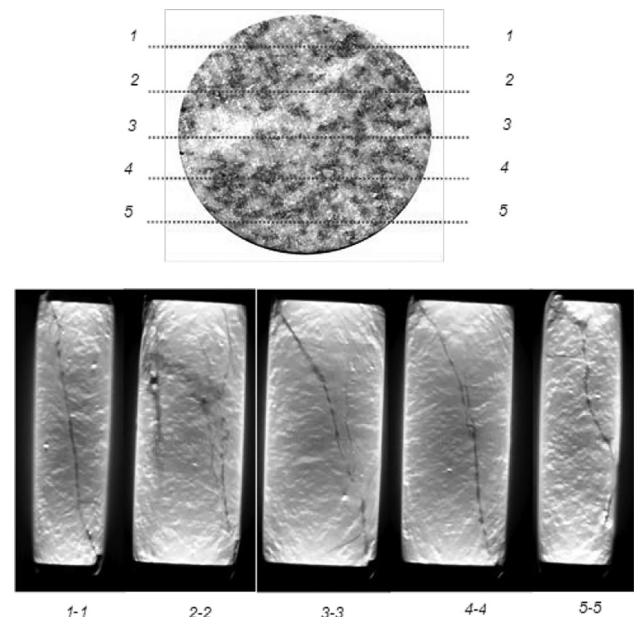


**Figure 10** - CT images of the deformed specimen (red dot line represents the position of scanning slice of post-test).

ity enhanced by tensile cracks at uniaxial compression, the increasing confining pressure obviously reduced the aperture of fractures and momentarily expelled large amounts of gas.

The sequential seismic activities and gasburst are closely related to the fault movement.

The experiment performed by the same procedure with various confining pressure are given in Fig. 8. The gas emission is characterized by the abrupt release of high concentration and large volume of mixed gas as the increasing confining pressure. During the closure of aperture of crack network, the gas flux decay rapidly with loading-induced crack closure. Brittle processes, from millimeter-scale microcracking to kilometer-scale earthquake rupture, change differentially the permeability of fluid filled rock strata, which frequently alters the direction of preferred fluid movement driven by the fluid pore pressure variation. In most of the previous publications (Etiopie and Klusman, 2002; Yang *et al.*, 2003; Weinlich *et al.*, 2006; Li *et al.*, 2007; Shen *et al.*, 2008), at the later stage of the mining induced failure of tunnel, the local cracks within surrounding rocks began to coalesce and develop large fracture or failure structure planes, where stresses and displacements change significantly.

It seems reasonable to suggest, from these field observation together with our test results, that the transient change of porous structures under stressed conditions definitely contribute to the unbalanced distribution of pore pressure in gas reservoirs, which in turn controls the transport of gases within the voids and fractures, as also reported field observation of gas concentration drop.

## 6. Conclusions

An investigation about preexisting fluid flow in granite samples from Creighton mine in Canada in a closed system under controlled physical conditions was performed. The samples under 47 °C were subjected to uniaxial compression, as well as with monitoring the AE activities. Results obtained indicate that the released gas not only probably comes from the fluid inclusion trapped in granite matrix, but also depends on the volumetric change of stressed rock.

The pre-existing gas can be driven out from the failure of stressed granite sample in laboratory. The results show that the clustered AE activities that increasingly grow in stressed rock indicate the coalescence between cracks, and also provide the fluids with ample reservoirs. Such instant increase in gas reservoir may plummet down the gas pressure, correspondingly resulting in the gas pressure gradient among different gas reservoirs and subsequently equilibrating the distribution of pore pressure. It is believed from the relation between the deformation of sample and gas pressure in our test results that the instantaneous variation of pore structure can contribute to the suck-emission of fluids within the deforming rock.

The approximate dilute density method as a qualitative method describes the change of pore pressure in closed micro-pore, which is based on simple analysis of the relationship between pore pressure and volumetric strain of the entire sample. The change in pore pressure of matrix is determined by the volumetric strain of rock bulk. When the volumetric strain is changing from the compression to dilatancy, namely over the zero dilatancy boundary, pore gas pressure is experiencing firstly drop and then rise at shortly time. We can therefore consider the zero dilatancy boundaries as the threshold of pore pressure in closed pore.

A vast of pre-existing gas emission is controlled by the closure of stratified structure of rock mass in terms of amounts of gas releasing from the specimen. Among the gaseous mixture, CO<sub>2</sub> is the largest component, while H<sub>2</sub>S accounts for the least one. Although the experimental results obtained can be interpreted as gas transport within the stressed rock, it cannot be quantitatively analogized by the data obtained from *in situ* observation. Further study should be focused on the coupling effect of high-stressed fluids and stressed fluids taking the complication of the failure of deep rock stratum influenced by geophysics and geochemistry process. Also further study should include the scale effect in the investigations on gas flow, like for large field gas operations and for the occurrence of rockbursts, taking into consideration the existence of faults and other discontinuities

## Acknowledgments

This work was supported by the National Basic Research Program of China (2006CB202200) and National Science Foundation of China (Nos. 41172116, 41202194). We are grateful to Prof. P.K. Kaiser and Dr. M. Cai for their helps in the specimen supply.

## References

- Alkana, H.; Cinarb, Y. & Pusch, G. (2007) Rock salt dilatancy boundary from combined acoustic emission and triaxial compression tests. *International Journal of Rock Mechanics & Mining Sciences* v. 44:1, p. 108-119.
- Benson, P.M.; Vinciguerra, S. & Meredith, P.G. (2008) Laboratory Simulation of Volcano Seismicity. *Science* v. 322, p. 249-252.
- Camiro (1996) Rockburst research handbook. CAMIRO Mining Division, Canadian Rockburst Research Programme, 1990-1995. Sudbury, 6 volumes, p. 977.
- Chen Y.; Wong T.F. & Liu E.R. (2009) *Rock Physics*. University of Science and Technology of China Press, Anhui, p. 86.
- Diederichs, M.S.; Kaiser, P.K. & Eberhardt, E. (2004) Damage initiation and propagation in hard rock during tunneling and the influence of near-face stress rotation. *International Journal of Rock Mechanics & Mining Sciences* v. 41:5, p. 785-812.

- Elsworth, D.; Wang S.; Izadi, G. Kumar H.; Mathews J.; Liu J.S. & Lee D.S. (2011) Complex process couplings in systems pushed far-from-equilibrium: Applications to CO<sub>2</sub> sequestration in carboniferous formations. In: CO<sub>2</sub> Storage in Carboniferous Formations and Abandoned Coal Mines, He, Sousa, Elsworth & Vargas, (eds) Taylors & Francis, London, p. 55-67.
- Etiopie, G. & Klusman, R.W. (2002) Geologic emissions of methane to the atmosphere. *Chemosphere* v. 9, p. 777-789.
- Fjaer, E.; Holt, R.M.; Horsrud, P.; Raaen A.M. & Risnes R. (2008) *Petroleum Related Rock Mechanics*. 2<sup>nd</sup> ed. Elsevier, London, p. 114.
- He M.C.; Wang C.G.; Feng J.L.; Li D.J. & Zhang G.Y. (2010) Experimental investigations on gas desorption and transport in stressed coal under isothermal conditions. *International Journal of Coal Geology*. v. 83, p. 377-386.
- He M.C.; Miao J.L. & Feng, J.L. (2009) Rockburst process of limestone and its acoustic emission characteristics under true-triaxial unloading condition. *International Journal of Rock Mechanics and Mining Sciences*, v. 47:2, p. 286-298.
- He M.C.; Sousa, L.R.; Elsworth, D. & Vargas, E. (2011) CO<sub>2</sub> Storage in Carboniferous Formations and Abandoned Coal Mines. Taylors & Francis, London, p. 201.
- He M.C.; Sousa, L.R. & Farmarzi, L. (2012) Rockburst process evaluation using experimental and artificial intelligence techniques. 1<sup>st</sup> Iranian Congress of Mining, Yazd, p. 24.
- Kaiser, P. (2009) Failure mechanisms and rock support aspects. Proc. Int. Consultation Report on the Key Technology of Safe and Rapid Construction for Jinping II Hydropower Station High Overburden and Long Tunnels, Jinping II, p. 62-71.
- Karacan, C.O. (2007) Swelling-induced volumetric strains internal to a stressed coal associated with CO<sub>2</sub> sorption. *Int. Journal of Coal Geology*, v. 72, p. 209-220.
- Karacan, C.O.; Ulery, J.P. & Goodman, G.V. (2008) A numerical evaluation on the effects of impermeable faults on degasification efficiency and methane emissions during underground coal mining. *Int. Journal of Coal Geology*, v. 75, p. 195-203.
- Kidybinski, A. (1980) Significance of in situ strength measurements for prediction of outburst hazard in coal mines of Lower Silesia. Symposium on the occurrence, prediction and control of outbursts in coal mines. Aust Inst Min Metall, Melbourne, p. 193-201.
- Lespinasse, M.; Desindes, L.; Fratzak, P. & Petrov, V. (2005) Microfissural mapping of natural cracks in rocks: Implications for fluid transfers quantification in the crust. *Chemical Geology*, v. 223, p. 170-178.
- Li T.; Cai M.F. & Cai M. (2007) Earthquake-induced unusual gas emission coalmines - A km-scale in-situ experimental investigation at Laohutai mine. *International Journal of Coal Geology* v. 71, p. 209-224.
- Li X.Z. & Hua A.Z. (2006) Prediction and prevention of sandstone-gas outbursts in coal mines. *International Journal of Rock Mechanics & Mining Sciences*, v. 43:1, p. 2-18.
- Marisett, S.D. (2001) Assessing pillar design at INCO'S Creighton mine using the local energy release density method. Queen's University, Canada, December.
- Mercer, R.A. & Bawden, W.F. (2005) A statistical approach for the integrated analysis of mine-induced seismicity and numerical stress estimates, a case study-Part I: developing the relations. *International Journal of Rock Mechanics and Mining Sciences*, v. 42:1, p. 47-72.
- Micarelli, L.; Benedicto, A. & Wibberley, C.A.J. (2006) Structural evolution and permeability of normal fault zones in highly porous carbonate rocks. *Journal of Structural Geology*, v. 28, p. 1214-1227.
- Molli, G.; Cortecci, G. & Vaselli, L. (2010) Fault zone structure and fluid-rock interaction of a high angle normal fault in Carrara marble (NW Tuscany, Italy). *Journal of Structural Geology*, v. 32, p. 1334-1348.
- Molnár, F.; Watkinson, D.H. & Everest, J.O. (1999) Fluid-inclusion characteristics of hydrothermal Cu-Ni-PGE veins in granitic and metavolcanic rocks at the contact of the Little Stobie deposit, Sudbury, Canada. *Chemical Geology*, v. 154, p. 279-301.
- Qu H.; Liu J.S.; Chen Z.; Pan Z. & Connell, L. (2011) A fully coupled gas flow, coal deformation, and thermal transport model for the injection of carbon dioxide into coal seams. In: CO<sub>2</sub> Storage in Carboniferous Formations and Abandoned Coal Mines, Ed. He, Sousa, Elsworth & Vargas (eds) Taylors & Francis, London, p. 69-93.
- Rutqvist, J.; Wu Y.S.; Tsang C.F. & Bodvarsson, G. (2002) A modeling approach for analysis of coupled multi-phase fluid flow, heat transfer, and deformation in fractured porous rock. *International Journal of Rock Mechanics & Mining Sciences*, v. 39:4, p. 429-442.
- Shen B.; King, A. & Guo H. (2008) Displacement, stress and seismicity in roadway roofs during mining-induced failure. *International Journal of Rock Mechanics & Mining Sciences*, v. 45:5, p. 672-688.
- Sousa, L.R. (2011) Present day conditions in the world of Carbon Capture and Storage (CCS) projects. In: CO<sub>2</sub> Storage in Carboniferous Formations and Abandoned Coal Mines, Ed. He, Sousa, Elsworth & Vargas (eds) Taylors & Francis, London, p. 1-23.
- Storti, F.; Billi, A. & Salvini, F. (2003) Particle size distribution in natural carbonate fault rocks: insights for non-self similar cataclasis. *Earth and Planetary Science Letters*, v. 206, p. 173-186.
- Vandamme, M.; Brochaard, L. & Coussy, O. (2010) Adsorption-induced deformation in porous media and ap-

- plication to CO<sub>2</sub>-injected coal beds. 3rd Int. Conference on Porous Media and its Applications in Science, Engineering and Industry, Ed. K. Vafai, American Institute of Physics, p. 319-324.
- Vargas, E.; Velloso, R.; Ribeiro, W.; Muller, A. & Vaz, L. (2011) Considerations on the numerical modelling of injection processes of CO<sub>2</sub> in geological formations with emphasis on carboniferous formations and abandoned coal mines. In: CO<sub>2</sub> Storage in Carboniferous Formations and Abandoned Coal Mines, Ed. He, Sousa, Elsworth & Vargas (eds) Taylors & Francis, London, p. 107-123.
- Wang G.X.; Wang Z.T.; Rudolph, V.; Massarotto P. & Finley R.J. (2007) An analytical model of the mechanical properties of bulk coal under confined stress. *Fuel*, v. 86, p. 1873-1884.
- Weinlich, F.H.; Faber, E.; Bouková, A.; Horalek J.; Teschner M. & Poggenburg J. (2006) Jürgen Poggenburg Seismically induced variations in Mariánské Lázně fault composition in the NW Bohemian swarm quake region, Czech Republic - A continuous gas monitoring. *Tectonophysics*, v. 421, p. 89-110.
- Xu T.; Tang C.A. & Yang T.H. (2006) Numerical investigation of coal and gas outbursts in underground collieries. *International Journal of Rock Mechanics & Mining Sciences*, v. 43:6, p. 905-919.
- Yang X.X.; Song D.L. & Chen Z. (2003) Forecast for disaster and gas explosion in Jixi colliery. *Northwestern Seismological Journal*, v. 5:1, p. 93-93.
- Yi J.; Akkutlu, I.Y.; Karacan, C.O. & Clarkson, C.R. (2009) Gas sorption and transport in coals: A poroelastic medium approach. *Int. Journal of Coal Geology*, v. 77, p. 137-144.
- Zhao Y.S. (1994) *Rock Fluid Mechanics in Mine*. Coal Industrial Press, Beijing, p. 84.

### List of Symbols and Acronyms

- $\varepsilon_v$ : volumetric strains  
 $\varepsilon_a$ : axial strains  
 $\varepsilon_r$ : circumferential strains  
 $\varphi$ : friction angle  
 $\nu$ : Poisson ration  
 $\rho$ : gas density  
 $\sigma_1, \sigma_2, \sigma_3$ : maximum, intermediate and minimum principal stresses  
 $\sigma_t$ : tensile strength of the rock mass  
 $c$ : cohesion  
 $E$ : deformability modulus of rock mass  
 $n$ : porosity  
 $P$ : current pore pressure  
 $P_{max}$ : upper limit pore pressure  
 $P_{min}$ : lower limit pore pressure  
 $P_n$ : normalized pore pressure  
 $R$ : ideal gas constant  
 $T$ : Temperature  
 $V_s$ : volume of solid particle

# Field Survey of Compressibility of Municipal Solid Waste

A.G.P. van Elk, L.M.S. Mañas, M.E.G. Boscov

**Abstract.** This paper presents a study on the compressibility of municipal solid waste (MSW) by means of a field survey in Valdemingomez Landfill in Madrid, Spain. Organic matter content was 59%, there was no waste segregation and field compaction, nor internal drainage systems for gas and leachate. Solid waste management changed significantly since then in Madrid, but former characteristics of this landfill are similar to those of present inadequate MSW disposal sites in more than 60% Brazilian municipalities. Initially a geotechnical exploration of the landfill was carried out by mechanically drilled boreholes with Standard Penetration Tests, determination of in-situ density and moisture content, and geophysical methods. Subsequently, vertical and horizontal displacements caused by a surcharge load applied by a trial soil embankment were measured, as well as settlements due to biodegradation of the organic materials, for 19 months. Displacements were monitored by topographical references, inclinometer, continuous lines of settlement, and a sliding micrometer. Young's modulus was estimated 1900 kN/m<sup>2</sup>. Shear modulus increased from 7 to 31 MPa with depth according to results of spectral analysis of surface waves. The auscultation campaign indicated that primary settlements occurred during approximately 100 days and that accumulated secondary settlements amounted to 0.600 m, representing 55% of the total settlements.

**Keywords:** landfill, compressibility, solid waste, settlements, field test.

## 1. Introduction

Land disposal is the usual destination for municipal solid waste (MSW) in developing countries. This disposal alternative tends to decrease in importance with time due to the lack of available areas near large urban centres and to the development of new technologies. Nevertheless, sanitary landfills are still considered safe and relatively low cost, and have reached heights of more than 100 metres, indicating the need to study compressibility of the waste mass as well as of the foundation in order to guarantee slope stability.

Study of MSW settlements is important to predict the increase of landfill storage capacity along time. Landfill compression is also relevant for post-closure projects such as parks, access ways, streets, secondary roads, airports, streets and new urbanizations, as geotechnical problems related to long term settlements are likely to occur in urban development over recovered sanitary landfills.

Design of waste landfills is based on geotechnical concepts and methods, although mechanical behaviour of MSW is remarkably different from soil, mainly as a consequence of biological decomposition of the putrescible organic matter, which transforms part of the solid constituents into gases and leachate. Furthermore, MSW is a complex material with components of different nature, its characteristics and properties change with time, and its mechanical behaviour is influenced by the topography of the disposal area, the compaction method and the landfill operation.

This paper presents a study of MSW compression based on in situ monitoring of a disposal area for fresh waste within one of the largest sanitary landfills in Europe, the Valdemingómez landfill in Madrid, during a period of approximately two years.

Spain changed the paradigm from the disposal of MSW in dumps and controlled landfills (MSW landfills with a few elements and procedures for sanitary protection such as daily soil cover and waste compaction, however insufficient for proper environmental protection) towards sanitary landfills (MSW landfills with complete sanitary and environmental protection) in the time span of 10 years.

This development has also started in Brazil, initially in large cities, where sanitary landfills are already centers of waste treatment with biogas collection for energy generation. Deactivation and recovery of inadequate disposal in small towns and medium-sized cities are being stimulated by the National Politics for Solid Waste, a federal law sanctioned in 2010. There is presently a great demand for a better understanding of the geo-mechanical behavior of controlled landfills and dump sites with the view to recovering and reinserting these areas in the urban context.

Field data presented in this paper aims to meet this demand, for the Valdemingómez landfill has great similarities with other controlled landfills in Latin America: high organic matter and water contents; presence of voluminous waste; lack of material segregation, field compaction, internal drainage systems for gas and leachate; all important factors for the compression behaviour of sanitary landfills.

---

Ana Ghislane Pereira van Elk, PhD, Visiting Professor, Universidade Estadual do Rio de Janeiro, Rio de Janeiro, RJ, Brazil. e-mail: ghislane@centroin.com.br.  
Luis Miguel Sopena Mañas, PhD, Full Professor, Universidad Politécnica de Madrid, Madrid, Spain. e-mail: sopena@upm.es.  
Maria Eugenia Gimenez Boscov, PhD, Full Professor, Universidade de São Paulo, São Paulo, SP, Brazil. e-mail: meboscov@usp.br.  
Submitted on June 5, 2013; Final Acceptance on November 22, 2013; Discussion open until July 31, 2014.

## 2. The Valdemingómez Landfill and Characteristics of MSW from the Community of Madrid

The Valdemingómez controlled landfill occupies an area of 110 ha distant 20 km from Madrid's city center (Spain). This landfill served Madrid and two small neighbor municipalities from 1978 to 2000, with an average daily production of 3.000 tons of waste. Presently there is biogas extraction and energy production, generating 75% of the annual electricity necessary for Madrid's street lighting.

Municipal solid waste, composed of domestic, commercial and public waste, was discarded at the Valdemingómez landfill, whereas hazardous and hospital waste was treated by an incinerator located within the landfill area. Figure 1 depicts the composition of the domestic waste of the Community of Madrid, while commercial and public wastes were composed, respectively, of 34% and 32% of organic materials.

While this study was being developed, a plan for solid waste management was implemented to radically change collection and final disposal of waste from the Community of Madrid.

## 3. Methodology

Initially a survey of the physical properties of the MSW landfill was carried out (inspection phase) by means of SPT tests, samples recovery for visual inspection, geophysical tests with spectral analysis of surface waves, electromagnetic sounding, in situ density tests and water content determination.

Five boreholes were constructed using a mechanical rotary drilling rig. Samples were recovered for visual analysis and determination of waste composition, and SPT tests were executed at intervals of 2 and 3 m. The boreholes were lined with casing to prevent collapse of the inside walls and to permit continuous sample recovery; casing was installed with the aid of water, although drilling was dry. The initial plan was to drill down to the natural substrate; however,

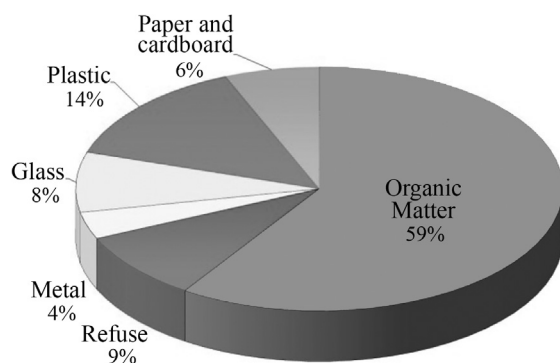


**Figure 1** - Gravimetric composition of domestic waste from the Community of Madrid (Plan of management of solids waste from the Community of Madrid, 1997-2005).

due to difficulties arisen during the execution of the first borehole, *i.e.* solid waste obstacles and emanation of gas and leachate, a 20-m depth was established for the remaining boreholes.

The survey also comprised 5 electromagnetic tests along a longitudinal profile located in the NW/SE direction, at 50-m intervals, carried out with a Transient Electromagnetic (TEM) equipment. The apparatus has two antennas: one transmits an electric current in the form of pulses of alternate signal, generating a primary magnetic field according to Ampère's Law and, consequently, diffusive currents in the interior of the waste mass according to Faraday's Law. Decrease in the diffusive currents generates a secondary magnetic field of low amplitude and rapid decrease, captured by the second antenna (receiver). Decrease in the intensity of the secondary field depends on conductive characteristics of the subsoil.

Two tests of Spectral Analysis of Surface Waves (SASW) were carried out in the landfill. SASW constitutes a non-destructive method to obtain surface wave velocity. Its rapid execution offers advantages when compared to other techniques which require borehole drilling, such as cross-hole and down-hole.

After the inspection phase, instruments were installed inside the waste mass and a trial soil embankment was built over the MSW landfill surface to perform as a test load (Fig. 2). The site selected for the load test was an area of approximately 2 ha and a thickness of 33 m of waste with a maximum age of 4 years. Most of the waste had been deposited and spread without mechanical compaction, and part of the waste had been deposited in the form of compressed blocks. Before starting the load test, the area was sealed with a 0.80 m-thick soil layer and surrounded by a 0.80 m-high soil dike. The trial soil embankment was built with a height of 4 m, a width of 20 m and a length of 40 m, equivalent to a vertical surcharge of 64 kN/m<sup>2</sup>.

Exploration tests were performed over the entire area; however, auscultation equipments were installed only



**Figure 2** - Construction of the trial soil embankment.

where the waste had been operated as usual, *i.e.* discharge and spread. The second (auscultation) phase, which took place for 19 months, consisted of a campaign of sounding tests comprising 18 reference points, a fixed reference in order to generate absolute values for the topographical ref-

erence points, a sliding micrometer, 2 continuous settlement lines, 1 inclinometer and 1 thermistance line, located according to Fig. 3.

The position immediately after the construction of the soil embankment was assumed as the zero reference, con-

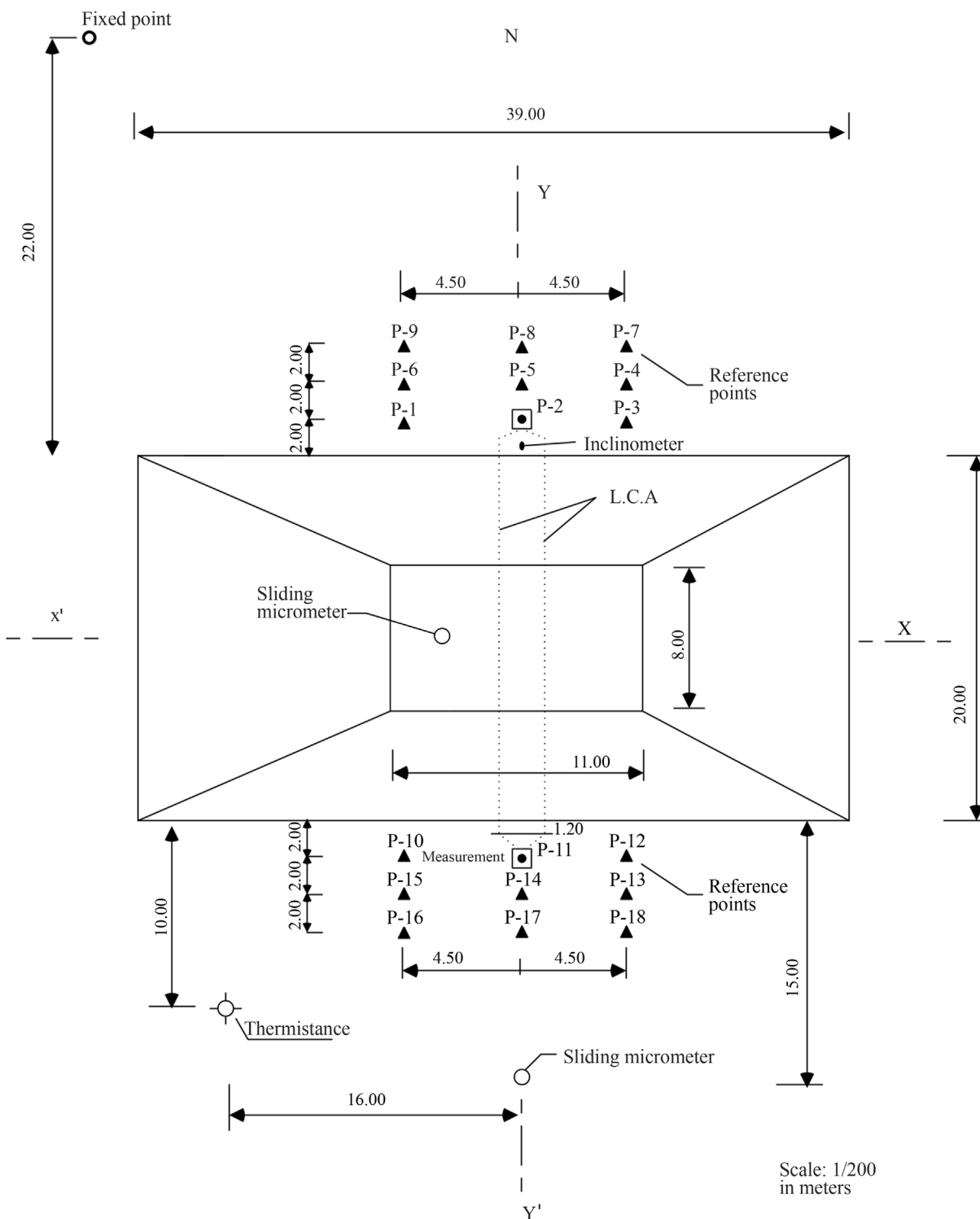


Figure 3 - Layout of the embankment and equipments for the auscultation phase.

sidering that previous stresses and compression in the waste mass during the disposal operations were much lower than those induced by the test load.

The continuous settlements lines (LCA in Fig. 3) allowed measurement of displacements at several depths below the surcharge load and of settlement evolution at two parallel cross sections located near the bisector of the largest sides of the trial embankment. Measurements from the continuous lines and the reference points located near the embankment were applied to evaluate immediate and primary displacements.

A Sliding Micrometer to measure secondary displacements was installed at a 15-m horizontal distance from the embankment, outside the influence area of the load test, in order to guarantee that immediate and primary settlements due to waste self-weight had already occurred during the landfill operation and before the construction of the soil embankment for the load test. Time zero was considered as that corresponding to the end of waste disposal. This apparatus was developed by the Zurich Federal Institute of Technology (Switzerland) and measures axial displacement along depth.

#### 4. Inspection Tests in the Landfill Area

##### 4.1. SPT tests

Results in Fig. 4 show a great dispersion due to the presence of obstacles of voluminous waste. If the pair of abnormal results is disregarded, N-value would be in the range 5-15 and resistance would show an increase with depth as described by Marbri (1977), Carvalho & Villar (1998) and Jucá *et al.* (2000).

##### 4.2. Unit weight

The bulk unit weight of MSW landfills is difficult to evaluate because of the heterogeneous composition of the material, the variety in size of the components and the presence of soil cover layers. The bulk unit weight of the waste was determined in situ, excavating a trench 1.5 m long, 1.0 m wide and 0.5 m high in the waste mass after removal

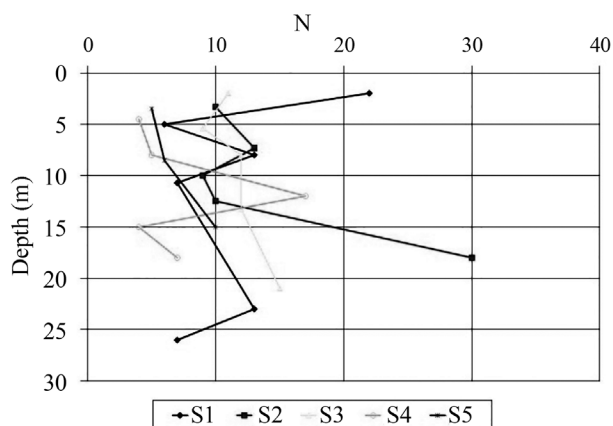


Figure 4 - Results of SPT tests.

of a 0.80-m thick soil cover. The obtained density of 5.0 kN/m<sup>3</sup> is consistent with fresh and loose (not compacted) waste.

##### 4.3. Water content

The water content within the waste mass is influenced by initial composition, climatic conditions, construction method, presence of internal drainage system for leachate (non-existent in this case), landfill cover, moisture generated by biological processes, and amount of water eliminated by the gases generated in the landfill.

Water content ranged from 13 to 70% (Fig. 5). The peak value of 70% measured at 16 m depth, confirmed by electromagnetic tests, was associated to a leachate pocket. Leachate pockets generally occur inside the waste mass in the absence of an internal drainage system. This also explains the large amount of leachate expelled when the first borehole reached the depth of 16 m.

##### 4.4. Spectral analysis of surface waves

Figure 6 shows results obtained with Spectral Analysis of Surface Waves. Tangential wave velocity varied from 210 m/s to 100 m/s within the top layer (0 to 1-m depth), and increased from 100 m/s up to 250 m/s with depth. At a depth of 33 m the natural subsoil surface was reached, where wave velocity reached 800 m/s. Rigidity is higher in the superficial layer because it is constituted of a soil cover. A velocity of 210 m/s was measured in the upper 0.20 m of this layer, which could be the effect of compression by trucks or of desiccation (Cuéllar & Valerio, 2000).

Results for the depths between 1 m and 33 m are within the variation range of 50-350 m/s indicated by Singh & Murphy (1990), Sharma *et al.* (1990), Kavazanjian *et al.* (1994) and Del Greco *et al.* (2007).

Tangential wave velocity varies with depth and age of solid waste (Kavazanjian & Matasovic, 1995; Matasovic & Kavazanjian, 1998). Haker *et al.* (1997) add type of waste, density, confinement, disposal method and soil content as influential factors, while adverting that it is difficult to ascertain the separate influence of each factor. The authors

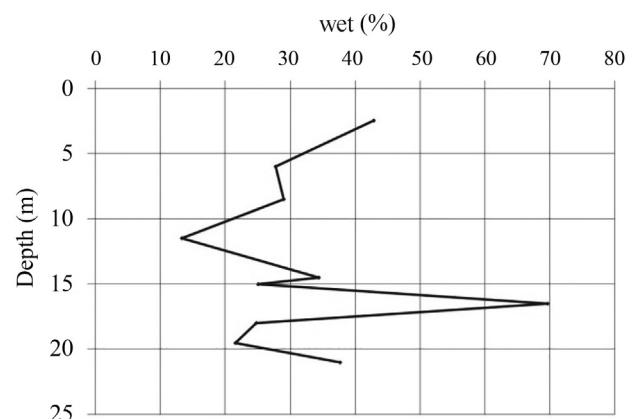


Figure 5 - Variation of water content with depth.

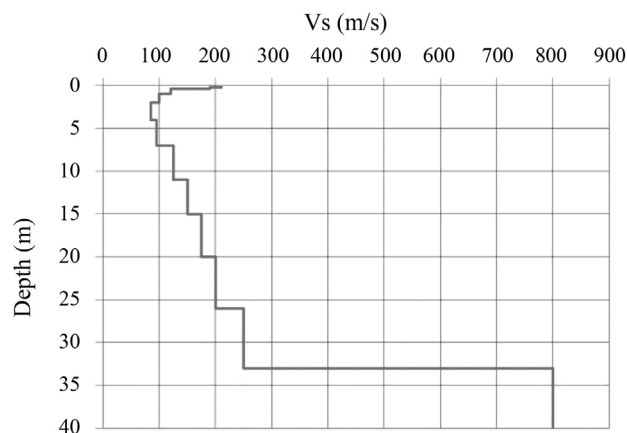


Figure 6 - Velocity profiles.

measured wave velocities at three landfills with a variation range of 122 m/s to 365 m/s.

Shear modulus ( $G$ ) was calculated by:

$$G = \rho V_s^2 \quad (1)$$

where  $G$  = shear modulus (MPa),  $V_s$  = tangential wave velocity (m/s),  $\rho$  = bulk unit weight ( $= 500 \text{ kg/m}^3$ ).

$G$  values depend significantly on the bulk unit weight. Fasset *et al.* (1994), Kavazanjian *et al.* (1995) and Jessberger (1996) suggest that MSW bulk unit weight increases with depth as a result of compression under self-weight, loads, machinery activities and soil covers. However,  $G$  was calculated considering a constant bulk unit weight equal to the value obtained by trench excavation due to the operational difficulty of repeating this test at greater depths.

Excluding the soil cover, the shear modulus  $G$  increases with depth from 7.2 MPa to 31 MPa (Fig. 7) at a bulk unit weight of  $5 \text{ kN/m}^3$  ( $500 \text{ kf/m}^3$ ).  $G$  obtained by cross-hole tests for the Richmond landfill in California, USA, was 30 MPa for a bulk unit weight of  $7.3 \text{ kN/m}^3$  (Sharma *et al.*, 1990), and 8.0 MPa for the Bandeirantes

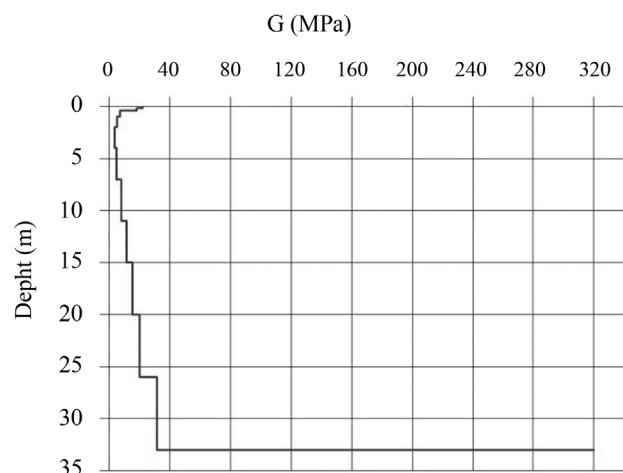


Figure 7 - Shear modulus as a function of depth.

landfill in Sao Paulo, Brazil, at a bulk unit weight of  $8.0 \text{ kN/m}^3$  (Carvalho, 1999).

#### 4.5. Electromagnetic tests

Figure 8 summarizes results of five electromagnetic tests performed in a longitudinal profile in the investigation area and includes the original geometry of the terrain surface. Four distinct layers can be observed:

- The superficial or top layer, extending until a depth of 7-12 m, where two zones can be differentiated: compressed waste blocks with a resistance of 60-80 ohm-m and loose waste with a resistance of 200-500 ohm-m.
- The second layer, not continuous and showing a lower resistance, between 20 and 30 ohm-m, possibly due to a partial contamination by leachate.
- The third layer, homogeneous and very conductive (resistance of 0.6 ohm-m) due to saturation by leachate, behaving as a piezometric level.
- Finally, the soil substrate upon which the MSW landfill is founded, displaying a resistance of 100 ohm-m. The bedrock was identified (900 ohm-m) at a spot located 5 m below the subsoil surface.

#### 5. Auscultation Phase

The auscultation phase begun with the installation of equipments to measure vertical and horizontal displacements as a function of time and surcharge load, and temperature variation as a function of depth. A trial soil embankment was built to act as load test, and the area was monitored for 19 months.

Significant settlements started 7 days after the construction of the experimental embankment was finalized. Readings were taken every 10 days during the first month and thereafter at intervals of 30 and 60 days.

##### 5.1. Reference points

In order to measure vertical displacements caused by the surcharge, 18 reference points were installed at the northern and southern sides of the embankment (Fig. 3). Displacements are referred to a fixed point especially installed for this purpose.

Figures 9 and 10 show the evolution of settlements with time obtained, respectively, in the northern and southern sides of the landfill. Settlements are greater in the southern than in the northern side, what could be explained by the significant heterogeneity of the waste mass.

The immediate settlement was considered as that developed during the first 7 days after the completion of the trial embankment. The average immediate settlement was 0.066 m on the northern side and 0.061 m on the southern side.

After 100 days average settlements were approximately 0.40 m at both sides of the embankment. In the end of the monitoring period, 19 months, average settlements were 1.23 m on the southern side and 1.06 m on the north-

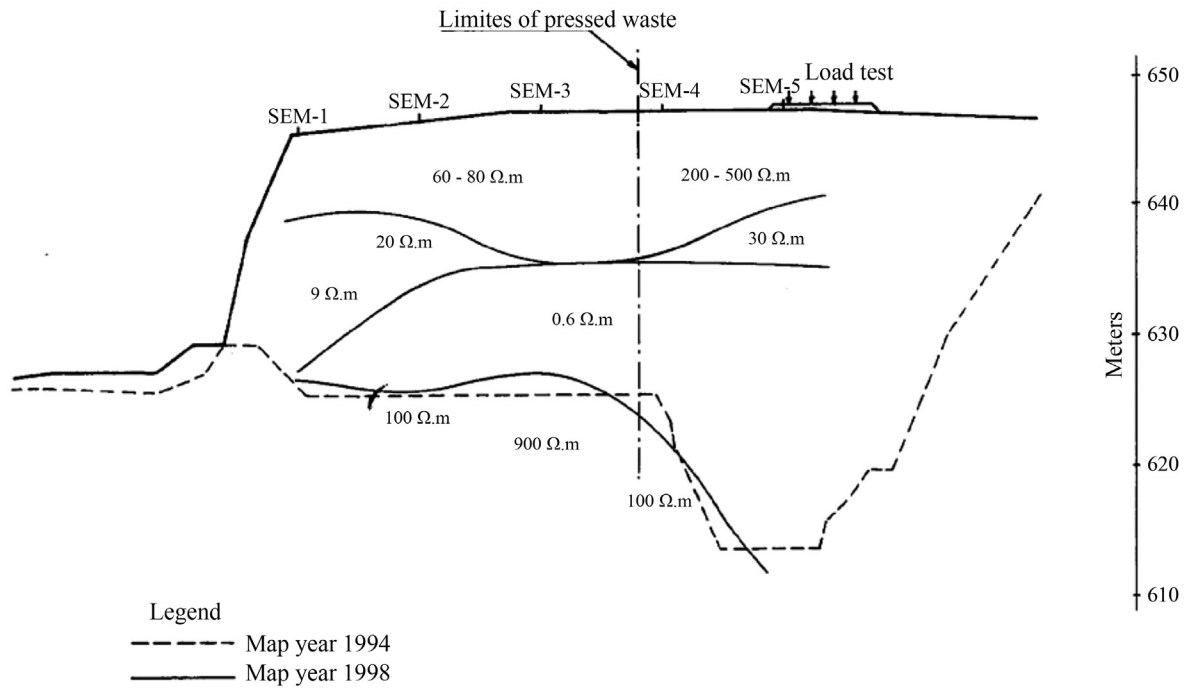


**Figure 8** - Profile obtained from electromagnetic tests.

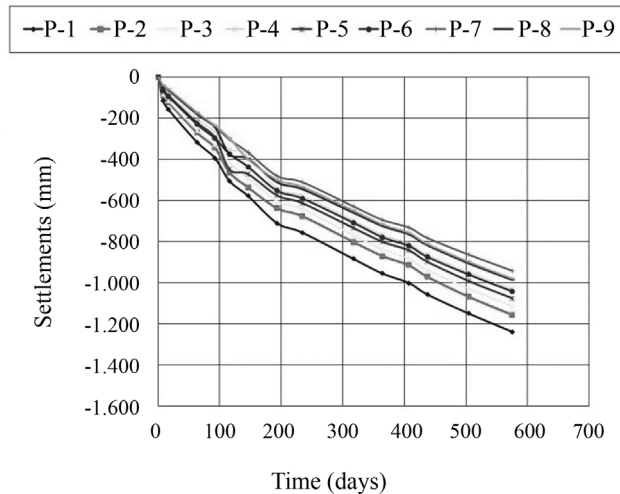


**Figure 9** - Vertical displacements - Northern side.

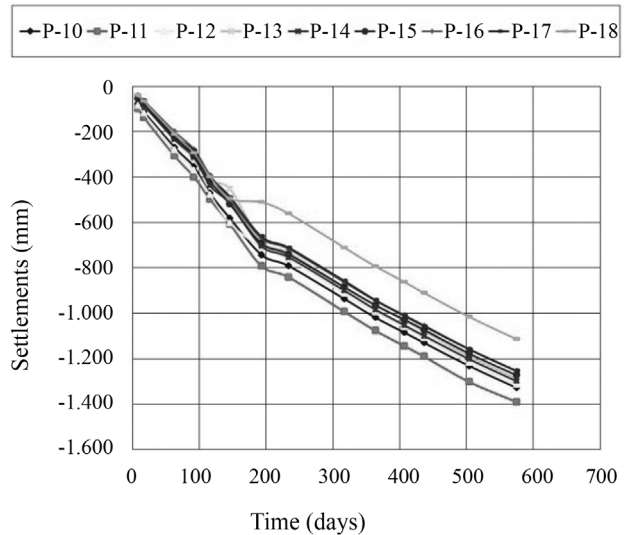


**Figure 10** - Vertical Displacements - Southern side.

ern side, corresponding to specific deformations (relative to the average height of the landfill, 33 m) of 3.9% and 3.2% respectively.

**5.2. Continuous settlement lines**

The two continuous settlement lines showed similar settlements during the entire monitoring period (Figs. 11 and 12). Initial settlements measured seven days after the construction were approximately 0.50 m in the embankment centre (point 12 of each line) and 0.15 m in the ex-

termities. Long term settlement was approximately 2.0 m in the centre and 1.4 m in the extremities of the embankment. Settlements measured in the extremities of the lines are very close to those obtained through the reference points.

Immediate settlement was used to calculate Young's modulus based on the hypothesis of a flexible plate resting on a semi-infinite space (Eq. 2):

$$E = \frac{Kqb(1-v^2)}{S_i} \quad (2)$$

where  $E$  = Young's or elastic modulus ( $\text{kN/m}^2$ ),  $K$  = coefficient ( $n = 40/20 = 2$ ),  $q$  = surcharge ( $64 \text{ kN/m}^2$ ),  $b$  = rectangle side (20 m),  $v$  = Poisson coefficient (0.3),  $S_i$  = immediate settlement (0.50 m).

The calculated elastic modulus is  $1864 \text{ kN/m}^2$ , consistent with the values for domestic waste of  $1000\text{-}2000 \text{ kN/m}^2$  appointed by Charles (1984) and  $1000\text{-}4000 \text{ kN/m}^2$  by Campi (2011).

Figure 13 shows that settlement velocity obtained from the continuous settlement lines decreases with time, more significantly in the first 100 days and apparently asymptotically for longer times. Initial higher velocities are related to immediate and primary settlements. The varia-

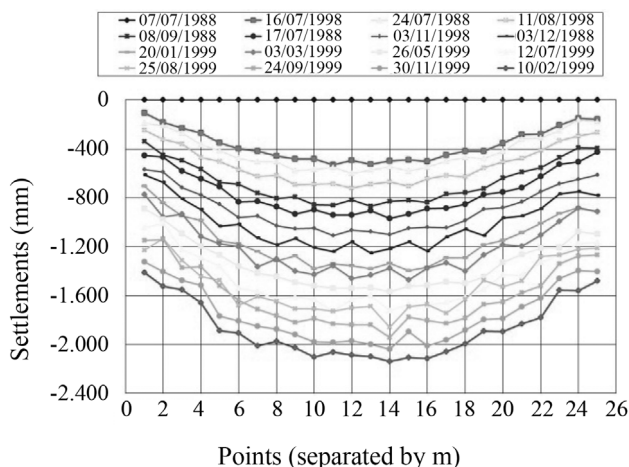


Figure 11 - Evolution of settlements of the trial embankment, Section 1.

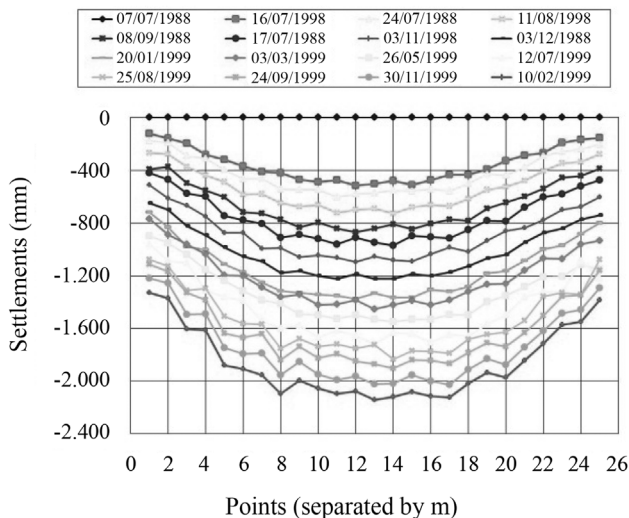


Figure 12 - Evolution of settlements of the trial embankment, Section 2.

tion amplitude is considerable: for the two continuous settlement lines, average velocity decreases from  $64.0 \text{ mm/day}$  to  $3.6 \text{ mm/day}$  in 19 months. The decrease of settlement velocity with time is a consensus for the great majority of authors in the specialized literature (Sowers, 1973; Frantzis, 1991; König & Jessberg, 1997; Carvalho, 1999; Abreu, 2000).

### 5.3. Sliding micrometer

Figure 14 shows measured differential settlement as a function of depth and time. Considering each time, measured settlements are very variable with depth; however, results are consistent: layers that show smaller or larger settlements at distinct dates are the same during the entire monitoring period. The variation can be explained by the presence of soil, which is less deformable, between waste layers; by the heterogeneity of the soil mass, with zones of more deformable materials; by different densities; and by variations in water content. A higher settlement is observed at depth 2-3 m, consistent with a water content of 43% at

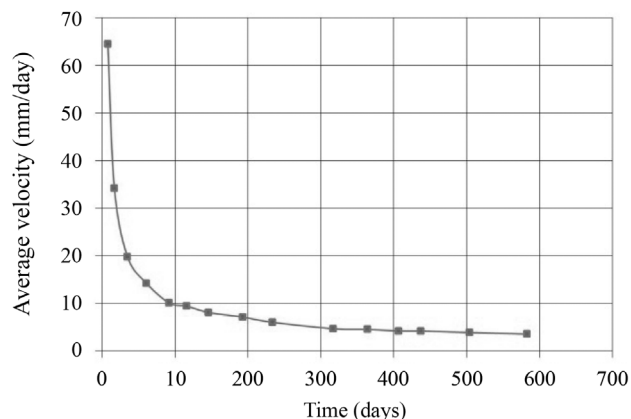


Figure 13 - Variation of velocity as a function of time.

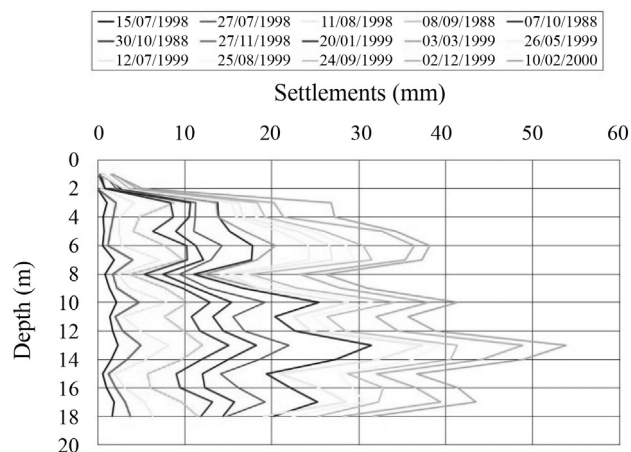


Figure 14 - Secondary settlement measured by the sliding micrometer.

the depth of 2.5 m; while the lowest water content, 13%, occurred at a depth that developed low settlements. Likewise, a water content of 70% was registered at a depth of 16.5 m, while from depth 16-17 m deformation was considerably larger than at 15 m, where the water content was 25%.

It should be noted that excessive differential settlements can lead to fissures or cracks in the internal drainage systems for leachate and gases, as well as in the landfill cover. Fig. 15 shows accumulated secondary settlements as a function of time and depth.

Accumulated secondary settlements amounted to 0.60 m after 19 months of monitoring at the depth of 18 m. Secondary settlements are caused by two processes: creep, which occurs under constant stress and water content conditions, and decomposition of organic matter. The first process is influenced by landfill height and compaction degree (Charles, 1984), and the second process, by environmental conditions, such as water content, temperature, pH and waste composition.

### 5.4. Inclinometer

The inclinometer was installed inside borehole S2. For each inclinometer, the bottom extremity was considered as a reference point with zero horizontal movement.

Due to the occurrence of settlements that resulted in the accommodation of the inclinometer tube, it was not possible to measure horizontal displacements along the entire depth and to calculate accumulated horizontal displacements.

Figures 16 and 17 present horizontal displacements as a function of depth for directions AB and CD. It can be noticed that measured horizontal displacements are small. The influence of the surcharge load from the trial embankment is much more significant on vertical than on horizontal displacements. The influence of the surcharge load is

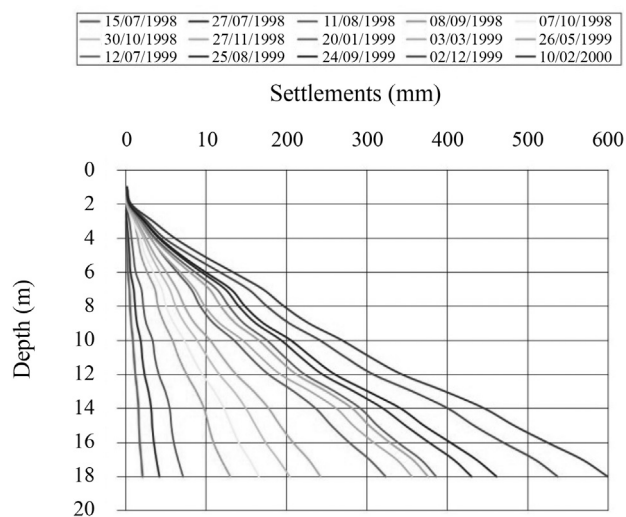


**Figure 15** - Accumulated secondary settlements measured by the sliding micrometer.

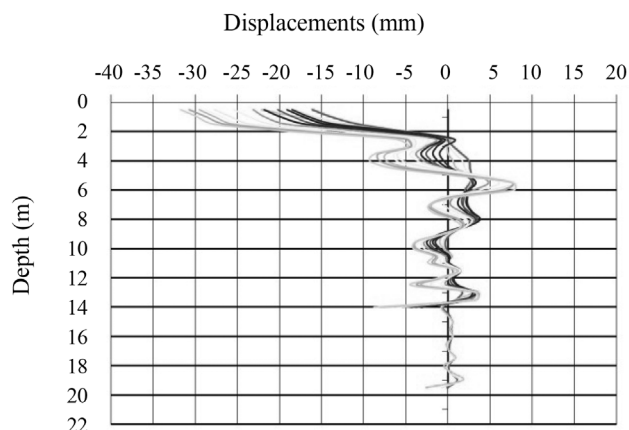


**Figure 16** - Inclinometer measurements for direction AB: positive displacement towards North.

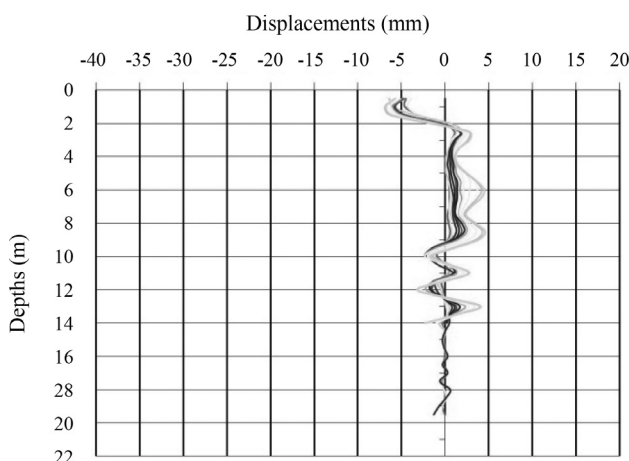


**Figure 17** - Relative inclinometer measurements for direction CD: positive displacement towards East.

superficial and reaches just about the depth of 2.5 m (Fig. 16), causing a maximum horizontal displacement of 0.030 m. At a depth of 4 m a maximum displacement of 0.009 m was measured, and displacements tend to zero with increasing depth. The oscillations of positive and negative horizontal displacements below a depth of 4 m can result from the presence of soil layers inside the waste mass.

In the direction parallel to the embankment axis (Fig. 17), the maximum displacement is 0.005 m at a depth of 2 m. In this direction displacements are less pronounced than in the perpendicular direction.

These results are consistent with observations of Coducto & Huitric (1990) and Siegel *et al.* (1990): higher displacements occur near the landfill surface, while displacements tend to zero at increasing depths; and displacements mainly occur in the direction perpendicular to the embankment axis, while no significant movements were measured in the direction parallel to the embankment.

Velocity of the horizontal displacements is apparently not correlated to rain periods, since seasons changed along the monitoring period whereas no variation in the velocity was observed.

The ratio between horizontal and vertical displacements due to the surcharge load of the trial embankment is very low (less than 1-2%) and shows that there is an unimportant lateral transmission of the load influence. This can be reported to the low bearing capacity of waste, which behaves as a loose soil and leads to a puncture or indentation of the embankment into the waste material, with very moderate lateral effects (low equivalent Poisson coefficient) compared to the remarkably large vertical displacements.

**5.5. Thermistance line**

Temperature profiles were obtained from 21 temperature sensors installed inside the boreholes (Fig. 18) in order to investigate a relation of temperature to processes of biochemical decomposition inside the waste mass.

Temperature varies between 30 °C and 55 °C in the superficial layer (0 to 5 m), and rises progressively with depth until 63 °C to 70 °C at a depth of 20 m.

The high temperature values, associated to available water content (Fig. 5) and high organic matter content (Fig. 1), indicate that the waste mass undergoes a very active decomposition process, as expected for fresh waste, and suggest a significant methane production.

Figure 19 highlights temperatures registered in July and December 1998, corresponding to summer and winter seasons in Spain. It is interesting to observe that temperature fluctuation is only reflected down to a depth of 12 m; at greater depths temperatures measured during winter are equal or even higher than those measured during summer. These data confirm results obtained by Rees (1982), Coumoulous *et al.* (1995) and Junqueira & Palmeira (1999).

**6. Conclusions**

Visual inspection revealed that the waste was in an advanced stage of decomposition, despite the maximum age of 4 years. In situ investigation indicated water contents

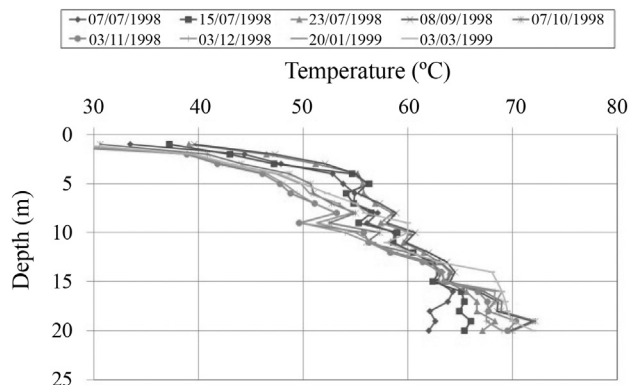


Figure 18 - Variation of temperature with depth.

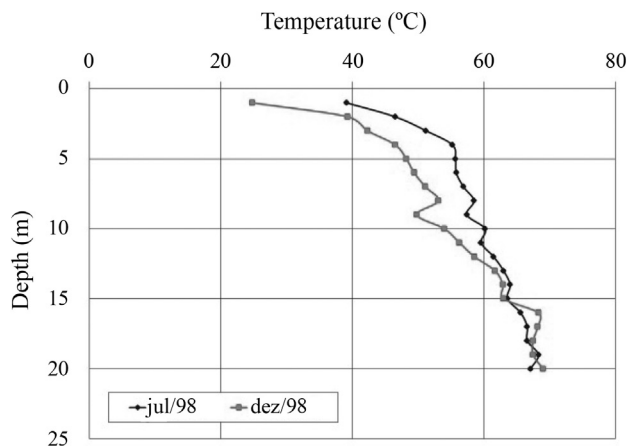


Figure 19 - Temperature variation between winter and summer.

of 13% to 70% and occurrence of leachate pockets. Electromagnetic scans divided the landfill in zones with different resistances depending on leachate content. Saturation by leachate in the bottom layers was detected by results of electromagnetic tests and mechanical drilling. SPT results showed a significant dispersion (N values between 6 and 63), probably because of obstacles of voluminous waste. Estimated Young's modulus is approximately 1900 kN/m<sup>2</sup>. Spectral analysis of surface waves indicated that rigidity of the waste mass increases with depth (shear modulus increases from 7 to 31 MPa with depth), as a result of compression by self-weight.

The auscultation campaign after the construction of the soil embankment as a trial test load exposed that the settlement velocity decreased from 64.0 mm/day after the construction of the embankment to an asymptotic value of 3.6 mm/day in 19 months. In the embankment extremities, immediate settlements were measured as 0.06-0.15 m and settlements after 19 months, as 1.0-1.4 m. In the embankment centre, immediate settlements were 0.50 m and settlements after 19 months, 1.5 m. Accumulated secondary settlements amounted to 0.600 m after 19 months of monitoring. The ratio of horizontal to vertical displacements due to the load test is very low, of 1-2%, characterizing the behavior of a loose material.

Settlements developed along this study, caused both by surcharge and biodegradation, were of great magnitude and therefore characterize the landfill material as highly deformable. Furthermore, results indicate that secondary compression represents 55% of the total settlements; this percentage will increase with time, since settlements induced by surcharge load take place in a short time, while secondary settlements continue to develop over the years.

The analysis of settlement velocity as a function of time curves suggests that primary settlements occurred during approximately 100 days. This period of time is higher than that proposed by Sowers (1973), but is in accordance

with results from other authors (Bjarngard & Edgers, 1990; Stulgis *et al.*, 1995; Fasset *et al.*, 1994).

Secondary settlements during the investigation amounted to 3% of the landfill height. The occurrence of secondary settlements can be related to the high temperatures measured inside the landfill, up to 70 °C at a depth of 20 m, which indicate the existence of intensive biochemical activity. Furthermore, these high temperatures are unrelated to seasonal variations.

The sliding micrometer tests indicated the existence of layers with different deformability, consistent with the water content profile and also explained by the heterogeneity of the waste mass and the presence of soil cover layers.

## Acknowledgments

The authors would like to thank Centro de Estudios y Experimentación de Obras Publicas (CEDEX – Madrid, Spain), especially Director Vicente Cuellar and Field Investigation Chief Luis Quero for the laboratorial infrastructure used in this investigation, and Ibero-American Cooperation Program Mutis for the Ph.D. scholarship.

## References

- Abreu, R.C. (2000) Compressibility of sanitary landfills. MSc Thesis, Department of Structural and Geotechnical Engineering, Polytechnic School of Engineering, University of São Paulo, Sao Paulo, Brazil, 241 p. (in Portuguese).
- Autonomous Community of Madrid (1998) Plan of management of solids waste from the Community of Madrid (1997-2005). Official Spanish Report, BOCM n° 13, Spain (in Spanish).
- Bjarngard, A. & Edgers, L. (1990) Settlement of municipal solid waste landfills. Proc. 13<sup>th</sup> Annual Madison Waste Conference, University of Wisconsin, Madison, USA, p. 192-205.
- Carvalho, M.F. (1999) Geotechnical behavior of municipal solid waste. Ph.D. Thesis, Department of Geotechnics, Engineering School of São Carlos, University of São Paulo, São Carlos, Brazil, 330 p. (in Portuguese).
- Carvalho, M.F. & Vilar, O. M. (1998) In-situ tests in urban waste sanitary landfill. Proc. 3<sup>th</sup> International Congress on Environmental Geotechnics - ICEG, Seco e Pinto, P.S. (ed), Balkema, Rotterdam, Netherlands, p. 121-126.
- Charles, J.A. (1984) Settlement of fill. Attewell, P.B. & Taylor, R.K. (eds) *Ground Movements and Their Effects on Structures*, Surrey University Press, New York, USA, p. 26-35.
- Campi, T.M.O. (2011) Evaluation of MSW shear strength parameters and elastic modulus by means of static load tests in a sanitary landfill. Department of Structural and Geotechnical Engineering, Polytechnic School of Engineering, University of São Paulo, Sao Paulo, Brazil, 117 p. (in Portuguese).
- Coumoulos, D.G.; Koryalos, T.P.; Metaxas, I.L. & Gioka, D.A. (1995) Geotechnical investigation at the main landfill of Athens. Proc. 5<sup>th</sup> International Waste Management and Landfill Symposium, Cagliari, Italy, p. 885-895, CD-ROM.
- Coduto, D.P. & Huitric, R. (1990) Monitoring landfill movements using precise instruments. Landva, A. & Knowles, G.D. (eds) *Geotechnics of Waste Fills - Theory and Practice*, American Society for Testing and Materials – STP 1070, Philadelphia, USA, p. 358-370.
- Cuéllar, V. & Valerio, J. (2000) Aplicaciones geotécnicas del análisis espectral de ondas superficiales. Book Tribute to J.A. Jimenez Salas, Geotechnics in Year 2000, CEDEX, Spain, p. 301-310 (in Spanish).
- Del Greco, O.; Fassino, A. & Godio, A. (2007) Seismic investigation for the assessment of the elastic settlement in MSW landfill. Proc. 11<sup>th</sup> International Waste Management and Landfill Symposium, Cagliari, Italy, CD-ROM.
- Fasset, J.B., Leonards, G.A. & Repetto, P.C. (1994) Geotechnical properties of municipal solid waste and their use in landfill design. Proc. Waste Technical Conference, National Solid Wastes Association, Charleston, USA, p.1-31.
- Frantzis, I. (1991) Settlement in the landfill site of Schisto. Proc. 3<sup>rd</sup> International Waste Management and Landfill Symposium, Cagliari, Italy, CD-ROM.
- Haker, C.D.; Rix, G.J. & Lai, C.G. (1997) Dynamic properties of municipal solid waste landfills from surface wave tests. Proc. 10<sup>th</sup> Symposium on the Application of Geophysics to Engineering and Environmental Problems, Environmental and Engineering Geophysical Society – SAGEEP, Wheat Ridge, USA, p. 301-310.
- Jucá, J.F.T.; Melo, V.L.A. & Monteiro, V.E.D. (2000) Dynamic penetration tests in solid waste landfills. Proc. 9<sup>th</sup> Luso-Brazilian Symposium of Environmental and Sanitary Engineering - SILUBESA, Porto Seguro, Brazil, CD-ROM, (in Portuguese).
- Jessberg, H.L. (1996) TC5 activities. Proc. 2<sup>th</sup> International Conference on Environmental Geotechnics, Kamon, M. (ed), Balkema, Rotterdam, Netherlands, p. 1227-1254.
- Junqueira, F.F. & Palmeira, E. (1999) Monitoring waste behavior in geotechnically prepared cells. Proc. 4<sup>th</sup> Brazilian Congress on Environmental Geotechnics - REGEO, Brazilian Society for Soil Mechanics and Geotechnical Engineering – ABMS, São José dos Campos, Brazil, p. 428-433, (in Portuguese).
- Kavazanjian, E.; Snow, M.S.; Matasovic, N.; Poran, C.J. & Satoh, T. (1994) Non-intrusive Rayleigh wave investigations at solid waste landfill. Proc. First Int. Conference on Environmental Geotechnics - ICEG, International Society for Soil Mechanics and Geotechnical Engineering - ISSMGE, Edmonton, Canada, p. 707-712.

- Kavazanjian, E. & Matasovic, N.P. (1995) Seismic analysis of solid waste landfills. Yalcin, B.A. & Daniel, D.E. (eds) *Geoenvironmental 2000*, Geotechnical Special Publication GSP 46, 2, ASCE, New Orleans, p. 1066-1080.
- Konig, D. & Jessberger, H.L. (1997) Report of the Technical Committee 5 (Environmental Geotechnics). Sub Committee 3 (Waste Mechanics). International Society for Soil Mechanics and Geotechnical Engineering - ISSMGE, Hamburg, p.35-51.
- Matasovic, N. & Kavazanjian, E. (1998) Cyclic characterization of OII Landfill solid waste. *Journal of Geotechnical and Geoenvironmental Engineering*, v. 124:3, p. 197-210.
- Marbri, E.R. (1977) Building development on a municipal refuse fill. Proc. Conf. on Geotechnical Practice for Disposal of Solid Waste Material. Specialty Conference of the Geotechnical Engineering Division, ASCE, Univ. of Michigan Ann Arbor, p. 795-809.
- Rees, J.F. & Grainger, J.M. (1982) Rubbish dump or fermentation? Prospects for the control of refuse fermentation to methane in landfills. *Process Biochemistry*, v. 17:6, p. 41-44.
- Sharma, H.D.; Mechae, T.D. & Olsen, D.M. (1990) Field measurements of dynamic moduli and Poisson's ratios of refuse and underlying soils at a landfill site. Landva, A. & Knowles, G.D. (eds) *Geotechnics of Waste Fills - Theory and Practice*, American Society for Testing and Materials – STP 1070, Philadelphia, USA, p. 57-70.
- Siegel, R.A.; Robertson, R.J. & Anderson, D.G. (1990) Slope stability investigation at a landfill in southern California. Landva, A. & Knowles, G.D. (eds). *Geotechnics of Waste Fills - Theory and Practice*, American Society for Testing and Materials – STP 1070, Philadelphia, USA, p. 259-284.
- Singh, S. & Murphy, B. (1990) Evaluation of the stability of sanitary landfills. Landva, A. & Knowles, G.D. (eds) *Geotechnics of Waste Fills - Theory and Practice*, American Society for Testing and Materials – STP 1070, Philadelphia, USA, p. 249-258.
- Sowers, G.F. (1973) Settlement of waste disposal fills. Proc. 8<sup>th</sup> Int. Conf. on Soil Mechanics and Foundation Engineering, ISSMFE, Moscow, Russia, v. 2, p. 207-210.
- Stulgis, R.P.; Soydemir, C. & Telgener, R.J. (1995) Predicting landfill settlement. Yalcin, B.A. & Daniel, D.E. (eds) *Geoenvironmental 2000*, Geotechnical Special Publication GSP 46, ASCE, New Orleans, USA, p. 980-984.

### List of Symbols

- $G$  = shear modulus  
 $V_s$  = tangential wave velocity  
 $\rho$  = bulk unit weight  
 $E$  = Young's or elastic modulus  
 $K$  = Schleicher coefficient  
 $q$  = surcharge  
 $b$  = rectangle side  
 $\nu$  = Poisson coefficient  
 $w$  = water content  
 $S_i$  = immediate settlement  
 $N$  = SPT result